School of Electrical Engineering, Computing and
Mathematical Sciences

International Centre for Radio Astronomy Research

A forensic examination of remnant radio galaxies and the implications for AGN life-cycles

Benjamin Quici

This thesis is presented for the Degree of
Doctor of Philosophy
of
Curtin University of Technology

July 2023

To the best of my knowledge and belief this thesis contains no material previously published by any other person except where due acknowledgement has been made. This thesis contains no material which has been accepted for the award of any other degree or diploma in any university.

Benjamin Quici

"*One day, when you grow up, you're going to build me a rocket and send me to the stars.*"

— My grandmother

Acknowledgements

First and foremost, I acknowledge the Noongar people as the owners and custodians of Wadjak Noongar Boodjar, the land on which the majority of this work was completed.

Undertaking this thesis has undoubtedly proven to be my most demanding, yet profoundly rewarding, accomplishment to date. In the beginning, back in 2019, I felt out of my depth and unsure of my abilities. However, through four years of independent research, I've gained genuine self-confidence and the belief that I can conquer any challenge that comes my way. Getting to where I am today would not have been possible without the care, support, and guidance provided to me by so many people along this journey. To all of you, no matter how large or small your contribution was, thank you.

To all my academic peers and colleagues with whom I have shared this journey, it has been an absolute privilege to collaborate and learn from such a talented and insightful group of individuals. To my supervisors, Nick, Natasha, and Ross, without you I simply would not be here.

Nick, I owe you a special thank you for igniting that spark back in my third-year undergraduate project for the fascinating world of extended radio galaxies. Despite not originally being a part of this research project, you came on anyway to make sure that the project could continue. Thank you for always providing unique suggestions and advice, and for all those whiteboard brainstorms that will sorely be missed!

Natasha, thank you for treating me as your research equal from the very first

week I started this thesis. You have always valued my insights into radio galaxy physics, even at times when you likely had the better understanding. Thank you for always going out of your way to celebrate my wins with me, no matter how big or small, and for making it known that you were proud of my achievements.

Ross, I want to extend a massive debt of gratitude to you for taking interest in an early-career researcher, who at the time was still trying to find his footing in the field. For almost a year you helped me formulate ideas and methodologies for my research papers, before even becoming my thesis supervisor. Thank you for all the time and dedication you gave to me, despite the timezone difference which often kept you up until midnight.

A special acknowledgement also goes out to my PhD sibling, Kathryn, who has been an unwavering presence throughout this journey. We have experienced many hardships, tears, celebrations, and laughs over these past four years, and I've been fortunate enough to become close friends with this wonderful person. Although it seems our careers have taken their own distinct trajectories, I will always be on the lookout for all the remarkable achievements coming your way.

My heartfelt gratitude goes out to all my family members for their unwavering support and pride in my accomplishments. To mum and dad, for always making life just that little bit easier when things were difficult. To my sister, Valerii, whose own personal academic achievements were a massive source of inspiration for me. To my uncle, aunty, and cousins, who were never short on praise and celebrations, particularly when my research papers were published.

Lastly, these acknowledgments would not be complete without acknowledging the never-ending support of my partner, Ellie. Her constant encouragement and belief in me have felt like a life-raft in the middle of an ocean, keeping me afloat during challenging times. Thank you, Ellie, for being my rock throughout this journey.

Abstract

An accreting super-massive black hole can launch relativistic jets into its intergalactic environment, leading to the formation of synchrotron-emitting lobes known as a radio galaxy. While most ($\gtrsim$ 90%) radio galaxies are observed in conjunction with active jets, the active galactic nucleus (AGN) is also known to switch off, resulting in a "remnant" phase wherein the lobes are cut off from their energy supply. Together with "restarted" radio galaxies, in which remnant lobes are observed concurrently with renewed jet activity, this observed 'life cycle' offers key evidence in support of a duty cycle in the jets of a radio-loud AGN. In this thesis I investigate how the energetics of AGN jets can be constrained and studied through observations of remnant radio galaxies.

I begin by examining the feasibility of utilising the "absent radio core criterion" as a method to select remnant radio galaxies from survey data. Using a range of low-frequency instruments (0.1-9 GHz), I compile an observationally-complete sample of extended radio galaxies within $\sim 8\,\mathrm{deg}^2$. Sensitive ($\sigma \approx 45\,\mu$Jy/beam), high-frequency (5.5 GHz) observations are used to classify 10/104 radio galaxies as remnant candidates based on the absence of radio emission from the host galaxy. By studying their properties, I find that six of the ten selected candidates display bright regions of high-frequency emission in their lobes, suggesting either that the jets have only recently switched off, or that the objects are incorrectly classified due to the radio core failing to meet the detection threshold. I propose that while the absent radio core criterion is effective at selecting remnant radio galaxy candidates, the technique alone does not have the capability to

definitively rule out the existence of the AGN jets. The corresponding remnant fraction is constrained between 4-10%, which, although consistent with previous literature results, requires greater refinement to offer meaningful constraints on models of the AGN lifetime function.

With the emergence of new-generation all-sky radio surveys, studies of remnant radio galaxies will need to confront the general lack of complementary high-frequency ($\gtrsim 5\,\mathrm{GHz}$) survey data. Due to the preferential depletion of high-energy synchrotron emitting electrons, the shape of a radio source spectrum encodes the age of the underlying plasma. The steepening is exacerbated in the integrated spectrum of remnant lobes, which, when captured by sufficient high-frequency coverage, allows for a robust observation-based selection of remnant lobes and the modelling of the jet 'switch-off'. In this work, I develop a new simulation-based method to model the energetics of remnant lobes, which relies on spatially-resolved observations of the plasma backflow to constrain the off-time. I measure the fractional duration of the remnant phase, $R_{\mathrm{rem}} = 0.23 \pm 0.02$, in the remnant radio galaxy *J225337-344745* using standard spectral ageing techniques based on beam-matched, high-resolution imaging over a broad frequency range. I then constrain a dynamically-estimated remnant ratio of $R_{\mathrm{rem}} = 0.26^{+0.04}_{-0.03}$ by comparing the observed surface-brightness distribution of the remnant to synthetic radio sources generated by the *Radio-loud AGN in Semi-analytic Environments* (RAiSE) model. Using mock catalogues I show that with observations up to 1.4 GHz, the method is able to measure the jet power and active lifetime in remnants across a wide range of evolutionary histories.

In contrast to active lobes, which encode only the age of the jet at the time of observation, remnant lobes capture the full duration of the previously-active jet. In my final body of work, I select a sample of 79 nearby ($z < 0.2$) remnant radio galaxies from all-sky radio survey data, and utilise the technique presented above to fit the jet kinetic powers and jet lifetimes of the sample. I then simulate mock populations of remnant sources using independent power-law seed functions for

their jet powers and lifetimes. These simulations account for the sample selection biases, and are used to predict the observed jet powers and lifetimes. Comparing these predictions to the observed distributions in the sample, I constrain seed functions for the jet power function and jet lifetime function as $p(Q) \propto Q^{-1.50\pm0.09}$ and $p(t_{\rm on}) \propto t_{\rm on}^{-1.00\pm0.12}$, respectively.

Contents

List of Figures

Chapter 1

Introduction

1.1 The need for heating in galaxy evolution

The formation of large-scale structure in our Universe is a complex process driven by the interplay of dark and baryonic matter under the influence of gravity. Dark matter, which constitutes an overwhelming fraction of the total mass in the Universe (Page et al., 2003; Planck Collaboration et al., 2014), is attracted gravitationally to hierarchically form a complex web of large-scale structure (see Fig. 1.1). The formation of baryonic over-densities are subsequently driven by the accumulation of molecular gas within the gravitational potential wells of the dark matter haloes (Kravtsov & Borgani, 2012). The cooling and condensation of the gas eventually leads to the formation of galaxies (White & Rees, 1978), and give rise to most-massive gravitationally bound baryonic systems in the local universe – galaxy clusters.

In approximately one-third of galaxy clusters, a strong "cool core" region exists with high central density and low central temperature, capable of cooling within a few billion years (e.g. Chen et al., 2007; Hudson et al., 2010). This region, covering $\sim 10\%$ of the virial radius, is centered on the brightest cluster galaxy (e.g., White et al., 1997; Hudson et al., 2010; McDonald et al., 2012), for which the estimates of the mass cooling rate range between $\sim$ 100–1000$M_{\odot}$

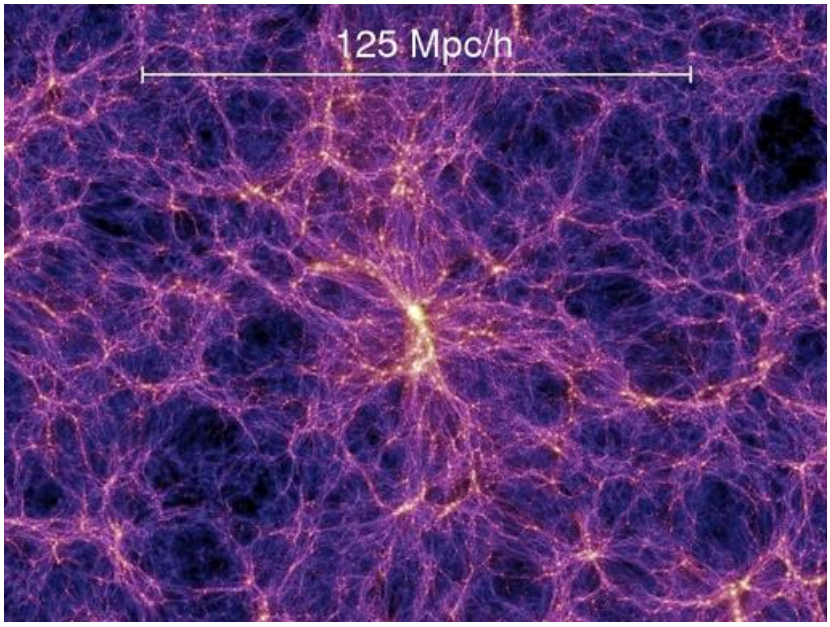

Figure 1.1: Predictions of the Bolshoi simulation for the redshift zero ($z = 0$) distribution of dark matter, for a slice of thickness $15h^{-1}$ Mpc. The matter surface density and local velocity dispersion are mapped to intensity and colour, respectively. Figure taken from Croton et al. (2006).

yr^{-1} (e.g., White et al., 1997; Peres et al., 1998; Allen et al., 2001; Hudson et al., 2010). Observations of the X-ray emitting cluster gas reveal that the cooling timescales are shorter compared to dynamical time (Lea et al., 1973), suggesting cooling flows should develop and deposit cold gas at cluster centers. However, observations consistently found far less cold gas and young stars than predicted (e.g., Johnstone et al., 1987; Heckman et al., 1989; McNamara & O'Connell, 1989; Crawford et al., 1999; Donahue et al., 2000; Edge, 2001; Edge et al., 2002; Hatch et al., 2005; O'Dea et al., 2008; McDonald et al., 2010, 2011; Hoffer et al., 2012; Molendi et al., 2016), which thus became known as the "cooling flow" problem.

By the late 20th century, the prevalence of low-luminosity radio emission (formally introduced in Sect. 1.2) in massive, early-type galaxies, particularly elliptical galaxies, was observed, with optical luminosity scaling proportionately (Sadler et al., 1989). This was further evidenced in S0 galaxies, as well as spiral galaxy bulges (see review by; Sadler, 1990). Fabbiano et al. (1989) explored the relationship between the hot interstellar medium (ISM) and nuclear radio sources

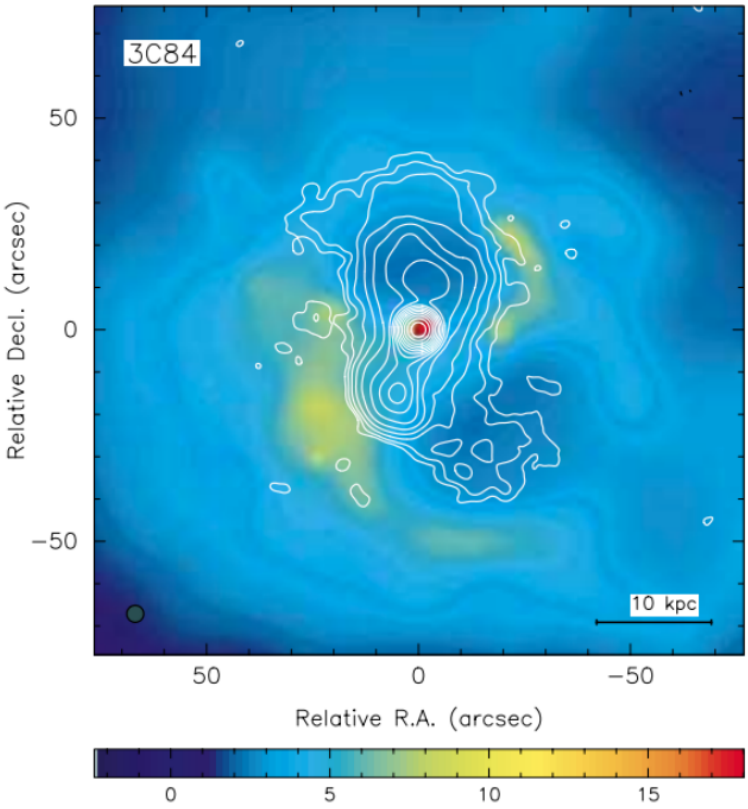

Figure 1.2: The dynamics of the Perseus cluster, shown at radio (contoured lines) and X-ray (background image) frequencies. The emission intensity of the radio source 3C 84, represented by the contours, coincides with the 'cavities' (darker-blue regions) in the X-ray surface brightness emission. The result shows a clear connection between the hot intracluster gas, and the processes giving rise to the observed radio source. Image taken from Fabian et al. (2000).

in elliptical and S0 galaxies, finding a correlation between the 5 GHz radio core power and the X-ray to optical flux ratio. These findings suggested a scenario in which the condensation and subsequent accretion of gas onto the galactic SMBHs resulted in the generation of the observed radio emission.

In light of the the apparent connection between cluster cooling flows and the prevalence of radio emission, Tabor & Binney (1993) presented a working model in which these cooling flows were responsible for triggering the release of energy from a central super-massive black hole (SMBH). In their model, the energy released by the SMBH acts to convectively heat the surrounding atmosphere, thus providing a mechanism by which to suppress the cooling flow. Subsequent ob-

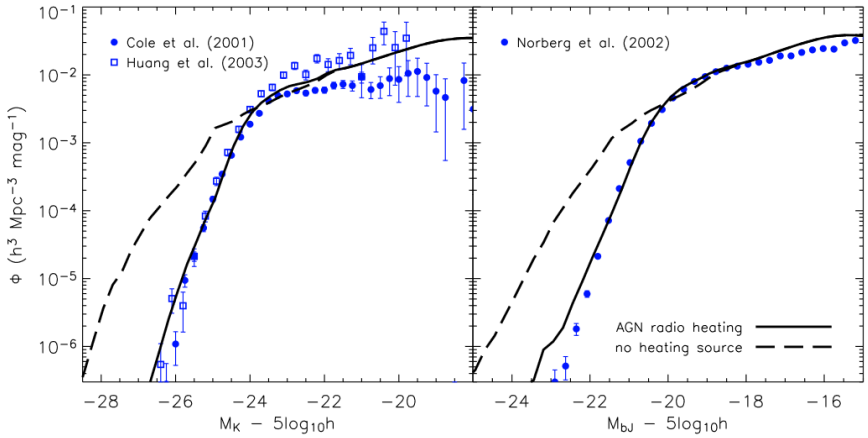

Figure 1.3: Comparisons between of the observed galaxy luminosity function (blue markers), together with predictions from galaxy formation models which assume either the existence (solid black line) or absence (dashed line) of heating. The results show that a source of heating is needed in order to reproduce the observed rapid decline of the most massive galaxies. Image taken from Croton et al. (2006)

servational evidence supporting this hypothesis soon emerged with the advancement of higher-resolution X-ray observations enabled by the Chandra instrument. These observations unveiled the existence of cavities in the X-ray emission, arising from the hot intra-cluster gas in the Hydra A cluster (McNamara et al., 2000), the Perseus cluster (Fabian et al., 2006), and the Centaurus cluster (Sanders et al., 2008; Sanders & Fabian, 2008). Remarkably, these studies consistently showed that the position and morphology of the X-ray cavities were coincident with the morphologies of an extended radio source (e.g., Fig. 1.2), demonstrating that the radio source is capable of displacing molecular gas in its surrounding atmosphere. Such a result would suggest the existence of a feedback mechanism, in which the radio source generated by the accreting material is capable of suppressing its own fuel supply.

To further support the connection between the accretion-driven heating and the hot atmospheres of galactic/cluster haloes, Croton et al. (2006) and Bower et al. (2006) pioneered simulated-based investigations into the evolution of galaxies by providing a prescription for the energies (heating) released by accretions

onto the SMBHs. Their results showed that in the absence of heating, the predicted galaxy luminosity function (which can be related to a global mass function for a fixed mass-to-light ratio) vastly over-predicted the space-density of luminous (massive) galaxies. By contrast, the assumption of a heating mechanism is successfully able to explain the observed 'quenching' of high-mass galaxies (see Fig. 1.3), and is invoked in modern galaxy formation models to suppress the star formation rate in the present epoch (see also; Croton et al., 2006; Bower et al., 2006; Shabala & Alexander, 2009; Weinberger et al., 2018; Raouf et al., 2019).

1.2 Radio-loud active galactic nuclei

Jets launched from a supermassive black hole are thought to play a key role in shaping the evolution of their large-scale environments. In the following section, I introduce the phenomenon known as the active galactic nucleus (Sect. 1.2.1), and subsequently discuss the formation of radio galaxy lobes (Sect. 1.2.2). The mechanisms by which the lobes can provide a kinetic-mode of feedback are then discussed (Sect. 1.2.3).

1.2.1 The active galactic nucleus

It is widely accepted that most galaxies contain a SMBH located at their centre, with masses typically ranging from 10^6-$10^{10}\,M_\odot$ (Magorrian et al., 1998; Woo & Urry, 2002; Häring & Rix, 2004; Gültekin et al., 2009). The SMBHs accrete material at a wide range of rates, with the highest-accreting SMBHs showing indications of being an active galactic nucleus (AGN). For an AGN, the gravitational potential energy liberated by the in-falling material is released in the form of highly energetic radiation, which can be observed across a broad range of the electromagnetic spectrum (see review by; Padovani et al., 2017). In many cases, the AGN far outshines the radiation produced by the stellar/gaseous component of the galaxy; while the X-ray luminosities of the interstellar gas typically lie in

the range of 10^{36}-10^{38} W (McNamara & Nulsen, 2007), the bolometric luminosity of the AGN itself can a reach up to 10^{41} W (Krolik, 1999; Woo & Urry, 2002). Considering these energy budgets, AGNs possess the necessary heating capacity to quench the cooling flows which fuel the SMBHs in the most massive galaxies (Alexander & Hickox, 2012; Fabian, 2012).

AGNs exhibiting radio emission are typically classified as either 'radio-loud' or 'radio-quiet'. The distinction between these two groups is still debated, however radio-loud AGNs typically exhibit much higher radio-to-optical luminosity ratios (e.g., $L_{5\,\mathrm{GHz}}/L_{B-\mathrm{band}} \gtrsim 10$, Kellermann et al. 1989) and are commonly associated with powerful (e.g. $10^{34} \lesssim Q \lesssim 10^{39}$ W, Celotti & Fabian, 1993; Gu et al., 2009; Godfrey & Shabala, 2013; Turner & Shabala, 2015; Ineson et al., 2017) relativistic jets that dominate the bolometric luminosity of the AGN. About 15-20% of the AGN population are radio-loud (Kellermann et al., 1989), noting that the radio-loud fraction exhibits a clear dependence on the mass of its host galaxy by becoming increasingly pronounced at higher stellar masses (Best et al., 2005). Moreover, recent insights driven by highly sensitive low-frequency observations have revealed that the radio-loud fraction reaches 100% among the most massive elliptical galaxies (Sabater et al., 2019). These results are intriguing, given that star formation appears to be quenched in these massive galaxies (Sect. 1.1), and hint at a potential feedback cycle in which the growth of the galaxy and the activity near their supermassive black holes may be causally linked (discussed further in Sect. 1.3).

The 'feedback' provided by a radio-loud AGN refers to the complex interplay between the fuel needed to grow the SMBH and its host galaxy, and the energies imparted by the AGN onto its surrounding environment. This feedback mechanism is known to operate over two distinct modes: the radiative form, and the kinetic form (Penrose & Floyd, 1971). In the early universe ($z \sim$ 2-3), radio-loud AGNs predominately interact with their surrounding environments through winds and radiation pressure (Zakamska & Greene, 2014; Feruglio et al., 2015;

Tombesi et al., 2015), and is commonly referred to as the radiative-mode (or quasar mode) feedback (Fabian, 2012). By contrast, kinetic-mode (also known as jet-mode) feedback dominates in the present epoch. In this mode, the energy released by radio-loud AGNs takes the form of mechanical jets comprising relativistic plasma, which directly interact and impart energy onto the surrounding circumgalactic gas (Rawlings & Jarvis, 2004; Raouf et al., 2017). Jet-mode feedback plays a crucial role in halting the catastrophic cooling in cool-core clusters (Fabian et al., 2003; Forman et al., 2005; Mittal et al., 2009; Alexander & Hickox, 2012; Fabian, 2012), and is invoked in semi-analytic galaxy evolution models to quench star-formation within the most massive galaxies at late times (Croton et al., 2006; Bower et al., 2006; Shabala & Alexander, 2009; Weinberger et al., 2018; Raouf et al., 2019).

1.2.2 From jets to lobes

A radio-loud AGN expels a pair of bipolar and highly energetic jets from the vicinity of the SMBH. The jets propagate at relativistic speeds (e.g. Jorstad et al., 2001; Kellermann et al., 2004; Piner et al., 2006), which extend out towards kpc-Mpc scales (e.g. Singal, 1988; Mullin et al., 2008; O'Dea et al., 2009). Although the process responsible for the jet production remains poorly understood, it is theorised that rotational energy of the SMBH is liberated via the twisting and torquing of the magnetic fields (Penrose & Floyd, 1971; Meier, 1999).

The interaction of the AGN jets with the material in the surrounding environment results in the inflation of cocoon-like structures known as lobes. The plasma content of the jet, whose predominant composition is likely that of electrons (Croston et al., 2018) though an electron-positron mix is also plausible (e.g. Kawakatu et al., 2016), is shock-accelerated by the advancement of the jet and is continuously injected into the lobes throughout jet lifetime (Scheuer, 1974). The observed luminosity from the lobes is primarily due to non-thermal synchrotron radiation and is typically detected by radio instruments within a

frequency range of 10 MHz to 100 GHz. To first order, the electron energy distribution of the jet-injected plasma at the point of acceleration follows that of a power-law distribution, such that $N(E) = N_0 E^{-s}$ where s is the power-law energy index and denotes the slope of the distribution (Rybicki & Lightman, 1979). In the optically-thin regime, the observed radio luminosity of the lobes forms a continuum that also takes the form of a power-law, such that $L_\nu = L_0 \nu^{-\alpha}$ where ν denotes the emitting frequency, and the slope of the observed spectrum is related to the energy-index through $\alpha = (s-1)/2$.

Lobes inflated by AGN jets can range over many orders of magnitude in size. The smallest are observed on parsec (pc) scales (e.g. Dallacasa et al., 1995; Tzioumis et al., 2002; Dallacasa et al., 2013; Caccianiga et al., 2017; Ross et al., 2023), and they are thought to represent either the beginning stages in the evolution of a radio galaxy, or a situation where the AGN jets are significantly hindered by the surrounding environment (O'Dea, 1998; Orienti, 2016; Callingham et al., 2017). This small class of radio AGN seem to play an important role in the evolution within the galaxy itself, such as promoting or halting star formation (Morganti & Oosterloo, 2018), however based on their physical scales it is unlikely that they are responsible for displacing gas out to large radii in the galactic dark matter haloes.

Conventionally, the term 'radio galaxy' refers to a radio source in which the pair of lobes have extended beyond the boundaries of the host galaxy and into the intergalactic or intracluster environment. These sources typically grow to sizes on the order of 100 kpc, however are also known to extend out to Mpc-scales (e.g. Barthel et al., 1985b; Schoenmakers et al., 2000; Dabhade et al., 2017, 2020; Andernach et al., 2021; Delhaize et al., 2021). Observationally, the morphological structure of radio galaxy lobes can be grouped into Fanaroff Riley type I and type II classes (FR-I and FR-II, respectively; Fanaroff & Riley, 1974), a distinction that in part can be attributed to the environmental influence on the structure and kinetic power of the propagating jet (Laing, 1994; Bicknell, 1995;

Kaiser & Alexander, 1997).

The lobes of FR-II radio galaxies are described as having an edge-brightened morphology, owing to the fact that the luminosity of the radio emission is typically brightest at the lobe edges. Bright, compact regions of emission near the lobe edges are often found in FR-IIs; these structures are known as the hotspots, and reflect the jet termination points through which plasma is fed to the lobes. The plasma left behind by the advancement of the jet forms the diffuse emitting regions of the lobes. Throughout the lifetime of the jet, the lobes are continuously supplied with fresh plasma accelerated by the jet, which forms a bulk flow back towards the host galaxy (e.g., see; Turner et al., 2018a) referred to as the lobe backflow. Older plasma, which has sustained greater radiative and adiabatic expansion losses, is thus found closer to the host galaxy, and gives rise to the observed dimming of the lobes further from the hotspot. FR-IIs also exhibit a compact, often unresolved, radio core centered at the location of the host galaxy. The emission from the core is thought to represent the radio emission from either the base of the jets or the accretion disk itself, and the luminosity of this region is typically between 2-3 orders of magnitude fainter than the total luminosity of the radio galaxy (de Ruiter et al., 1990).

On the other hand, the morphologies of FR-Is are described as being 'core-brightened', due to the fact that the luminosity of the diffuse radio emission is brightest near the core, and diminishes at larger radii. Unlike an FR-II, FR-I jets are disrupted nearby to the radio core and widen as they interact with the ambient environment. FR-Is can be further grouped by either a "lobed" or "flaring" classification, where the latter class is formed when the flaring jet can not be stabilised by a recollimation shock. Flaring FR-Is thus resemble that of a smoke-like plume, whereas a lobed FR-I will have the defined lobe structures similar to an FR-II. An analysis of flaring FR-Is is not within the scope of this thesis.

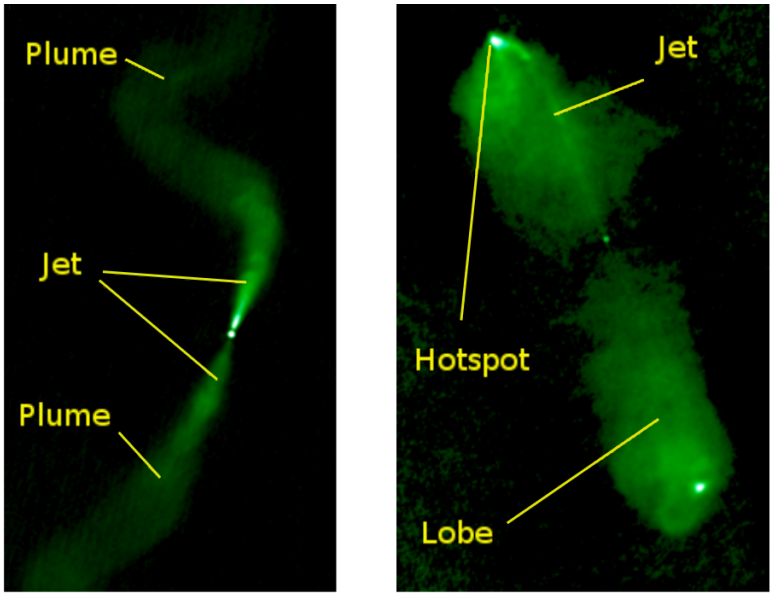

Figure 1.4: Typical FR-I (3C 31, left panel) and FR-II (3C 98, right panel) radio source morphologies. FR-IIs are edge-brightened, while the radio emission is more core-dominated in FR-Is. Image courtesy of the DRAGN atlas (Leahy et al., 2013)

1.2.3 Kinetic-mode of AGN feedback

Kinetic mode feedback, known also as jet mode feedback, describes the dominant process in the present epoch through which the energies released by the AGN are connected to the properties of their surrounding gaseous environments (see reviews by; McNamara & Nulsen, 2007; Cattaneo et al., 2009; McNamara & Nulsen, 2012; Fabian, 2012; Alexander & Hickox, 2012; Harrison, 2017; Morganti, 2017b). In this mechanism, the jets inject energy capable of suppressing cooling flows, preventing them from reaching the cluster centre (e.g; Fabian et al., 2003), and can also result in the clearing of gas in their surrounding atmospheres. The surrounding gas impacted by the jets is also the likely source of fuel for the accretion process driving the production of the jets (Sect. 1.1); as such, energies imparted by the jets can be expected to regulate their own activity (explored further in Sect. 1.3). The effectiveness of this kinetic-mode feedback depends on both: (1) the efficiency with which the jet energy is imparted into the environment, and (2) the ability for this energy to prevent gas cooling onto the cluster

core (e.g. heating in regions with cooling times $\gg 1\,\mathrm{Gyr}$ is not very effective). Kinetic mode feedback is thus intricately linked to the formation of galaxies and the fueling of SMBH jets.

While the total energies released by an AGN are an important ingredient to feedback studies (Binney et al., 2007), understanding how efficiently the jet energy couples to the environment and how this influences the temporal evolution of the surrounding gas is just as important in studies of kinetic mode feedback (Tadhunter, 2008; Alexander & Hickox, 2012). In the case of a powerful FR-II radio galaxy, the bow shock generated by the supersonic expansion of the lobes acts to sweep up and heat the gas in the intracluster medium (Worrall & Birkinshaw, 2014). The degree to which appreciable feedback is done will depend on whether the shocked gas evolves isothermally or adiabatically (Alexander, 2000). In the isothermal case, the temperature of the shocked gas will increase typically by only a factor of less than two, irrespective of environment. For shock heating to be efficient here, the jets would need to be at the centre of a strong cooling flow, where the cooling time of the undisturbed gas could be expected to be at least an order of magnitude less than the source age. On the other hand, if the shocked gas evolves adiabatically and the jets inflate within a steeply-falling atmosphere, the gas lifted by the lobes will have a much shorter cooling time than the gas ahead of the jets. In this case, the feedback from shock heating will be inefficient.

Kinetic mode feedback can also be facilitated by the buoyant ascent of jet-inflated bubbles or cavities. This phenomenon is commonly linked with the lobes of Fanaroff-Riley Class I radio galaxies (FR-Is), low-powered FR-IIs, or old inactive radio galaxies (refer to Section 1.3.1.3). As these bubbles expand into the ambient medium, they perform pressure-volume (pV) work on the surrounding gas, as detailed by (Churazov et al., 2002). This exchange of thermal energy is observed to be 3.7 times more substantial than in an equivalent volume of the ambient gas (Graham et al., 2008). The energy utilised by the expanding bubble

can be transferred to the surrounding medium through processes such as the viscous damping of sound waves or heating due to mixing, as suggested by (Shabala & Alexander, 2009).

Even after the central engine switches off, feedback from the rising bubble can persist (Churazov et al., 2001). In cases of radio sources associated with either low-powered jets or dense external environments, the lobe plasma expands slowly until reaching pressure equilibrium with the surrounding gas. At this point, the lobes become under-dense compared to the external gas, leading to a "pinching" effect caused by the pressure exerted by colder, denser gas closer to the core. Consequently, the hot contents of the radio lobes buoyantly rise out of the galactic/cluster halo's gravitational potential well (as observed in the Perseus cluster, Fig. 1.2). The gas displaced by the rising bubble collapses back toward the core, and this process heats the gas as the gravitational potential is converted into kinetic energy.

Quantifying the distribution of AGN jet properties is an important step towards understanding the details behind kinetic-mode feedback in our universe. In particular, the jet kinetic powers and jet lifetimes of radio-loud AGNs directly inform their energy budgets, and carry implications for their feedback efficiencies. Both the jet kinetic power and age map to the linear size of the radio source (Kaiser & Alexander, 1997), indicating where in the cluster halo the energy takes place. Given the radial dependence of the gas cooling rate, characterising these 'cluster-interaction' radii are important to examine how efficient the jets are at impacting the dynamics of the cluster; a powerful FR-II, while having a high energy budget, may do very little to feedback into the environment, if a majority of the interaction occurs at high cluster radii where the gas cooling time is already large. Knowledge of the AGN duty cycle is also important here. Intermittent activity is required to maintain the balance of heating and cooling in the atmospheres of AGNs (Heckman & Best, 2014), and is shown to modify the the feedback efficiency through repeated outbursts (Yates et al., 2018).

1.3 Constraining the AGN feedback cycle

By imparting energy and momentum into their surrounding environments, AGN jets introduce a feedback mechanism that regulates the supply of gas needed to fuel the nuclear activity itself. An expectation of this mechanism is for the jet activity to show evidence of intermittency, reflecting the underlying heating and cooling cycles that are set by the properties of the large-scale environment. In this section, the observational evidence supporting the cyclical nature of kinetic-mode feedback is discussed (Sect. 1.3.1 - 1.3.2). Subsequently, a discussion ensues regarding the methods and approaches employed by past authors to establish constraints on jet triggering from observations of radio galaxies (Sect. 1.3.3).

1.3.1 The life cycle of radio galaxies

Observations of the extragalactic radio source population have revealed that certain radio galaxies encode evidence of either a break or even a renewal in their AGN activity. These observations suggest that there is an evolutionary life cycle among the radio galaxy population (see reviews by e.g. Kapinska et al., 2015; Morganti, 2017a), whereby the regulation of the jet activity gives rise to observationally-distinct "remnant" and "restarted" radio galaxy classes (see Fig. 1.5). As the evolution of large-scale radio lobes is intricately connected to the accretion processes at the SMBH, investigating the nature of the radio galaxy life cycle provides crucial insights into the fundamental physics governing the jet triggering mechanism and their duty cycle. In this section, the physical and observational differences between active, remnant, and restarted radio galaxies are summarised.

1.3.1.1 The progenitors of kpc-scale radio galaxies

Within the boundaries of their interstellar environments, galaxies are known to harbour diffuse, jet-driven radio sources such as High Frequency Peakers (HFP),

Gigahertz Peaked Spectrum (GPS), and Compact Steep Spectrum (CSS) sources (O'Dea, 1998; Orienti, 2016; Callingham et al., 2017). Aside from their small pc-scale sizes, these objects are also known to exhibit a peak in their observed synchrotron spectrum, where the turnover at lower frequencies arises due either to synchrotron self-absorption (Snellen et al., 2000; Fanti, 2009), or free-free absorption (Callingham et al., 2015; Tingay et al., 2015).

The cause behind the compact linear sizes in these objects is currently a subject of debate, with two prevailing scenarios being proposed. In the "youth" scenario, these compact objects are small simply because they are young, and therefore have not had enough time to grow to kpc-scales (O'Dea & Baum, 1997; Owsianik & Conway, 1998; Tinti & de Zotti, 2006). This is consistent with estimates of their spectral and dynamical ages, which show that the age of these sources typically lies between from $\sim 10^1$ to $\sim 10^5$ years (O'Dea, 1998; Owsianik & Conway, 1998; Orienti et al., 2010; Ross et al., 2023). On the contrary, the "frustration" scenario suggests that these radio sources remain small due to their confinement within the dense medium of the interstellar environment (van Breugel et al., 1984; Wilkinson et al., 1984; O'Dea et al., 1991). Hydrodynamic simulations find typical jets take $\lesssim 1$ Myr to break through the multi-phase ISM of an elliptical galaxy (Bicknell et al., 2014), suggesting that their growth is slowed rather than stopped by the galaxy.

Though these pc-scale sources are not within the scope of this thesis, it is important to recognise that these objects are the likely progenitors to kpc-scale radio galaxies. The discussions below in Sect. 1.3.1.2 to 1.3.1.4 mostly pertain to the processes that occur once the radio galaxy has broken through the dense interstellar environment of its host galaxy.

1.3.1.2 Active radio galaxies

A majority of the radio galaxy population is 'active' (e.g. $\gtrsim 80\%$; Giovannini et al., 1988; Brienza et al., 2017; Mahatma et al., 2018), meaning that the AGN

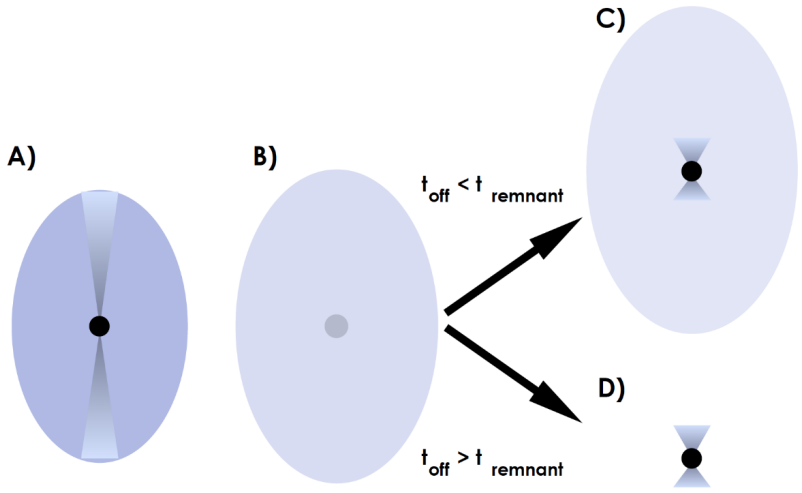

Figure 1.5: A simplified schematic of the radio galaxy life cycle discussed in Sect. 1.3.1.2 - 1.3.1.4. During the active phase, jets continuously inject fresh plasma into the radio lobes (panel A). Subsequently, the cessation of the jet leads to a remnant phase, during which the lobes rapidly fade due to the absence of fresh shock-accelerated plasma (panel B). Jets may eventually restart, resulting in the observation of either two epochs of activity (panel C) or a single epoch of activity (panel D), depending on the visibility of the remnant lobes. Image taken from Jurlin et al. (2020)

jets are actively supplying the radio lobes with young, recently shock-accelerated plasma. These kpc-scale radio galaxies are commonly observed to have ages of approximately 10-100 Myr (e.g. Parma et al., 2007; Shabala et al., 2008; Turner & Shabala, 2015; Harwood et al., 2015, 2016; Turner et al., 2018b; Mahatma et al., 2020). Furthermore, recent modelling of radio galaxy populations indicates that the duration of this activity is likely distributed as a power-law, with longer duration outbursts being much less frequent (Hardcastle et al., 2019; Shabala et al., 2020). Gaining insights into the timescales of AGN jet activity is a valuable input to studies of AGN feedback and galaxy evolution models. Evaluating the energetics of radio-loud AGNs necessitates knowledge of the outburst duration (together with the kinetic power of the jets). Moreover, as the age of the jets correlates strongly with their linear size (Kaiser & Alexander, 1997), the durations of AGN outbursts play a pivotal role in understanding where they deposit their energy in relation to the gravitational potential-well of the dark matter halo.

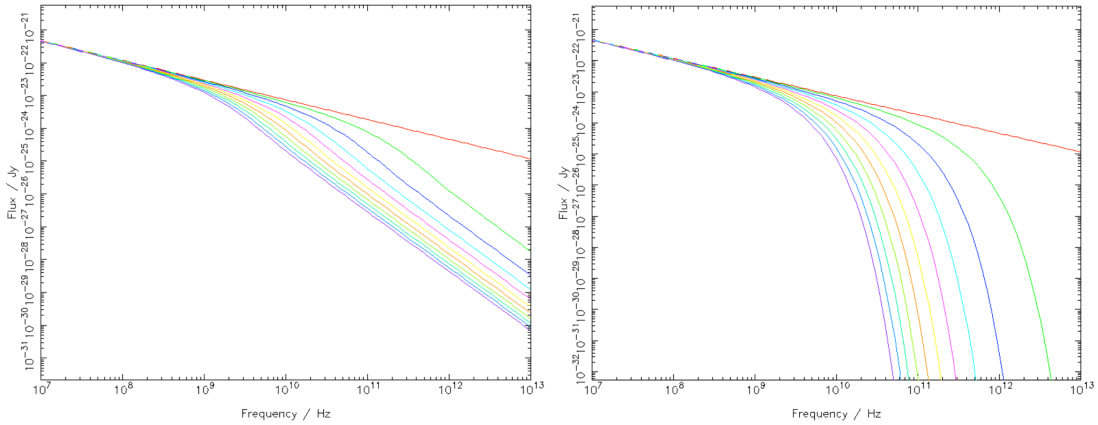

Figure 1.6: The simulated temporal evolution of a KP (left) JP (right) radio spectrum is shown between 10 MHz and 10 THz. At $t = 0$ Myr (red), the radio spectrum arising from the fresh, shock-accelerated plasma follows that of a classical power law. The spectral ageing is shown up to $t = 10$ Myr (purple), revealing the gradual shift of the break frequency towards lower frequencies. Image taken from Harwood et al. (2013).

The spectral evolution of the lobes is driven by energy losses experienced by the aging plasma. Discrete electron packets are impulsively injected into the lobes by the jets, each containing an ensemble of same-age electrons. The synchrotron spectrum arising from an impulsively-injected plasma population has historically been described by the Jaffe-Perola (JP; Jaffe & Perola, 1973) or Kardashev-Pacholczyk (KP; Kardashev, 1962) spectral aging models. Both the JP and KP models assume that the ensemble of electrons is injected at the same time, $t = 0$, and that the magnetic field is homogeneous throughout the plasma. The models differ in their treatment of pitch-angle scattering, with the KP model assuming no scattering, and the JP model adopting a more realistic assumption of isotropic scattering. Once electrons are injected, they undergo energy losses due to synchrotron, inverse-Compton (IC), and adiabatic processes, all of which impact their radio spectrum. It should be noted that the assumption of a fixed magnetic field can also be modified to that of a spatially non-uniform field, which has been presented as a more realistic approach to modelling the lobe magnetic field structure (Tribble, 1991, 1993, 1994). In these cases, the standard impulsive injection models are referred to as the Tribble JP (TJP) and Tribble KP (TKP)

models. Hardcastle (2013) demonstrated that the synchrotron spectrum arising from these 'Tribble' models can be derived by integrating the conventional energy losses across a Maxwell–Boltzmann distribution in field energy density.

For synchrotron energy losses, the energy loss-rate is proportional to the square of the electron energy (Kardashev, 1962; Longair, 2011). At the time of acceleration ($t = 0$), the impulsive injection models predict a power-law synchrotron spectrum with a slope characterised by the injection index, $\alpha_{\rm inj}$. Once the plasma begins to age, the energy losses introduce a spectral break frequency, ν_b, above which the observed radio spectrum steepens. The break frequency relates to the age of the plasma, and thus shifts towards lower frequencies as the plasma continues to age (see Fig. 1.6). The assumption of an isotropic electron pitch-angle scattering results in the sharper exponential cut-off above the break frequency in the JP model, in comparison to the KP model which predicts a flatter spectral steepening.

Many authors have adopted the impulsive injection models to measure the spectral ages within the lobes of active radio galaxies (e.g. Harwood et al., 2013, 2015; Turner et al., 2018a; Mahatma et al., 2020). This involves fitting an impulsive spectral ageing model to the spectra arising from narrow regions across the lobes, and using χ^2 minimisation to fit an optimal injection index for the source. A lobe magnetic field strength, which provides the normalisation for the radio spectrum, is typically estimated based on dynamical arguments together with an assumption of lobe equipartition. Using the fitted injection index and magnetic field strength as inputs, the spectral age of each region is subsequently determined by fitting the impulsive injection model to its spectrum. This technique relies on the assumption that the plasma confined to each narrow region was injected at the same time, thus necessitating the use of high spatial-resolution radio observations. Hydrodynamic simulations have shown that this assumption may not always hold true due to the turbulent mixing of lobe plasma, leading to a slight underestimation of the spectral age in (Turner et al., 2018a). Nevertheless, the

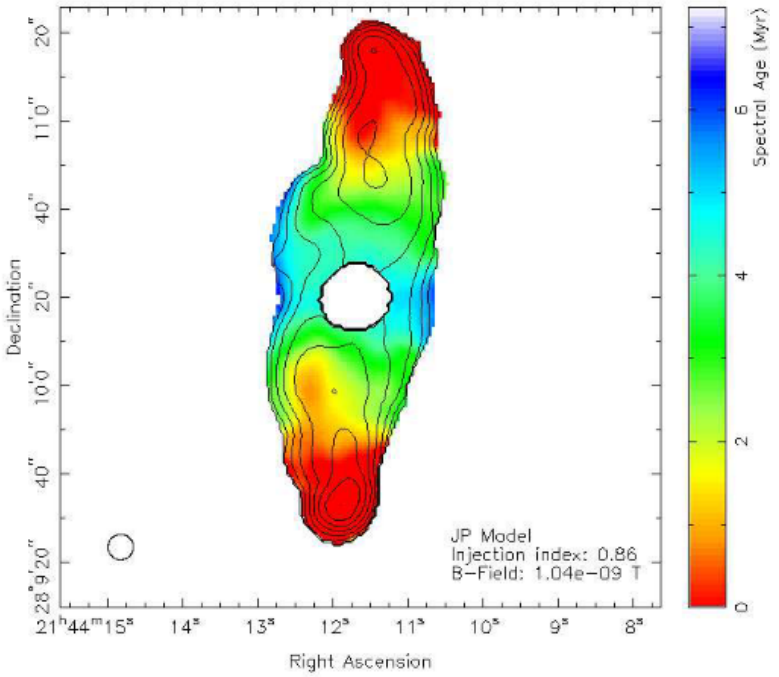

Figure 1.7: The spectral age map of 3C436 with 7.2 GHz flux contours overlaid. Spectral ages are constrained by fitting the impulsive JP model to the spectra arising from narrow regions across the lobes. The shape of the synthesized beam is given in the lower left corner. Image taken from Harwood et al. (2013).

application of these models reveals a gradient in the spectral age, thus probing the bulk flow of lobe plasma which, for FR-II radio lobes, flows away from the hotspot and towards the radio core (see Fig. 1.7).

In the limit of poor spatial resolution, i.e., an unresolved radio source, the spectral evolution of radio lobes is often studied using their integrated radio spectrum. In this case, the assumptions of the impulsive injection models no longer hold as the integrated radio luminosities include the full breadth of plasma ages in the lobe. Instead, the integrated radio spectrum of active lobes is well described by the continuous injection model (CI-on model[1]; Kardashev, 1962), which assumes a mixed-age plasma, $0 \leq t \leq \tau$, where τ represents the age of the radio source. In contrast to the impulsive-injection models, the CI model dictates that the observed radio spectrum can only steepen a finite amount due to ageing, such that $\alpha \leqslant \alpha_{\rm inj} + 0.5$ (see Fig. 1.8). Assuming a typical injection index of $\alpha_{\rm inj} = 0.7$, the observed spectral indices of active radio lobes can therefore be expected not to exceed $\alpha \sim 1.2$.

It is possible to derive the spectral age of radio lobes by fitting the integrated radio spectrum using the CI models. In contrast to the resolved spectral-age method, which use impulsive injection models to fit the oldest age observed in the lobes, this method relies on deriving the age of the source based on the spectral break frequency in the integrated spectrum. Harwood (2017) fit the spectra of six radio sources, demonstrating a statistical rejection for 4/6 objects fit by the CI models. Moreover, they showed that the spectral-age estimates obtained through integrated and resolved spectral ageing methods differed by factors of up to six. The continuous-injection models assume a time-invarying magnetic field, which is violated as the lobe magnetic field strength decreases with the adiabatic expansion of the lobes (Turner & Shabala, 2015). Turner et al. (2018b) used synthetic radio sources (which include magnetic field evolution; see Turner et al. 2018a) to show good agreement between the spectral ages fitted by the CI model

[1]The CI-on model is also known as the CIJP model in the literature.

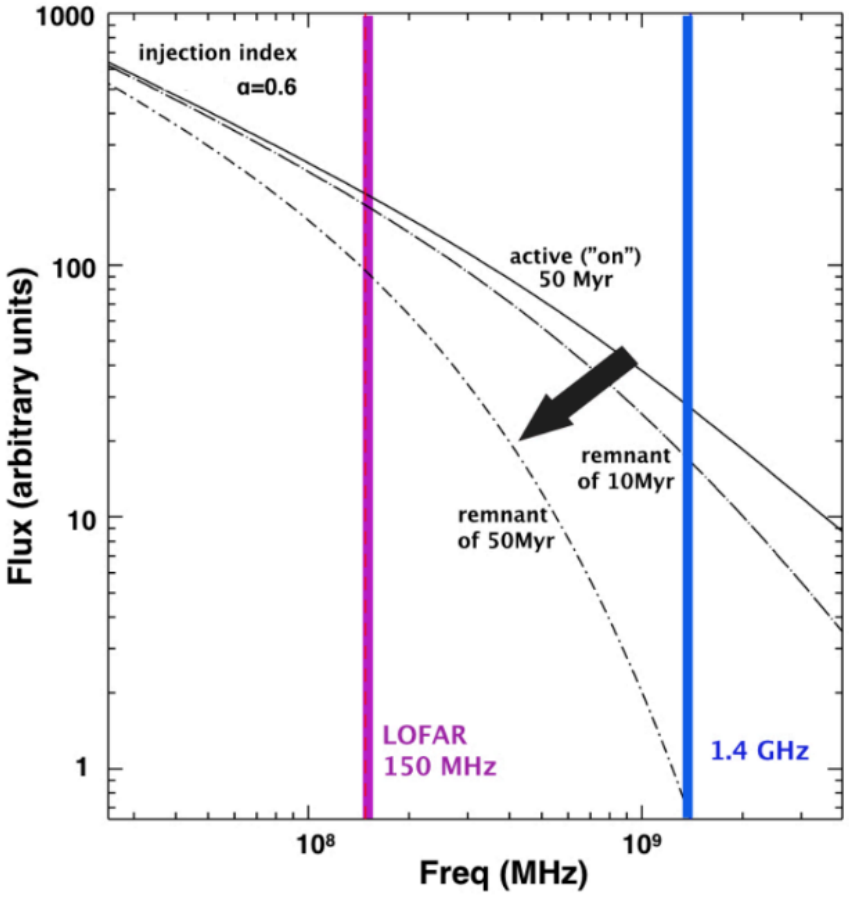

Figure 1.8: The simulated evolution of an integrated radio spectrum described by continuous-injection models. The solid black line represents a 50 Myr plasma that is actively rejuvenated by the jets. Moderate steepening from the initially power-law spectrum can be seen, which reflects the energy losses sustained by the ageing plasma. The lack of fresh, shock-accelerated plasma results in additional losses during the remnant phase, which are shown for a 10 Myr (dashed) and 50 Myr (dot-dashed) remnant phase, respectively. The rapid spectral steepening in this phase gives rise to the existence of 'ultra-steep' remnant lobes. Image taken from Morganti (2017a)

and the dynamical source ages – in contrast to the results of Harwood (2017). This is because the bulk of the synchrotron radiation hails from the youngest $\sim 5-15\%$ of the lobe plasma content, allowing for the assumption of a constant magnetic field strength to remain approximately valid. It is possible then that the problem presented by Harwood (2017) is, in part, driven by the nature of high-precision collected across a broad bandwidth from various instruments with inherent callibration uncertainties and varying sensitivities to extended structure.

1.3.1.3 The remnant phase

Remnant radio galaxies, not to be confused with radio relics[2], refer to the class of radio galaxy in which the relativistic jets are currently inactive, resulting in the rapid fading of the lobes due to the absence of fresh, shock-accelerated plasma. These objects provide the observational evidence to suggest that the lifetime of AGN jets is finite, and are thus encode valuable constraints towards the triggering of AGN jets. Modern studies suggest that the fraction of radio galaxies that are remnant, i.e. the remnant fraction, is low (approximately 5-15%; Giovannini et al., 1988; Saripalli et al., 2012; Brienza et al., 2017; Mahatma et al., 2018); the uncertainty in the reported remnant fraction driven mostly by small-number statistics, survey selection biases (namely surface brightness sensitivities), sample selection criteria, and classification difficulties. While these results shed valuable light onto the dynamics and evolutionary cycles of radio galaxies, it is difficult to relate the remnant fraction to an AGN jet duty cycle, given that it is also a function of the fading timescale of the lobe plasma. Moreover, the remnant fraction alone is unable to constrain whether the jet duty cycle is fixed or obeys a distribution, with each scenario posing vastly different implications for the jet-driven feedback. Recent insights from simulations show that the properties of remnants can, however, help to constrain the bulk distribution of the jet prop-

[2]In the past, the term 'relic' has been used to describe the remnant radio galaxy. However, in current usage, 'radio relics' specifically refer to the diffuse radio emission associated with galaxy clusters.

erties (e.g. Hardcastle et al., 2019; Shabala et al., 2020, and discussed further in Sect. 1.3.3.2), underpinning their value towards AGN jet studies.

The first unambiguous discovery of such a remnant radio galaxy was presented by Cordey (1987). They identified B2 0924+30, citing its 'ultra-steep' radio spectrum and the lack of radio emission from the core as evidence that the radio lobes lacked an active transport of energy.

Once the cessation of the jet has propagated to the lobes, which now become remnant, the integrated radio spectrum starts to develop a sharper exponential steepening than that expected from the CI-on model. Without the injection of fresh, shock-accelerated plasma, the distribution of high-energy electrons quickly depletes as the time since the jet switched off increases. As the remnant lobes continue to age, the number of electrons capable of producing high-frequency radiation will quickly deplete until no emission at high-frequencies can be observed, thus leading to a rapid decline in the observed radio spectrum. This process is described by the continuous injection with an 'off' component (CI-off; Komissarov & Gubanov, 1994, also known as KGJP) spectral ageing model, which is an extension to the regular CI-on model by assuming the radio source spends some duration of time in a remnant phase. In the CI-off model, the dearth of high-frequency-emitting electrons is encoded in the spectrum by a second break-frequency, $\nu_{b,\mathrm{high}}$, above which the radio spectrum reduces to zero. This break-frequency shifts to lower frequencies as the remnant ages (see Fig. 1.8), and relates the duration of the remnant phase, t_{remnant}, to the age of the source as follows: $\tau = t_{\mathrm{remnant}} \times (\nu_b/\nu_{b,\mathrm{high}})^2$. This expression also demonstrates that the ratio of the two break frequencies relates to the fraction of the total source age that the source has spent in a remnant phase, $t_{\mathrm{remnant}}/\tau$, which in this work is referred to as the remnant ratio, R_{rem}.

As such, the CI-off model is ideally suited towards describing the integrated spectra arising from remnant lobes, as has been conducted by many authors (e.g. Cordey, 1987; Parma et al., 2007; Murgia et al., 2011; Hurley-Walker et al., 2015).

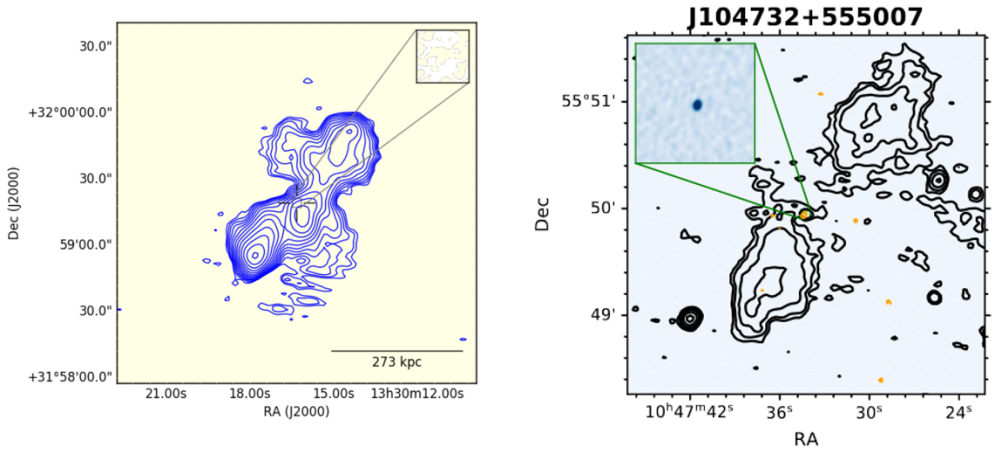

Figure 1.9: The nature of radio emission from the core in remnant radio galaxies. Each image shows contours of the remnant lobe emission at 150 MHz (LOFAR). The insets in each panel provide a high-resolution view at the coordinates of the host galaxy. Remnant radio galaxies are typically expected to lack a radio core (e.g. left panel). Recent results show that this is not always true (right panel), however it is unclear whether the nuclear activity is associated with the outer lobes, or if it reflects a new epoch of activity. Left image taken from Mahatma et al. (2018). Right image taken from Jurlin et al. (2021).

Within the CI-off model, an ultra-steep radio spectrum indicates a lack of high-energy electrons, as would be expected for a sufficiently-aged remnant. However, given that $\nu_{b,\mathrm{high}}$ evolves with age, the ability to observe the ultra-steep portion of the radio spectrum depends also on the frequency of observation; e.g. see 3C 28 of Harwood et al. (2015) and 'Blob 1' of Brienza et al. (2016). The consequence of this on the selection of remnants is discussed in Sect. 1.4.

Aside from their spectral properties, the morphological properties of a radio galaxy are also modified as the source enters a remnant phase. Upon the cessation of the jet, the emission arising from the radio core is expected to disappear practically instantaneously with respect to the typical age of a radio galaxy ($\sim$ 100 Myr, Sect. 1.3.1.2), given that the light crossing time over a 1 pc distance is $t_{\mathrm{crossing}} \approx 10$ yr. This is observed by various authors (e.g. left panel of Fig. 1.9), and has been used to aid with their selection (Saripalli et al., 2012; Brienza et al., 2017; Mahatma et al., 2018). It should be noted that very recent work by Jurlin et al. (2021) demonstrated that remnant lobes can be associated with an active

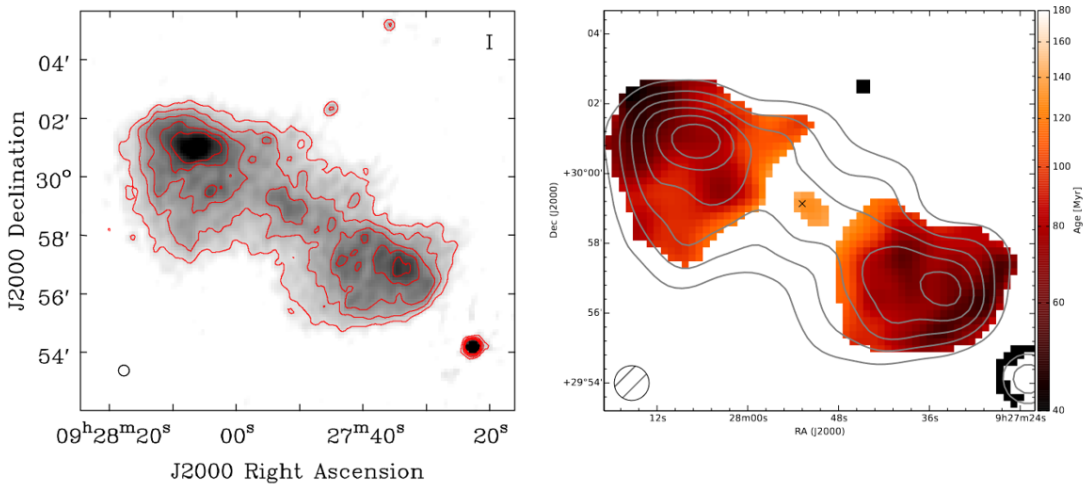

Figure 1.10: The 150 MHz surface brightness distribution (left) and spectral age map (right) of the remnant radio galaxy B2 0924+30. In comparison to the morphologies of active radio galaxies (e.g. see Fig. 1.4), remnant lobes can offer exhibit lower surface-brightness profiles that lack the bright hotspots associated with ongoing activity. Turbulent mixing of the remnant lobe plasma will also act to homogenise the distribution of plasma ages. Images taken from Shulevski et al. (2017).

radio core (right panel of Fig. 1.9), and it is unclear whether the radio cores represents a new phase of activity (see restarted radio galaxies in Sect. 1.3.1.4), or whether the jets drop to a low-level of activity. It is not unreasonable to expect that the latter scenario is true, given the recent discovery that the jetted activity is ubiquitous among the most massive galaxies (Sabater et al., 2019).

Studies of remnant radio galaxies have also shown that they can exhibit low surface-brightness, amorphous morphologies (see left panel of Fig. 1.10, taken from Shulevski et al. 2017). Due to the absence of a jet, the regions of high pressure created at the jet termination shocks quickly dissipate as the hotspots expand adiabatically. This, together with the lack of new (high-energy) plasma, causes the already-fading remnant lobes to quickly approach a more-uniform, low surface-brightness profile. This is also exacerbated by the turbulent mixing of the lobe plasma, which acts to further homogenise the age (and therefore brightness) of the lobe plasma (see right panel of Fig. 1.10). Deformation of the lobe plasma can also occur due to the external pressures of the inter-galactic/intra-cluster

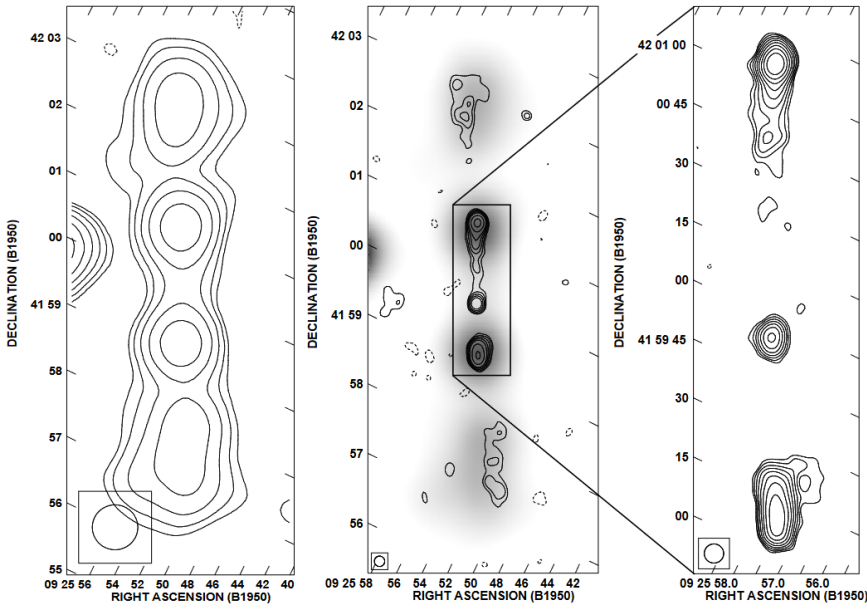

Figure 1.11: Radio contour plots at 1.4 GHz showcasing the radio morphology of the 'double-double' radio galaxy B 0925+420. The source displays two distinct lobe pairs, an inner and outer pair, providing direct evidence for a restarted jet. Image taken from Schoenmakers et al. (2000).

environment, resulting in amorphous and poorly-defined extended structures (e.g. Hurley-Walker et al., 2015; Brienza et al., 2016).

1.3.1.4 The restarted phase

Restarted radio galaxies represent the class of radio source in which multiple epochs of activity can be observed (e.g. see early discoveries by; Subrahmanyan et al., 1996; Lara et al., 1999). In these objects, evidence of a previously-active (now remnant) phase is observed simultaneously with a second, currently-active phase, thus providing strong observational evidence for an intermittent triggering of the AGN jets. Noting that there is no reason to suspect that the physics of the jet triggering is any different for such objects in comparison to active radio galaxies, the existence of such restarted sources lends further weight towards the scenario in which AGN jets obey an underlying duty cycle of activity.

Historically, the best evidence for restarted jets came from the observation of radio galaxies in which two pairs of lobes were observed concurrently and with

a common projected centre (see Fig. 1.11). Such sources, termed the 'double-double radio galaxy' by Schoenmakers et al. (2000), have since been discovered by numerous authors (e.g. see review by; Saikia & Jamrozy, 2009, and references therein), and are observationally-unique in that the dynamics of the lobes can be studied separately. By conducting a population study of DDRGs, Mahatma et al. (2019) show that the properties of their host galaxies are statistically no different to those of 'regular' radio galaxies. Their results imply that the existence of DDRGs is a natural result of the life cycle in radio galaxies, and that the restarting nature of AGN jets must be driven by perturbations in the accretion process, rather than an external event.

It is important to recognise that the DDRG reflects an observation-based classification, and that restarting jets can often appear in various different ways. For example, the simultaneous observation of a CSS/GPS radio source (Sect. 1.3.1.1) embedded within larger-scale diffuse radio emission has been reported on by many authors (e.g. Willis et al., 1974; Barthel et al., 1985a; O'Dea, 1998; Stanghellini et al., 2005; Tremblay et al., 2010; Shulevski et al., 2012; Brienza et al., 2018; Bruni et al., 2019), whereby the restarting jets are confined within the host galaxy. Renewed jet activity can also take place within the confines of the previously-active lobes, making it difficult to separate each phase morphologically. Turner (2018) show that such restarted radio galaxies will exhibit a 'steep-flat' radio spectrum, owing to the high-frequency spectral flattening introduced at high frequencies due to the re-injection of a new plasma population (see also Brienza et al. (2020a) for a practical application of this technique).

Recently, Jurlin et al. (2020) adopt a range of selection methods to identify a complete sample of restarted radio galaxies using the LOw Frequency ARray (LOFAR). Their results showed approximately 15% of their radio galaxy sample was classified as 'restarted', comparable to their remnant fraction of 13%. Moreover, based on the properties of their host galaxies they concluded that radio sources in 'active', 'remnant', and 'restarted' phases were all drawn from the

same parent population, thus lending further weight towards each phase making up a evolutionary component of the radio galaxy life cycle.

1.3.2 The radio-loud fraction

As discussed in Sect. 1.3.1, the coexistence of 'active', 'remnant' and 'restarted' radio galaxies shows that AGN jets are intermittent, lending weight towards the existence of a jet duty cycle. Such a scenario is in qualitative agreement with our understanding of the radio-loud fraction, which refers to the fraction of galaxies hosting a radio-loud AGN (at the time of observation). Assuming that all galaxies of a given stellar and/or black hole mass will trigger radio-loud jets, the radio-loud fraction can thus be used as a proxy for the AGN jet duty cycle. Best et al. (2005) demonstrated that the radio-loud fraction rises strongly with the stellar mass of the AGN host galaxies and the masses of their SMBHs. By taking advantage of the unparalleled sensitivity of the LOFAR telescope, Sabater et al. (2019) built on this result by extending the analysis of the radio-loud fraction out to low radio luminosities (see Fig. 1.12). Their results show that the radio loud fraction approaches unity for the most massive galaxies, implying that the jets must always be active at these masses.

By fitting their data, Best et al. (2005) showed that the best fit for the dependence of the radio-loud fraction on the mass of the SMBH exhibited an empirical relationship of the form $f_{\rm RL} \propto M_{\rm BH}^{1.6\pm0.1}$, where $M_{\rm BH}$ represents the mass of the SMBH. The authors further demonstrated that the mass cooling rate of gas out of an isothermal atmosphere is related to the SMBH mass through $\dot{M} \propto M_{\rm BH}^{1.5}$. The agreement between the two values suggests that the triggering of AGN jets may be related to the cooling of hot gas out of the atmospheres of their host galaxies, in which case the intermittency observed in radio-loud jets could naturally be explained by the heating and cooling in these environments (see also; Shabala et al., 2008; Pope et al., 2012; Turner & Shabala, 2015).

One limitation of the insights derived from the radio-loud fraction is the in-

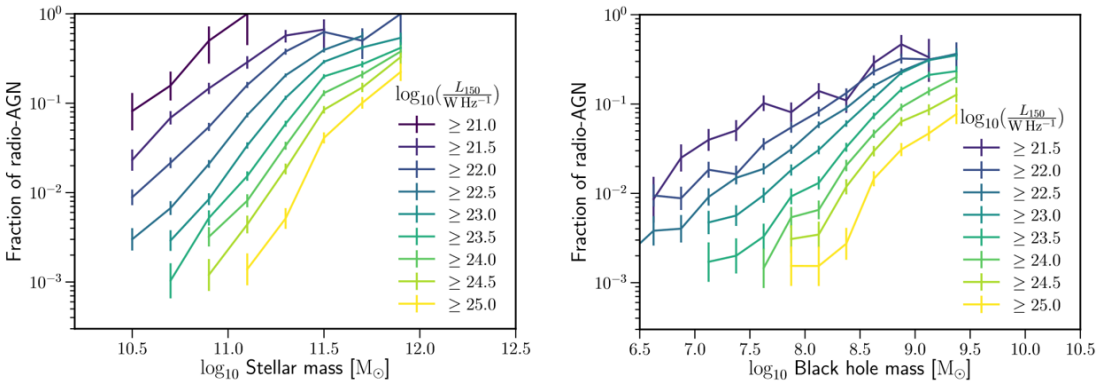

Figure 1.12: For a population of $L_{150,\mathrm{MHz}} > 10^{21}$W/Hz radio-loud AGNs in the local ($z < 0.3$) universe, the observed dependence of the radio-loud fraction on their stellar (left) and black hole (right) masses are shown. The radio loud fraction gives a statistically-based insight into the AGN jet duty cycle, showing that both stellar and black hole masses are strong drivers of radio-loud activity. Image taken from Sabater et al. (2019).

ability to discern whether, for example, higher radio-loud fractions are a result of longer-duration outbursts or an increase in the jet triggering frequency. Frequent intermittent jet outbursts will have an appreciably different coupling efficiency with their environments (Yates et al., 2018), and thus it is valuable to also understand the durations of AGN outbursts.

1.3.3 Radio galaxy constraints on AGN jet physics

1.3.3.1 Constraining the jet duty-cycles in remnant and restarted sources

By studying their spectral ageing and/or dynamical evolution, remnant and restarted radio galaxies allow for constraints to be placed on the time between outbursts, which in turn provide a sampling point of a larger jet duty cycle, δ.

Given that a restarted radio galaxy exhibits multiple phases of activity separated by a period of quiescence, this class of object enables a direct measurement of the duty cycle by deriving the time between outbursts. For two distinct outbursts, the duration of the previous jetted outburst, $t_{\mathrm{on},1}$, is encoded by the remnant lobes. Considering that the secondary outburst, with an observed

age τ_2, must have occurred at some point throughout the age of the first outburst, this means that the time between the two outbursts must be equal to $t_{\rm off} = t_{\rm remnant,1} - \tau_2$. The duty cycle of the activity can thus be directly measured as $\delta = t_{\rm on,1}/(t_{\rm on,1} + t_{\rm off})$. In many cases, a DDRG should allow for the relatively straight forward measurement of these timescales and duty cycle, given that each epoch of activity is often observed as distinct, non-overlapping lobes. However, as pointed out in Sect. 1.3.1.4, restarted radio sources can exhibit vastly different observed properties.

Previous attempts have been made to measure the duty cycle in restarted radio galaxies where the restarted jet is observed as a GPS/CSS source. One such example is carried out by Brienza et al. (2018) for the radio galaxy B2 0258+35 (see left panel of Fig. 1.13). Using spectral ageing models, they were able to set a conservative upper bound on the age of the outer lobes at $\tau_{\rm outer} \lesssim 110\,{\rm Myr}$. By modelling the spectral break frequency in the optically-thin regime of the CSS source (right panel of Fig. 1.13), they estimated the spectral age of the inner component as $\tau_{\rm inner} = 0.4\,{\rm Myr}$. These observations provide a direct measurement of the time the jet is inactive between these two outbursts, however, the duty cycle cannot be constrained without knowledge of the active age of the first jet outburst. This in principle could be estimated based on the size of the jet and a rough expansion speed (e.g. 240 kpc and a $0.01c$ velocity gives an age of 78 Myr).

Similarly, by studying the spatially-resolving spectral energy distribution in the lobes of 3C388, Brienza et al. (2020a) were able to estimate the time between outbursts and thus constrain the jet duty cycle. By analysing the radio spectral properties, they were able to identify a younger pair of lobes embedded within the lobes associated with a previous outburst (see Fig. 1.14). To measure $t_{\rm on,1}$, they employed impulsive injection models to fit the oldest age (τ_1) and the youngest age ($t_{\rm remnant,1}$) in the outer western lobe, and computed the difference between the two values. Measurements of the youngest plasma age were limited to regions where the outer lobe was clearly uncontaminated by the plasma associated with

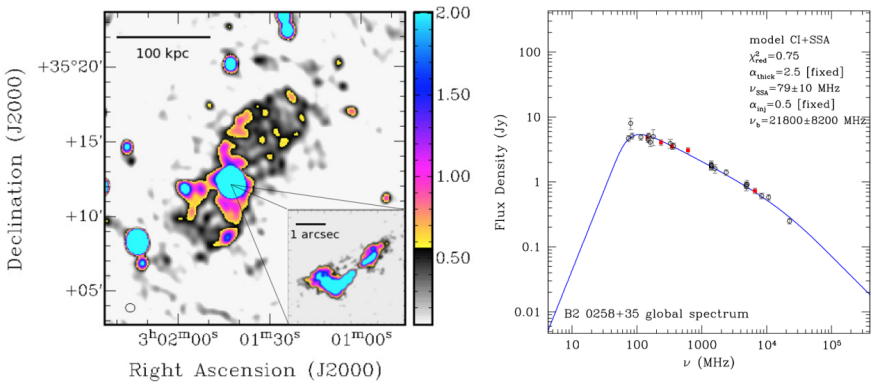

Figure 1.13: Observational evidence for several epochs of activity in the radio galaxy B2 0258+35. The left panel shows a 1.4 GHz view of the extended remnant radio emission, obtained by the Westerbork Synthesis Radio Telescope. The inset provides a high-resolution view at 8.4 GHz, obtained by the Very Large Array, of the central CSS source. The right panel shows the integrated radio spectrum of the CSS radio source. The spectral break frequency in the optically-thin regime enables the derivation of the plasma spectral age. Figure taken from Brienza et al. (2018).

the recent outburst. This resulted in an upper limit on $t_{\mathrm{remnant},1}$, and thus a lower bound on the duration of the first outburst. By fitting the oldest age of the secondary outburst (τ_2), they were able to compute an upper limit on the time between outbursts, and thus constrained a lower-bound the jet duty cycle at $\delta \gtrsim 0.6$.

Notwithstanding some of the methodological challenges outlined above, restarted radio galaxies can therefore provide valuable insights into their jet duty cycles. However, it should be noted that measuring the duty cycles in restarted radio galaxies may introduce a bias towards AGNs with higher duty-cycles, given that the time between outbursts necessarily needs to be short enough for the remnant lobes to still be observed. This is supported by the fact that for restarted radio galaxies, the typical estimates of the inactive periods between the two jetted outbursts seems to vary within the range of 1-10 Myr (Schoenmakers et al., 2000; Saikia et al., 2006; Konar et al., 2012; Shulevski et al., 2015; Brienza et al., 2018). To achieve a more complete sampling of lower jet duty cycles, remnant radio galaxies should also be taken into consideration.

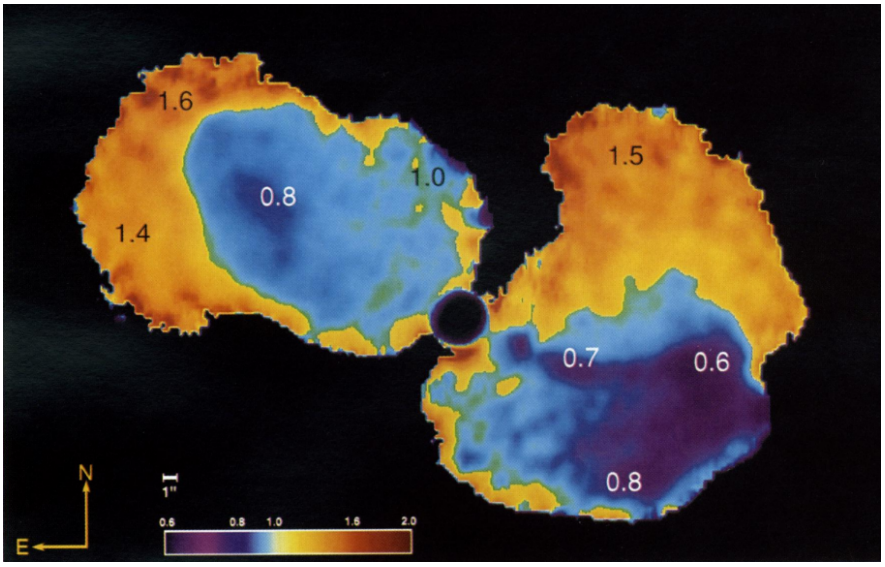

Figure 1.14: A high-resolution map of the 1.4–5 GHz spectral in the radio galaxy 3C 388. Cocoons of flatter-spectrum plasma (blue regions) are embedded within steeper-spectrum (orange regions) lobes, suggesting that the observed radio emission is arising from two distinct phases of activity. Figure taken from Mahatma (2023).

Historically, insights provided by remnant radio galaxies into their jet duty cycles have been explored by comparing the durations of their active and remnant phases. While a remnant radio galaxy enables the direct measurement of the jet lifetime, it's constraint on the jet duty cycle are that of an upper bound, $\delta < t_{\rm on,1}/(t_{\rm on,1} + t_{\rm remnant})$, given that the age at which the source is observed does not encompass the total duration until the future outburst (i.e. $t_{\rm remnant} < t_{\rm off}$). Measurements of the active and remnant phases are typically done either by fitting them from the integrated radio spectrum (e.g. Parma et al., 2007; Murgia et al., 2011; Brienza et al., 2016; Duchesne et al., 2020), or by fitting the oldest and youngest spectral ages in the lobes (e.g. Harwood et al., 2015; Shulevski et al., 2017). It should be noted that the derivation of the spectral ages in the plasma additional requires knowledge of the lobe magnetic field strength; i.e. $\tau = \frac{\upsilon B^{1/2}}{B^2 + B_{\rm IC}^2}\big(\nu_{\rm b}(1+z)\big)^{-1/2}$, where B is the field strength, $B_{\rm IC} = 0.318(1+z)^2\,{\rm nT}$ gives the magnetic field equivalent of the cosmic microwave background at redshift z, and υ is a constant of proportionality (see Equation 4 of Turner et al. 2018b).

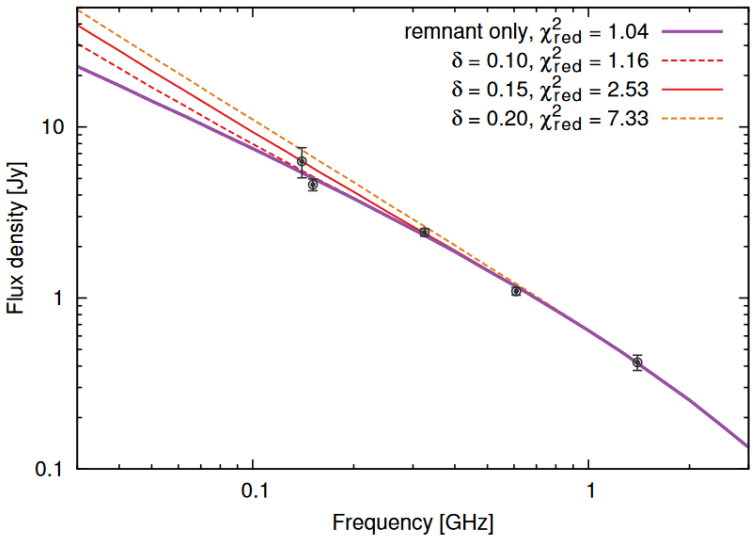

Figure 1.15: The integrated radio spectrum of the remnant radio galaxy B2 0924+30 (solid markers) alongside its best-fit CI-off model (purple line). By assuming a duty cycle, the expected spectral signature of the corresponding previous outburst is studied in relation to the observed spectrum; e.g. $\delta = 0.1$ (red dashed), $\delta = 0.15$ (red solid), and $\delta = 0.2$ (orange dashed) lines. The duty cycle is constrained to $\delta < 0.15$, since larger duty cycles would result in a steeper low-frequency spectrum. Figure taken from Turner (2018).

It is possible to estimate the pressure in the ambient environment of the lobes, which, together with an assumption of the lobe equiparition factor, can derive a lobe magnetic field strength. While an assumption of equipartition is often assumed, empirical measurements (e.g., Croston et al., 2004; Harwood et al., 2016; Ineson et al., 2017) and insights from dynamical modelling (e.g., Turner et al., 2018b) both reveal that the lobes of FR-II radio galaxies are typically sub-equipartition.

To address the issue outline above, Turner (2018) showed that rather than attempting to derive the plasma ages directly from the radio spectrum, the CI-off model can be used to fit the spectral break frequency and remnant ratio, neither of which require knowledge of the magnetic field strength. The fitted parameters can then be used as inputs to help constrain the dynamical evolution of the lobes, which together with the source size and luminosity, allow for the simultaneous fitting of the jet kinetic power and lifetime, the lobe magnetic field strength,

and the duration of the remnant phase. In that work, the author employed the *Radio-loud AGN in Semi-analytic Environments* (RAiSE; Turner & Shabala, 2015; Turner et al., 2018a; Turner, 2018; Turner et al., 2020, 2023) dynamical model, however the results should hold true for any dynamical model capable of describing the evolutionary histories of radio galaxy lobes. As such, remnant radio galaxies can be exploited to offer direct constraints on the lifetimes of radio-loud AGNs.

Turner (2018) further demonstrated that the upper limits on the duty cycle in remnant lobes can potentially be tightened by considering how long ago a previous outburst could have occurred without showing signatures the observed radio spectrum. As discussed in Sect. 1.3.1.4, multiple phases of jet activity will result in a spectral flattening of the radio galaxy's integrated radio spectrum at higher frequencies. Turner (2018) applied this reasoning to analyse the observed radio spectrum of B2 0924+30, which displays a standard spectral index of $\alpha \sim 0.85$ at low ($\sim$ 100,MHz) frequencies. Their goal was to ascertain the shortest possible time a previous outburst would need to have occurred (and thus the largest possible duty cycle) in order for the spectrum to lack the 'steep-flat' shape at the low-frequency end. Following this approach, they were able to constrain the jet duty cycle to $\delta < 0.15$ – a major improvement over the $\delta < 0.64$ constrained by the conventional approach.

The picture painted by these results thus suggests that both remnant and restarted radio galaxies can be analysed to understand their jet duty cycles.

1.3.3.2 Modelling bulk jet properties from radio galaxy populations

Constraining the bulk properties of AGN jets has also been achieved through the application of dynamical models and simulations towards radio galaxy populations.

Using the RAiSE dynamical model, Turner & Shabala (2015) fit the jet powers and active ages for a volume-limited sample of low-redshift ($0.03 \leq z \leq 0.1$) radio

galaxies. By reconciling their results together with the properties of the radio galaxy hosts, they found that radio sources in massive galaxies remain active for longer and spend less time in a quiescent phase, qualitatively consistent with a higher radio-loud fraction in higher-mass galaxies. They demonstrated that the energetic impact of radio-loud AGNs is greatest among powerful radio sources ($L_{1.4} \sim 10^{25}\,\mathrm{W/Hz}$) hosted by massive ($M_\star \gtrsim 10^{11.4} M_\odot$) galaxies, though this result does not consider the effect of coupling efficiency, which may modify the importance of low-power radio source to jet-mode AGN feedback (see Sect. 1.2.3).

Jurlin et al. (2020) used sensitive observations from the LOFAR Two-metre Sky Survey (LoTSS, Shimwell et al., 2019, 2022) to study the life-cycle of radio galaxies within an observationally-complete sample. Using this sample, Shabala et al. (2020) applied forward modeling with the RAiSE model to constrain the seed jet power and lifetime functions. Their method relied on the comparison between mock and observed distributions in flux density and angular size, as well as the constraints from the observed fraction of remnant and restarted radio sources. Their findings indicated that power-law lifetime models were necessary to reproduce the observed properties of their reference sample, whereas constant-age models fell short in predicting the fraction of remnant radio galaxies. See also Hardcastle et al. (2019) for a similar method, who demonstrated that the physical properties of their radio galaxy sample agreed with a log-uniform lifetime function.

In the exploration of the energetic impact of radio-loud AGNs, population studies play a crucial role in encompassing a broad range of jet kinetic powers (Sect. 1.2.1) and lifetimes (Sect. 1.3.1). One of the challenges with these approaches is that the survey and sample selection biases cast a redshift-dependent limitation onto the range of jet kinetic powers and lifetimes that can be observed. Consequently, when examining a complete sample of radio sources, the derived jet properties only represent a subset of their underlying seed distributions. Here it is worth noting that a radio source model with sufficient explanatory power can

be exploited to overcome these challenges, by allowing the predictions of mock radio source populations to be filtered by a given set of selection biases. This approach allows for a model-dependent translation between intrinsic-parameter space and observer space, and has been implemented by various authors to study their extended radio source populations; e.g. see Shabala & Godfrey (2013), Turner & Shabala (2015), Godfrey et al. (2017), Brienza et al. (2017), Hardcastle et al. (2019), and Shabala et al. (2020).

1.4 Selecting remnant radio galaxies

Given the important insights and implications remnant radio galaxies offer towards the properties of AGN jets, it is crucial that their selection is well-understood and robust. In this section, I summarise the various ways remnants have been selected within the literature, while also emphasizing the potential caveats and biases that should be taken into account. This discussion is presented for spectral-based (Sect. 1.4.1) and morphological-based (Sect. 1.4.2.2) methods.

1.4.1 Spectral-based methods

The jets associated with a radio-loud active nucleus provide a continuous supply of shock-accelerated, high-energy electrons to the radio galaxy lobes. Upon the cessation of the jets, the plasma content of the now remnant lobes undergoes a rapid cooling due to synchrotron and adiabatic energy losses. As the remnant lobe-plasma continues to age, the number of high-energy electrons capable of producing high-frequency radio emission is rapidly depleted, which results in a sharp spectral curvature in the observed synchrotron spectrum. Observationally, this gives rise to several unique spectral characteristics that allow for the distinction between active and remnant radio galaxy lobes. These are summarised below.

1.4.1.1 Ultra-steep or highly-curved radio spectra

Many authors have invoked an ultra-steep or highly-curved radio spectrum criterion to classify radio galaxies as remnant (e.g. see; Cordey, 1987; Jamrozy et al., 2004; Parma et al., 2007; Murgia et al., 2011; Hurley-Walker et al., 2015; Brienza et al., 2016, 2017; Godfrey et al., 2017; Duchesne & Johnston-Hollitt, 2019). These classification criteria are based on the expectations from continuous-injection theory (see Sect. 1.3.1.3), which suggest that remnant lobes can display spectral indices significantly steeper than the injection index (i.e., $\alpha > \alpha_{\rm inj} + 0.5$).

Historically, the threshold for an ultra-steep criterion has been typically set at $\alpha \geq 1.2$, although this value has varied slightly among different authors. By considering such steep spectral indices, the criterion aims to select radio galaxies with evidence for pronounced spectral ageing, far greater than what would be expected for radio lobes still fed by active jets. Given the growing number of catalogued all-sky radio survey spanning a combined decade in frequency range (e.g. 150 MHz–1.4 GHz), and that the derivation of a spectral index can be done using two independent measurements, a key advantage of this criterion lies in its straightforward ability to systematically select remnant radio galaxy candidates. The greatest drawback of the ultra-steep criterion is that it is known to preferentially select old remnant plasma. Since the observation of an ultra-steep spectrum can only occur above the higher-frequency turnover, the technique will naturally miss sufficiently-young remnants whose radio spectrum has not appreciably steepened over the observing window (e.g. 3C 28, Harwood, 2017). For an observationally-complete radio galaxy sample, the ultra-steep criterion will therefore select an incomplete sample of remnant radio galaxies, as shown by Brienza et al. 2017; Mahatma et al. 2018.

The spectral-curvature criterion aims to capture the same underlying physics as the ultra-steep criterion, however should in principle have greater selection completeness over a given frequency range. In the limit of sparse radio data, the criterion derives a spectral curvature based on the difference between a low-

frequency and high-frequency spectral index (i.e. SPC $= \alpha_{\rm high} - \alpha_{\rm low}$) and identifies remnants based on a typical threshold of SPC ≥ 0.5 (e.g. see, Murgia et al., 2011). Although this criterion is still largely susceptible to the age bias discussed above, it is worth noting that by separating a low and high-frequency spectral index, the criterion is more tolerable to flatter injection indices. The advantage here is that, assuming the observed radio spectrum of a remnant radio galaxy exhibits $\alpha_{\rm low} = 0.5$ but has not steepened enough to meet the ultra-steep spectrum criterion, the remnant could still be selected by the spectral-curvature criterion if the radio emission has steepened enough to exhibit $\alpha_{\rm high} = 1.0$.

One important point when discussing the efficacy of the above two criteria is that the frequency range over which they are used dictates the completeness in their remnant selection. By synthesizing mock radio source populations at low redshift ($z < 0.5$), Godfrey et al. (2017) demonstrated that the selection efficiency of the ultra-steep criterion can increase by a factor of four when the highest considered frequency goes from 1.4 GHz to 10 GHz. This result is not surprising; at higher frequencies, less time needs to elapse from jet cessation in order for a detectable change to appear in the observed synchrotron spectrum, thus allowing spectral-based classifications to identify younger remnant radio galaxies. The limitation here is that the synthesis of high-frequency ($\nu > 5$ GHz) radio sky surveys requires significantly more observing time compared to lower-frequency analogs (due to the smaller fields of view), and thus such high-frequency constraints are often lacking without dedicated follow-up observations. Future all-sky surveys that aim to provide a higher-frequency view of the sky, such as those produced by the Square Kilometre Array, are expected to greatly improve the recovery rate of remnants using spectral-based criteria.

It should also be noted that given there are other astrophysical processes that can give rise to the spectral characteristics listed above, the reliability of both the ultra-steep and highly-curved radio spectrum criteria should be addressed. Assuming that the due diligence has been made to ensure the radio sources are

extragalactic in origin, the criteria listed above are known to also identify high-redshift radio galaxies (e.g. De Breuck et al., 2000; Drouart et al., 2020). This is due to two key reasons. Firstly, for sources at higher redshifts, the observed synchrotron emission reflects a higher rest-frame frequency range where the slope of the synchrotron spectrum is intrinsically steeper. Secondly, considering that the energy density in the CMB is related to redshift through $u_C \propto (1+z)^4$, and that the synchrotron energy loss-rate is a function of both u_B and u_C, this results in a faster evolution of the synchrotron radio spectrum and can give rise to a steep, highly-convex radio spectrum. Additionally there is the simple bias that the most luminous sources at high redshift will have steep spectral indices due to the k-correction. In the absence of spectroscopic redshifts to robustly rule out these objects, the observed characteristics of the lobed radio emission can help to filter out any potential contaminants; remnant population studies based on sensible angular size thresholds would reduce contamination from high-redshift radio sources, which are likely to present as more compact radio sources.

1.4.1.2 Spectral modelling-based classification

The remnant selection methods presented above in Sect. 1.4.1.1 adopt simple criteria based on the observed spectral properties of the lobes to identify remnant lobe plasma. Due to the typical sparseness of good-quality radio survey data spanning several decades in frequency, such methods are generally better geared towards the identification of remnant radio galaxies in large sample studies. However, it should be noted that without these practical limitations, a detailed modelling of the synchrotron radio spectrum can provide a more robust remnant classification.

Synchrotron spectral ageing models have been utilised by many authors to parameterise the integrated radio spectrum of remnant radio galaxies (e.g. see; Cordey, 1987; Brienza et al., 2016; Turner, 2018; Duchesne & Johnston-Hollitt, 2019). This has typically been achieved by fitting the extension to the continuous-

injection model presented by Komissarov & Gubanov (1994), which considers the additional spectral evolution sustained during the inactive-jet phase, to the observed integrated radio spectrum of the lobes. While these models have typically been used to derive the plasma spectral age, in which case the lobe magnetic field strength was required, it should be noted that the re-parameterised models of Turner (2018) allow for the observed spectral shape to be parameterised using only an injection index, a break frequency, and a remnant ratio. The advantage provided by these models is that they allow for the remnant ratio, which is expected to be non-zero for a genuine remnant radio galaxy, to be parameterised using radio observations alone. An example of this can be seen in Duchesne & Johnston-Hollitt (2019), who show that the integrated radio spectrum of the remnant radio galaxy associated with NGC 1534 is better explained by the remnant spectral ageing model as oppose to that used to explain active radio sources.

1.4.2 Morphological-based methods

1.4.2.1 The absent radio core criterion

Various authors have utilised the absence of a compact radio core as a criterion to select remnant radio galaxies (e.g., Cordey, 1987; Giovannini et al., 1988; Saripalli et al., 2012; Mahatma et al., 2018). Due to the light crossing time along the jet, compact features such as the radio core, jets, and hotspots, are all expected to disappear many orders of magnitude faster than the radio emission arising from the remnant lobes (see Sect. 1.3.1.3). Unlike most literature-established remnant selection methods, the absent radio core criterion does not depend upon detectable changes in the properties of the lobes. Instead, the criterion uses the absence of the radio core as a proxy for an inactive radio-loud AGN, which would imply that the associated radio lobes are not currently fed by an active plasma channel.

Considering that the spectral-based methods have been shown to favor the selection of aged remnant plasma (see Sect. 1.4.1.1), one of the key advantages of

the absent radio core criterion is that it is expected to select a sample of remnants unbiased to spectral properties. This is clearly shown by Mahatma et al. (2018) who identified remnants from an observationally-complete sample of extended radio galaxies, revealing that the 150–1400 MHz spectral index of the selected remnants spanned a wide range of values, ranging from -1.5 to -0.5 (see also; Brienza et al., 2017).

An important constraint limiting the application of this criterion stems from the requisite for sensitive and spatially-resolved radio observations. Since the criterion separates between active and remnant radio galaxies based on the absence of radio emission from the core, the quality of the non-detection can only be as good as the data permits. Poor survey sensitivity and/or low spatial resolution can both contribute to the deselection of a faint radio core, thereby promoting the selection of spurious contaminants. A good example of this can be demonstrated by the results of Mahatma et al. (2018), who followed up a sub-sample of 34/122 LOFAR-selected radio galaxies that did not have a radio-core detected in the Faint Images of the Radio Sky at Twenty-one centimeters (FIRST) survey. Using dedicated VLA observations at 6 GHz, they were able to achieve a background RMS noise of approximately $10 - 15\,\mu$Jy/beam for a $0.47'' \times 0.28''$ beam shape (deeper than FIRST and higher in spatial resolution by about an order of magnitude) and consequently were able to reduce the number of remnant candidates down to 9/122. Importantly, these results highlight that the recovery rate of the absent radio core criterion is largely dependent on the quality of the radio data, and it is unclear whether that criterion alone can reliably classify remnants beyond mere candidates.

1.4.2.2 Relaxed and low surface-brightness lobes

With the advent of LOFAR, which provides sensitive low-frequency radio observations with high sensitivity to low surface-brightness radio emission and high spatial resolution, the ability to select remnant radio galaxies based on the mor-

phological properties of their lobes has gained much attention recently. By conducting a preliminary search of the LOFAR fields, Brienza et al. (2016) searched for remnant radio galaxy candidates based on properties such as diffuse, low surface brightness lobes without compact features. Their selection revealed the discovery of a 700 kpc remnant radio galaxy (i.e. Blob 1), whose integrated radio spectrum did not meet the necessary criteria to be considered as ultra-steep or highly-curved at frequencies up to 1.4 GHz. This result helped to underline the growing need for alternative methods to complement the spectral-based selection of remnant lobes, and set the tone for future studies to adopt lobe-based morphological selections of remnant radio galaxies.

While the morphological criteria used for classifying remnant radio galaxies have shown variations among different authors, they share a common underlying theme. Saripalli et al. (2012) present distinct classifications for remnants associated with FR-I and FR-II radio galaxies. A remnant FR-II is expected to retain the edge-brightened morphology, yet lack the bright compact regions of emission such as the radio core, jets, and hotspots that are typically associated with ongoing nuclear activity. Depending on the degree to which the remnant FR-II has aged, these sources can also be expected to show weak contrast in the lobe surface brightness profile, and exhibit diffuse, low surface-brightness radio emission. On the other hand, a remnant FR-I is expected to be brightest near the core, and should exhibit a pair of diffuse extensions absent any bright channels of collimated emission. Brienza et al. (2017) present a similar morphological classification, though additionally include a maximum mean surface-brightness criterion of 50 mJy/arcmin^2 at 150 MHz. It is also possible for old remnant radio galaxies to present as amorphous radio structures, much like 'Blob 1' of Brienza et al. (2016), owing to the deformation and mixing of the plasma content within the ambient medium of the surrounding inter-galactic/intra-cluster environment.

1.5 This thesis

This introductory chapter has provided a background to the radio galaxy life cycle, and its connection to the triggering of supermassive black hole jets. Since the cessation of the jets is encoded in the observable signatures of remnant lobes, this class of radio galaxy is expected to offer valuable insights towards the intrinsic properties of the jets. In this thesis, I combine observation, modelling, and simulations to use remnant lobes as a tool to make progress towards studying the life cycle and energetics of radio-loud AGN jets. The subsequent chapters are structured as follows. In Chapter 2, I use a multi-frequency radio survey to examine the viability of selecting remnant radio galaxies using the absent radio core criterion. Spectral and morphological properties of the selected objects are examined in detail, allowing for the caveats and limitations of the selection method to be explored. Chapter 3 details the development of a new model-based method for the selection and modelling of remnant lobes, the development of which is motivated by the general sparsity in high-frequency radio survey data. The method is independently tested against standard spectral ageing techniques using observations of a known remnant, and its adaptability to a wide range of radio sources is tested using mock simulations. In Chapter 4, I deploy the previously-developed method to measure the jet properties over a sample of remnant lobes selected from all-sky survey data. By using mock simulations to model the sample selection biases, I am able to infer the true jet kinetic power and jet lifetime distributions for the sample. Finally, Chapter 5 provides a summary of the significant outcomes of this thesis, together with suggested future extensions of this work.

Chapter 2

Remnant radio galaxies discovered in a multi-frequency survey

In the following chapter, I present my first major contribution of work undertaken during this thesis. The contents of this chapter have been published as "Remnant radio galaxies discovered in a multi-frequency survey" (2021) in the Publications of the Astronomical Society of Australia, volume 514, 10.1017/pasa.2020.49 (Quici et al., 2021). The accepted manuscript is reproduced, with permission, in full in this chapter. Minor typographical and grammatical changes have been make to ensure consistency with the rest of the Thesis.

Abstract

The remnant phase of a radio galaxy begins when the jets launched from an active galactic nucleus are switched off. To study the fraction of radio galaxies in a remnant phase, we take advantage of a 8.31 deg^2 sub-region of the GAMA 23 field which comprises of surveys covering the frequency range 0.1–9 GHz. We present a sample of 104 radio galaxies compiled from observations conducted by the

Murchison Wide-field Array (216 MHz), the Australia Square Kilometer Array Pathfinder (887 MHz), and the Australia Telescope Compact Array (5.5 GHz). We adopt an 'absent radio core' criterion to identify 10 radio galaxies showing no evidence for an active nucleus. We classify these as new candidate remnant radio galaxies. Seven of these objects still display compact emitting regions within the lobes at 5.5 GHz; at this frequency the emission is short-lived, implying a recent jet switch-off. On the other hand, only three show evidence of aged lobe plasma by the presence of an ultra-steep spectrum ($\alpha < -1.2$) and a diffuse, low surface-brightness radio morphology. The predominant fraction of young remnants is consistent with a rapid fading during the remnant phase. Within our sample of radio galaxies, our observations constrain the remnant fraction to $4\% \lesssim f_{\rm rem} \lesssim 10\%$; the lower limit comes from the limiting case in which all remnant candidates with hotspots are simply active radio galaxies with faint, undetected radio cores. Finally, we model the synchrotron spectrum arising from a hotspot to show they can persist for 5–10 Myr at 5.5 GHz after the jets switch off – radio emission arising from such hotspots can therefore be expected in an appreciable fraction of genuine remnants.

2.1 Introduction

The jets launched from a radio-loud active galactic nucleus (AGN) arise from the accretion onto a super-massive black hole, and form synchrotron-emitting radio lobes in the intergalactic environments of their host galaxies (Scheuer, 1974). Whilst the jets are active, a radio galaxy will often display compact features such as an unresolved radio core coincident with its host galaxy, bi-polar jets, and hotspots in the lobes of Fanaroff Riley type II (FR-II; Fanaroff & Riley, 1974) radio galaxies. The radio continuum spectrum arising from the lobes is usually well approximated by a broken power-law for radio frequencies between 100 MHz and 10 GHz; the observed spectral index, α[1], typically ranges within

[1]The spectral index α is defined through $S_\nu \propto \nu^\alpha$

$-1.0 < \alpha < -0.5$. Steepening in the radio lobe's integrated spectrum is allowed by $\Delta\alpha \leq 0.5$ (e.g. the CI model; Kardashev, 1962; Pacholczyk, 1970; Jaffe & Perola, 1973), and is attributed to ageing of the lobe plasma.

Such active radio galaxies do not offer a complete picture to the life-cycle of radio galaxies, due to a seemingly intermittent behaviour of the AGN jet activity. The remnant phase of a radio galaxy begins once the jets switch off. During this phase the lobes will fade as they undergo a rapid spectral evolution, e.g. as shown observationally by Murgia et al. (2011), Shulevski et al. (2012), Godfrey et al. (2017), Brienza et al. (2017), Mahatma et al. (2018), Jurlin et al. (2020), and shown with modelling conducted by Turner (2018), Hardcastle (2018) and Shabala et al. (2020). Remnant radio galaxies, remnants herein, will remain observable for many tens of Myr at low ($\sim 150\,\mathrm{MHz}$) frequencies, which is comparable but shorter than the duration of their previous active phase (Shulevski et al., 2017; Turner, 2018; Brienza et al., 2020b). Jets are also known to restart after a period of inactivity (e.g; Roettiger et al., 1994), giving rise to a restarted radio galaxy. Several observational classes exist to describe such sources; double-double radio galaxies (DDRG; Schoenmakers et al., 2000) describe sources in which two distinct pairs of lobes can be observed, however restarting jets can also appear as compact steep spectrum sources embedded within larger-scale remnant lobes (e.g; Brienza et al., 2018).

Compiling samples of remnant (Saripalli et al., 2012; Godfrey et al., 2017; Brienza et al., 2017; Mahatma et al., 2018) and restarted (Saripalli et al., 2012; Mahatma et al., 2019) radio galaxies sheds new light on their dynamics and evolution, and by extension, the AGN jet duty cycle. Jurlin et al. (2020) present a direct analysis of the radio galaxy life cycle, in which their sample is decomposed into active, remnant and restarted radio galaxies. To complement these observational works, Shabala et al. (2020) present a new methodology in which uniformly-selected samples of active, remnant and restarted radio galaxies are used to constrain evolutionary models describing the AGN jet duty cycle.

However, using radio observations to confidently identify radio sources in these phases is a challenging task, even in the modern era of radio instruments. Remnant radio galaxies, which are the focus of this work, display various observational properties that correlate with age, presenting a challenge for identifying complete samples of such sources. Various selection techniques exist amongst the literature, each with their selection biases. Due to the red preferential cooling of higher-energy synchrotron-radiating electrons (Jaffe & Perola, 1973; Komissarov & Gubanov, 1994), many authors have identified remnants by their ultra-steep radio spectrum ($\alpha < -1.2$), reflecting the absence of a source of energy injection, e.g. (Cordey, 1987; Parma et al., 2007; Hurley-Walker et al., 2015). However, Brienza et al. (2016) demonstrates that this technique preferentially selects aged remnants and will miss those in which the lobes have not had time to steepen over the observed frequency range. Murgia et al. (2011) propose a spectral curvature (SPC) criterion, which evaluates the difference in spectral index over two frequency ranges, e.g. SPC = $\alpha_{\rm high}$ - $\alpha_{\rm low}$ such that SPC >0 for a convex spectrum. Sources with SPC > 0.5 demonstrate highly curved spectra, and are likely attributed to remnant lobes. However, modelling conducted by Godfrey et al. (2017) shows that not all remnants will be selected this way, even at high ($\sim$10 GHz) frequencies.

Morphological selection offers a complementary way to identify remnants, independent of spectral ageing of the lobes. This technique often involves searching for low surface brightness (SB) profiles (SB $< 50\,{\rm mJy\ arcmin^{-2}}$), amorphous radio morphologies, and an absence of hotspots (e.g; Saripalli et al., 2012; Brienza et al., 2017). However, young remnants in which the hotspots have not yet disappeared due to a recent switch-off of the jets, (e.g 3C 028; Feretti et al., 1984; Harwood et al., 2015), will be missed with these techniques.

An alternative approach is to identify remnants based on an absent radio core; a radio core should be absent if the AGN is currently inactive (Giovannini et al., 1988). This property is often invoked to confirm the status of a remnant

radio galaxy, e.g. see Cordey (1987), and is recently employed by Mahatma et al. (2018) as a criterion to search for remnant candidates in a LOw Frequency ARray (LOFAR)-selected sample. The caveat here is the plausibility for a faint radio core to exist below the sensitivity of the observations, meaning this method selects only for remnant candidates. This method will also miss remnant lobes from a previous epoch of activity in restarted radio galaxies. A likely example of such a source is MIDAS J230304-323228, discussed in Sect 2.3. These sources are beyond the scope of this work, however are a promising avenue for future work.

A common aspect of almost all previously-mentioned observational studies of remnant radio galaxies, is their selection at low frequencies (typically around 150 MHz). The preferential radiating of high-energy electrons means that the observable lifetime of remnant lobes increases at a lower observing frequency. Incorporating a low-frequency selection thus plays an important role in improving the completeness of remnant radio galaxy samples; quite often the oldest remnant lobes are detectable only at such low frequencies.

In this work, we take advantage of a broad range of radio surveys targeting the Galaxy And Mass Assembly (GAMA; Driver et al., 2011) 23 field to identify and study new remnant radio galaxies candidates in which the central AGN is currently inactive. We use new low-frequency observations provided by the Murchison Wide-field Array (MWA; Tingay et al., 2013) and the Australian Square Kilometre Array Pathfinder (ASKAP; Johnston et al., 2007; McConnell et al., 2016) to compile a sample of radio galaxies, and use high-frequency (5.5 GHz) observations provided by the Australia Telescope Compact Array (ATCA) to identify remnant candidates by the 'absent radio core' criterion. In Sect. 2.2 we present the multi-wavelength data used for this work. In Sect. 2.3 we discuss the compilation of our radio galaxy sample, the classification of remnant candidates, and the matching of host galaxies. In Sect. 2.4 we discuss each of the selected remnant candidates. In Sect. 2.5 we discuss the observed radio properties of the sample and emphasise the caveats of various remnant selection methods. We also

discuss the rest frame properties of the sample, present the fraction of remnants constrained by our observations, and examine a particularly interesting remnant with detailed modelling. Finally, our results are concluded in Sect. 2.6.

We assume a flat ΛCDM cosmology with $H_0 = 67.7 \mathrm{kms}^{-1}\mathrm{Mpc}^{-1}$, Ω_M=0.307 and Ω_Λ=1-Ω_M (Planck Collaboration et al., 2014). All coordinates are reported in the J2000 equinox.

2.2 Data

Our sample is focused on a 8.31 deg^2 sub-region of the GAMA 23 field (RA = 345°, Dec = −32.5°; Figure 2.1). The rich multi-wavelength coverage makes the absent radio-core criterion a viable method to search for remnant radio galaxies, and allows us to match the radio sample with their host galaxies.

2.2.1 Radio data

Below we describe the radio observations used throughout this work, summarised in Table 2.1 and 2.2.

2.2.1.1 GLEAM SGP (119, 154, 185 MHz)

From 2013 to 2015, the MWA observed ∼30,000 deg^2 of the sky south of Dec = 30°. The GaLactic and Extragalactic All-sky MWA (GLEAM; Wayth et al., 2015) survey adopted a drift scan observing method using the MWA Phase I configuration and a maximum baseline of ∼3 km. Observations exclusive to 2013–2014 (year 1) were used to generate the public extragalactic GLEAM first release (Hurley-Walker et al., 2017)[2]. GLEAM spans a 72–231 MHz frequency range, divided evenly into 30.72 MHz wide-bands centered at $\nu_c = \{88, 119, 154, 185, 216\}$ MHz. Observations conducted during 2014–2015 (year 2) covered the same sky area as GLEAM, but with a factor of two increase in the observing time due

[2]GLEAM catalogue publicly available on VizieR: http://cdsarc.u-strasbg.fr/viz-bin/Cat?VIII/100

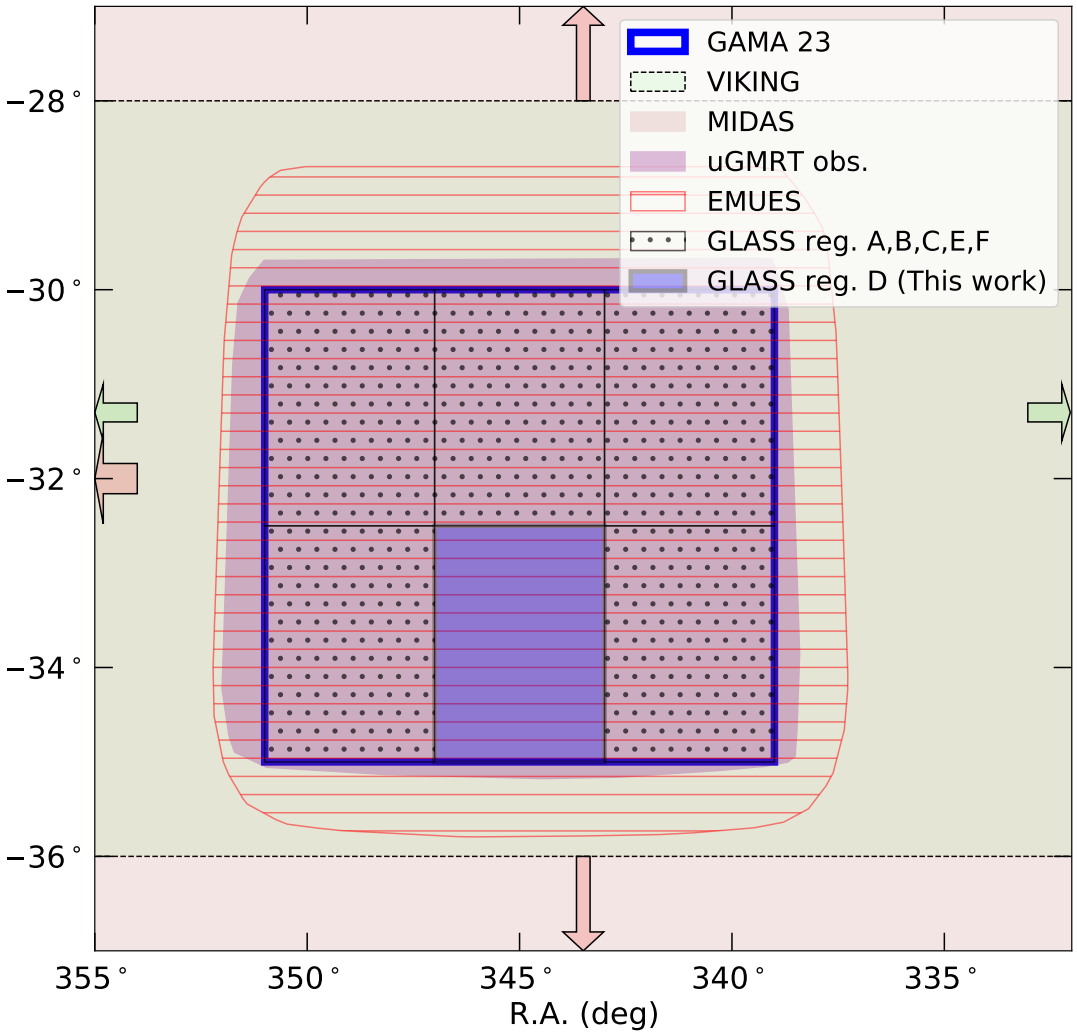

Figure 2.1: Sky coverage of radio surveys dedicated to observing GAMA 23, described in Sect. 2.2.1. Near-infrared VIKING observations (Sect. 2.2.2.1) are also displayed. Thick-red and thin-green arrows indicate the directions in which MIDAS ES and VIKING extend beyond the represented footprint.

Telescope	Survey	Date observed	Frequency [MHz]	Bandwidth [MHz]	Noise [mJy beam^{-1}]	Beam shape Bmaj[″], Bmin[″], PA[°]
MWA Phase I	GLEAM SGP	2013–2015	119	30.72	16.2	241, 202, -57
			154		9.3	199, 157, -51
			186		6.7	162, 129, -47
MWA Phase II	MIDAS ES	2018–2020	216	30.72	0.9	54, 43, 157
uGMRT	–	2016	399	200	0.1	15.8, 6.7, 9.5
ASKAP	EMU-ES	2019	887.5	288	0.035	10.5, 7.8, 87
VLA	NVSS	1993–1996	1400	50	0.45	45, 45, 0
ATCA	GLASS	2016–2020	5500, 9500	2000, 2000	0.024, 0.04	(4, 2, 0), (3.4, 1.7, 0)

Table 2.1: Summarised properties of the radio surveys spanning the GAMA 23 field. Each column, in ascending order, details the telescope used to conduct the observations, the name of the radio survey, the dates observations were conducted, the central frequency of the observing band, the bandwidth available in each band, the average noise properties within region D, and the shape of the restoring beam.

to offset ($\pm$1 hour in median RA) scans. Within a footprint of: $310° \leq \mathrm{RA} \leq 76°$, $-48° \leq \mathrm{Dec} \leq -2°$ ($\sim 5,100$ deg^2 sky coverage), Franzen et al. (2021) independently reprocessed the overlapping observations from both years to produce the GLEAM South Galactic Pole (SGP) survey, achieving a factor ~ 3 increase in integration time over GLEAM. Due to calibration errors associated with Fornax A and Pictor A entering the primary beam side-lobes, the lowest wide-band centered at 88 MHz was discarded at imaging. Despite its declination-dependence, the GLEAM SGP root-mean-square (RMS) remains effectively constant within the footprint of our (8.31 deg^2) study. The point spread function (PSF) varies slightly across the survey; at 216 MHz the PSF size within GAMA 23 is approximately $150'' \times 119''$, and an RMS of $\sigma \sim 4 \pm 0.5$mJy beam^{-1} is achieved. This is consistent with a factor 2 increase in sensitivity over GLEAM. We use an internal GLEAM SGP component catalogue, developed by the method used for GLEAM. Franzen et al. (2021) quote an 8% absolute uncertainty in the GLEAM SGP flux density scale, consistent with the value reported for GLEAM by Hurley-Walker et al. (2017).

2.2.1.2 MIDAS ES (216 MHz)

In 2018 the MWA was reconfigured into an extended baseline configuration (MWA Phase II; Wayth et al., 2018). The MWA Phase II provides a maximum baseline of 5.3 km which, at 216 MHz, improves the angular resolution to $54'' \times 43''$. This drives down the classical and sidelobe confusion limits, allowing for deeper imaging to be made with an RMS of $\sigma \ll 1$ mJy beam^{-1}. MWA Phase II science is presented in Beardsley et al. (2020). The MWA Interestingly Deep Astrophysical Survey (MIDAS, Seymour et al. in prep) will provide deep observations of six extragalactic survey fields, including GAMA 23, in the MWA Phase II configuration. Here, we use an early science (MIDAS ES herein) image of the highest frequency band centered at 216 MHz. Data reduction followed the method outlined by Franzen et al. (2021) where each snapshot was calibrated using a model

derived from GLEAM. Imaging was performed using the WSCLEAN imaging software (Offringa et al., 2014) using a robustness of 0 (Briggs, 1995). Altogether, 54 two-minute snapshot images, each achieving an average RMS of $\sim 8\,\mathrm{mJy\,beam^{-1}}$ without self calibration, were mosaiced to produce a deep image. Stacking of individual snapshots reproduced the expected $\sqrt{t}$ increase in sensitivity, where t is the total integration time, and implied the classical and sidelobe confusion limits were not reached. After a round of self calibration the final deep image, at zenith, achieved an RMS of $\sim$0.9 mJy beam^{-1} with a $\lesssim 1'$ restoring beam. Radio sources were catalogued using the Background And Noise Estimation tool BANE, to measure the direction-dependent noise across the image, and AEGEAN to perform source finding and characterisation (Hancock et al., 2012, 2018)[3]. Using the GLEAM catalogue, sources above 10σ in MIDAS ES and GLEAM were used to correct the MIDAS ES flux-scale. For 887 such sources in GAMA 23, correction factors were derived based on the integrated flux density ratio between MIDAS ES and GLEAM. The correction factors followed a Gaussian distribution, and indicated an agreement with GLEAM within 5%. Given the 8% uncertainty in the GLEAM flux density scale (Sect. 2.2.1.1), we prescribe an 8% uncertainty in the MIDAS ES flux density scale.

2.2.1.3 EMU Early Science (887 MHz)

In 2019 the ASKAP delivered the first observations conducted with the full 36-antenna array configuration. The design of ASKAP opens up a unique parameter space for studying the extragalactic radio source population. With a maximum baseline of 6 km, ASKAP produces images with $\sim 10''$ resolution at 887 MHz. The shortest baseline is 22 m, recovering maximum angular scales of $\sim 0.8°$. As part of the Evolutionary Map of the Universe (EMU; Norris, 2011) Early Science, the GAMA 23 field was observed at 887 MHz and made publicly available on the

[3]AEGEAN and BANE publicly available on GitHub: https://github.com/PaulHancock/Aegean. This work made use of 2.0.2 version of AEGEAN

CSIRO ASKAP Science Data Archive (CASDA[4]). Details of the reduction are briefly summarized here. This data has been reduced by the ASKAP collaboration using the ASKAPsoft[5] data-reduction pipeline (Whiting et al. in prep) on the Galaxy supercomputer hosted by the Pawsey Supercomputing Centre. PKS B1934-638 was used to perform bandpass and flux calibration for each of the unique 36 beams. Bandpass solutions were applied to the target fields. The final images are restored with a $10.55'' \times 7.82''$ (BPA $= 86.8°$) elliptical beam, and achieves an RMS of $\sigma \approx 34 - 45 \mu$Jy beam^{-1}. Henceforth we refer to these observations as EMU-ES.

2.2.1.4 NVSS (1.4 GHz)

We use observations conducted by the National Radio Astronomy Observatory (NRAO) using the Very Large Array (VLA; Thompson et al., 1980) to sample an intermediate frequency range. The NRAO VLA Sky Survey (NVSS; Condon et al., 1998)[6] surveys the entire sky down to Dec$= -40°$ at 1400 MHz. Observations for NVSS were collected predominately in the D configuration, however the DnC configuration was used for Southern declinations. Final image products were restored using a circular synthesized beam of $45'' \times 45''$. At 1400 MHz, NVSS achieves an RMS of $\sigma = 0.45$ mJy beam^{-1}.

2.2.1.5 GLASS (5.5 & 9.5 GHz)

The GAMA Legacy ATCA Sky Survey (GLASS; Huynh et al. in prep) offers simultaneous, high-frequency (5.5, 9.5 GHz) observations of GAMA 23 observed by the ATCA. Observations for GLASS were conducted over seven semesters between 2016 – 2020 (PI: M. Huynh, project code: C3132). Data at each frequency were acquired with a 2 GHz bandwidth, made possible by the Compact Array

[4] https://data.csiro.au/collections/domain/casdaObservation/search/

[5] https://www.atnf.csiro.au/computing/software/askapsoft/sdp/docs/current/pipelines/introduction.html

[6] NVSS catalogue publicly available on VizieR: https://vizier.u-strasbg.fr/viz-bin/VizieR?-source=%20NVSS

Config.	Date observed	Frequency [GHz]	Bandwidth [GHz]	Duration [min]	Secondary calibrator	Noise [mJy beam^{-1}]	Beam shape Bmaj[″], Bmin[″], PA[°]
H168	18/10/19	2.1	2	22	PKS B2259-375	0.7	104, 127, 0
H75	24/10/19	5.5, 9.0	2, 2	25	PKS B2254-367	0.22, 0.14	(88, 110, 0), (54, 67, 0)

Table 2.2: Details of the additional ATCA data collected here under project code C3335, PI: B. Quici. Each column, in ascending order, details the configuration used to conduct observations, the date observations were conducted, the central frequency of the receiver band, the bandwidth available within each band, the approximate time spent per-source in each configuration, the secondary calibrator observed, the average noise per pointing, and the shape of the restoring beam. Note, primary calibrator PKS B1934-638 was observed for all observations.

Broadband Backend (Wilson et al., 2011), with the correlator set to a 1 MHz spectral resolution. Observations for GLASS were conducted in two separate ATCA array configurations, the 6A and 1.5C configurations, contributing 69% and 31% towards the total awarded time, respectively. The shortest interferometer spacing is 77 m in the 1.5C configuration, providing a largest recoverable angular scale of 146″ at 5.5 GHz. As part of the observing strategy, GLASS was divided into six 8.31 $\deg^2$ regions (regions A − F), for which region D (RA=345°, Dec=-33.75°) was observed, reduced and imaged first. For this reason, this paper focuses only on region D.

Processing and data reduction were conducted using the Multichannel Image Reconstruction, Image Analysis and Display (MIRIAD) software package (Sault et al., 1995), similar to the method outlined by Huynh et al. (2015, 2020). The 1435 region D pointings are restored with the Gaussian fit of the dirty beam, and convolved to a common beam of 4″ × 2″ (BPA=0°) at 5.5 GHz, and achieves an RMS of $\sim 24\,\mu\mathrm{Jy\,beam^{-1}}$. A similar process at 9.5 GHz results in a 3.4″ × 1.7″ (BPA=0°) synthesized beam and achieves an RMS of $\sim 40\,\mu\mathrm{Jy\,beam^{-1}}$. Although the same theoretical sensitivity is expected at 5.5 GHz and 9.5 GHz, the sparse overlap in adjacent pointings, larger phase calibration errors, and increased radio frequency interference (RFI) all result in a drop in sensitivity. Henceforth, we refer to GLASS observations conducted at 5.5 GHz and 9.5 GHz as GLASS 5.5 and GLASS 9.5 respectively.

2.2.1.6 uGMRT legacy observations (399 MHz)

As part of the GLASS legacy survey (Sect. 2.2.1.5), uGMRT has observed GAMA 23 in band-3 (250–500 MHz) centered at 399 MHz. The project 32_060 (PI: Ishwara Chandra) was awarded 33 hours to cover 50 contiguous pointings spanning a 50 square-degree region. Observations were conducted in a semi-snapshot mode, with ≈ 30 minutes per pointing distributed through three 10 minute scans. In band-3, the wide-band correlator collects a bandwidth of 200 MHz divided into

4,000 fine channels. Data reduction was conducted using a Common Astronomical Software Application (CASA; McMullin et al., 2007) pipeline[7]. Data reduction followed the standard data reduction practices such as data flagging, bandpass and gain calibration, application of solutions to target scans, imaging and self-calibration (see Ishwara-Chandra et al. 2020 for details). The image is restored by a $15.8'' \times 6.71''$ (BPA$= 9.5°$) beam, and achieves a best RMS of $\sim$100 μ Jy beam^{-1}. We note that several bright sources throughout the field adversely impact the data reduction, resulting in large spatial variations in the RMS. The uGMRT has a shortest baseline of $\sim$ 200 m, which corresponds to a largest recoverable scale of $\sim 10'$ at 500 MHz (i.e. the highest frequency in band-3). As such, despite the high spatial resolution in these observations, we expect that sensitivity to large-scale structure is sufficient to recover the largest angular scale probed by our radio source sample ($\sim 2'$).

2.2.1.7 Low resolution ATCA observations (2.1, 5.5 & 9 GHz)

Due to their power-law spectral energy distributions, the integrated luminosities of radio galaxy lobes decrease with increasing frequency (Sect. 2.1). Given that remnants can display ultra-steep radio spectra, this presents a sensitivity challenge associated with their detection. For a survey such as GLASS which has high $\theta \sim 5''$ angular resolution, owing to the extended baseline configurations within which the observations were conducted (Sect. 2.2.1.5), the survey lacks the necessary short baselines coverage that is needed to detect extended and large-scale emission. As a result, we carried out low-resolution observations in the compact configurations of ATCA.

The project C3335 (PI: B. Quici) was awarded 14 hours to conduct low-resolution observations of each remnant identified for this work, at 2.1, 5.5 and 9 GHz. Observations at 2.1 GHz (*LS*-band) were conducted in the H168 configuration; observations at 5.5 and 9 GHz (*CX*-band) were conducted in the

[7]Pipeline can be found at http://www.ncra.tifr.res.in/~ishwar/pipeline.html, and makes use of CASA version 5.1.2-4

H75 configuration. The minimum and maximum baselines achieved within each configuration are 61 m and 192 m for H168, 31 m and 89 m for H75 respectively (excluding baselines formed with antenna CA06). Bandpass, gain and flux calibration was performed using PKS B1934-638. Due to the small angular separation between each target, the secondary calibrator was held constant for each target. At 2.1 GHz, PKS B2259-375 was used for phase calibration. At 5.5 and 9 GHz, phase calibration was performed with PKS B2254-367. To maximize *uv* coverage, each target was observed on a rotating block of length ∼30 minutes, with approximately[8] 2 minutes allocated per target per block. Secondary calibrators were observed twice per block to ensure stable phase solutions.

Data reduction was performed using the CASA software package[9], and followed the standard data reduction practices. As part of preliminary flagging, the data are 'clipped', 'shadowed' and 'quacked' using the `flagdata` task, in order to flag for zero values, shadowed antennas and the first five seconds of the scans, respectively. Forty edge channels of the original 2049 are also flagged due to bandpass roll-off (Wilson et al., 2011). Again using the `flagdata` task, the uncalibrated data are then automatically flagged for RFI using `mode='tfcrop'`, which calculates flags based on a time and frequency window. The data are manually inspected in an amplitude versus channel space, to ensure RFI is adequately flagged. Observations conducted in the *LS*-band and *CX*-band were split into four and eight sub-bands, respectively. Calibration was performed per sub-band per pointing. To perform calibration, the complex gains and bandpass are solved for first using the primary calibrator. Complex gains and leakages were solved for next using the secondary calibrator. After applying a flux-scale correction based on PKS B1934-638, the calibration solutions were copied individually to each target scan. A secondary round of automatic RFI flagging is performed with `flagdata` where `mode='rflag'`, which is used for calibrated data. The primary and secondary calibrator, as well as each target scan are flagged in this way. In to-

[8]Time per source was varied slightly to accommodate for the fainter/brighter sources.
[9]This work makes use of CASA version 5.1.2-4

tal, approximately $\approx 52\%$ and $\approx 15\%$ of the available bandwidth was flagged due to RFI present in the LS and CX bands, respectively. Within the hybrid configurations the first five antennas, CA01–CA05, provide the dense packing of short (10–100 m) spacings. Antenna CA06 is fixed and provides much larger spacings of ∼4500 m. Given that this results in a large gap in the uv coverage, all baselines formed with antenna CA06 are excluded to achieve a well-behaved point-spread-function. The average noise properties and restoring beams at 2.1, 5.5 and 9 GHz are respectively: $\sigma \sim 0.7\,\mathrm{mJy\,beam^{-1}}$ and $\theta = 104'' \times 127''$, $\sigma \sim 0.22\,\mathrm{mJy\,beam^{-1}}$ and $88'' \times 110''$, and $\sigma \sim 0.14\,\mathrm{mJy\,beam^{-1}}$ and $\theta = 54'' \times 67''$. We use any unresolved GLASS sources present within the target scans to evaluate a calibration uncertainty. At 5.5 GHz, the ratio of the integrated flux density between the low-resolution ATCA observations and GLASS was consistently within 3%. We use this value as the absolute flux-scale uncertainty. Details of these observations are summarized in Table 2.2. A comparison of these observations and GLASS, at 5.5 GHz, is presented in Figure 2.2. The reader should note, due to persistent RFI in the LS-band, we were unable to make a detection of most of our targets at this frequency.

2.2.2 Optical/near-infrared data

2.2.2.1 VIKING near-infrared imaging

Observed with the Visible and Infrared Survey Telescope for Astronomy (VISTA), the VISTA Kilo-degree INfrared Galaxy survey (VIKING) provides medium-deep observations over $\sim 1500\,\mathrm{deg^2}$ across the Z, Y, J, H & K_s bands, each achieving a 5σ AB magnitude limit of 23.1, 22.3, 22.1, 21.5 and 21.2 respectively. VIKING imaging is used to perform both an automated and manual host galaxy identification (see Sect. 2.3).

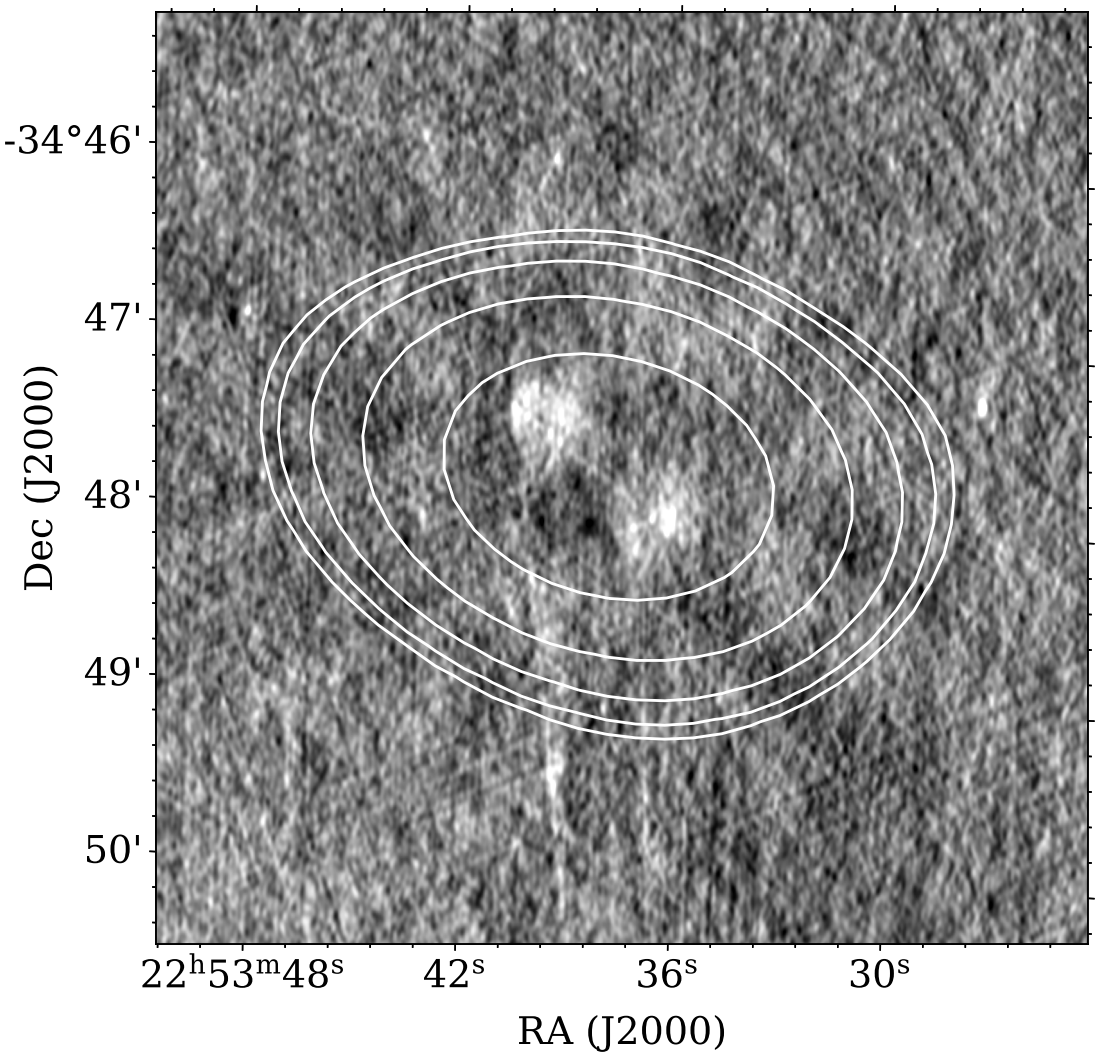

Figure 2.2: A 5.5 GHz view of the radio source MIDAS J225337−344745. The image offers a comparison between (i) GLASS (Sect. 2.2.1.5) presented as the gray-scale image on a linear stretch, and (ii) the low-resolution ATCA observations (Sect. 2.2.1.7) represented by the solid white contours. Contour levels are set at [5, 6.3, 9.6, 17.3, 35.5]$\times\sigma$, where $\sigma = 210\mu$ Jy beam^{-1} and is the local RMS.

2.2.2.2 GAMA 23 photometry catalogue

The GAMA 23 photometry catalogue (Bellstedt et al., 2020) contains measured properties and classifications of each object catalogued by the ProFound[10] (Robotham et al., 2018) source finding routine, which uses a stacked $r+Z$ image to perform initial source finding. Approximately 48,000 objects have spectroscopic redshifts provided by the Anglo-Australian Telescope (AAT), and the survey is $\sim$95% spectroscopically complete up to an i band magnitude of 19.5 (Liske et al., 2015). For objects without spectroscopic redshifts, we use the near-UV to far-IR photometry (available in the photometry catalogue) to obtain photometric redshifts using a public photometric redshift code (EAZY; Brammer et al., 2008)[11].

2.3 Methodology

2.3.1 Sample construction

Our methodology for compiling a sample of radio galaxies, and classifying their activity status, is presented below. We begin our selection at low frequencies where steep-spectrum radio lobes are naturally brighter. Not only does MIDAS ES provide access to such low frequencies, but also its relatively low spatial resolution results in a sensitivity to low-surface-brightness emission that is required to recover emission from diffuse, extended radio sources.

Genuine remnant radio galaxies will not display radio emission from the core associated with the AGN jet activity at the centre of the host galaxy. As such, we classify any radio galaxy as 'active' if positive radio emission is observed from the radio core. Similarly, we prescribe a 'candidate remnant' status to any radio galaxy that demonstrates an absence of radio emission from the core. True emission from the radio core will be unresolved even on parsec scales, meaning observations with high spatial resolution are ideal for their detection. This also

[10]Publicly available on GitHub: https://github.com/asgr/ProFound
[11]EAZY publicly available on GitHub: https://github.com/gbrammer/eazy-photoz

No.	Sample step	Criteria	Sample size
1	Limit footprint within GLASS region D	$343° \leq \mathrm{RA} \leq 347°$ $-32.5° \leq \mathrm{Dec} \leq -35°$	676
2	Flux-density cut	$S_{216\mathrm{MHz}} > 10\,\mathrm{mJy}$	446
3	Angular size cut†	$\theta \geq 25''$	109
3.1		$\theta_{\mathrm{GLASS}} \geq 25''$	*(82)*
3.2		$\theta_{\mathrm{GLASS}} < 25''$ & $\theta_{\mathrm{EMU-ES}} \geq 25''$	*(27)*
4	AGN dominated	Remove radio sources tracing the optical/near-IR galaxy component	106
5	Activity status	Radio core in GLASS 5.5 (Active)	94
		No radio-core in GLASS 5.5 (Remnant cand.)	10
6	Host identification (Active)	Visually match radio core with VIKING galaxy	26 (z_s) 54 (z_p) 14 (no z)
	Host identification (Remnant)	See Sect. 2.4	3 (z_s) 7 (z_p)

Table 2.3: Summary of each sample criteria discussed in Sect. 2.3. Steps 1–4 describe the radio galaxy sample selection. Step 5 describes the active/remnant classification. Step 6 describes host galaxy association.
†Step 3 is broken into two parts, denoted by steps 3.1 and 3.2, for which the resulting sample size is the sum total.

ensures that the emission from the radio core is not contaminated by emission from the radio lobes. As demonstrated by Mahatma et al. (2018), sensitive observations are equally important to enable the detection of radio cores. GLASS addresses both of these considerations by providing sensitive ($\sim 30\,\mu$Jy beam^{-1}), high resolution ($4'' \times 2''$) radio observations at 5.5 GHz. Our sample is constructed by following the steps outlined below (see Table 2.3), and is presented in full as a supplementary electronic table (see Table A.1 for column descriptions).

1. *Limit the search footprint within GLASS region D*

   The footprint, within which radio galaxies are selected, is constrained to $343^\circ \leq \mathrm{RA} \leq 347^\circ$, $-35^\circ \leq \mathrm{Dec} \leq -32.5^\circ$. This excludes the outer regions of higher noise from the GLASS mosaic thus ensuring the GLASS noise levels range between $25{-}35\mu$Jy beam^{-1} at 5.5 GHz. By maintaining almost uniform noise levels across the field, this reduces the bias of selecting brighter radio cores in higher-noise regions. By applying this footprint to the MIDAS ES component catalogue, 676 components are selected. The resulting sky coverage within this footprint is 8.31 deg^2.

2. *Flux-density cut*

   A 10 mJy flux density cut at 216 MHz is imposed on the sample. Given the low angular resolution, this ensures the MIDAS ES detections are robust, e.g. greater than 10σ for an unresolved source. We identify 446 radio sources brighter than 10 mJy at 216 MHz.

3. *Angular size cut*

   Our decision to impose a minimum size constraint was motivated by two factors: firstly to minimise blending of the radio core with the radio lobes, and secondly to allow for an interpretation of the radio source morphology. By imposing a minimum $25''$ angular size constraint, we ensured a minimum of six GLASS 5.5 synthesized beams spread out across the source. For each

of the 446 radio sources, we produce $2' \times 2'$ cutouts[12] centered at the catalogued MIDAS ES source position. EMU-ES, GLASS 5.5, GLASS 9.5 and VIKING K_s-band cutouts are generated, and contours of the radio emission are overlaid onto the VIKING K_s-band image. Henceforth, we refer to these as image overlays. While GLASS 5.5 has the advantage in spatial resolution, EMU-ES has a significantly better brightness-temperature sensitivity. This consideration is important since faint radio lobes, while seen in EMU-ES, may become undetected by GLASS 5.5.

As such, a first pass is conducted by identifying any radio source with an angular size greater than $25''$ in GLASS 5.5 (e.g. $\theta_{\text{GLASS 5.5}} \geq 25''$). Due to the manageable size of the sample, we do this step manually by visually matching the correct components of each radio source, and measure the linear angular extent across each radio source. We identify 82 radio sources this way. For radio sources with $\theta_{\text{GLASS 5.5}} < 25$", we use the aforementioned image overlays to identify any radio sources for which the low-surface-brightness lobes escape detection in GLASS 5.5. For such cases, the angular size is measured using EMU-ES, and are accepted if $\theta_{\text{EMU}-\text{ES}} \geq 25''$ (e.g. see Figure 2.3). An additional 27 radio sources are identified this way, giving a total of 109 radio sources greater than $25''$. For consistency, the angular size of each radio source is re-measured using EMU-ES, by considering the largest angular size subtended within the footprint of radio emission above 5σ.

4. *AGN dominated*

   As a result of their sensitivity to low-surface-brightness emission, both MIDAS ES and EMU-ES are able to detect radio emission from a typical face-on spiral galaxy. Radio emission from these objects is not driven by a radio-loud AGN, but by stellar processes, and therefore these sources need to be removed from the sample. At the angular scales probed by this

[12]Image cutouts are generated using ASTROPY module `Cutout2D`

work, radio emission from such stellar processes can be identified through the coincidence of the radio morphology relative to its host galaxy. While it is known that compact AGN-driven radio emission can also be confined within the host galaxy, the radio morphologies of such sources still resemble a jet-lobe structure. Using the aforementioned image overlays, we therefore remove three radio sources that trace the optical/near-infrared component of the host galaxy, as revealed with VIKING K_s-band imaging. We provide an example in Figure 2.4. The remaining sample contains 106 extended radio galaxies, forming the parent sample for this analysis.

5. *Activity status*

   To constrain the nuclear activity associated with an AGN, we use GLASS 5.5 imaging to search for evidence of a radio core. For a successful radio core detection, we require a compact object with a peak flux density greater than 3σ. We use BANE to produce an RMS image associated with each GLASS 5.5 image cutout. Only pixel values above 3σ are considered. We use the orientation and morphology of the radio lobes as a rough constraint on the potential position of the radio core. Following this method, we classify 94 radio galaxies as active, and a further 11 as candidate remnant radio galaxies. We emphasise that this method only selects *candidate* remnant radio galaxies, since the existence of a faint, undetected radio core is still possible. For each remnant candidate we place a 3σ upper limit on the peak flux density of the core. Here, σ is measured by drawing a circle equivalent to four GLASS synthesized beams at the position of the presumed host galaxy and measuring the RMS within this region.

6. *Host identification*

   For radio sources with a core, we use a $1''$ search radius to cross match the position of the radio core with the GAMA 23 photometry catalog. Out of 94 such sources, the hosts of 80 radio galaxies are identified this way, of which 26 and 54 have spectroscopic and photometric redshifts, respec-

tively. The hosts of the remaining 14 sources are either extremely faint in K_s-band, or remain completely undetected in VIKING, potentially due to lying at higher redshift. Host identification for remnant candidates is discussed on a per-source basis in Sect. 2.4, as this is a complicated and often ambiguous procedure. For each radio source we also use WISE (Wright et al., 2010) 3.4μ m and 4.6μ m images to determine if any potential hosts were not present in the VIKING imaging, however this did not reveal any new candidates.

2.3.2 Collating flux densities

For each of the 104 radio galaxies, integrated flux densities are compiled from the data described in Sect. 2.2.1. To compile the integrated flux densities at 119, 154 and 186 MHz (GLEAM SGP), 216 MHz (MIDAS ES), and 1400 MHz (NVSS), we use their appropriate source catalogues described in their relevant data sections. As a result of the high spatial resolution at 399 MHz (uGMRT observations), 887 MHz (EMU-ES) and 5.5 GHz (GLASS 5.5), sources are often decomposed into multiple components. To ensure the integrated flux densities are measured consistently across these surveys, we convolve their image cutouts of each source with a 54″ circular resolution (e.g. the major axis of the MIDAS synthesized beam). Integrated flux densities are then extracted using AEGEAN by fitting a Gaussian to radio emission. For each remnant candidate observed with ATCA at low resolution at 2.1, 5.5 and 9 GHz, we use AEGEAN to measure their integrated flux densities. The 5.5 GHz integrated flux density reported for each remnant candidate is exclusively taken from these low resolution ATCA observations, not GLASS. Finally, for each integrated flux density measurement, uncertainties are calculated as the quadrature sum of the measurement uncertainty and the absolute flux-scale uncertainty.

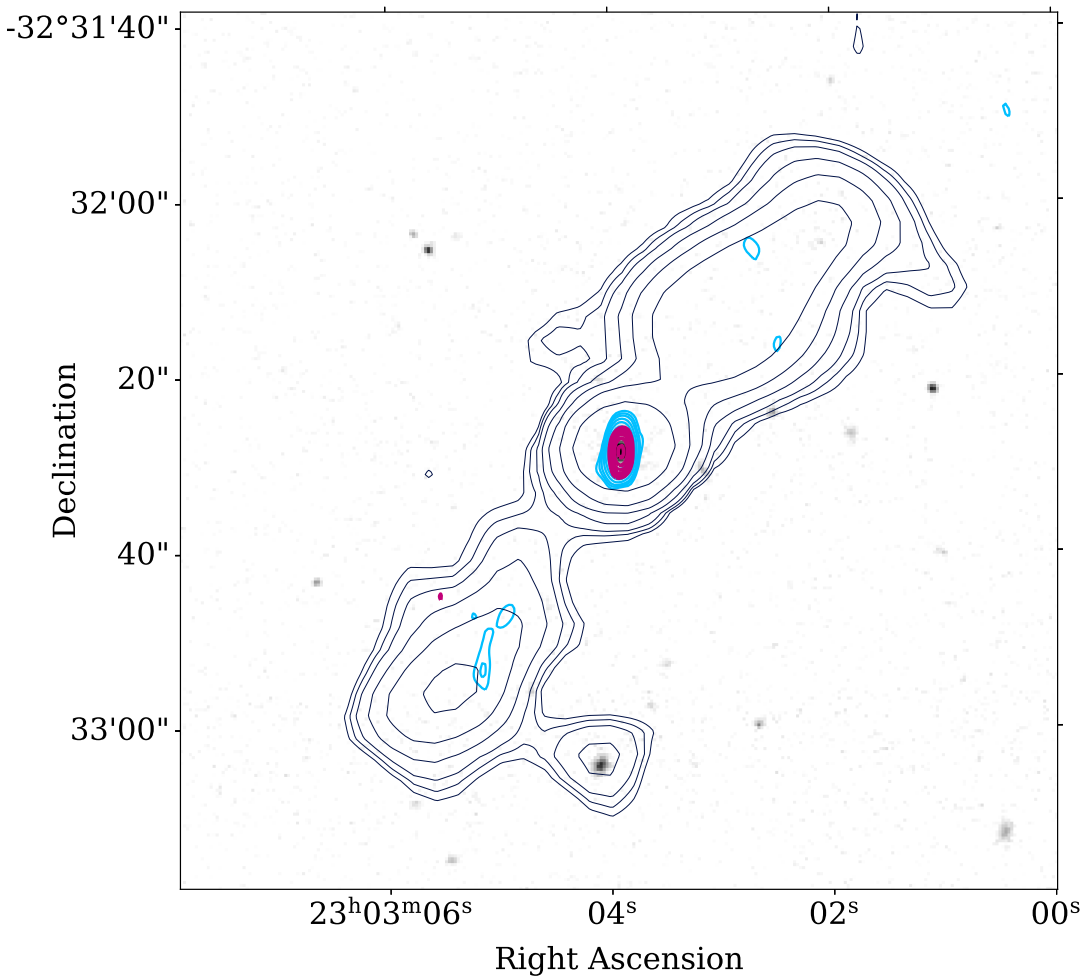

Figure 2.3: Example of the radio source MIDAS J230304-323228 satisfying the criterion: $\theta_{\rm GLASS} < 25'' \ \& \ \theta_{\rm EMU-ES} \geq 25''$. The low-surface-brightness lobes are escaping detection in GLASS, resulting in an incomplete morphology. The contours represent EMU-ES (navy blue), GLASS 5.5 (cyan) and GLASS 9.5 (magenta), with levels set at [3,4,5,7,10,15,25,100]$\times\sigma$, where σ is the local RMS of 43, 26 and 40 μJy beam^{-1} respectively. Contours are overlaid on a linear stretch VIKING K_s-band image. The seemingly absent hotspots would imply these are remnant lobes, however the presence of a radio core means this source is classified as 'active'. The true nature of this source *may* be a restarted radio galaxy, however the lack of any resolved structure around the core is puzzling.

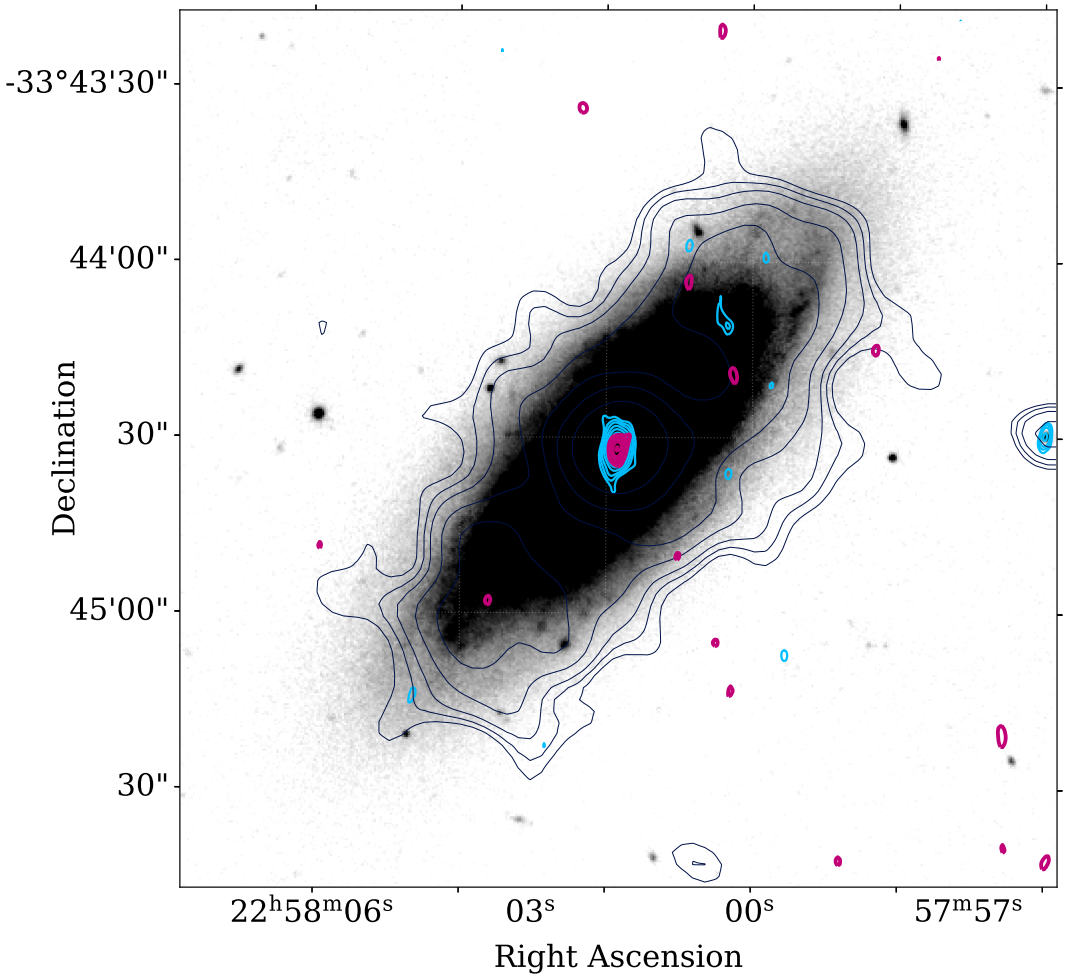

Figure 2.4: Example of a non AGN-dominated radio source, MIDAS J225802-334432, excluded from the sample. Analysis of the radio morphology shows that the radio emission traces the optical component of the host galaxy. The contours represent EMU-ES (navy blue), GLASS 5.5 (cyan) and GLASS 9.5 (magenta), with levels set at [3,4,5,7,10,15,25,100]$\times\sigma$, where σ is the local RMS of 45, 28 and 41 μ Jy beam^{-1} respectively. Contours are overlaid on a linear stretch VIKING K_s-band image. The radio emission is hosted by IC 5271 (ESO 406-G34).

2.3.3 Radio SED Fitting

To better understand their energetics, we model the integrated radio spectrum of each remnant candidate. We use a standard power-law model of the radio continuum spectrum (Eqn 2.1), where the spectral index, α, and the flux normalization S_0 are constrained by the fitting, and ν_0 is the frequency at which S_0 is evaluated:

$$S_\nu \;=\; S_0 \; (\nu/\nu_0)^\alpha \tag{2.1}$$

Given we can expect to see evidence of a curvature in their spectra, especially over such a large frequency range, we also fit a generic curved power-law model (Eqn 2.2). Here, q offers a parameterization of the curvature in the spectrum, where $q < 0$ describes a convex spectrum. For optically-thin synchrotron emitted from radio lobes, q typically ranges within $-0.2 \leq q \leq 0$. Although q is not physically motivated, Duffy & Blundell (2012) show that it can be related to physical quantities of the plasma lobes such as the energy and magnetic field strength.

$$S_\nu \;=\; S_0 \; \nu^\alpha e^{q(\ln\nu)^2} \tag{2.2}$$

Fitting of each model is performed in Python using the CURVE_FIT module; fitted models are presented in Figures 2.5a–2.5j. Additionally, we calculate a Bayesian Information Criterion (BIC) for each model. To compare each model, we calculate a $\Delta\mathrm{BIC} = \mathrm{BIC}_1 - \mathrm{BIC}_2$ which suggests a preference towards the second model for $\Delta\mathrm{BIC} > 0$ (and similarly, a preference towards the first model if $\Delta\mathrm{BIC} < 0$). Weak model preference is implied by the following range $0 < |\Delta\mathrm{BIC}— < 2$, whereas a model is strongly preferred if $|\Delta\mathrm{BIC}— > 6$. In Table 2.4, we calculate $\Delta\mathrm{BIC} = \mathrm{BIC}_{\mathrm{power-law}} - \mathrm{BIC}_{\mathrm{curved-power-law}}$.

MIDAS Name	Fig.	S_{216} (mJy)	LAS ($''$)	S_{core} (μJy beam^{-1})	Power-law		Curved power-law			ΔBIC
					α_{fit}	χ^2_{red}	α_{fit}	q	χ^2_{red}	
J225522−341807	2.5a	24.7±1.9	100	< 73	-1.40±0.09	2.2	-1.50±0.10	-0.11±0.08	1.5	-13.2
J225607−343212	2.5b	18.3±2.0	83	< 72	-1.10±0.04	1.2	-1.20±0.01	-0.073±0.01	0.1	3.1
J225608−341858	2.5c	14.7 ± 2.0	60	< 72	-0.86±0.05	0.3	-0.91±0.1	-0.04±0.07	0.3	-2.2
J225337−344745	2.5d	170.6 ± 5.8	105	< 74	-0.92±0.05	12.1	-0.89±0.02	-0.12±0.02	0.8	23.8
J225543−344047	2.5e	192.7 ± 5.8	84	< 117	-0.87±0.01	0.4	-0.87±0.02	-0.003±0.01	0.5	-2.8
J225919−331159	2.5f	36.6 ± 2.0	70	< 60	-0.86±0.02	1.0	-0.89±0.02	0.035±0.01	0.5	-6.9
J230054−340118	2.5g	113.4 ± 6.7	106	< 86	-0.73±0.03	2.8	-0.72±0.03	-0.027±0.02	2.5	-4.1
J230104−334939	2.5h	55.4 ± 2.2	37	< 57	-0.72±0.03	2.0	-0.69±0.04	-0.023±0.01	2.0	2
J230321−325356	2.5i	153.6 ± 6.0	93	< 74	-0.86±0.01	0.9	-0.85±0.01	-0.019±0.01	0.5	6.4
J230442−341344	2.5j	198.1 ± 6.1	50	< 84	-1.00±0.02	1.2	-1±0.02	-0.008±0.02	1.5	-1.3

Table 2.4: Summarized radio properties of the selected remnant candidates. S_{216} gives the 216 MHz integrated flux density. LAS gives the largest angular size measured from EMU-ES. S_{core} gives the 5.5 GHz upper limit placed on the radio core peak flux density using GLASS. α_{fit} denotes the spectral index fitted by each model. The curvature term modelled by the curved power-law model is represented by q. As per Sect. 2.3.3, the ΔBIC is calculated between each model and presented in the final column. A reduced chi-squared (χ^2_{red}) is also evaluated for each model.

2.4 Remnant radio galaxy candidates

We present and discuss each of the 11 candidate remnant radio galaxies below. Seven are found to display hotspots in GLASS. Image overlays and the radio continuum spectrum are presented in Figure 2.5. General radio properties are presented in Table 2.4.

2.4.1 Remnant candidates without hotspots

2.4.1.1 MIDAS J225522-341807

Radio properties. Figure 2.5a shows extremely relaxed lobes and an amorphous radio morphology. No compact structures that would indicate hotspots are observed. The average 154 MHz surface brightness is $\sim 32\,\mathrm{mJy\,arcmin^{-2}}$, satisfying the low SB criterion ($\mathrm{SB} < 50\,\mathrm{mJy\,arcmin^{-2}}$) employed by Brienza et al. (2017). The diffuse radio emission is undetected by the uGMRT observations, NVSS, GLASS, as well as the 2.1 GHz and 9 GHz ATCA follow-up observations. Unsurprisingly, we find that the source spectrum appears ultra-steep at low frequencies, and demonstrates a curvature ($q = -0.11$) across the observed range of frequencies. The radio properties point towards an aged remnant.

Host galaxy. Identification of the host galaxy is rather challenging here as the amorphous radio morphology provides little constraints on the host position. No clear host galaxy is seen along the centre of the radio emission, however this can easily be explained if the radio lobes have drifted. We approximate the central position of the radio emission by taking the centre of an ellipse drawn to best describe the radio source. G1 ($z_p = 0.474$) is located $10.2''$ from the radio center, corresponding to a 61 kpc offset. G2 ($z_p = 0.433$) is located $14.1''$ from the radio center, corresponding to a 80 kpc offset. G3 ($z_p = 0.294$) is located $23''$ from the radio center, corresponding to a 102 kpc offset. Without any additional information, we take G1 as the likely host galaxy. We note that G4 ($z_p = 0.41$) shows compact radio emission at 887 MHz, however it is unclear whether this is

related to the extended structure. We include the radio spectrum arising from G4 in Figure 2.5a, and note that it contributes approximately 5% to the total radio flux density at 887 MHz. If G4 is unrelated, its radio spectrum should be subtracted from the integrated spectrum of MIDAS J225522-341807.

2.4.1.2 MIDAS J225607-343212

Radio properties. Figure 2.5b shows a pair of relaxed radio lobes, with a diffuse bridge of emission connecting each lobe along the jet axis. The 154 MHz average surface brightness is calculated as $\sim$ 26mJy arc-minute^{-2}, satisfying the low surface brightness criterion. The edge brightened regions likely represent the expanded hotspots of the previously active jet, similar to what is observed in B2 0924+30 (Shulevski et al., 2017). The source is undetected by the uGMRT observations, GLASS, as well as the ATCA follow-up at 2.1 GHz and 9 GHz. Curvature is evident in the spectrum, which becomes ultra-steep above 1.4 GHz.

Host galaxy. Along the projected centre of the jet axis, a collection of three potential host galaxies exist within a $\sim 7''$ aperture. The redshift of each host, G1 ($z_s = 0.31307$), G2 ($z_p = 0.361$), G3 ($z_s = 0.27867$), suggests they are all at similar redshift, and thus would not result in an appreciable difference to the corresponding physical size and radio power. We take G1 as the most likely host as it lies closest to the projected centre of the radio lobes.

2.4.1.3 MIDAS J225608-341858

Radio properties. Figure 2.5c shows two relaxed, low surface brightness lobes that are asymmetrical in shape. The flattened 'pancake'-like morphology of the Northern lobe can be explained by the buoyant rising of the lobes (Churazov et al., 2001). The surface brightness of each lobes is approximately 43 mJy arcmin^{-2}, satisfying the low SB criterion employed by Brienza et al. (2017). The source is undetected by the follow-up 2.1 GHz and 9 GHz ATCA observations. The spectrum seems consistent with a single power law ($\alpha = -0.86$), and the detection

at 5 GHz is too weak to determine whether spectral curvature is evident at higher frequencies.

Host galaxy. G1 ($z_p = 0.57$) lies 4.8″ away from the radio center, corresponding to a 32 kpc offset. G2 ($z_p = 0.321$) lies 13″ away from the radio center, corresponding to a 61 kpc offset. This assumes that the lobes are equidistant from the host, which is not always the case. However, we retain G1 as the likely host galaxy.

2.4.2 Candidates with hotspots

2.4.2.1 MIDAS J225337-344745

Radio properties. Figure 2.5d shows a typical low-resolution FR-II radio galaxy as evidenced by the edge-brightened morphology. The average 154 MHz surface brightness is 160 mJy arcmin^{-2}. The source is firmly detected by the ATCA follow-up at all frequencies, revealing that the spectrum is highly curved ($q = -0.12$) over the observed frequency range and only becomes ultra-steep at $\nu \gtrsim 2$ GHz. An evaluation of its spectral curvature reveals SPC $= 0.78 \pm 0.17$, suggesting the lobes are remnant. The properties of the spectrum strongly suggest a lack of energy supply to the lobes, however, GLASS 5.5 reveals compact emitting regions at the edges of each lobe that may suggest recent energy injection. We divert a detailed analysis of this source to Sect. 2.5.3.

Host galaxy. The radio lobes are unambiguously associated with galaxy G1 ($z_s = 0.2133$) based on the close proximity to the geometric centre of the lobes.

2.4.2.2 MIDAS J225543-344047

Radio properties. Figure 2.5e demonstrates an elongated, 'pencil-thin', radio galaxy with an edge-brightened FR-II morphology. GLASS detects only the brightest and most compact emitting regions, and misses the lower surface brightness emission seen at 887 MHz. The radio source is detected in all but the 2.1 GHz

ATCA follow-up observations. The radio spectrum is well modelled by a power-law ($\alpha = -0.87$), and shows no evidence of a curvature up to 9 GHz.

Host galaxy. G1 ($z_p = 1.054$) lies closest to the projected radio center. G2 ($z_p = 1.019$) and G3 ($z_p = 1.342$) are also likely, however the difference in implied redshift would not result in an appreciable change to the derived physical size and radio power.

2.4.2.3 MIDAS J225919-331159

Radio properties. Figure 2.5f demonstrates a pair of lobes with compact emitting regions seen by GLASS. The radio spectrum is well approximated as a power-law ($\alpha = -0.86$) with no evidence of a spectral curvature over the observed range of frequencies.

Host galaxy. G1 ($z_p = 0.504$) is taken as the likely host galaxy due to its central position between each lobe.

2.4.2.4 MIDAS J230054-340118

Radio properties. Figure 2.5g shows a peculiar radio morphology; while the western lobe shows bright emitting regions in GLASS, the counter lobe is completely diffuse and does not show a hotspot. It is unclear what is causing this.

Host galaxy. The galaxies G1 ($z_p = 0.32$) and G2 ($z_s = 0.306$) are considered as host candidates, given their position between each lobe. We find that G2 is not associated with any galaxy group; if the lobe asymmetry is due to an environmental effect, we would not expect a field galaxy host. We can not comment on whether G1 is associated with a group, given the lack of a spectroscopic confirmation.

2.4.2.5 MIDAS J230104-334939

Radio properties. Figure 2.5h shows a typical FR-II radio galaxy, as implied by the edge-brightened morphology. The source exhibits clear hotspots in each

lobe, as seen by GLASS 5.5 and GLASS 9.5. The source is detected in all but the 2.1 GHz ATCA follow-up. Modelling the radio continuum spectrum gives a spectral index of approximately $\alpha = -0.7$, revealing no significant energy losses. The ΔBIC offers tentative evidence for some spectral curvature, however this may just be a result of a poorly constrained spectrum at low (≤ 215 MHz) frequencies.

Host galaxy. The radio source is unambiguously associated with G1 ($z_s = 0.312$), which almost perfectly aligns with the projected centre of the source.

2.4.2.6 MIDAS J230321-325356

Radio properties. Figure 2.5i shows two distinct radio lobes with compact emitting regions observed at 5.5 GHz and 9.5 GHz. The spectral index is approximately $\alpha = -0.86$ showing no significant evidence of spectral ageing. The ΔBIC does indicate a preference towards the curved power law model, however any real curvature in the spectrum is marginal ($q \sim -0.02$) and does not necessarily require an absence of energy injection. *Host galaxy.* Three likely host galaxies are identified by their alignment along the projected jet axis; G1 ($z_p = 1.327$), G2 ($z_p = 0.622$) and G3 ($z_p = 0.775$). We assume G1 is the true host, due to its smaller separation from the projected radio center.

2.4.2.7 MIDAS J230442-341344

Radio properties. Figure 2.5j . Both lobes are detected in GLASS 5.5, however, only the southern lobe shows emission in GLASS 9.5. It is unclear what is causing this; both components are resolved by GLASS and show similar morphologies, so it is unlikely they are unrelated. The radio spectrum is well approximated by a power-law ($\alpha = -1$), with no evidence of a spectral curvature. *Host galaxy.* G1 ($z_p = 0.9$) is a favourable host galaxy candidate, due to its small angular separation from the projected centre between the lobes. G2 ($z_p = 0.8075$) is located further off centre towards the South, at a similar implied redshift.

(a) **MIDAS J225522−341807**. EMU-ES contour levels: [3,4,5,7,10]×σ. GLASS 5.5 contour levels: [3,4,5]×σ. GLASS 9.5 contours are not presented due to an absence of radio emission above 3σ. Compact component at RA=$22^{h}55^{m}25.5^{s}$, Dec= -34°18′40″ is unrelated. The radio spectrum of the compact radio component, G4, is demonstrated by the blue markers. Radio emission from G4 is undetected by GLASS 5.5, we thus present a 3σ upper limit.

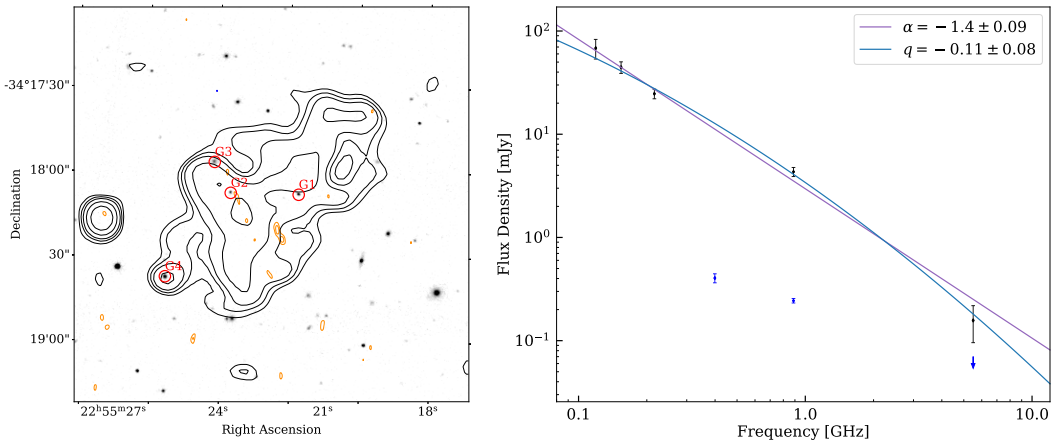

(b) **MIDAS J225607−343212**. EMU-ES contour levels: [3,4,5,7,10,12,15,20]×σ. GLASS 5.5 contour levels: [3,4,5]×σ. GLASS 9.5 contours are not presented due to an absence of radio emission above 3σ. Compact component at RA=$22^{h}56^{m}03^{s}$, Dec= -34°32′55″ is unrelated.

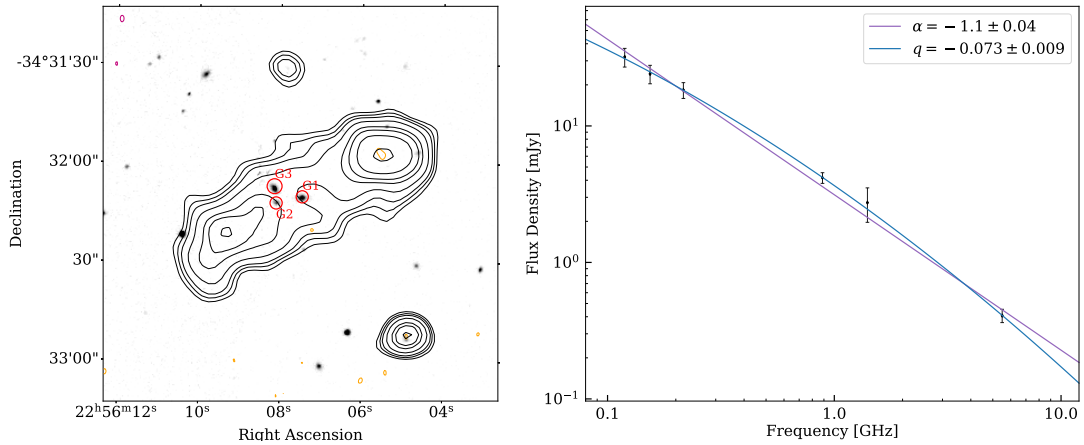

Figure 2.5: **Left:** Plotted are the remnant candidates presented in Sect. 2.4. Background image is a VIKING K_s band cutout set on a linear stretch. Three sets of contours are overlaid, representing the radio emission as seen by EMU-ES *(black)*, GLASS 5.5 *(orange)* and GLASS 9.5 *(blue)*. Red markers are overlaid on the positions of potential host galaxies. **Right:** The radio continuum spectrum between 119 MHz and 9 GHz. The integrated flux densities at 5.5 GHz come from the low-resolution ATCA observations (Sect. 2.2.1.7) not the lower resolution GLASS images. A simple power-law (Eqn 2.1) and curved power-law (Eqn 2.2) model are fit to the spectrum, indicated by the *purple* and *blue* models, respectively.

(c) **MIDAS J225608−341858**. EMU-ES contour levels: [3,4,5,7,10]×σ. GLASS 5.5 contour levels: [3,4,5]×σ. GLASS 9.5 contours are not presented due to an absence of radio emission above 3σ.

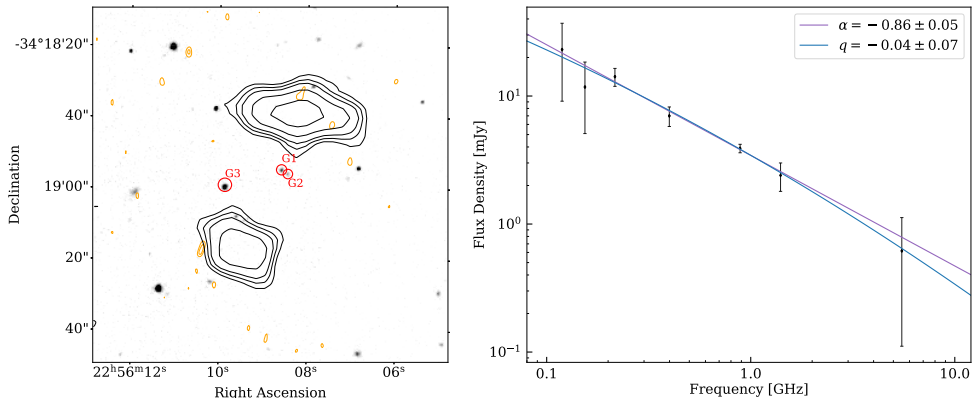

(d) **MIDAS J225337−344745**. EMU-ES contour levels: [4,5,10,30,50,70]×σ, GLASS 5.5 contour levels: [3,4,5,6]×σ. GLASS 9.5 contours are not presented due to an absence of radio emission above 3σ.

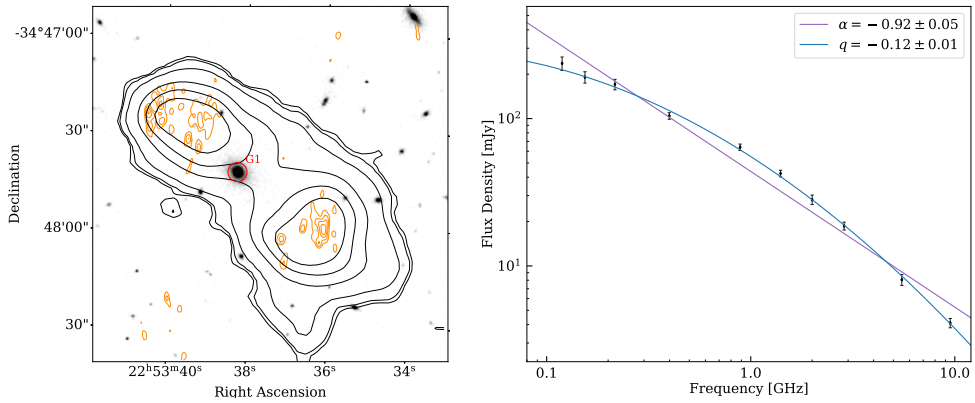

(e) **MIDAS J225543−344047**. EMU-ES contour levels: [3,4,5,7,15,30,100]×σ, GLASS 5.5 contour levels: [3,5,10,20]×σ. GLASS 9.5 contour levels: [3,5,10,20]×σ

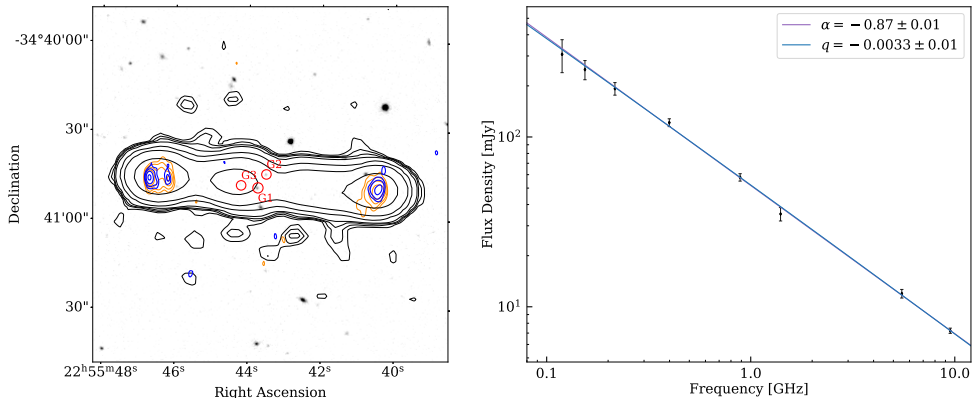

Figure 2.5: – continued.

(f) **MIDAS J225919-331159**. EMU-ES contour levels: [5,10,20,40,60]×σ, GLASS 5.5 contour levels: [3,4,5,6,10,20]×σ. GLASS 9.5 contour levels: [3,4,5,6]×σ

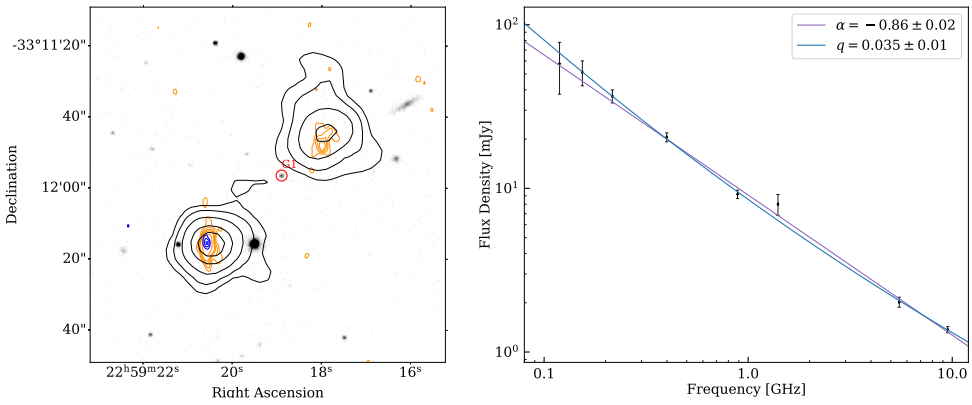

(g) **MIDAS J230054−340118**. EMU-ES contour levels: [3,4,5,7,15,30,100,300]×σ, GLASS 5.5 contour levels: [3,5,10,20,30]×σ. GLASS 9.5 contour levels: [3,5,10,20]×σ

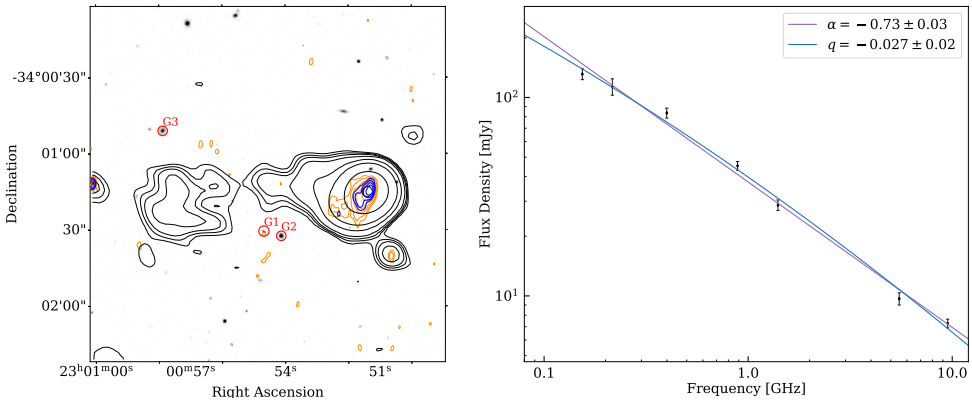

(h) **MIDAS J230104-334939**. EMU-ES contour levels: [5,8,15,35,50]×σ, GLASS 5.5 contour levels: [3,5,7,9,11]×σ. GLASS 9.5 contour levels: [3,4,5,6]×σ

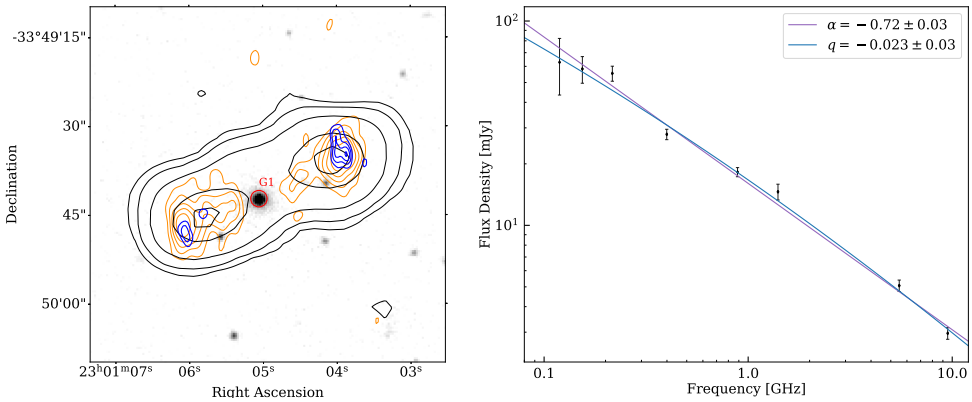

Figure 2.5: – continued.

(i) **MIDAS J230321−325356**. EMU-ES contour levels: [5,10,30,100,300]×σ, GLASS 5.5 contour levels: [3,5,10,20,30,40,50]×σ. GLASS 9.5 contour levels: [3,5,10,20]×σ

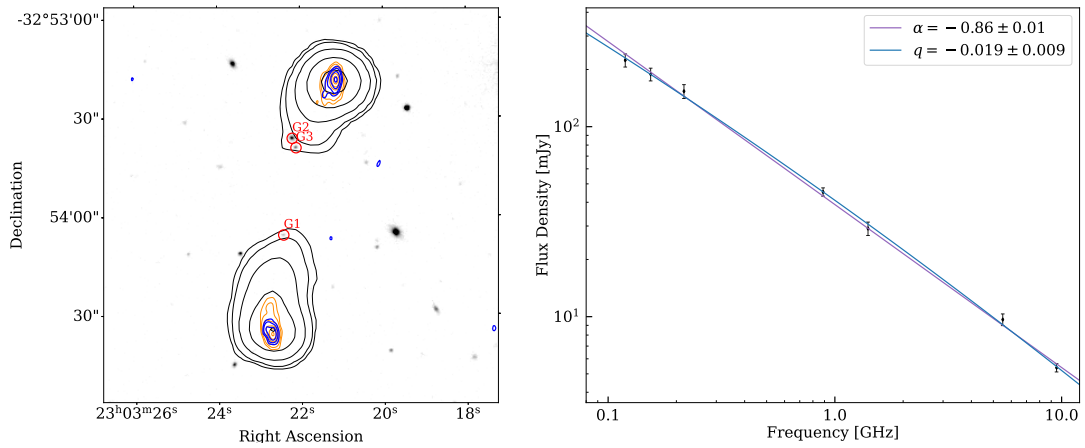

(j) **MIDAS J230442−341344**. EMU-ES contour levels: [5,10,30,100,300]×σ, GLASS 5.5 contour levels: [3,5,10,20,30,40,50]×σ. GLASS 9.5 contour levels: [3,5,10,20]×σ

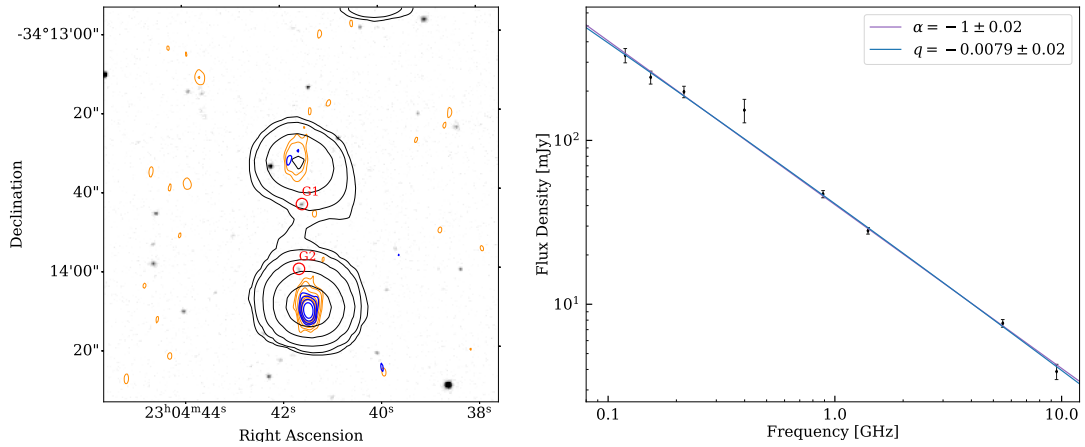

Figure 2.5: – continued.

2.5 Discussion

2.5.1 Sample properties

2.5.1.1 Core prominence distribution

To understand the limitations imposed by our selection criteria, we investigate the core prominence distribution across our sample. We define the core prominence (CP) as the ratio of core to total flux density, i.e. CP $= S_{\rm core}/S_{\rm total}$. The total integrated flux density is measured at 216 MHz. We take the GLASS 5.5 measurement of the radio core flux density, and re-scale to 216 MHz assuming the spectrum of the radio core is a flat spectrum ($\alpha = 0$) (e.g; Hardcastle & Looney, 2008). For the selected remnant candidates, we present upper limits on their CP by using the 3σ upper limits on their core peak flux density. Our results are presented in Figure 2.6.

Sources with radio cores show a wide distribution in their CP, varying within the range 10^{-1} – 10^{-4}. The median CP of the sample is $\sim 1 \times 10^{-2}$, almost two orders of magnitude larger than the median CP reported by Mullin et al. (2008) for the 3CRR sample (e.g. $\sim 3 \times 10^{-4}$). This can be expected given the most powerful radio galaxies are preferentially selected by 3CRR. Instead, comparing our CP range to the LOFAR-selected sample compiled by Mahatma et al. (2018) – e.g. see their Figure 4 – we find the ranges are consistent. Although the reader should note Mahatma et al. (2018) compute their CP at 150 MHz, meaning a $\Delta\nu = 66$ MHz frequency shift should be accounted for if a direct comparison is made.

As discussed in Sect. 2.1, the 'absent radio core' criterion only selects remnant candidates. Genuine remnant radio galaxies will not display a radio core, meaning their CP should approach null. In fact, the CP in such sources should be lower than any active radio source in which a radio core is present. This implies

that a clean separation should exist between active and remnant radio galaxies, however, this is not what we see in Figure 2.6. Instead, we find that the CP upper limits imposed on the remnant candidates overlap with core-detected radio galaxies. This comes as a result of our sample criteria. Given the GLASS detection limit ($\sim 75\mu$Jy beam^{-1}), only remnant candidates brighter than ~ 500 mJy will show CP upper limits below what is observed for core-detected radio galaxies (e.g. $\log(\mathrm{CP}) \lesssim -3.7$). This result indicates that it is still possible for some of the selected remnant candidates to display a faint radio core that is missed by GLASS. For remnant candidates without hotspots this is less of a concern, as we have additional information that would suggest the jets have switched off. However, for those with hotspots, decreasing the upper limits on their CP is required to confidently assert whether their AGN has switched off. As such, these sources must retain their remnant candidate classification.

A low core-prominence criterion is indeed necessary to classify recently switched off remnants. However, we find that the three remnant candidates with the weakest constraints on their CP upper limits are also those without hotspots, two of which have ultra-steep spectra, e.g. see Sect. 2.4.1. While the sample size is rather small, this observation would suggest that aged remnants may be preferentially deselected if only a low ($\lesssim 10^{-4}$) CP criterion is used. This observation echoes the results of (Brienza et al., 2017), who show that none of their ultra-steep spectrum remnants are selected by low CP (e.g. < 0.005), and, only 3/10 morphologically-selected remnants are selected by low CP.

2.5.1.2 Spectral index distribution

The integrated spectral properties of our sample are explored over two frequency ranges. The integrated flux densities at 119, 154, 186, 216 and 399 MHz are used to develop a low-frequency spectral index, α_{119}^{399}. To compute correct fitting uncertainties, we fit power-law models to the data in linear space. A high-frequency

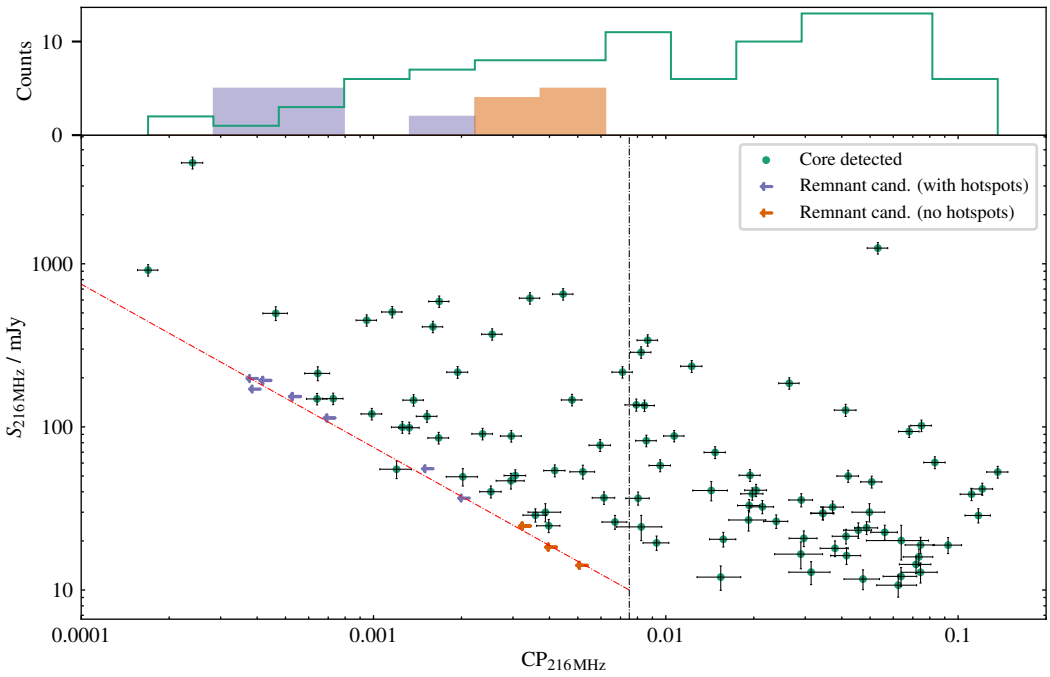

Figure 2.6: 216 MHz CP distribution of radio sources (see Sect. 2.5.1.1). Core-detected radio galaxies are represented by light-green markers. 3σ upper limits are placed on the remnant CP, denoted by the left-pointing arrows. Purple and orange colored arrows are used to indicate remnant candidates with and without hotspots, respectively. The vertical dot-dashed black line represents the value above which the distributed CP is complete across the sample. The red dot-dashed line traces the lowest CP that can be recovered at the corresponding total flux density. Uncertainties on the CP are propagated from the uncertainties on the total and core flux density. A histogram of CP is presented in the top panel.

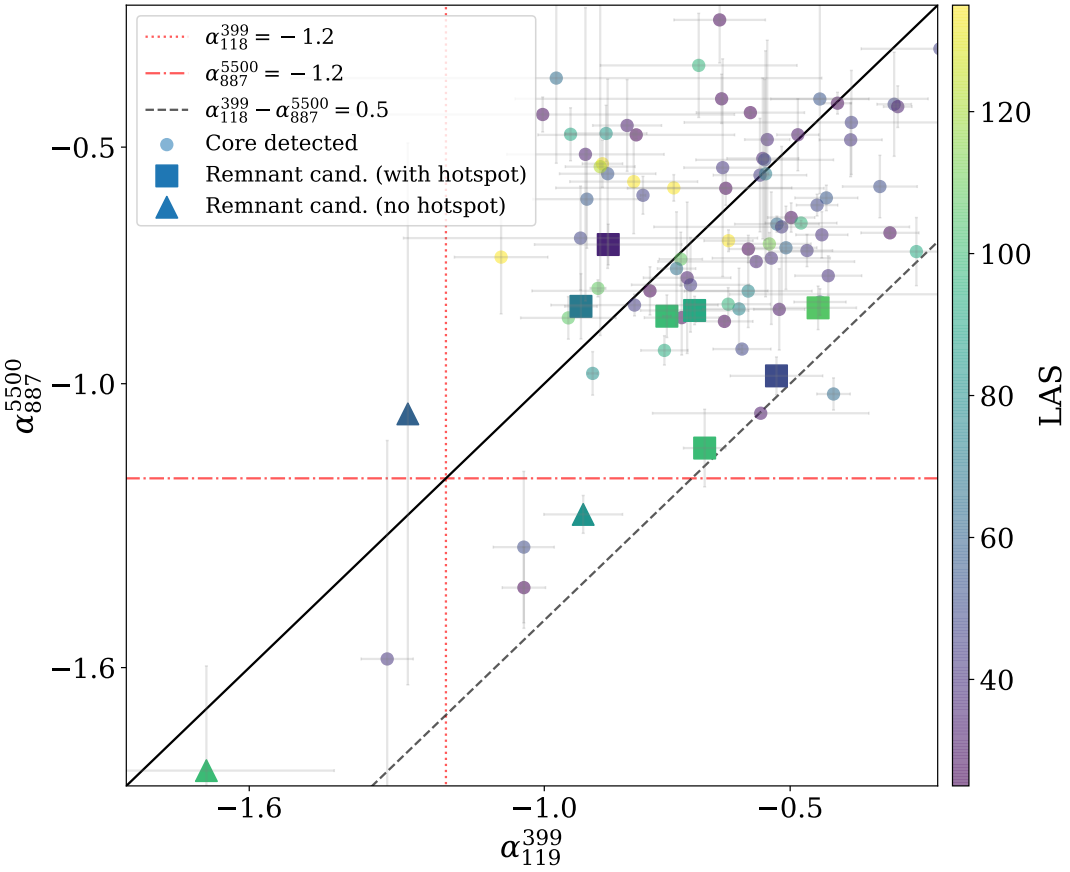

Figure 2.7: The high-frequency spectral index α_{887}^{5500} is plotted against the low-frequency spectral index α_{119}^{399}. A third color-bar axis is over-plotted to show the largest angular size in arc-seconds. Solid black line represents a constant spectral index across both frequency ranges. Dashed black line represents a spectral curvature of SPC = 0.5. The red dotted and dot-dashed lines represent a $\alpha = -1.2$ spectral index across the low- and high- frequency range, respectively.

Sample	$\alpha^{399}_{119,\,\mathrm{med}}$	$\alpha^{399}_{119,\,\mathrm{mean}}$	$\alpha^{5500}_{887,\,\mathrm{med}}$	$\alpha^{5500}_{887,\,\mathrm{mean}}$	$f_{\mathrm{US,\,low}}$	$f_{\mathrm{US,\,high}}$
Core-detected	-0.60	-0.63	-0.66	-0.67	0/94	3/94
Remnant cand. (with hotspot)	-0.69	-0.69	-0.84	-0.88	0/7	1/7
Remnant cand. (without hotspot)	-1.27	-1.29	-1.27	-1.38	1/3	$(2-3)^{\dagger}$/3

Table 2.5: Spectral index statistics calculated based on data represented in Figure 2.7. The median and mean spectral index, indicated by $_{\mathrm{med}}$ and $_{\mathrm{mean}}$ subscripts, are presented for the low α^{399}_{119} and high α^{5500}_{887} frequency ranges. $f_{\mathrm{US,\,low}}$ and $f_{\mathrm{US,\,high}}$ represent the low- and high-frequency ultra-steep fractions, respectively.
† A range is given here, as it is unclear whether MIDAS J225608−341858 (Fig. 2.5c) is ultra-steep at high frequencies.

spectral index, α_{887}^{5500}, is computed using $\alpha = \frac{\log_{10}(S_{887}/S_{5500})}{\log_{10}(887/5500)}$, and an associated uncertainty $\Delta\alpha = \frac{1}{\ln(887/5500)}\sqrt{\left(\frac{\Delta S_{887}}{S_{887}}\right)^2 + \left(\frac{\Delta S_{5500}}{S_{5500}}\right)^2}$. We populate our results onto an $\alpha - \alpha$ plot, e.g. Figure 2.7, and summarize our results in Table 2.5.

Despite the access to high frequencies (ν = 5.5 GHz), we find that the selected remnant candidates with hotspots show similar spectral properties to radio galaxies with an active radio core. At low frequencies, remnant candidates with hotspots display spectral indices that are consistent with continuous injection. The high frequency spectral index does appear to be steeper than for the bulk of remnant candidates with hotspots, however, this is also observed for core-detected radio sources and simply reflects the preferential ageing of higher-energy electrons. No remnant candidates with hotspots display an ultra-steep low-frequency spectral index, and only one such source (e.g. Sect. 2.4.2.1) demonstrates a high-frequency ultra-steep spectral index. Regarding these remnant candidates with non ultra-steep spectra, their position on the $\alpha - \alpha$ plot can be explained if these are young, recently switched off remnants. However, their spectral properties can just as easily be explained if these are active radio galaxies in which the radio core is below the GLASS detection limit. We can not rule out either of these possibilities based on their spectra alone, and as such they must remain as remnant candidates. We note that Mahatma et al. (2018) also report on a large overlap in the observed spectral index (150 MHz–1.4 GHz) between their active and candidate remnant radio galaxies. Only one of their remnant candidates display hotspots at 6 GHz with the Very Large Array telescope, meaning it is not necessarily only the remnant candidates with hotspots which display similar spectral indices as active radio galaxies. A great example of this is the remnant radio galaxy Blob 1 identified by Brienza et al. (2016).

We also find a small fraction (3/94) of core-detected radio sources which demonstrate an ultra-steep spectral index. The angular size of these sources is well below the largest angular scale that GLASS can recover at 5.5 GHz, sug-

gesting the curvature is genuine. This tells us that ultra-steep selection will not only select radio galaxies in which the AGN has switched off, however it is interesting to note these sources also do not display GLASS hotspots. It is possible these sources represent restarted radio galaxies in which the 'core' represents a newly-restarted jet.

Unsurprisingly, we find that the remnant candidates without hotspots also display steeper spectra than those with hotspots. The absence of compact features in their morphologies implies a lack of recent jet activity, and is supported by their ultra-steep spectra which implies significant spectral ageing within the lobes. Our low fraction of ultra-steep spectrum remnant candidates echoes the result of Brienza et al. (2016) who discuss the bias of preferentially selecting aged remnant radio galaxies via their ultra-steep spectra.

2.5.1.3 Power–size distribution

We investigate the sample distribution in redshift, total radio power, and largest linear size, given the host galaxy identifications. We stress that many of the selected remnant candidates have uncertain host galaxy associations, presenting a major challenge in analysing their rest-frame properties. An additional uncertainty comes from the photometric redshifts, which make up 60/104 (57%) of the sample. In addition, 14 active radio galaxies do not have an optical identification, meaning photometric redshift estimates can not be attained. If we assume their host galaxies are at least $10^{10.6}\mathrm{M}_{\odot}$, e.g. the lowest stellar mass reported by Best et al. (2005) to host a radio-loud AGN, we can apply the $K-z$ relation (e.g. see; Longair & Lilly, 1984; Rocca-Volmerange et al., 2004) to estimate the lowest redshift for which a $10^{10.6}\mathrm{M}_{\odot}$ galaxy will be undetected below the VIKING K_s-band AB magnitude limit (Sect. 2.2.2.1).

The absent detection from the VIKING K_s-band suggests that the host galax-

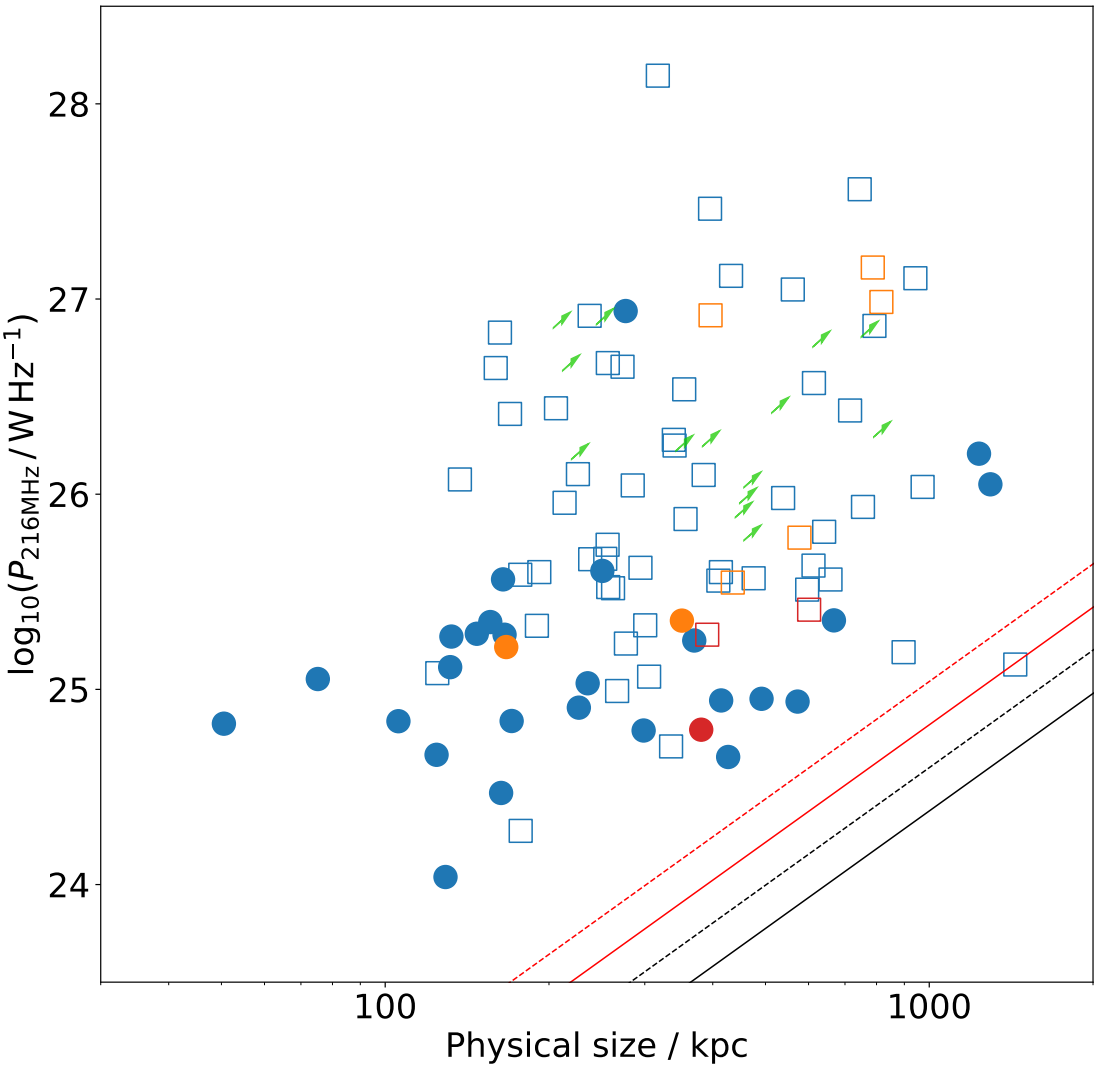

Figure 2.8: 216 MHz radio power against the largest linear size. Core-detected radio sources (blue markers), remnant candidates with hotspots (orange markers) and remnant candidates without hotspots (red markers) are displayed. Circular and square markers are used to denote spectroscopic and photometric redshifts, respectively. Lower limits on the 14 radio sources without host identifications are denoted by green arrows. Plotted also are the largest linear sizes that would result in a 5σ detection at 216 MHz at $z = 0.3$ (black) and $z = 1$ (red). Limits are calculated assuming a uniform brightness ellipse, and a lobe axis ratio of 2.5 (solid line) and 1.5 (dashed line). Aged remnants often display low axis ratios, e.g. MIDAS J225522−341807 (Sect. 2.4.1.1).

Sample	N	$z_{\rm med}$	$z_{\rm mean}$	$P_{\rm med}$	$P_{\rm mean}$	$\rm LLS_{med}$	$\rm LLS_{mean}$
				$\log_{10}(\rm W\,Hz^{-1})$	$\log_{10}(\rm W\,Hz^{-1})$	kpc	kpc
Full sample.							
Core-detected	80	0.519	0.59	25.2	25.2	277	379
Core-detected†	94	0.549	0.651	25.3	25.3	294	388
Remnant candidates	10	0.504	0.619	25.5	25.8	435	512
Spectroscopic redshifts.							
Core-detected	25	0.303	0.290	25.1	25.2	171	322
Remnant candidates	3	0.312	0.279	25.2	25.1	351	299

Table 2.6: Derived distribution averages from Sect. 2.5.1.3. The number of radio sources included in each category are denoted by N. The redshift, z, radio power, P, and largest linear size (LLS) are presented. The subscripts med and mean refer to the median and mean values. In the upper half of the table, we consider the entire sample of 104 radio sources. In the lower half, we consider only those with spectroscopic redshifts.
† Including the 14 core-detected radio galaxies with $z \geq 1$ lower limits.

ies of the 14 radio galaxies are likely above $z = 1$. The caveat here is that Best et al. (2005) investigate local ($z \leq 0.3$) radio-loud AGN samples, whereas here we are assuming higher redshift. Figure 1 of Smolčić et al. (2017) shows a hint of a decline in stellar mass with redshift, however, our assumption of the minimum stellar mass seems valid up to $z \sim 1$. For each radio source, we calculate the total radio power following: $P = 4\pi S D_L^2 (1+z)^{-\alpha-1}$, where D_L is the luminosity distance. For the 14 radio galaxies without optical identifications, the radio power is calculated assuming $z \geq 1$. Our results are presented in Table 2.6 and Figure 2.8.

Assuming radio lobes continue expanding once the jets switch off, which at least appears to be the case for FR-II radio galaxies as shown by Godfrey et al. (2017), an expectation of this is for remnants to display larger physical sizes with respect to their active radio galaxy progenitors. Interestingly, our results suggest that the largest linear sizes of core-detected radio galaxies and remnant candidates are similar. This may be explained by the observational bias against remnant radio galaxies of large linear size; such sources will preferentially fall below a fixed detection limit due to their lower surface brightness profiles. Since the linear size and age of a radio galaxy are correlated, for a fixed jet power and environment, it is not unreasonable to suggest that these 'missing' remnants also correspond to older remnant radio galaxies, which in turn would imply our sample predominately comprises of young remnants (see also Mahatma et al. 2018). If so, this result is consistent with the low fraction of ultra-steep remnants discussed in in Sect. 2.5.1.2. We do however caution this analysis since seven remnant candidates have ambiguous host galaxy associations, as well as the uncertainties surrounding the photometric redshift estimates.

We instead consider the sample of 28 spectroscopically-confirmed radio galaxies to see whether we can draw the same conclusions as above. Within this

'spectroscopic sample', we can be confident not only of the sample redshifts, but also of the three remnant candidates (e.g. see Sect. 2.4.1.2, 2.4.2.1, and 2.4.2.5) which have unambiguous host galaxy associations, meaning we can be confident of their positions on the power-size diagram. As demonstrated in Figure 2.8, the absence of remnant radio galaxies of large linear size becomes quite clear in the 'spectroscopic sample', and is consistent with the previously-discussed conclusions. Our limiting factor here is the small sample size, however this will be addressed in future work where we can expect a factor ~ 6 increase in the sample size of radio galaxies in GAMA 23. The additional benefit here will be the GAMA 23 group catalogue, which provides group/cluster associations for galaxies with spectroscopic redshifts, as well as virial estimates for the group mass. This will allow us to begin decomposing the degeneracy between radio power, linear size and environment.

2.5.2 Constraining a remnant fraction

2.5.2.1 Remnant fraction upper limit

The fraction of remnant radio galaxy candidates identified in this work provides an upper limit to the genuine fraction of remnant radio galaxies, $f_{\rm rem}$, present within this sample. Of 104 radio galaxies, 10 are identified as remnant radio galaxy candidates, resulting in a $f_{\rm rem} \approx 10\%$ upper limit on the remnant fraction. Saripalli et al. (2012), Brienza et al. (2017) and Mahatma et al. (2018) each constrain a remnant fraction from radio observation and their results are presented in Table 2.7. At face value, the remnant fraction obtained in this work is consistent with that of Brienza et al. (2017) and Mahatma et al. (2018), and shows a considerable increase over the fraction constrained by Saripalli et al. (2012). The apparent inconsistency with Saripalli et al. (2012) may very well be a result of their selection. Their sample was selected at 1.4 GHz, where ultra-steep remnants may potentially be missed, and they also excluded sources without a

Ref.	Sky coverage (deg^2)	Flux limit (mJy)	Sample frequency (MHz)	θ_{cut} ($''$)	Sample size	f_{rem}
1	7.52	1	1400	30	119	$< 4\%$
2	35	40	150	60	158	$< 11\%$
3	140	80	150	60	127	$< 9\%$
4	8.31	10	216	25	104	$4 \lesssim f_{\mathrm{rem}} \lesssim 10\%$

Table 2.7: Remnant fractions constrained by previous authors. Each column, in ascending order, represents the cited study, the sky coverage over which the sample is compiled, the flux limit across the sample (or the faintest source in the sample), the frequency at which the flux cut is made, the angular size cut of the sample, the number of radio galaxies within the sample, and the resulting remnant fraction.

References. (1) Saripalli et al. (2012), (2) Brienza et al. (2017) and Jurlin et al. (2020), (3) Mahatma et al. (2018), (4) This work.

radio core but hotspots still present within the lobes. It is interesting to note that despite the difference in the flux limit and angular size cut compared to the samples complied by Mahatma et al. (2018), Brienza et al. (2017), and Jurlin et al. (2020), the upper limits on the remnant fraction appear consistent. Shabala et al. (2020) show that the remnant fraction predicted by constant-age models, e.g. those in which the jets are active for a constant duration, is highly sensitive to observable constraints, e.g. the flux and angular size limit. On the other hand the remnant fraction predicted by power-law age models, e.g. those in which the duration of the active phase is power-law distributed, shows little dependence on observable parameters. It is therefore possible that the similarity in remnant fractions implies a preference towards power-law age models that describe AGN jet activity, although this needs to be pursued in more detailed future work.

2.5.2.2 Remnant candidates without hotspots

As presented in Sect. 2.4, the lobes of seven remnant candidates display compact emitting regions in GLASS, potentially indicating a hotspot formed by an active jet. As discussed in Sections 2.5.1.1 and 2.5.1.2, these sources could be interpreted either as recently switched off remnants, or, active radio galaxies with unidentified radio cores. We thus propose a lower limit to the remnant fraction, by considering the limiting case where each remnant candidate with a hotspot is an active radio galaxy. This would suggest a $f_{\rm rem} = 4/104$ ($\approx 4\%$) lower limit on the remnant fraction, consistent with the value reported by Saripalli et al. (2012). As discussed in Sect. 2.5.3, an appreciable fraction of genuine remnants with hotspots can potentially be expected.

2.5.3 Evolutionary history of MIDAS J225337-344745

A particularly interesting source to examine is MIDAS J225337−344745, which as mentioned in Sect. 2.4.2.1, demonstrates two seemingly contradictory features: the higher-frequency ultra-steep ($\alpha < -1.52$) spectrum of the lobes, suggesting

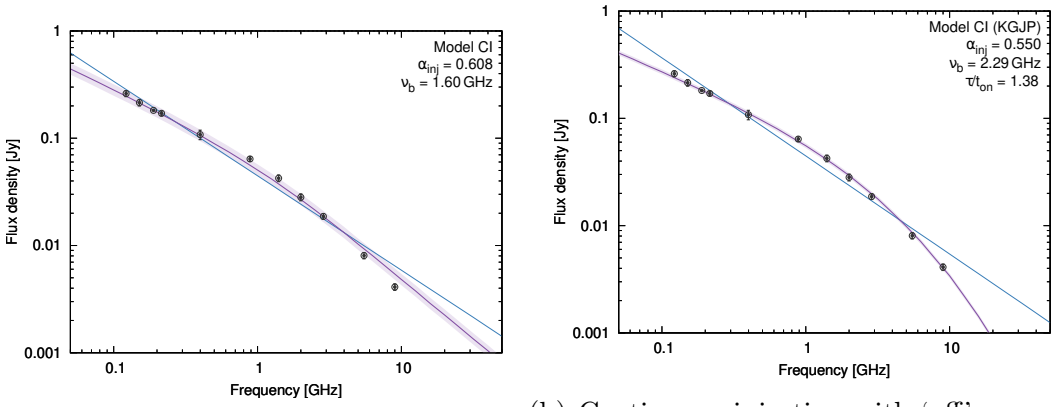

(a) Continuous injection model (CI)

(b) Continuous injection with 'off' component model (CI off)

Figure 2.9: Modelled integrated spectrum of MIDAS J225337−344745. Figure 2.9a models the spectrum assuming a continuous injection model (CI). Figure 2.9b models the spectrum assuming a continuous injection model with an 'off' component, encoding a jet switch-off (CI off). In each model, a 2σ uncertainty envelope is represented by the violet shaded region. As discussed in Sect. 2.5.3, the model uncertainties take into account only the uncertainties on the flux density measurements, and do not reflect the underlying uncertainties due to an inhomogeneous magnetic field. For reference, a best-fit to the data using single power-law model is represented by a blue line.

Table 2.8: Summarized properties of MIDAS J225337−344745 spectral modelling (Section 2.5.3). A reduced chi-squared ($\chi^2_{\rm red}$) is provided to assess the quality of fit. The injection index $\alpha_{\rm inj}$, observed-frame break frequency ν_b and quiescent fraction T are presented for the fitted continuous injection (CI) and continuous injection-off CI-off models. We quote a ΔBIC calculated between the two models.

Model fitted	$\chi^2_{\rm red}$	$\alpha_{\rm inj}$	ν_b GHz	T	ΔBIC
CI	3.43	-0.608	1.60±0.08	–	2.1
CI-off	0.64	-0.55	2.2±0.09	0.28±0.004	

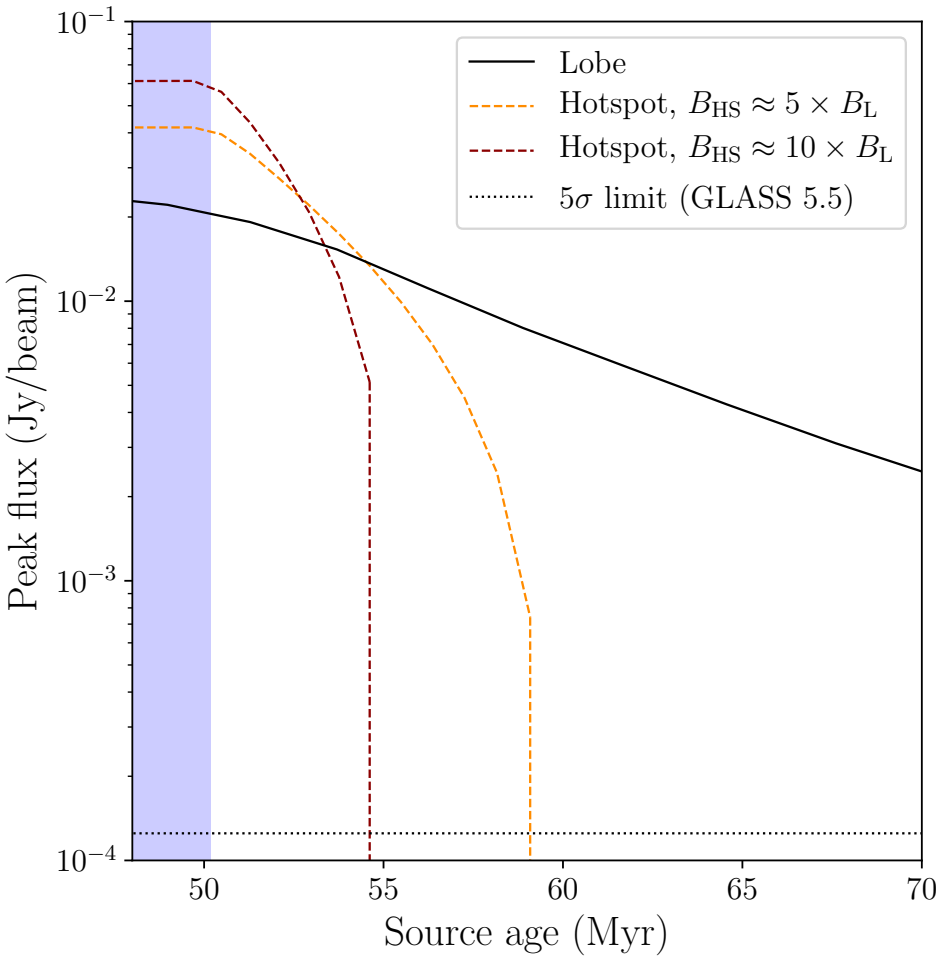

Figure 2.10: A 'MIDAS J225337−344745' type remnant radio galaxy is modelled by assuming a jet power $Q = 10^{38.1}$ W, an injection energy index of $s = 2.1$, an equipartition factor of $B/B_{\rm eq} = 0.22$, and a total source age of 71 Myr of which 50 Myr is spent in an active phase, and a further 21 Myr is spent as a remnant. The shaded blue bar corresponds to the time during which the source is active, after which the jets are switched off and the hotspots/lobes begin to fade. The evolution of the synchrotron emission from the lobes (solid black tracks) and the hotspots (dashed tracks) are shown as a function of the total source age. The assumption that the hotspot magnetic field strength is a factor five greater than the lobes (colored in orange) comes from Cygnus A, however we also assume a factor ten increase in the hotspot magnetic field strength (colored in red) to consider shorter fading timescales. We explore this in terms of the peak flux density, as this ultimately decides whether the emitting regions are detected in observations. The vertical drop in the flux density tracks reflects the depletion of electrons capable of producing emission at 5.5 GHz. As expected, the synchrotron emission evolves faster in the hotspot, however, their fading timescale is non-negligible in comparison to that of the lobes.

energy losses consistent with an aged remnant radio galaxy, and the compact 5.5 GHz emitting regions in GLASS, which may in turn suggest current or recent energy injection. It is unclear whether these are genuine hotspots; the north-eastern lobe is detected just above the noise level and thus demonstrates many 'hotspot-like' features. A singular, bright 'hotspot' is evident in the south-western lobe, however, the emitting region is clearly resolved at a physical resolution of 7×14 kpc (the physical resolution of GLASS 5.5 at $z = 0.213$), and so it is unclear whether this 'hotspot' is formed by an active jet, or, whether it is the expanding hotspot of a previously-active jet. It is also possible that the compact emitting region is a combination of the lobe and hotspot. Fortunately, the radio continuum spectrum appears to preserve the original spectrum at low frequencies, while also encoding the energy losses evident at higher frequencies. This allows us to model and parameterise the spectrum in terms of physically meaningful parameters, allowing us to probe the energetics along with the dynamics. Our ultimate objective here is to determine whether the compact emitting regions can be expected within a remnant radio galaxy. Our analysis is laid out as follows.

We model the radio source using the *Radio AGN in Semi-analytic Environments* (RAiSE) code which considers, amongst other things: (i) the evolution of the magnetic field strength; (ii) the adiabatic losses contributing to the radio luminosity evolution of the lobes; and (iii) the Rayleigh-Taylor mixing of the plasma contained within the remnant lobes. These processes are described by the dynamical (Turner & Shabala, 2015) and synchrotron emissivity (Turner et al., 2018b) models for lobes FR-II radio lobes, which follow the continuous injection model (CI model; Kardashev, 1962; Pacholczyk, 1970; Jaffe & Perola, 1973). The remnant spectrum follows the continuous injection 'off' model (CI-off; Komissarov & Gubanov, 1994) alternatively known as the KGJP model, which Turner (2018) parameterise with two break frequencies. A jet power $Q = 10^{38.1}$ W, magnetic field strength $B = 1.08$ nT, and total source age $\tau = 71$ Myr are constrained by the method of Turner et al. (2018b). The synchrotron spectrum is modelled

by the method of Turner (2018) which, provided sufficient spectral sampling, allows the injection index $\alpha_{\rm inj}$, break frequency ν_b and quiescent fraction[13] T to be uniquely constrained. Our results are shown in Figure 2.9. Both models constrain an injection index that is consistent within their typically observed range of $-1.0 < \alpha_{\rm inj} < -0.5$ (see Table 2.8). The discrepancy between the modelling becomes evident at the highest frequencies, for which the CI model begins to over-predict the integrated flux density. On the other hand, the CI-off model is able to comfortably reproduce the observed spectral curvature. We calculate a reduced chi^2 ($\chi^2_{\rm red}$) for each model, and a $\Delta\,$BIC$=$ 2.1 (by BIC$_{\rm CI}$ $-$ BIC$_{\rm CI-off}$) which demonstrates a preference towards the CI-off model (see Table 2.8). Although the distinction between the two models is ultimately driven by the 9 GHz measurement, CI-off provides a better model of the observed spectrum suggesting these are remnant lobes. Modelling the spectrum as a remnant suggests the source spends approximately 21 Myr in a remnant phase.

Turner et al. (2018b) showed that the CI model provides a statistically significant fit to the broad frequency radio spectra of over 86 per cent of FR-IIs in the Mullin et al. (2008) sample of 3C sources (typically 12 measurements between 0.01 and 10 GHz from Laing & Peacock 1980; but see Harwood 2017). Further, despite the non-physical CI model assumption of time-invariant magnetic fields, Turner et al. (2018b) find that CI model is an excellent fit to the simulated spectra of lobed FR-II which do consider magnetic field evolution, and are able to recover the source dynamical age.

As a final sanity check on the duration of the remnant phase fitted above (by the integrated CI-off model), we constrain the age of the most recently accelerated electron populations which we assume are located near the 'hotspots'. We convolve the radio observations at 399 MHz, 887 MHz and 5.5 GHz images to a common 11″ circular resolution and measure the integrated flux density within an aperture centered at the southern 'hotspot'. We fit the spectrum with a Tribble

[13]The quiescent fraction is defined as $T = t_{\rm off}/\tau$, where $t_{\rm off}$ is the duration of the remnant phase, and τ is the total age of the radio source.

JP model assuming the magnetic field derived previously in our RAiSE modelling. We arrive at a remnant age of $t_{\rm off} = 13^{+8}_{-4}\,$Myr, consistent with the $t_{\rm off} \approx 21\,$Myr derived from the integrated CI-off model. We stress that the observations are not properly *(u,v)* matched, and thus are not necessarily seeing the same radio emission; e.g. at 5.5 GHz, the flux density is likely underestimated due to resolving out the extended radio emission. We leave a more detailed analysis of this source to future work.

Next, we model the hotspot to better understand its typical fading timescale. We model a 'MIDAS J225337−344745 like' radio galaxy, meaning we adopt the same values for the jet power, active age, lobe axis ratio, energy injection index and equipartition factor. By the method of Turner et al. (2018a) we forward model the 5.5 GHz lobe spatial emissivity (without the hotspot) and convolve the output map with the GLASS 5.5 synthesized beam. We consider the GLASS 5.5 beam with the largest integrated flux (e.g. the maximum peak flux density), as this ultimately determines whether the youngest emitting regions of the lobes are detected. The hotspot is modelled assuming a JP spectrum (Jaffe & Perola, 1973) for the same initial properties as the lobe, but for an increased magnetic field strength. Cygnus A displays a factor five increase in the hotspot magnetic field strength, in comparison to that of the lobes (Carilli & Barthel, 1996). We make the same assumption for MIDAS J225337−344745, however also consider a case where the hotspot magnetic field strength is a factor 10 greater than the lobes. We also assume the same ratio of hotspot to lobe volume as that measured in Cygnus A; this only shifts the spectrum along the log-frequency log-luminosity plane and does not influence the spectral shape (i.e. the slope). Our results are presented in Figure 2.10. As expected, the hotspot fades rapidly once injection switches off. Bright radio emission from the hotspot is driven by the freshly injected electrons which have a short lifetime at high frequencies due to the strong magnetic field. Despite the hotspot fading rapidly, its fading timescale is non-negligible when compared to the characteristic active and rem-

nant ages. It is not unreasonable to suggest that recently switched off remnants may still display hotspots, and that some of the selected remnant candidates with hotspots (Sect. 2.5.2.2) may indeed be such cases. The main result of Figure 2.10 is that the hotspots of a recently switched off jet should *not* be visible in MIDAS J225337−344745, assuming a $t_{\rm off} \approx 21$ Myr remnant phase. At the implied age of the remnant, the modelled emitting regions of the lobes range between 100–150 kpc in size. This is consistent with the observed emitting regions in GLASS, which demonstrate a projected linear size of ~ 96 kpc. This indicates that the bright features in GLASS are entirely consistent with the youngest plasma regions, and are not necessarily the hotspots of an active jet.

As such, the interpretation of this source is challenging for the following reasons. Modelling the spectrum suggests these are the lobes of a remnant radio galaxy. While hotspots will remain visible for a non-negligible period of time after injection is switched off, they should not be visible in this source assuming the remnant age is correct. The two pieces of evidence are consistent with one another if the bright GLASS features are just the youngest emitting regions of the lobes. If we alternatively assume MIDAS J225337−344745 is an active source, the RAiSE modelling of Turner et al. (2018b) finds a comparable age ($\tau = 100$ Myr) to the remnant case but a substantially lower jet power of $Q = 10^{36.7}$ W is required to match the relatively low observed flux density. This jet power is typically associated with an FR-I morphology for the known host galaxy mass (e.g. Ledlow, 1994; Best, 2009), potentially resulting in a broad flare point rather than compact hotspots at the end of a jet. This morphology may explain the large spatial extent of the GLASS 5.5 GHz observations, however does not resolve the discrepant spectral curvature.

Finally, the result presented in Figure 2.10 makes a rather interesting prediction for the observed properties of genuine remnants. As discussed in Sect. 2.5.2, the upper limit on the remnant fraction is $f_{\rm rem} \approx 10\%$. For a *characteristic* active lifetime of ~ 100 Myr, our observed remnant fraction would thus sug-

gest an observable remnant phase lasting $\sim 10\,\mathrm{Myr}$. The modelling of a 'MIDAS J225337−344745 like' radio galaxy shows that the hotspot can persist for at least several Myr before fading out completely. As such, we can expect an appreciable fraction of remnants to still display hotspots.

2.6 Conclusions

Within a sub-region of $8.31\,\mathrm{deg}^2$ of the GAMA 23 field, we have compiled a sample consisting of 104 extended, low-frequency selected (216 MHz) radio galaxies. Using the 5.5 and 9.5-GHz GLASS survey, we have adopted the 'absent radio core' criterion to search for remnant radio galaxy candidates. Our conclusions are summarized as follows:

- We identify 10 new remnant radio galaxy candidates, thereby constraining an $f_{\mathrm{rem}} \leq 10\%$ upper limit on the fraction of radio galaxies with quiescent AGN. Our upper limit is consistent with that proposed by previous authors, and suggests that remnants must have a short observable lifetime.

- Seven remnant candidates show compact emitting regions in GLASS, an observation that can only be explained if the jets have recently switched off. A much smaller fraction (3/10) show relaxed, hotspot-less lobes, and only one displays an ultra-steep spectrum across the entire frequency range. This implies remnants are detected soon after switching off, suggesting a rapid fading during the remnant phase.

- The small fraction of ultra-steep ($\alpha < -1.2$) remnants is likely a result of the oldest remnant lobes escaping detection due to their expansion.

- At present, the upper limits placed on the remnant core prominence are too weak to confidently rule out the presence of AGN activity. Those with compact hotspots and a non ultra-steep spectrum must therefore retain their remnant candidate classification. Considering the limiting case in

which *all* these are active radio galaxies, we would expect a $f_{\rm rem} \approx 4\%$ remnant fraction.

- MIDAS J225337−344745 represents an interesting object for future study. Modelling the integrated lobe spectrum shows consistency with a remnant radio galaxy. We find that although the hotspot has a non-negligible fading timescale, we do not expect to see hotspots in this source.

- By modelling the synchrotron spectrum arising from a 'MIDAS J225337−344745-like' hotspot, we show that the hotspot can persist for $5-10$ Myr at 5.5 GHz after the jets switch off. This would imply that the presence of a hotspot in radio maps may not necessarily reflect an active jet, and by extension we can expect an appreciable fraction of genuine remnants to still display hotspots.

2.7 Acknowledgements

BQ acknowledges a Doctoral Scholarship and an Australian Government Research Training Programme scholarship administered through Curtin University of Western Australia. NHW is supported by an Australian Research Council Future Fellowship (project number FT190100231) funded by the Australian Government. This scientific work makes use of the Murchison Radio-astronomy Observatory, operated by CSIRO. We acknowledge the Wajarri Yamatji people as the traditional owners of the Observatory site. Support for the operation of the MWA is provided by the Australian Government (NCRIS), under a contract to Curtin University administered by Astronomy Australia Limited. We acknowledge the Pawsey Supercomputing Centre which is supported by the Western Australian and Australian Governments. The Australian SKA Pathfinder is part of the Australia Telescope National Facility which is managed by CSIRO. Operation of ASKAP is funded by the Australian Government with support from the National Collaborative Research Infrastructure Strategy. The Australia Telescope Com-

pact Array is part of the Australia Telescope National Facility which is funded by the Australian Government for operation as a National Facility managed by CSIRO. We thank the staff of the GMRT that made these observations possible. GMRT is run by the National Centre for Radio Astrophysics of the Tata Institute of Fundamental Research. CHIC acknowledges the support of the Department of Atomic Energy, Government of India, under the project 12-R&D-TFR-5.02-0700. SW acknowledges the financial assistance of the South African Radio Astronomy Observatory (SARAO) towards this research is hereby acknowledged (www.ska.ac.za). IP acknowledges support from INAF under the SKA/CTA PRIN "FORECaST" and the PRIN MAIN STEAM "SAuROS" projects. The National Radio Astronomy Observatory is a facility of the National Science Foundation operated under cooperative agreement by Associated Universities, Inc. H.A. benefited from grant CIIC 90/2020 of Universidad de Guanajuato, Mexico. We acknowledge the work and support of the developers of the following following python packages: Astropy (Astropy Collaboration et al., 2013; Price-Whelan et al., 2018) and Numpy (van der Walt et al., 2011). We also made extensive use of the visualisation and analysis packages DS9[14] and Topcat (Taylor, 2005). We thank an anonymous referee for their insightful comments that have improved the manuscript. This work was compiled in the very useful free online LaTeX editor Overleaf.

[14] http://ds9.si.edu/site/Home.html

Chapter 3

A novel simulation-based method for selecting and modelling remnant radio galaxies

In the following chapter, we present our second major contribution of work undertaken during this thesis. The contents of this chapter have been published as "Selecting and Modelling Remnant AGNs with Limited Spectral Coverage" (2022) in the Monthly Notices of the Royal Astronomical Society, volume 514, 10.1093/mnras/stac1328 (Quici et al., 2022). The accepted manuscript is reproduced, with permission, in full in this chapter. Minor typographical and grammatical changes have been make to ensure consistency with the rest of the Thesis.

Abstract

Quantifying the energetics and lifetimes of remnant radio-loud active galactic nuclei (AGNs) is much more challenging than for active sources due to the added complexity of accurately determining the time since the central black hole switched off. Independent spectral modelling of remnant lobes enables the derivation of the remnant ratio, $R_{\rm rem}$, (i.e. 'off-time/source age'), however, the

requirement of high-frequency ($\gtrsim 5\,\mathrm{GHz}$) coverage makes the application of this technique over large-area radio surveys difficult. In this work we propose a new method, which relies on the observed brightness of backflow of Fanaroff-Riley type II lobes, combined with the *Radio AGN in Semi-Analytic Environments* (RAiSE) code, to measure the duration of the remnant phase. Sensitive radio observations of the remnant radio galaxy J2253-34 are obtained to provide a robust comparison of this technique with the canonical spectral analysis and modelling methods. We find that the remnant lifetimes modelled by each method are consistent; spectral modelling yields $R_{\mathrm{rem}} = 0.23 \pm 0.02$, compared to $R_{\mathrm{rem}} = 0.26 \pm 0.02$ from our new method. We examine the viability of applying our proposed technique to low-frequency radio surveys using mock radio source populations, and examine whether the technique is sensitive to any intrinsic properties of radio AGNs. Our results show that the technique can be used to robustly classify active and remnant populations, with the most confident predictions for the remnant ratio, and thus off-time, in the longest-lived radio sources (> 50 Myr) and those at higher redshifts ($z > 0.1$).

3.1 Introduction

The supermassive black holes (SMBHs) residing at the heart of most galaxies (Magorrian et al., 1998; Häring & Rix, 2004; Gültekin et al., 2009), play a profound role in the evolution of their host galaxies and large-scale (intergalactic) environments. Accretion onto the SMBH powers an active galactic nucleus (AGN), which, when radio-loud, drives a pair of jets comprising relativistic plasma. The jets inflate synchrotron-emitting lobes in the surrounding atmosphere, which act to heat up and expel the surrounding intergalactic gas, and eventually halt accretion onto the SMBH (e.g. see reviews by; McNamara & Nulsen, 2007; Fabian, 2012; Alexander & Hickox, 2012). This *jet mode* of AGN feedback is needed to quench star formation in the most massive galaxies (Croton et al., 2006), and to suppress cooling flows in the cores of massive clusters (Fabian et al., 2003) at low

redshifts ($z \lesssim 2-3$; Fabian, 2012).

Prescriptions for these feedback mechanisms require more than just the energetics and lifetimes of the jetted outbursts (Binney et al., 2007); the manner by which the jet power couples with the surrounding gas is equally as important (Tadhunter, 2008; Alexander & Hickox, 2012). The lifetime of the active jet phase has a large influence on the mechanism coupling the jet power to the environment; e.g. through shock-heating driven by the global expansion of the lobes (Worrall et al., 2012), versus the clearing of gas through the late buoyant rise of jet-inflated bubbles (Churazov et al., 2001). This active lifetime also strongly maps to the radio source linear size (Kaiser & Alexander, 1997), which determines the cluster radius of interaction where the energy deposition takes place. The duration of a quiescent phase, in which there is either no or reduced jet activity, can additionally be constrained from the active lifetime when combined with measurements of the duty cycle. The duty cycle can be directly constrained for "double-double radio galaxies" (DDRG; Schoenmakers et al., 2000) and some remnant radio galaxies (Turner, 2018), or estimated on a population level from the radio-loud fraction (e.g. Best et al., 2005; Shimwell et al., 2019). Feedback mechanisms can therefore be examined by considering the spatial and temporal scales over which the energy deposition takes place; i.e. does the cluster environment have sufficient time to reach its equilibrium state before jet activity resumes (e.g. Turner & Shabala, 2015).

The feedback mechanisms that regulate the supply of the surrounding gas are thought to give rise to an intermittency in jet activity, and the observed "remnant" and "restarted" radio galaxy populations (e.g. see reviews by; Kapinska et al., 2015; Morganti, 2017a); the latter representing those in which jet activity has renewed prior to the remnant lobes fading from view. Importantly, remnant radio galaxies offer valuable constraints on the active lifetimes of AGN jets, a necessary step towards our general understanding of AGN jet feedback. Shabala et al. (2020) demonstrate that models describing the global distribution of jet

lifetimes and duty-cycles can be inferred from the observed fractions of remnant and restarted radio sources (relative to active ones). On a per-source basis, remnants offer direct constraints on the total duration of the jet phase. The age measured for an active radio galaxy represents only the age at which the source is observed, sampling only some fraction of the true jet phase. In contrast, remnants, marking the conclusion of the active phase, encode the true lifetime of the jet. For these reasons, methods to select and model remnant radio galaxy lobes need to be robust.

Methodologies for selecting remnant radio galaxies are explored by many authors, particularly since the advent of the Low Frequency Array (LOFAR; van Haarlem et al., 2013). The overall consensus, as first proposed by Brienza et al. (2016), is that a combination of morphological- and spectral-based methods are needed to select a representative sample of remnant radio galaxies.

It is possible to select remnants based on an ultra-steep (e.g. $\alpha \geq 1.2$; Cordey, 1987), or highly curved (e.g. $\Delta\alpha \geq 0.5$; Murgia et al., 2011) radio spectrum criterion. These methods rely on sufficient fading (ageing) at the highest observing frequency, and will therefore miss recently switched-off remnants in which the break frequency lies beyond this frequency; this is confirmed based on observed and mock radio source populations (e.g see; Godfrey et al., 2017; Brienza et al., 2017; Mahatma et al., 2018; Shabala et al., 2020). The bias associated with these spectral-based methods can be mitigated through the inclusion of a morphological-based selection, where remnant lobes are selected based on diffuse, low surface-brightness, amorphous lobes (e.g. Blob 1; Brienza et al., 2016), however such methods may be less effective for recently switched-off remnants (e.g. 3C 28; Harwood et al., 2015).

Upon cessation of the jets, a bright radio core is expected to disappear rapidly (< 0.1 Myr). The selection of remnant radio galaxies can therefore also be made based on the absence of compact radio emission from the core (e.g; Mahatma et al., 2018; Quici et al., 2021), however we note the recent results of Jurlin et al.

(2021) who demonstrate the co-existence of faint radio emission from the core together with ultra-steep remnant radio lobes for a handful of objects. Their results suggest radio emission from the core, alone, may not necessarily determine whether the radio galaxy is active, and that high-frequency ($\nu \gtrsim 5\,\mathrm{GHz}$) observations are needed to confirm whether radio galaxy lobes are truly remnant.

High frequency radio observations are also critical to modelling the energetics of both active and remnant AGNs (Turner et al., 2018b). Ageing of the lobe plasma results in a spectral steepening due to the preferential radiating of high-energy electrons (Kardashev, 1962; Pacholczyk, 1970), and is characterised by an optically-thin break frequency that can be related (given a lobe magnetic field strength) to the plasma spectral age. However, a major challenge in modelling the dynamical evolution of remnant AGNs comes from the unknown time since the jets switched off. Turner (2018) show that this problem can be resolved by modelling the fractional duration of the remnant phase, based on the observed steepening in the integrated lobe spectrum, reducing the required model complexity to that of active radio sources. However, this method requires a well-sampled radio spectrum, where high-frequency ($\nu \gtrsim 5\,\mathrm{GHz}$) observations are often needed to properly characterise the observed spectral curvature.

Sensitive, wide-area radio surveys conducted with telescopes such as LOFAR; the Karoo Array Telescope (MeerKAT; Jonas & MeerKAT Team, 2016); the Australian Square Kilometre Array Pathfinder (ASKAP; Johnston et al., 2007); and eventually the Square Kilometre Array (SKA), are expected to offer an unprecedented view of the radio galaxy life-cycle. In principle, such surveys enable the compilation of large samples of active, remnant and restarted radio sources, which will offer invaluable constraints on mechanisms describing the jet-triggering and AGN feedback. However, it is unrealistic to expect matching, high-frequency ($\nu \gtrsim 5\,\mathrm{GHz}$) sky coverage which, at present, is needed to robustly confirm the status of remnant lobes (Jurlin et al., 2021), and tightly constrain their energetics (Turner, 2018).

In this work, we therefore explore whether measurements of the off-times of remnant lobes can be made based on their surface brightness distributions. To do this, we collect new data for the remnant radio galaxy J225337-344745 (J2253-34 hereafter), originally discovered by Quici et al. (2021), which data are needed to conduct various spectral and dynamical modelling of the source (Sect. 3.2). In Sect. 3.3, we apply an established spectral ageing method to provide an independent measurement of the off-time in J2253-34. In Sect. 3.4, we develop a new dynamical model-based method that uses the observed lobe backflow to measure the off-times in remnant radio galaxies. Here, we apply our method to J2253-34, and validate the estimate of its off-time against that derived previously from its radio spectrum. In Sect. 3.5, we use mock radio source populations, simulated at 150 MHz and 1.4 GHz, to examine whether the off-times in a wide range of remnants can be constrained by this method. Final discussions and conclusions are summarised in Sect. 3.6.

The ΛCDM concordance cosmology with $\Omega_M = 0.3$, $\Omega_\Lambda = 0.7$ and $H_0 = 70\,\mathrm{km\,s^{-1}\,Mpc^{-1}}$ (Komatsu et al., 2011) is assumed throughout the paper.

3.2 Data

In this section, we describe the observations taken as part of this work, or larger observing projects, for J2253-34, and the methods used to image these data. We make use of new data collected by the Australia Telescope Compact Array (ATCA; Frater et al., 1992), MeerKAT, and the upgraded Giant Meterwave Radio Telescope (uGMRT), together with several ancillary data products. A multi-wavelength view of J2253-34 using these new data can be seen in Fig. 3.1. All measurements of the integrated flux density are reported in Tab. B.1.

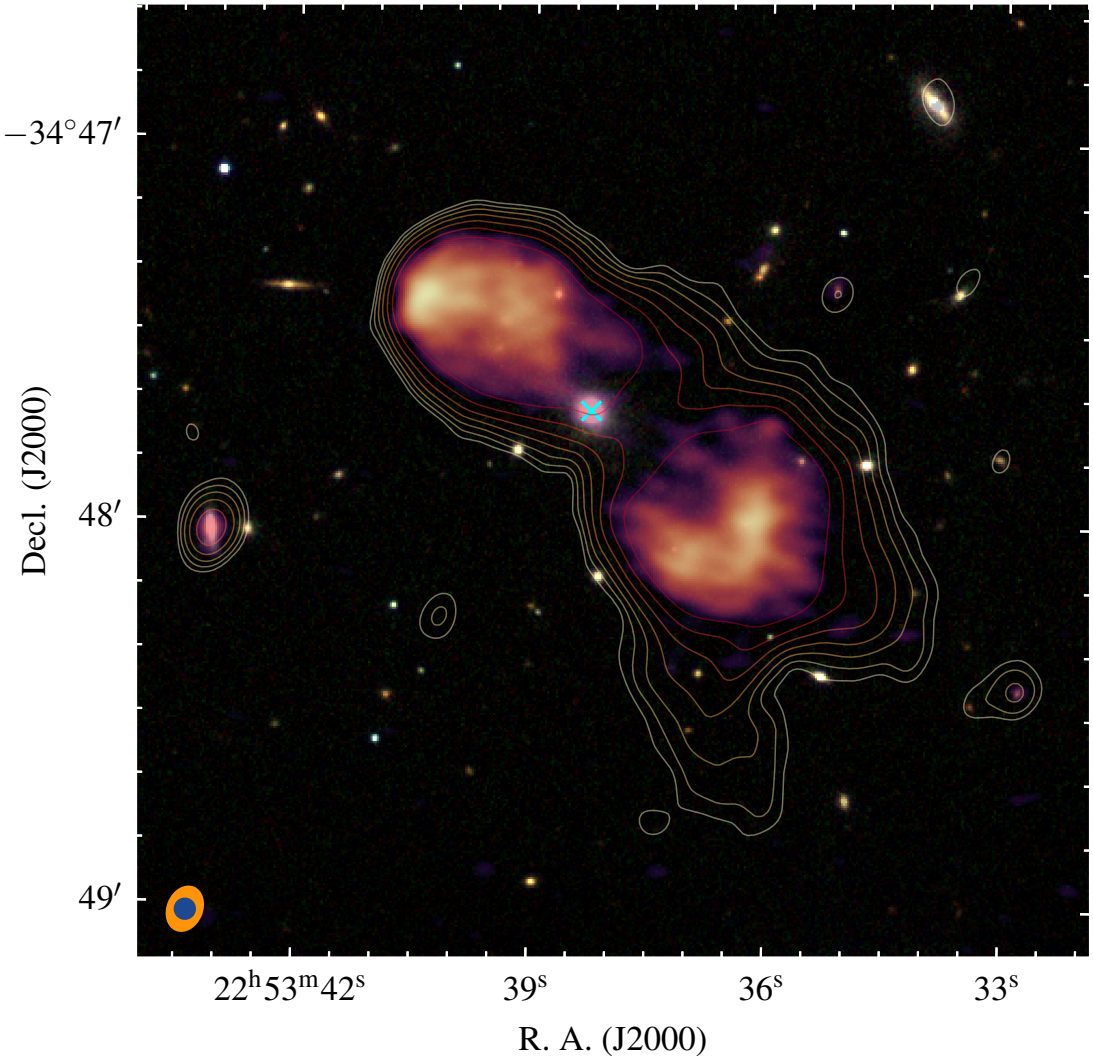

Figure 3.1: The remnant radio galaxy J2253-34 and its intergalactic environment. The background image is an RGB composite constructed from mid-infrared K_s (red), H (green) and J (blue) bands, respectively (e.g. see; Quici et al., 2021). The host galaxy is indicated by a cyan-coloured 'x' marker. A 5.5 GHz view of J2253-34 with 4″ resolution is superimposed onto the background. Coloured contours show the 1.42 GHz radio emission ('sub-band 3' in Sect. 3.2.2), with levels increasing uniformly in log-space by 0.2 dex between $[3, 80] \times \sigma$. Ellipses in the lower-left corner denote the shape of the restoring beam at 1.42 GHz (orange) and 5.5 GHz (blue).

PI	Project code	Config.	Date dd/mm	t (h)	B_{min} – B_{max} (m)	$\theta_{max,5.5}$ (′)	$\theta_{max,9}$ (′)
Benjamin Quici	C3335	H75	03/06	8	31 – 89	6.0	3.7
	C3335	H168	22/07	5.5	61 – 185	3.1	1.9
	C3402	750C	14/02	12	46 – 704	4.1	2.5
	C3402	1.5A	03/01	12	153 – 1469	2.4	1.5
	C3402	6C	(12, 15)/11	10	337 – 5939	1.2	0.7

Table 3.1: Summary of the new ATCA observations in different configurations described in Sect. 3.2.1. In order, columns denote: the principal investigator; the project code; the ATCA configuration; the date of observation, each conducted during the year 2021; the total integration time; the range of shortest to longest baseline lengths; and the largest recoverable scales at 5.5 GHz and 9 GHz. We note, B_{max} quoted for all but the 6C configuration excludes baselines formed with the ∼6 km outrigger antenna (CA06), due to the gap in (u, v) coverage.

3.2.1 ATCA data

Pointed observations of J2253-34 were awarded through a series of observing proposals (Tab. 3.1). Observations were conducted within the 4 cm–band, which allows simultaneous observing over two 2 GHz-wide bands which were centered at 5.5 GHz and 9 GHz. The collection and reduction of these data are presented below.

To produce images with high spatial-resolution and sensitivity to large-scale structure, coverage of the (u, v) plane was maximised by observing in various ATCA configurations (see Tab. 3.1). Baselines ranged between 31–5939 m, ensuring an appropriate sampling of the largest angular scale of J2253-34 ($\theta \sim 100''$). The combined integration time on the target was 39.5 hours. At the beginning of each observation, we observed PKS B1934-638 for 10 minutes to derive bandpass, gain and flux calibration solutions. 12 minute scans of J2253-34 were interleaved with two-minute scans of PKS B2255-282; a source used to calibrate the time-varying gains.

Data reduction was performed using the Multichannel Image Reconstruction, Image Analysis and Display (MIRIAD; Sault et al., 1995), and closely followed the method outlined by Huynh et al. (2015, 2020); we used the primary scan to solve for the shape of the bandpass, the secondary scan to calibrate for the time-varying gains and the polarization leakages, and then transferred the solutions to J2253-34 where the gain solutions were averaged over a two-minute interval (the length of each phase calibrator scan). Throughout all these steps, channels known to be contaminated by radio frequency interference (RFI) were automatically flagged.

Calibrated data-sets associated with each unique observation, with equal weighting, into a single data-set. To improve the imaging dynamic range, three rounds of phase-only self calibration were conducted using a `Robust 0.0` Briggs weighting (Briggs, 1995), corresponding to an image resolution of approximately $3'' \times 6''$. For each round, gains were solved over 2, 1, and 0.5 minute time intervals, respectively. We refer to this data below as the 'calibrated data-set', and discuss

the synthesis of our science-ready images in Sects. 3.2.1.1 & 3.2.1.2. For these data, we assume a 3% calibration uncertainty in the ATCA flux density scale (Reynolds, 1994).

3.2.1.1 Low-resolution imaging

We first produced images with lower spatial resolution to improve constraints on the high-frequency, integrated, spectral energy distribution (SED). This was done by splitting each 2-GHz band of the calibrated data-set into four 512 MHz sub-bands. Each sub-band was imaged in MIRIAD using a `Robust 0.0` Briggs weighting, with an additional 30″ Gaussian taper on the visibilities so as to reduce contribution and noise from the longer baselines. The data were CLEANed to an initial depth of 3σ, after which a deeper CLEAN to 1σ was performed around pixels already in the model. Images were corrected for attenuation of the primary beam.

To extract the photometry, we used POLYGON_FLUX[1], which uses the shape of the restoring beam to evaluate a background-subtracted integrated flux density corresponding to a user-defined region (e.g. see Hurley-Walker et al. 2019). Measurement uncertainties were calculated by multiplying the RMS noise by the square-root number of beams corresponding to the region volume, which we added in quadrature with the absolute calibration uncertainty.

3.2.1.2 High-resolution imaging

We further produced images with high spatial resolution so we could map the radio spectrum across the lobes (in conjunction with our data at other frequencies). To maximise signal-to-noise, we imaged the entire 2 GHz bandwidth available in each wide-band. To produce these images, we used a `uniform` Briggs weighting and applied a 8″ taper to the visibilities; although it was possible to improve the spatial resolution beyond $\theta_{\mathrm{FWHM}} = 8''$, this corresponded to the best possible

[1] https://github.com/nhurleywalker/polygon-flux

circular resolution that could be achieved across all radio images presented in this work. To demonstrate this in Fig. 3.1, we present a higher-resolution view of J2253-34 at 5.5 GHz by instead applying a 4″ taper to the visibilities. The data were CLEANed to an initial depth of 3σ, after which a deeper CLEAN to 1σ was performed around pixels already in the model. After correcting images for the frequency-dependent primary beam attenuation, they achieved a mean root mean square (RMS) sensitivity of 11 μJy beam^{-1} and 13 μJy beam^{-1} at 5.5 GHz and 9 GHz, respectively. We refer to these images as 'high-resolution ATCA images'.

3.2.2 MeerKAT data

We obtained 3.5 hours of time to observe J2253-34 on the MeerKAT radio telescope (PI: B. Quici, project code: MKT 20212). Observations took place in the 'L-band' (0.89–1.71 GHz), thus offering sensitive, high spatial-resolution observations at an intermediate frequency range. To collect the data, we used PKS 1934-638 to calibrate the bandpass, and PKS 2259-37 to calibrate the time-varying gains. The MeerKAT bandpass response is stable to within 3% over 2–3 hours. As such, the observations were conducted in two 'blocks' by visiting the bandpass calibrator twice; once at the beginning of the observation, and again 1.5 hours later. Each bandpass calibrator scan lasted 10 minutes. Observations of J2253-34 were carried out by interleaving a two minute gain calibrator scan with a 15.5 minute target scan. In total, the target received 2.6 hours of exposure time. Using the calibrated measurement set made available from the South African Radio Astronomy Observatory (SARAO) Web Archive[2], we performed a single round of RFI flagging using AOFlagger (Offringa et al., 2012). We identified four frequency ranges as having RFI-clean, unflagged visibilities, and we refer to these as 'sub–bands' (see Tab. B.1).

Imaging was conducted using WSClean (Offringa et al., 2014). Each sub–

[2]The SARAO Web Archive is found at https://archive.sarao.ac.za/

band was imaged independently by blindly CLEANing the data down to a depth of 3σ, followed by a deeper CLEAN down to a 1σ level around the model. Imaging of sub–bands 1–4 was performed using an image weighting of `robust -1.0`, `-0.6`, `0.0` and `+0.25`, respectively. In this way, all but the lowest sub–band achieved an image resolution of $\theta_{\rm FWHM} \lesssim 8''$. All imaging was performed using the `multiscale` option, which enables multi-scale deconvolution (Offringa & Smirnov, 2017). Each sub–band was then corrected for the frequency-dependent primary beam attenuation. Finally, images associated with sub–bands 2–4 were convolved to a circular $8''$ resolution, in order to match the resolution in the high-resolution ATCA images. The image associated with sub–band 1 was excluded from this final step, as the restoring beam exceeded $8''$. A 5% calibration uncertainty is assumed throughout this work. Following the method as described in Sect. 3.2.1.1, the integrated flux density of J2253-34 (and associated measurement uncertainty) was measured from each sub–band using the same user-defined polygon.

3.2.3 uGMRT data

We finally made use of two low-frequency, high-resolution radio images, created using data collected with the upgraded Giant Meterwave Radio Telescope (uGMRT), which contained J2253-34 within their fields of view. Observations were conducted in band-3 ($250-500$ MHz; proposal code 37_057, PI: Ross Turner), and in band-4 ($550-900$ MHz; proposal code 35_022, PI: C. H. Ishwara Chandra). The data was reduced using the CAPTURE Pipeline (Kale & Ishwara-Chandra, 2021), which uses the Common Astronomy Software Applications (CASA; McMullin et al., 2007) package. After the initial gain calibration, the data was channel averaged to keep the bandwidth smearing negligible. Using a Briggs weighting of robust `0.0`, the channel averaged source data was subjected to four rounds of phase-only self-calibration followed by 4 more rounds of amplitude and phase self-calibration. A final band-3 image, centered at 417 MHz, was produced

using a robust `0.0` weighting, resulting in a native resolution of $\sim 8'' \times 5''$. A final band-4 image, centered at 682 MHz, was produced using a robust `0.0` weighting, resulting in a native resolution of $\sim 5'' \times 3''$. The resolution in each image was convolved to a circular beam of $\theta = 8''$, achieving a local RMS of $52\mu\text{Jy beam}^{-1}$ and $43\mu\text{Jy beam}^{-1}$ at 417 MHz and 682 MHz, respectively.

3.2.4 Ancillary data

To fill out the sampled integrated radio spectrum of J2253-34, particularly at frequencies not covered by our new data, we take several measurements previously compiled by Quici et al. (2021). We take their integrated flux densities reported at: 119 and 154 MHz, measured from the GaLactic and Extragalactic All-sky Murchison Widefield Array (GLEAM; Hurley-Walker et al., 2017) survey; 887 MHz, measured from the Evolutionary Map of the Universe (EMU; Norris, 2011); 1.4 GHz, measured from the NRAO VLA Sky Survey (NVSS; Condon et al., 1998), and; 2 and 2.868 GHz, measured using pointed observations collected in the *LS*-band ($\lambda = 4$ cm) of ATCA (see Tab. B.1).

3.3 Spectral modelling of remnant lobes

Before we develop a new method to measure the off-time in remnant radio sources, we must ensure that our result can be verified against an established method. The off-time can be derived from the rapid steepening of their high-frequency spectrum due to the cessation of the jet activity and the subsequent lack of freshly shock-accelerated synchrotron-emitting electrons. In Sect. 3.3.1–3.3.3, we outline the theory of several literature-established spectral ageing models, and discuss their applications to radio lobe spectra. In Sect. 3.3.4, these models are applied to a combination of low- and high-resolution radio observations, in order to tightly parameterise the spectral ageing observed for J2253-34. Further, in Sect. 3.3.2, we briefly describe a PYTHON package we developed as part of this work to model

synchrotron spectra for a diverse range of applications in astrophysics.

3.3.1 Synchrotron emissivity

The total emissivity of a synchrotron-emitting plasma, $J(\nu)$, can be found by integrating the single-electron emissivity (e.g. $j(\nu)$; Longair, 2011) over the distribution of electron energies, $N(E)$; and the probabilistic distributions of the magnetic field strength, p_B, and pitch angle, p_ξ (Equation 4 of; Hardcastle, 2013)

$$J(\nu) = \int_0^\infty \int_0^\pi \int_0^\infty \frac{\sqrt{3}Be^2 \sin\xi}{8\pi^2 \epsilon_0 c m_e} F(x) N(E) p_\xi p_B dE d\xi dB, \tag{3.1}$$

where B gives the magnetic field strength; ξ the pitch angle; c the speed of light; e the electron charge; ϵ_0 the permittivity of free space; and m_e the electron mass. Rybicki & Lightman (1979) define $F(x)$ as the shape of the single-electron radiation spectrum, where x represents a dimensionless parameterisation of frequency, magnetic field strength, and electron energy, E, through:

$$x = \frac{\nu}{\nu_\mathrm{b}} = \frac{4\pi m_\mathrm{e}^3 c^4 \nu}{3eE^2 B \sin\xi}, \tag{3.2}$$

where ν_b is the break frequency above which (i.e. at higher frequencies) the spectrum steepens due to energy losses associated with the plasma ageing. Importantly, for a given magnetic field strength, the break frequency is related to the plasma spectral age through:

$$\tau = \frac{\upsilon B^{1/2}}{B^2 + B_\mathrm{IC}^2} \big(\nu_\mathrm{b}(1+z)\big)^{-1/2}, \tag{3.3}$$

where $B_\mathrm{IC} = 0.318(1+z)^2\,\mathrm{nT}$ gives the magnetic field equivalent of the cosmic microwave background at redshift z, and υ is a constant of proportionality (see Equation 4 of Turner et al. 2018b).

Parameterisation of meaningful attributes, such as ν_b, demands appropriate treatment of $N(E)$, p_B, and p_ξ. Kardashev (1962) initially proposed a model

with no pitch angle scattering, giving $p_\xi = 1$, however a more realistic model assuming an isotropic distribution for the pitch angle was subsequently suggested by Jaffe & Perola (1973), giving $p_\xi = \frac{1}{2}\sin\xi$; we assume the latter probabilistic distribution for the pitch angle in this work. Meanwhile, it is common to assume a locally-uniform magnetic field, such that $p_B = 1$, however, this assumption is likely not physical due to the turbulent mixing of lobe plasma. Tribble (1991) provide an alternative treatment for a turbulent (non-uniform) magnetic field, in which the field strength is drawn from a Maxwell-Boltzmann distribution; here, p_B is satisfied by

$$p_B = \sqrt{\frac{2}{\pi}}\frac{B^2\exp(-B^2/2a^2)}{a^3}, \tag{3.4}$$

where $a = B_0/\sqrt{3}$ for mean magnetic field strength, B_0 (Hardcastle, 2013). These assumptions can be paired together with an appropriate treatment of the electron energy distribution of the underlying plasma, $N(E)$ (described below), to create a range of spectral ageing models; these are referred to as either the "standard" (uniform B) or "Tribble" (Maxwell-Boltzmann distribution B) forms of each spectral ageing model.

3.3.1.1 Impulsive injection models

The radio spectrum arising from an impulsively-injected electron population is modelled as an ensemble of equal-age electrons $[t, t+dt]$ injected at $t = 0$ (Kardashev, 1962; Jaffe & Perola, 1973). Electrons are injected with an initial power-law distribution of energies, e.g $N(E) = N_0 E^{-s}$, where the power-law energy index, s, is related to the injection spectral index, $\alpha_{\rm inj}$, through $s = 2\alpha_{\rm inj} + 1$. Synchrotron and inverse-Compton (IC) radiative losses, the latter due to up-scattering of Cosmic Microwave (CMB) photons, occur as the electron packet ages; the resulting effect on the energy distribution is well understood (e.g. see; Pacholczyk, 1970; Longair, 2011). In the case of a uniform magnetic field, we follow the method of

Turner et al. (2018b) to remove the dependence on B by recasting $N(E)$ to:

$$N(x) = x^{-1/2} \begin{cases} (x^{1/2} - \iota^{1/2})^{s-2} & x > \iota \\ 0 & x < \iota \end{cases} \tag{3.5}$$

where $\iota(\nu, \xi) = \nu/(\nu_{\rm b} \sin \xi)$ assuming an isotropic distribution for the pitch angle, as proposed by Jaffe & Perola (1973). Here, the total synchrotron emissivity is thus evaluated as:

$$\mathcal{J}(\nu) = J_0 \, \nu^{(1-s)/2} \int_0^{\pi/2} \sin^{(s+3)/2} \xi \int_0^{\infty} F(x) N(x) \; dx \, d\xi, \tag{3.6}$$

where J_0 acts as a frequency-independent constant. In this work, we refer to this impulsively-injected spectral ageing model as the "standard" Jaffe-Parola (or JP) model. Importantly, parameterising the shape of this standard JP spectrum in this way only requires knowledge of the injection index and break frequency. By comparison, the shape of a "Tribble" Jaffe-Parola (or TJP) model spectrum additionally requires knowledge of B.

Considering some small region across a radio galaxy lobe (e.g. bounded by the FWHM of a restoring beam), it is reasonable to suspect that the plasma contained here will have been injected at approximately the same age. This means that the associated radio spectrum is likely that of the JP model, however we note the results of Turner et al. (2018a), Mahatma et al. (2020) and Yates-Jones et al. (2021, 2022) who show that mixing of plasma ages may violate this assumption.

3.3.1.2 Continuous Injection models

The above assumption of an impulsively-injected packet of electrons breaks down when considering the integrated spectrum of a radio AGN, which comprises multiple, or on-going, such injections throughout the lifetime of the source. A continuous injection model describes a radio spectrum arising from a time-averaged population of continuously-injected electron packets; that is, a mixed-age plasma

population with ages ranging within $[0, \tau]$. In the simpler and more common case, the CI model assumes continuous injection via an active jet throughout the entire lifetime of the source (e.g, the 'CI-on' or CIJP[3] model). To model remnant AGNs, Komissarov & Gubanov (1994) present an extension to the CI model, known as the 'CI-off' or KGJP model, by instead assuming some fraction of the total source age, $R_{\rm rem} = t_{\rm rem}/\tau$, is spent in a remnant phase; we refer to $R_{\rm rem}$ as the remnant ratio, where the total source age, τ, is given by the sum of the active and remnant durations, $\tau = t_{\rm on} + t_{\rm rem}$. As with the JP model, the effect of ageing on the plasma energy distribution is well understood (e.g. see; Longair, 2011). In the case of a uniform magnetic field, the recast form of $N(E)$ is given by (Equation 3 of; Turner, 2018)

$$\mathcal{N}(x) = x^{-1/2} \begin{cases} (x^{-1/2} - \zeta^{1/2})^{s-1} - (x^{1/2} - \iota^{1/2})^{s-1} & x > \iota \\ (x^{1/2} - \zeta^{1/2})^{s-1} & \zeta \leq x \leq \iota \\ 0 & x < \zeta \end{cases}, \tag{3.7}$$

where $\zeta(\nu, \xi) = \iota(\nu, \xi) R_{\rm rem}^2$. The total synchrotron emissivity of a CI spectrum is thus derived by:

$$\mathcal{J}(\nu) = J_0 \, \nu^{-s/2} \int_0^{\pi/2} \sin^{(s+4)/2} \xi \int_0^{\infty} F(x) N(x) \; dx \, d\xi, \tag{3.8}$$

In the limiting case where $R_{\rm rem} = 0$, the CI-off model reduces to the simpler CI-on form. For simplicity, we thus refer to the general form as the CI model. In this way, parameterising the shape of a standard CI spectrum requires only the injection index, break frequency, and remnant ratio. As with the TJP model, the shape of a "Tribble" Continuous Injection (or TCI) spectrum additionally requires knowledge of B.

Due to their assumption of a mixed-age plasma, the CI models are relevant

[3]Here, the 'JP' reflects only the isotropic distribution for the pitch angle proposed by Jaffe & Perola (1973), not their assumption of an impulsively-injected plasma.

for deriving the plasma spectral age from the integrated spectra of radio lobes (e.g; Parma et al., 2007; Murgia et al., 2011; Shulevski et al., 2012; Brienza et al., 2016; Turner, 2018; Duchesne & Johnston-Hollitt, 2019). However, it is worth mentioning that the CI model assumes no temporal evolution in the magnetic field, which we know not to be true for expanding lobes. Using synthetic radio source populations, for which all radiative losses and temporal evolution of the magnetic field were considered, Turner et al. (2018b) demonstrated that the radio emissivity reflects only the most recent $\sim 10\%$ of the magnetic field history. Importantly, their results showed that the spectral age derived using the break frequency, parameterised by the CI model, together with the present-time magnetic field strength, was in agreement with the dynamical age. As such, we can be confident that the quantities parameterised by the CI model are physically meaningful.

3.3.2 Spectral model fitting

We now discuss our approach taken to numerically implement the spectral ageing model described in the previous section, and to fit these spectra to observed data points. The code we developed to achieve this is expected to be highly valuable to the broader astrophysics community (e.g. synchrotron spectra from active galaxies, supernovae remnants, etc.), and so we have released it as the publicly-available **synchro**tron spectral **fit**ter (SYNCHROFIT)[4] PYTHON library. Principally, SYNCHROFIT offers a suite of routines that: 1) implement the JP and CI spectral ageing models described in Sect. 3.3.1.1 and 3.3.1.2, and 2) fit these models to real radio data.

For computational efficiency, the standard spectral ageing models are evaluated by numerically integrating over the electron energy and pitch angle, following the reduced dimensionality parameterisation of $J(\nu)$, first presented by Nagai et al. (2006, JP), Turner et al. (2018b, CI-on) and Turner (2018, CI-off). The

[4] https://github.com/synchrofit

Tribble spectral ageing models are evaluated in a similar fashion, however involve an additional numerical integration over the magnetic field strength, and as such incur a considerable cost to the computation time. An injection index and break frequency are required to parameterise the shape of the JP spectrum, with an additional normalisation to scale the fit appropriately. The shape of a CI spectrum is additionally parameterised by the remnant ratio, noting that $R_{\rm rem} = 0$ in the case of the CI-on model. Tribble forms of the spectral ageing models are parameterised similarly, however additionally require the redshift and magnetic field strength.

Fitting of these models is conducted using a grid-search informed by an adaptive maximum likelihood algorithm. Discrete samples in s, $\log \nu_b$ and $R_{\rm rem}$ are created by uniformly sampling their allowed ranges, which are used to construct a three-dimensional parameter grid. A spectral model is evaluated for each unique parameter combination, where a corresponding normalisation is optimised following $S_0 = \sum_{i=1}^{n}(S_{\rm o_i} \times \sigma_i) - \sum_{i=1}^{n}(S_{\rm p_i} \times \sigma_i) / \sum_{i=1}^{n} \sigma_i$, where n is the number of spectral measurements, $S_{\rm o_i}$ and $S_{\rm p_i}$ are the observed and predicted flux densities in logarithmic space, and σ_i is the measurement uncertainty for the ith datum. The quality of fit is evaluated using the lowest value of the Akaike information criterion (AIC; Akaike, 1974) following $\mathrm{AIC} = 2k - 2\ln\mathcal{L}$, where k is the number of model parameters[5]. The likelihood function, $\mathcal{L}$, is defined through:

$$\mathcal{L}(\mu, \sigma) = \prod_{i=1} \frac{1}{\sqrt{2\pi}\sigma_i} \exp\Big(- \frac{(x_i - \mu_i)^2}{2\sigma_i^2} \Big) \tag{3.9}$$

which, for each unique measurement, i, takes into consideration the observed value, x_i, measurement uncertainty, σ_i, and the corresponding predicted model value μ_i. Across all grid realisations, the set of parameters providing the optimal spectral fit are defined as those that minimise the AIC. The relative quality of each spectral fit is found using $p_i = e^{(\mathrm{AIC}_i - \mathrm{AIC}_{\rm best})/2}$, where p_i is the probability that

[5]For the standard JP and CI-on models, $k = 3$. For the standard CI-off models, $k = 4$. In the case of the Tribble forms, k increases by 1 due to the magnetic field.

the i^{th} spectral model provides a better fit to the observations than the selected 'best' model. Provided the marginal probability density functions (PDFs) in each model parameter are pseudo-Gaussian, the fitted uncertainty in each parameter is taken as the standard deviation, and the peak in the PDF as the approximate location of the global maximum. In order to increase the precision of the best estimate in each free parameter, a grid of points is then re-sampled around the global maximum; in this work, we repeat this over three iterations. We note, Gaussianity may not necessarily always hold for these PDFs, as this will depend upon the spectral fit, hence we make sure to inspect these throughout this work.

3.3.3 Effect of inhomogeneity in the local magnetic field

The standard form of the spectral ageing models have a considerable computational advantage over the (likely more physically accurate) Tribble forms in our implementation (due to the lower number of numerical integrations). We therefore investigate if the standard form can be used to reasonably approximate the Tribble form for either spectral ageing model, or for any range of magnetic field strengths.

Both the standard and Tribble forms of the spectral ageing models offer a physically-meaningful parameterisation of observed radio spectra. Due to the consideration of a variable magnetic field, the shape of the expected synchrotron spectrum differs to that in which the magnetic field is uniform. For example, Hardcastle (2013) show a significant departure of the TJP model from the standard form, notably due to the sharper spectral turnover around the break frequency in the TJP spectrum. Turner et al. (2018b) explore the consequence of using the standard spectral ageing models to parameterise simulated Tribble spectra; their results demonstrate an over-estimation of the break frequency, which appears to be more appreciable for the JP model as compared to the CI model.

The assumption of a locally uniform magnetic field will be at least somewhat violated in radio AGN lobes due to turbulent flow; the Maxwell-Boltzmann mag-

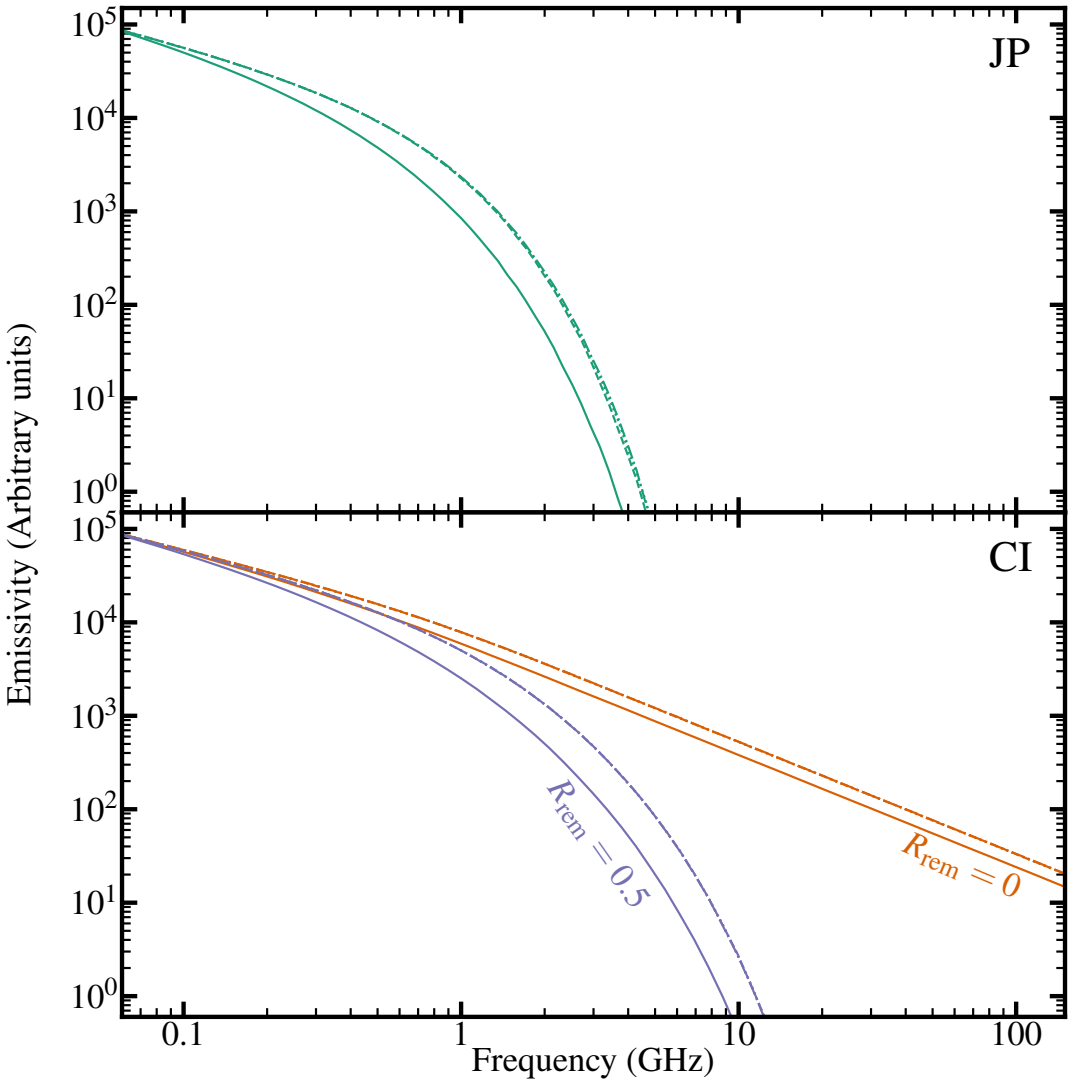

Figure 3.2: Comparison between standard (solid lines) and Tribble forms (broken lines) of the JP (top panel) and CI (bottom panel) spectra. SYNCHROFIT is used to simulate radio spectra for $s = 2.2$ and $\nu_{\rm b} = 2.1\,{\rm GHz}$. Tribble models are shown for $B = 0.1\,{\rm nT}$ (dot-dashed), $B = 1\,{\rm nT}$ (dotted), and $B = 10\,{\rm nT}$ (dashed). CI models are shown for $R_{\rm rem} = 0$ (orange) and $R_{\rm rem} = 0.5$ (purple). We note that the Tribble models almost exactly overlay each other and hence can not be distinguished.

netic field distribution of the Tribble spectral ageing models may provide a more realistic description, however this in turn requires knowledge of B_0 which, unless independent X-ray data is available, would require dynamical modelling.

As such, we seek to explore the dependence of the shape of the Tribble spectral ageing models on B_0. We use SYNCHROFIT to simulate standard and Tribble forms of the JP and CI models, assuming $s = 2.2$, and $\nu_\mathrm{b} = 2.1\,\mathrm{GHz}$. Tribble models are simulated for $B_0 = 0.1\,\mathrm{nT}$, $1\,\mathrm{nT}$ and $10\,\mathrm{nT}$, in order to cover a broad range of acceptable values. These are shown in Fig. 3.2.

As a consistency check with Hardcastle (2013), Harwood et al. (2013) and Turner et al. (2018b), we reassuringly find that integrating over a Maxwell-Boltzmann magnetic field modifies the shape of the predicted spectra to that in which the magnetic field is uniform. However, our results show that the shape of the predicted Tribble spectra are largely insensitive to values of the mean magnetic field strength. We find that electron packets with magnetic strengths in the exponential tail of the Maxwell-Boltzmann distribution (i.e. $B > \sqrt{3/2}\,B_0$) contribute the vast majority of the total synchrotron emission at all radio frequencies. Importantly, the mean magnetic field strength has no effect on the shape of this exponential portion of probability density function, albeit modifies its normalisation. As a result, the shape of the radio spectrum remains largely unaffected for moderate changes in the mean magnetic field. The implication here is it is possible to accurately parameterise the injection index, break frequency, and remnant fraction (in the case of the CI models), using the Tribble spectral ageing models without explicitly requiring knowledge of B_0; an informed guess of the mean magnetic field strength is sufficient (e.g. $B_0 \sim 0.1$ - $10\,\mathrm{nT}$).

3.3.4 Modelling the radio spectrum of J2253-34

We are now equipped with the tools needed to derive a robust measurement of the off-time from our observations J2253-34. However, we choose not to directly fit the integrated spectrum with the CI-off model as the three parameters are

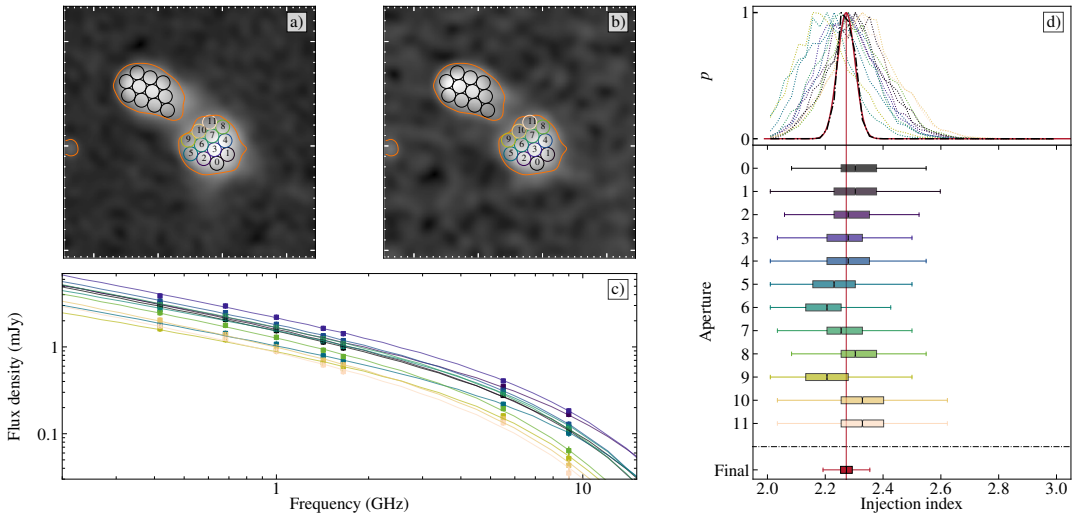

Figure 3.3: The injection index optimised for J2253-34. Panels a) and b) show the observed radio emission at 1.32 GHz and 5.5 GHz, respectively; each image is presented on a square-root stretch, and is normalised between the minimum/-maximum pixel values. A solid dark-orange contour denotes the 5σ brightness of the source at 9 GHz. Circular markers of an $8''$ aperture (the FWHM of the restoring beam) are used to represent independent regions from which a radio spectrum is extracted and used as a constraint on the injection index. Apertures overlaid on the south-western lobe are colour-coded and numbered based on aperture number, and are highlighted in panels c) and d); to avoid clutter in the figure we do not plot the spectral fits for apertures in the north-eastern lobe. Panel c) demonstrates fits of the TJP model ($B_0 = 0.1$ nT) optimised to their associated spectrum. Panel d) demonstrates the probability density function associated with each spectral fit, marginalised with respect to the injection index; these are also represented by the box and whisker plots, where the box is constrained by the 25^{th} - 75^{th} percentiles. A global optimisation for the injection index is found by multiplying the PDFs associated with each lobe (dot-dashed black curve), which is then approximated by a 1D Gaussian (solid red curve) in order to characterise the peak probable value and uncertainty: $s = 2.25 \pm 0.03$ (or alternatively, the injection spectral index; $\alpha_{\text{inj}} = 0.625 \pm 0.015$).

somewhat correlated, and may be misfitted if our observations include moderate systematic uncertainties. Instead, we independently constrain the injection index by considering the spectra arising from narrow regions across the lobes; it is reasonable to assume these spectra can be described by the JP model (see Sect. 3.3.1.1). Assuming a constant injection index throughout the lifetime of the source, the JP models can be jointly fit to these spectra, resulting in a precise measurement of the injection index optimised across the lobes. The integrated spectrum can now be fitted using the CI model for a known injection index, reducing any potential systematic errors in estimates for the break frequency and remnant ratio; the latter mapping directly to the duration of the remnant phase for any given source age. This is described in detail below.

3.3.4.1 Modelling the injection index

To model the injection index, we use the $8''$ beam-matched radio maps described in Sect. 3.2. We use MIRIAD to create a 2D cutout of J2253-34 from each image, and `regrid` the cutouts to have a common pixel scale ($d\theta = 1''$) and projection (`SIN`). To efficiently sample the resolved radio spectrum, we extract the radio spectra arising from individual circular apertures arranged in a hexagonal configuration across the lobes. The full width half maximum (FWHM) of each aperture is set to $\theta_{\rm FWHM} = 8''$ to reflect the size of the restoring beam. The integrated flux density within each aperture is then calculated following $S_{\rm int} = \sum_{i=1}^{n} S_{p,i} \times d\theta^2/\Omega$, where n is the number of pixels contained within each aperture, $S_{p,i}$ is the value of the $i^{\rm th}$ pixel in Jy beam^{-1}, $d\theta$ is the pixel angular scale, and Ω is the beam solid angle defined as $\theta^2_{\rm FWHM} \times \pi/(4 \ln 2)$. Given the spectra are extracted from exactly one resolution element, the measurement uncertainty is evaluated as the quadrature sum of the RMS noise in the observations and their absolute calibration uncertainty.

Following this method, the radio spectra are extracted from all regions across the lobes with 9 GHz radio emission above the 5σ noise level. This restriction is

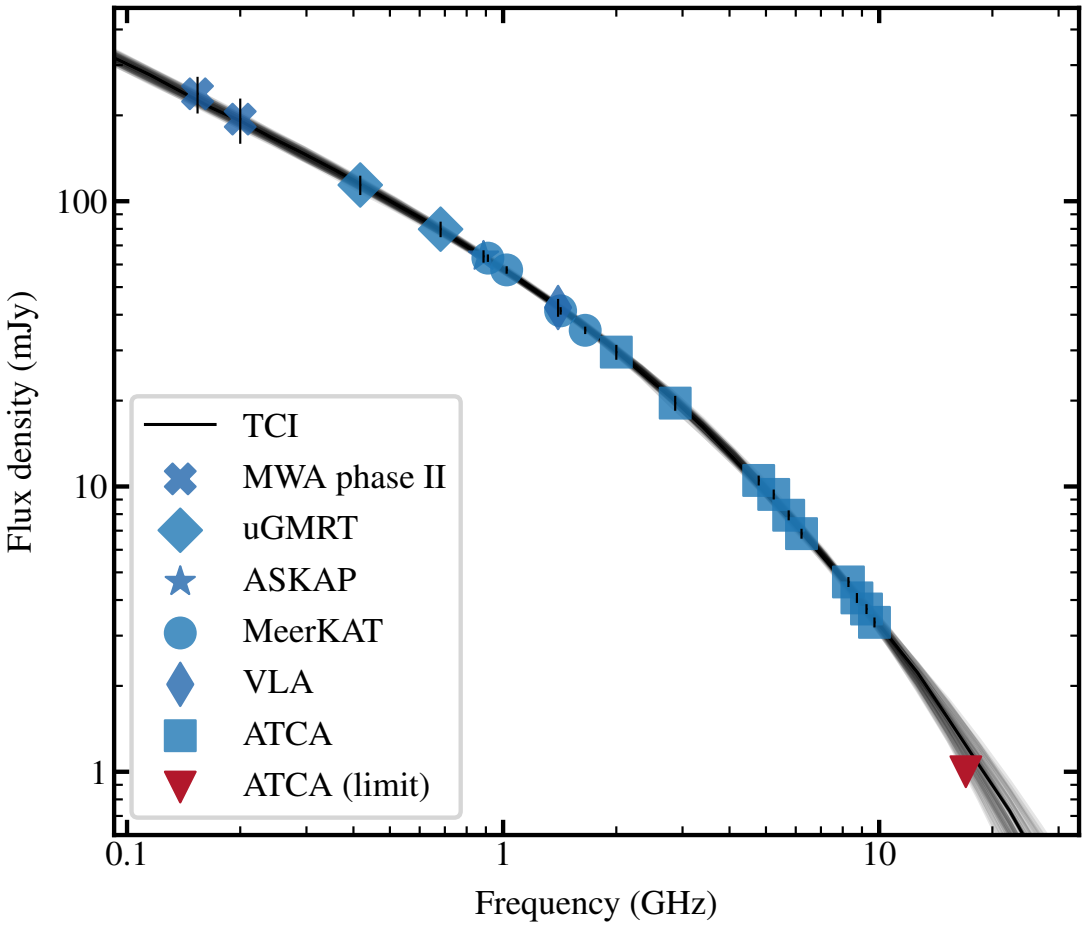

Figure 3.4: The spectral emissivity of J2253-34. Blue markers are used to display measurements of the integrated flux density. Error-bars represent 1σ measurement uncertainties. Overlaid is the fit of the TCI model, assuming $B_0 = 0.1\,\mathrm{nT}$ and $s = 2.25 \pm 0.03$ (Sect. 3.3.4.1). The optimal fit of the TCI model (Sect. 3.3.4.2) is displayed using a solid black line. Also shown in light-gray are all plausible spectral fits within a 99.7% (3σ) confidence interval. The spectral break frequency and remnant ratio are fitted as $\nu_\mathrm{b} = 1.26^{+0.06}_{-0.05}\,\mathrm{GHz}$, and $R_\mathrm{rem} = 0.23 \pm 0.02$, respectively.

done so as to maximise the number of observing frequencies contributing to the radio spectrum. The spectra arising from each aperture are independently fit using the JP (and TJP) models; importantly both the break frequency and the injection index are free parameters in their corresponding aperture spectral fit. In light of the results in Sect. 3.3.3, we use Equation 2 of Miley (1980) to calculate a crude approximation of the lobe equipartition magnetic field strength as $B_{\rm eq} \approx 0.35\,{\rm nT}$. Given that radio galaxy lobes generally exhibit sub-equipartition conditions, as demonstrated by Ineson et al. (2017) through X-ray inverse-Compton and radio synchrotron measurements, along with Turner et al. (2018b) through dynamical radio source modelling, we fit the TJP model assuming $B_0 = 0.1\,{\rm nT}$, $0.35\,{\rm nT}$ and $1\,{\rm nT}$.

Spectral models are evaluated by uniformly sampling the injection index within a range corresponding to [2.01, 2.99] and an initial grid spacing of $\Delta s = 0.05$. For each aperture spectral fit, a corresponding PDF is found by marginalising across the fitted injection index. Each PDF is then multiplied together to determine which value for the injection index provides an optimal fit across all aperture spectra; this assumes no correlation between the spectra arising from adjacent apertures, and also assumes a constant injection index throughout the lifetime of the source. Following this method, we optimise an injection index by considering the spectra arising from both lobes, which we present in Fig. 3.3. Importantly, we found that the optimal injection index modelled using the standard JP model is found to be $s = 2.10 \pm 0.05$ (or; $\alpha_{\rm inj} = 0.550 \pm 0.025$). For the Tribble model, we found an optimal value of $s = 2.25 \pm 0.03$ (or; $\alpha_{\rm inj} = 0.625 \pm 0.015$).

3.3.4.2 Modelling the break frequency & remnant ratio

We compile an integrated radio spectrum for J2253-34 using the two decades of radio-frequency data described in Sect. 3.2. The raw spectrum is presented in Fig. 3.4, and demonstrates a clear spectral curvature owing to the losses associated with an inactive jet; this is evidenced by an ultra-steep high-frequency spectral

index of $\alpha = 1.7$, computed between 4.5 - 9.5 GHz. With the injection index estimated in Sect 3.3.4.1, we seek to model the break frequency and remnant ratio of J2253-34 by parameterising the observed curvature using the CI spectral ageing models.

Similar to the resolved modelling to determine the injection index, we model the integrated spectrum using both the standard and Tribble forms of the CI model. For consistency, we use the injection indices estimated using the standard and Tribble JP models as inputs to the standard and Tribble CI models, respectively. Similarly, TCI models are evaluated for the same values of B_0 used in Sect. 3.3.4.1. To account for the small uncertainty in the injection index previously fitted by the JP models, we treat 's' as a free parameter in the CI models, but apply a tight Gaussian prior based on the fitted uncertainty. We find that fixing the injection index offers no appreciable difference to our results, unsurprising considering the uncertainties on the injection index are small. The CI model fitted to the integrated spectrum is shown in Fig. 3.4.

Results of the fitting are summarised as follows (see also Tab. 3.2). Modelling the integrated radio spectrum using the CI model gives a break frequency of $\nu_{\rm b} = 1.78^{+0.17}_{-0.15}$ GHz, and a remnant ratio of $R_{\rm rem} = 0.23 \pm 0.02$. Using instead the TCI model, gives a marginally different break frequency of $\nu_{\rm b} = 1.26^{+0.06}_{-0.05}$ GHz, and remarkably, a remnant ratio of $R_{\rm rem} = 0.23 \pm 0.02$, consistent with the value constrained from the standard CI model.

Finally, it is important to mention that the precise measurements of the break frequency and remnant ratio of J2253-34 are only made possible by the independently-fitted injection index. By inspecting the marginal distribution of the fitted break frequency and remnant ratio, we find that their PDFs are Gaussian-like, and importantly do not demonstrate any parameter degeneracy worth consideration. These results are in stark contrast to those found by blindly fitting each parameter of the CI models from the integrated radio lobe spectrum. Here, we find that a single precise measurement of the injection index can not

Table 3.2: The spectral modelling attributes of J2253-34, described in Sect. 3.3.4. Using the 8″ radio images, the radio spectra arising from small regions across the lobes are jointly fit by the JP models, in order to optimise the injection index. The broadband integrated radio spectrum is then fit by the CI models, propagating the fitted injection index and uncertainties through a Gaussian prior, to estimate the break frequency and remnant ratio.

Model	Injection index	Break frequency	Remnant ratio
JP	2.10 ± 0.05	–	–
TJP	2.25 ± 0.03	–	–
CI	–	$1.78^{+0.17}_{-0.15}$ GHz	0.23 ± 0.02
TCI	–	$1.26^{+0.06}_{-0.05}$ GHz	0.23 ± 0.02

be found; e.g. for the standard CI model, the fitted injection index can plausibly range anywhere between $s \sim 2.1$ - 2.3. Consequently, this introduces major uncertainties onto the fitted break frequency and remnant ratio, which become largely degenerate with one another; e.g. for the standard CI model, the break frequency demonstrates frequent local minima/maxima between $\nu_{\rm b} \sim 2$ - 5 GHz, and the PDF of the fitted remnant ratio is heavily asymmetric about its peak probable value of $R_{\rm rem} \sim 0.38$. It is interesting that these results are found even for an integrated radio spectrum as well-sampled as that of J2253-34, and thus reinforce the approach described in this section.

3.4 Dynamical modelling of remnant lobes

In the following section, we present a new dynamical model-based method that measures the off-time in remnant lobes, and is capable of identifying candidate remnant radio galaxies from observations. In Sect. 3.4.1, we present the dynamical model that underpins this work. In Sect. 3.4.2, we justify why the backflow of lobe plasma holds valuable constraints on the off-time, and necessarily devise a tool to parameterise the surface brightness distribution of radio lobes. In Sect. 3.4.3, we then outline the constraints necessary to model the energetics of lobed radio-loud AGNs. Finally in Sect. 3.4.4, we implement our new method to

constrain the energetics of J2253-34, which we then independently verify against the remnant ratio previously measured in Sect. 3.3.

3.4.1 Radio AGN in semi-analytic environments

Throughout this work, the *Radio AGN in Semi-analytic Environments* (RAiSE; Turner & Shabala, 2015; Turner et al., 2018a; Turner & Shabala, 2020) code is used to model the dynamics of 'lobed' Fanaroff & Riley type-I and type-II (FR-II/I; Fanaroff & Riley, 1974) remnant lobes. Remnants associated with 'flaring jet' FR-Is, which exhibit the prototypical smoke-like plumes (e.g. 3C31; Leahy et al., 2013), are not considered by this analysis since their dynamics are outside the scope of the RAiSE model. In this work, we employ RAiSE both as a tool to model the radio-loud AGN energetics, and to simulate mock radio source populations.

3.4.1.1 The RAiSE model

The RAiSE code consolidates models describing the expansion of lobed FR-II/I sources together with an observation-based treatment of the environments within which the jets expand; RAiSE has been tested to show consistency with hydrodynamical simulations, is able to reproduce the observed relationship between radio luminosity, morphology and host galaxy properties, is consistent with observed spectral ages maps of radio lobes, and is able to reconcile the discrepancy between spectral and dynamical ages in powerful radio galaxies. In this way, the temporal evolution of a radio source can be modelled for, amongst other intrinsic properties, any combination of source age, jet kinetic power, and intergalactic environment (forward modelling hereafter).

Quantifying an AGN environment requires knowledge of the distribution of gas in the associated dark matter halo. Ideally this is done by constraining a gas density and temperature profile through X-ray observations, however such observations are largely unavailable across the majority of haloes, especially at

higher redshifts. Turner & Shabala (2015) showed that estimates of the halo mass of the intergalactic environment can alternatively be inferred from the optically-observed stellar content based on outputs of semi-analytic galaxy evolution models (e.g. SAGE; Croton et al., 2006); however, the shape of the gas density profile remains unconstrained by this method. RAiSE therefore quantifies the intergalactic environment in one of two ways: 1) by directly specifying a gas-density profile; or 2) by providing a mass of the dark matter halo, distributing the total gas mass based on an observationally-based gas density profile reported by Vikhlinin et al. (2006). In the latter example, this can be done based on either the mean profile or by randomly sampling a distribution of environment profiles from a galaxy formation model.

RAiSE implements a lobe emissivity model that considers radiative losses due to synchrotron radiation and the inverse-Compton up-scattering of CMB photons, as well as the adiabatic losses related to the expansion of the lobes. This emissivity calculation is applied to small packets of electrons that are shock-accelerated at different points in the evolutionary history of the lobe. As a result, RAiSE considers the temporal evolution in the magnetic field; i.e. from the time electrons are shock-accelerated to the time they release their energy as synchrotron radiation. The magnetic field strength is derived from the lobe dynamics by assuming a constant ratio between the energy densities in the magnetic field and particles; referred to as the equipartition factor.

Over the past decade, models describing these processes have been incrementally added to the RAiSE code. Turner & Shabala (2015) provided the original implementation of a radio source model within a semi-analytic environment, and correspondingly modified the synchrotron emissivity model for the lobes. Turner et al. (2018a) used hydrodynamical simulations to spatially map the synchrotron emissivity across the lobes, allowing them to produce surface brightness maps of simulated radio sources; their model implemented tracer particles from hydrodynamical simulations to probe the average locations and ages of injected particles.

Turner (2018) extended the dynamical and synchrotron emissivity models to account for the remnant phase during which the jets are inactive. Of relevance to this work, the dynamics presented by Turner & Shabala (2020) offer a slight modification to include the effect of a shocked gas shell.

The latest version of the RAiSE code[6], as used in this work, is informed by the dynamics of Turner & Shabala (2020), and implements the method of Turner et al. (2018a) to produce intensity maps based on tracer particles from the higher-resolution hydrodynamical simulation of Yates-Jones et al. (2022). By using individual hydrodynamical simulation particles rather than population averages, this enables RAiSE to synthesise hydrodynamical-based, high-resolution maps of the radio lobes at any observing frequency (e.g. see Fig. 3.5).

3.4.1.2 Constraining a RAiSE model

The RAiSE model is characterised by a variety of model parameters that represent intrinsic parameters of a radio source. These parameters are constrained in one of three ways: 1) through a direct measurement (e.g. injection index); 2) a prior probability distribution based on measurements of well-studied objects (e.g. ambient density profile); or 3) by way of a parameter inversion based on simulated observable attributes (e.g. jet power and age from size and luminosity).

RAiSE-based parameter inversions have been implemented by several previous authors to constrain the energetics of radio-loud AGNs. Turner & Shabala (2015) demonstrated the ability to recover the jet powers and lifetimes of radio sources using only their observed physical size and monochromatic radio luminosity; in their work, halo masses for each source were inferred from the stellar masses of their hosts using SAGE, and intrinsic parameters such as the equipartition factor and injection index were fixed to typical values. Turner et al. (2018b) were additionally able to recover the lobe equipartition factors by including the break frequency as an observational constraint. Turner et al. (2020) demonstrated that

[6] https://github.com/rossjturner/RAiSEHD

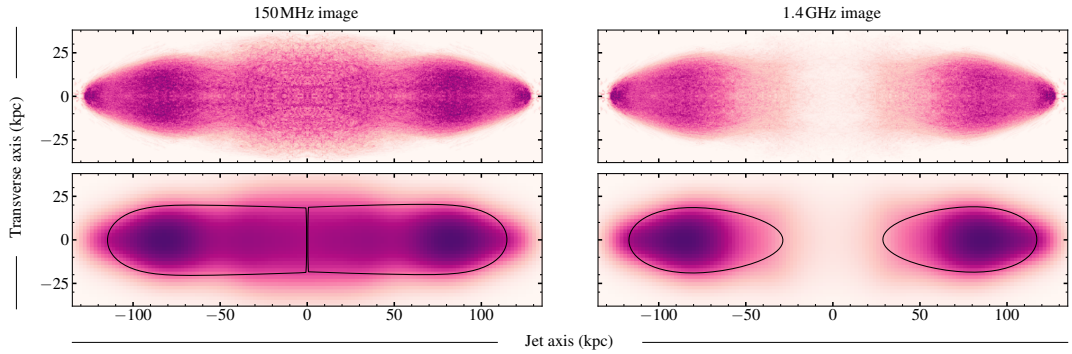

Figure 3.5: Intensity maps predicted by RAiSE for a redshift $z = 0.1$ radio source with a jet-power of $Q = 10^{38}$ W, source age of $\tau = 100$ Myr, and a remnant ratio of $R_{\rm rem} = 0.25$. The radio source is shown for 150 MHz (left panels) and 1.4 GHz (right panels), each of which is shown for a native resolution corresponding to 1.024×10^8 particles (upper panels) and for a convolved $10''$ image (lower panels). The pixel scale in the convolved image is $1''$. Following the method outlined in Sect. 3.4.2.2, the observed surface brightness distribution is optimally fit by a skewed two-dimensional Gaussian; this is shown by a solid black contour, which represents the edge bounding 95% of the Gaussian volume. Images of each fitted Gaussian are truncated at the core, resulting in the apparent abrupt cut-off at 150 MHz.

using only a reference flux density, angular size and width, break frequency and injection index, the cosmological redshift of radio sources can be constrained from the present epoch to the early-universe.

These results underline that the constraining power of the RAiSE-based parameter inversion is primarily limited by the input set of observational constraints. It is worth nothing that previous such applications of the RAiSE model have used attributes measured from observations with poor resolution. The capabilities of the current RAiSE model create a new opportunity to constrain intrinsic radio source parameters using additional attributes related to the observed surface brightness distribution of radio lobes. In the following sections, we exploit this opportunity to explore a new method for modelling the energetics of remnant AGNs.

3.4.2 The surface brightness distribution of radio lobes

In the absence of detailed spectral modelling, alternative constraints are needed to aid the modelling of the energetics of remnant AGNs. Here, we propose that the backflow of plasma in radio galaxy lobes offers such constraints, and subsequently develop a tool to parameterise the observed surface brightness distribution of radio lobes.

3.4.2.1 Constraints embedded in the lobe backflow

The plasma contained within FR-II radio lobes is injected throughout the active phase at the hotspot, and is carried away from the hotspot by the backflow (e.g. Turner et al., 2018a). This leads to a gradient in age across the lobes, *generally* in the form of an approximately linear increase in spectral age away from the hotspot. The dynamics of the bulk plasma flow of lobed FR-Is is similar to that of FR-IIs. Although the flow of plasma through the jet spreads closer to the core at a flare point, the accelerated plasma reaches the lobe-shocked shell contact discontinuity and flows backwards as for an FR-II. While the structure of FR-I jets may pose more discernible differences with FR-IIs during the active phase of the jet, the rapid fading of the jet relative to the diffuse lobe plasma makes these differences far less important in the remnant phase. Consequently, for both lobed FR-Is and FR-IIs, the observed shape of the emitting regions will vary depending on observing frequency; the low-frequency radiation produced by older electrons results in wider emitting regions along the jet-axis and transverse-axis, whereas at higher frequencies the bias towards observing younger electrons results in narrower emitting regions localised near the injection site. This is demonstrated in Fig. 3.5. Importantly, the manner by which the observing frequency modifies the observed spatial distribution of synchrotron-emitting electrons, should depend on factors such as the plasma age distribution and lobe magnetic field strength. In the absence of spectral modelling, it is therefore reasonable to suggest that well-resolved observations of remnant radio lobes should offer the constraints

necessary to help disentangle their active and remnant timescales.

3.4.2.2 Skewed two-dimensional Gaussian lobes

We require attributes to describe the observed surface brightness distribution of radio lobes, which can be compared between observations and simulations. We note that the reproduction of fine details is neither important nor captured by the RAiSE simulations (e.g. knots in the jets, or slight bending of the jets). Implementing a skewed Gaussian in two spatial dimensions is appropriate for the following reasons: 1) a Gaussian is able to describe the fall-off in brightness as a function of position; 2) in two dimensions, a Gaussian is able to characterise a measure of length of the lobe along the jet-axis, as well as a width along the transverse-axis; 3) introducing a 'skew' term along the major axis handles the asymmetry in brightness along the jet-axis (e.g. emission is typically brightest near the hotspot and falls off asymmetrically in each direction). In this way, the vastly different morphologies of, for example, a high-powered radio source (with a sharp fall-off in brightness away from the hotspot) and a low-powered aged remnant (with relatively smooth surface brightness profiles) can be characterised in a manner that is consistent.

To fit the skewed Gaussian to the observed surface brightness distribution of a radio lobe, the following free parameters are necessary:

- S_0, the amplitude of the Gaussian;
- μ_x & μ_y, the coordinates of the peak amplitude in each dimension;
- σ_x & σ_y, the standard deviation in each dimension;
- θ, the major axis position angle;
- β_x, the skew term along the Gaussian major axis.

Since RAiSE simulates a jet in an known orientation and positions the SMBH at the center of the image, the angle of rotation ($\theta = 0$) and μ_y are set by

default (and therefore do not need solving). A simple least-squares algorithm is used to optimise the fit by minimising the residuals between the radio lobe surface brightness distribution and Gaussian model. For stability, regression is performed to the square-root of the input image; this ensures fitting to the general shape, and down-weights bias towards the brightest pixels. The resulting Gaussian fit can then be used to parameterise key attributes related to the observed surface brightness distribution of a radio lobe (see Sect. 3.4.3.1 below). We make this code publicly available on GitHub[7].

3.4.3 Radio source attributes

In this work, radio source attributes refer to the observable quantities that describe either the spatial, photometric, or spectral properties of radio galaxy lobes. By implementing these attributes in a RAiSE-based parameter inversion, they facilitate the comparison between observed radio sources and those simulated by the RAiSE model. However, images of real radio sources are 'degraded' by the sensitivity and resolution of the observations; degrading simulated images with these same observing limitations therefore enables a more meaningful comparison. In the following section, we describe the methods for measuring these attributes from observed and simulated images.

3.4.3.1 Spatial attributes

Spatial attributes are measured based on the Gaussian fitting method described in Sect. 3.4.2.2. We do this by first considering the boundary of the 2D ellipse formed by slicing the fitted Gaussian at some critical brightness level (e.g. see Fig 3.5). We define this critical level as $S_0 e^{-2}$, above which 95% of the Gaussian volume is contained. We stress that the arbitrary selection of this value does not matter; instead, what is important is that the same value is used when comparing both observed and simulated radio images, such that the resulting attributes are

[7] https://github.com/benjaminquici/skewed-gaussian-lobes

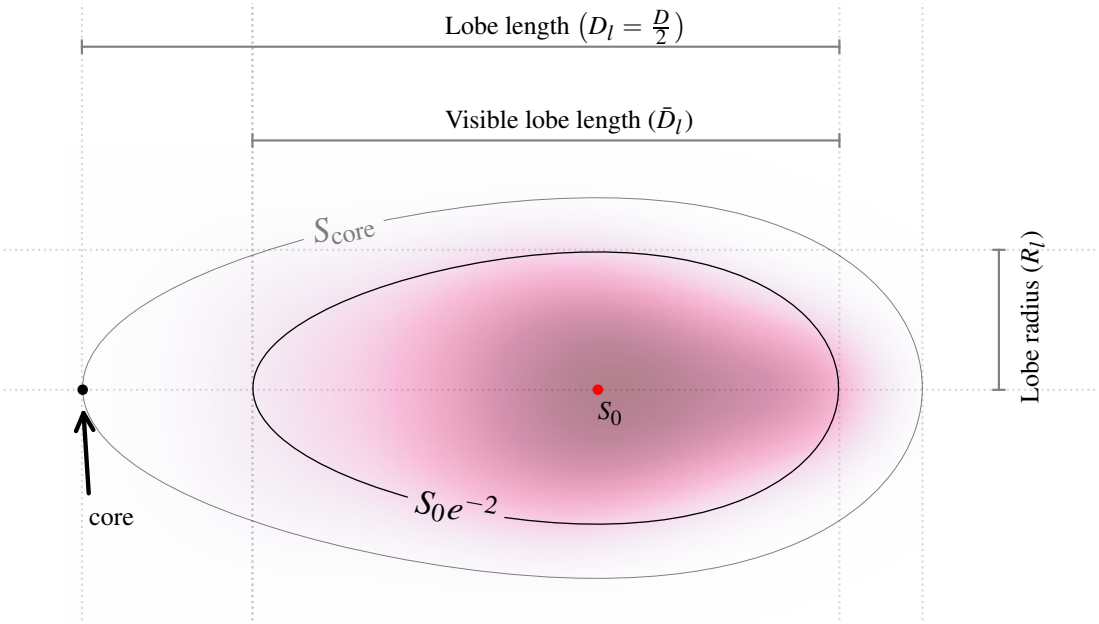

Figure 3.6: Schematic showing the key quantities necessary for computing the spatial attributes described in Sect. 3.4.3.1. The semi-transparent purple emission represents the right lobe of the 1.4 GHz convolved image from Fig 3.5. A skewed two-dimensional Gaussian is fit to the lobe surface brightness distribution following the method outlined in Sect. 3.4.2.2, where S_0 gives the amplitude of the fit. A solid black contour denotes the fitted Gaussian at a critical brightness level of $S_0 e^{-2}$, and bounds 95% of the Gaussian volume.

Table 3.3: Spatial attributes evaluated using the quantities shown in Fig. 3.6

Spatial attribute	Symbol	Expression	Limit
linear size	D	$D_l^{\rm lobe1} + D_l^{\rm lobe2}$	–
observed axis ratio	A	D_l/R_l	≥ 1
extent 1	E	$D_l/\bar{D}_l$	0 - 1
extent 2	$\bar{E}$	$S_{\rm core}/S_0$	0 - 1

measured consistently. The following distances are measured by considering the boundary of the 2D ellipse (Fig. 3.6): the length of the lobe, D_l; the visible length of the lobe, $\bar{D}_l$; and the radius of the lobe, R_l. We consider the backflow in each lobe separately, and thus bound the visible lobe length as $0 < \bar{D}_l \leq D_l$. From here, we define four key spatial attributes, including the linear size, D, and observed axis ratio, A, as shown in Tab. 3.3.

Importantly, to constrain the duration of the remnant phase we develop two new measures of "extent", which parameterise the observed backflow of lobe plasma. The "extent 1" attribute, E, considers what fraction of the total lobe length, parallel to the jet axis, is visible; e.g. how far back the lobe visibly sweeps towards the core. Lobes with emission localised near the hotspot will measure $E \to 0$, which is expected if a majority of the lobe plasma energy is stored in the most freshly injected electrons. Conversely, $E \to 1$ implies the observed radio emission sweeps all the way to (and beyond) the core, which is expected if a majority of the lobe plasma energy is stored in the older synchrotron-emitting electrons. The "extent 2" attribute, $\bar{E}$, considers how bright the lobes are at the core, relative to their peak brightness. We expect this attribute to be particularly useful at disentangling sources with backflow observed all the way to the core, where the measurement of the "extent 1" attribute will likely just reflect its upper limit of $E = 1$.

3.4.3.2 Photometric attributes

A total radio luminosity, L_ν, offers a powerful constraint on radio source energetics. For an observed radio source, the total radio luminosity can be derived from the total radio flux density by integrating over a region of the source bounded by a minimum brightness criterion; e.g. the region of the source above some signal to noise threshold. This means that, for a fixed sensitivity, the measured integrated flux density will depend on the surface brightness distribution of the lobes. The surface brightness maps produced by the RAiSE model allow us to include the effect of instrumental noise in the computation of the integrated flux density, thus accounting for this systematic bias. This is done by populating the simulated surface brightness maps with a Gaussian noise term, then the total observed radio luminosity is calculated considering only pixels brighter than 3σ (where σ represents the level of Gaussian noise). This process of adding the noise is repeated over 16 iterations to sample a mean integrated flux density, and to characterise an uncertainty, dL_ν, based on the standard deviation across each evaluation.

By measuring the integrated flux density over two observing frequencies, ν_0 and ν_1, a two-point spectral index can be calculated through:

$$\alpha \;=\; \log(L_{\nu,1}/L_{\nu,0})/\log(\nu_1/\nu_0), \tag{3.10}$$

which has an uncertainty corresponding to:

$$d\alpha \;=\; \left(1/\ln(\nu_0/\nu_1)\right)\sqrt{(dL_{\nu,0}/L_{\nu,0})^2 + (dL_{\nu,1}/L_{\nu,1})^2}. \tag{3.11}$$

With at least three observing frequencies a spectral curvature, SPC, can be calculated through: SPC $= \alpha_0 - \alpha_1$, which has an uncertainty corresponding to $d\mathrm{SPC} \;=\; \sqrt{(d\alpha_0)^2 + (d\alpha_1)^2}$.

Radio source attribute	Symbol	Measurement	Scale	FULL FIT	SPECTRAL	SPATIAL	IN BAND
radio luminosity (measured at 1.42 GHz)	$L_{1.4}$	$(6.48 \pm 0.25) \times 10^{24}\,\mathrm{W\,Hz^{-1}}$	$\log_{10}$	✓	✓	✓	✓
largest linear size (measured at 1.42 GHz)	$D_{1.4}$	326 kpc	$\log_{10}$	✓	✓	✓	✓
break frequency	ν_b	$1.26^{+0.06}_{-0.05}$ GHz	$\log_{10}$	✓	✓	✗	✗
observed axis ratio (1.42, 5.50 GHz)	$A_{1.4}$, $A_{5.5}$	2.4 ± 0.1, 2.7 ± 0.1	linear	✓	✓	✓	✓
extent 1 (1.42, 5.50 GHz)	$E_{1.4}$, $E_{5.5}$	0.9 ± 0.05, 0.8 ± 0.05	linear	✓	✗	✓	✗
extent 2 (1.42, 5.50 GHz)	$\bar{E}_{1.4}$, $\bar{E}_{5.5}$	0.76 ± 0.05, 0.65 ± 0.05	linear	✓	✗	✓	✗
spectral index (150−1420) MHz	α^{1420}_{150}	0.64 ± 0.03	linear	✗	✗	✗	✓
spectral curvature (150−1420−5500) MHz	$\mathrm{SPC}^{5500}_{150}$	0.53 ± 0.04	linear	✗	✗	✗	✓

Table 3.4: The measured radio source attributes of J2253-34, which are measured following the methods outlined in Sect. 3.4.3. In Sect. 3.4.4.2 these attributes are compared with corresponding RAiSE model outputs, using the scale shown in column 4, to constrain the energetics via a parameter inversion. To explore the constraints embedded in the lobe backflow, attributes are compared in four different combinations (columns 5-8). Tick (✓) and cross (✗) markers represent whether the attributes are included or excluded from the fitting, respectively.

3.4.3.3 Spectral modelling attributes

The injection index and remnant ratio attributes, derived from observations by modelling the spectra of remnant radio galaxy lobes (Sect. 3.3), represent intrinsic parameters of the RAiSE model. On the other hand, a break frequency can be predicted by the RAiSE model, which offers valuable constraints on the lobe equipartition factor. While it is possible to measure a RAiSE-predicted break frequency by modelling a simulated radio spectrum, the computational cost of simulating a radio source at many different frequencies makes this method inefficient. For any given set of model parameters, the RAiSE code uses the lobe pressure and equipartition factor to compute the lobe magnetic field strength. In turn, the field strength is used through Eqn. 3.3 to calculate the corresponding RAiSE-predicted break frequency, where the redshift and source age are those used as RAiSE model inputs. By modelling the spectra of RAiSE-simulated radio sources, Turner et al. (2018b) showed that the break frequency computed from the magnetic field strength is consistent with that derived by modelling their synthetic radio spectra (e.g. see their Fig. 3).

3.4.4 Modelling the energetics of J2253-34

We are now equipped with the tools needed to model the energetics of J2253-34. To begin with, we model the energetics closely following the dynamical model based method presented by Turner (2018). Here, the remnant ratio is already known (e.g. from Sect. 3.3.4.2), whilst the jet power, source age, and equipartition factor are principally constrained from a radio luminosity, physical size, and break frequency. We compare this established technique to our proposed method using the spatial attributes of the lobes (namely extent) to additionally constrain the remnant ratio. Finally, we provide our most precise constraints on the energetics by combining both the spectral and spatial attributes to best understand the physics of J2253-34.

Table 3.5: The intrinsic parameters of J2253-34, constrained via the four separate methods outlined in Tab. 3.4.
† parameterised by the CI model.

Param.	FULL FIT	SPECTRAL	SPATIAL	IN BAND
Q ($\times 10^{38}$ W)	$3.98^{+0.36}_{-0.40}$	$3.98^{+0.36}_{-0.40}$	$6.32^{+2.11}_{-1.63}$	1.0 - 7.9
τ (Myr)	$56.2^{+2.62}_{-1.28}$	$56.2^{+2.62}_{-1.28}$	$50.1^{+4.2}_{-3.8}$	31 - 158
B ($\times 10^{-10}$ T)	$1.98^{+0.16}_{-0.15}$	$1.98^{+0.16}_{-0.15}$	$1.41^{+0.30}_{-0.25}$	2 - 14
$R_{\rm rem}$	$^{\dagger}0.23^{+0.02}_{-0.02}$	$^{\dagger}0.23^{+0.02}_{-0.02}$	$0.26^{+0.04}_{-0.03}$	0.1 - 0.3

3.4.4.1 Observed properties of J2253-34

The radio galaxy J2253-34 was classified as a remnant by Quici et al. (2021) based on the absence of radio emission from the core, and further supported by the observed steepening in the integrated radio spectrum. In that work, the radio source was unambiguously associated with a $z = 0.2133$ host galaxy, for which a halo mass of $M_{\rm H} = 10^{13.5}\,{\rm M}_{\odot}$ was inferred based on the stellar mass of the host.

The radio source attributes of J2253-34 are measured following the methods outlined in Sect. 3.4.3, and are summarised in Tab. 3.4. All spatial attributes are measured from the 8″ images presented in Sect. 3.2, and we use the injection index, break frequency, and remnant ratio fitted in Sect. 3.3.4 by the Tribble spectral ageing models (e.g. row 2 & 4 of Tab. 3.2). In the following section, we implement these attributes to constrain the energetics of J2253-34 via a parameter inversion.

3.4.4.2 RAiSE-based parameter inversion of J2253-34

RAiSE can model the temporal evolution of radio lobes for any set of intrinsic radio source parameters, and subsequently generate mock images to make predictions for their respective radio source attributes. The intrinsic parameters of any radio source can therefore be estimated via a RAiSE-based parameter inversion; observed radio source attributes are compared to a corresponding set of mock

attributes generated over a multi-dimensional set of intrinsic parameters (e.g as is done by; Turner & Shabala, 2015; Turner et al., 2018b; Turner, 2018; Shabala et al., 2020).

For a fixed redshift of $z = 0.2133$ and halo mass of $M_{\rm H} = 10^{13.5}\,{\rm M}_{\odot}$, a grid of RAiSE models are created from the two-sided jet kinetic power, Q; the dynamical source age, τ; the equipartition factor, q (which parameterises the ratio of energy densities in the magnetic field and particles; Turner et al., 2018a); the initial supersonic phase value of the axis ratio, A_i; the remnant ratio, $R_{\rm rem}$; and the injection index, s. We use the results of Turner et al. (2018b), who fit the intrinsic properties of 3C radio sources, to ensure our model grid covers plausible parameter values. In this work, RAiSE models are evolved between 10 Myr to 1 Gyr, recording outputs at every $\Delta(\log\tau) = 0.05\,{\rm dex}$. We uniformly sample $\log Q$ between $[37, 40]$ with a precision of 0.05 dex; $\log q$ between $[-2.7, -0.7]$ with a precision of 0.05 dex; A_i between $[2, 8]$ with a precision of 0.25; $R_{\rm rem}$ between $[0, 5]$ with a precision of 0.01; and s between $[2.01, 2.61]$ with a precision of 0.1.

To explore the constraining power of the extent attributes, we perform the parameter inversion based on four separate combinations of the radio source attributes, summarised in cols. 5 - 8 of Tab. 3.4. The SPATIAL method tests a scenario where detailed spectral modelling (e.g. Sect. 3.3.4) can not be performed; here, each intrinsic radio source parameter is explicitly fit via the RAiSE-based parameter inversion, and the break frequency is omitted as a constraint. To independently verify results of this method, the fitted energetics are compared with that fitted by the FULL FIT and SPECTRAL methods; here, the injection index and, importantly the remnant ratio, are fixed to known values, and the strong constraint from the break frequency is included. The IN BAND method considers a limiting case where no constraints on the duration of the remnant phase are available.

To conduct the parameter inversion (for any of the above methods), simulated images are used to measure the same attributes as those measured for J2253-34,

ensuring that the images are degraded by the same set of observing constraints. Attributes are compared with model outputs through Eqn. 3.9, and we follow the same process described in Sect. 3.3.2 to select the best-fit model, and to estimate the uncertainty in each parameter.

The values fitted for the intrinsic parameters using each of these methods are presented in Tab. 3.5. Consistent with the results of Turner (2018), we find that the jet-power/age/equipartition-factor triplet, fitted by the SPECTRAL method, is tightly constrained by the observed radio-luminosity/linear-size/break-frequency. We inspect the marginal distributions of each fitted parameter to find approximately Gaussian-like PDFs centered about the peak probable value; i.e. the fitting appears stable and not degenerate. By including constraints from the extents, we find that the energetics constrained by the FULL FIT method do not change. This suggests that the break frequency is the dominant observable in this fitting process.

Using the source age constrained by FULL FIT method, together with the remnant ratio fit previously by the TCI model, the duration of the active and remnant phases in J2253-34 are calculated as $t_{\rm on} = 43.3 \pm 4.3\,{\rm Myr}$ and $t_{\rm rem} = 12.9 \pm 1.2\,{\rm Myr}$, respectively. Importantly, through this method we demonstrate the ability to accurately measure the duration of the active phase, and to place a weak upper bound on the AGN jet duty cycle ($\delta \lesssim 1 - R_{\rm rem} = 0.77$).

Remarkably, we find that the energetics modelled by the SPATIAL method are consistent with those derived by the previous methods. Uncertainties in each parameter are comparatively greater, as expected considering the constraints are relaxed and an additional free parameter is solved for, however inspecting the marginal distributions reveals similar Gaussian-like PDFs. What is particularly of interest is that the dynamically-modelled remnant ratio, $R_{\rm rem} = 0.26 \pm 0.02$, is consistent with that parameterised by the TCI model within a level of 1σ. Together with a source age of $\tau = 50.1^{+4.2}_{-3.8}\,{\rm Myr}$, the SPATIAL method therefore estimates the duration of the active and remnant phases as $t_{\rm on} = 37.2 \pm 4.3\,{\rm Myr}$

and $t_{\rm rem} = 13.1 \pm 1.5$ Myr, respectively. These timescales are consistent with those fitted by the FULL FIT method, suggesting that the surface brightness distribution of the lobe backflow can in fact be used to constrain the dynamics of the remnant phase.

Finally, we find that the stability of the model fitting breaks down severely with the IN BAND method (when only a few radio photometric points are available). Inspecting the marginal distributions reveals a large degeneracy in the fitted parameter space, where multiple unique values of equal likelihood are found over a wide range of parameter values. We quote these ranges in Tab. 3.5, by considering their minimum/maximum values. This tells us that the spectral index and curvature, alone, do not offer the constraining power needed to tightly constrain the energetics of J2253-34.

3.5 Mock radio source populations

The ability to measure the off-time in remnant radio galaxies, using attributes measured exclusively below ~ 1.4 GHz, is particularly attractive considering the parameter space unlocked by wide-area sky surveys such as the LOFAR Two-metre Sky Survey (LoTSS; Shimwell et al., 2019, 2022), the MeerKAT International GHz Tiered Extragalactic Exploration (MIGHTEE; Jarvis et al., 2016) survey, the APERture Tile In Focus (Apertif Oosterloo et al., 2010) survey, and EMU. However, the generalisability of this new method is currently unclear, as we do not know whether the constraining power of the spatial attributes, measured using telescope-degraded images, deteriorates for certain intrinsic source parameters; e.g. lower jet powers, older sources, or denser environments. In Sect. 3.5.1, we use our method to perform a parameter inversion of mock radio source populations simulated at 150 MHz and 1.4 GHz. In Sect. 3.5.2, we compare the input and recovered parameters to examine the internal consistency of our method within the RAiSE model; e.g. does the method recover the input parameters. In Sect. 3.5.3 we then examine whether the remnant ratio fitted by

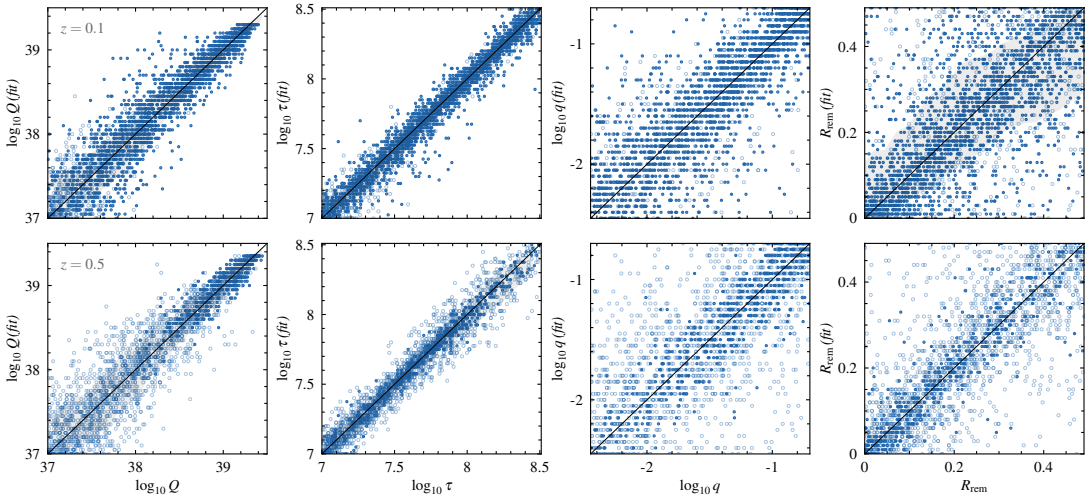

Figure 3.7: Results of the parameter inversion of the $z = 0.1$ (upper row) and $z = 0.5$ (lower row) mock catalogues are shown. Each plot demonstrates the fitted (vertical axis) versus mock (horisontal axis) parameter for the jet power (first column), source age (second column), equipartition factor (third column), and remnant ratio (fourth column). Each marker represents a unique mock radio source, where unfilled markers represent sources fainter than $S_{150} = 100\,\mathrm{mJy}$ or smaller than $\theta = 60''$. A solid black line is shown to represent a 1:1 relation between the fitted and mock quantities.

this method can be used to confidently select between active and remnant radio lobes.

3.5.1 Constructing mock radio source catalogues

For this analysis, mock radio source populations are simulated using the RAiSE model. We allow the following set of intrinsic parameters to vary over a wide range of values, typically associated with FR-IIs:

- *jet power:* $Q \in [10^{37},\ 10^{40}]$ W, to represent those typically associated with FR-II jets (Turner & Shabala, 2015)
- *source age:* $\tau \in [10^{7},\ 10^{8.5}]$ yr. Younger sources will likely fall below extended source criteria (see Fig. 3.7), and a genuine dearth of old ($>$ 400 Myr) radio sources has been reported by Shabala et al. (2020) in LOFAR data.

- *remnant ratio:* $R_{\rm rem} \in [0,\ 0.5]$, consistent with the observational bias towards selecting recently switched-off remnants (Mahatma et al., 2018; Turner, 2018; Jurlin et al., 2020; Shabala et al., 2020; Quici et al., 2021).

- *equipartition factor:* $q \in [10^{-2.7},\ 10^{-0.7}]$, which is approximately Gaussian-distributed about $\log q \approx -1.7$ (e.g. see; Turner et al., 2018b).

- *initial axis ratio:* $\mathrm{A}_i \in [2.5,\ 4.5]$, reflecting a subset of typical values for the 3C sample (e.g. see; Turner & Shabala, 2015).

- *injection index:* $s \in [2.01,\ 2.61]$, where the lower limit comes from predictions of first-order Fermi acceleration (Kardashev, 1962; Pacholczyk, 1970), and the upper limit from $\alpha_{\rm inj}$ not being too steep. We note that injection indices steeper than the selected upper limit have been demonstrated through resolved spectral age studies (e.g. Harwood et al., 2013). It is unlikely however for the outcomes of this analysis to differ for this unexplored region of the parameter space, considering that measurements of a low-frequency spectral index should help to constrain the injection index.

Two separate mock catalogues are created at redshift $z = 0.1, 0.5$ (hereafter the $z = 0.1$ and $z = 0.5$ catalogues). For each catalogue, 5000 mock radio sources are forward modelled using pseudo-random values for the intrinsic parameters. We use a representative $M_{\rm H} = 10^{13}\,\mathrm{M}_\odot$ halo mass (e.g. a typical environment of an FR-II, Turner & Shabala 2015), and simulate a random gas-density profile based on a prior distribution of environment profiles (as per discussion in Sect. 3.4.1.1).

A corresponding grid of RAiSE models is simulated with known values for each intrinsic parameter, so that a parameter inversion can be performed on each mock radio source catalogue. Our model grids are bound by the parameter space limits of the mock sample, however with uniform spacings as follows: $\Delta(\log Q) = 0.05\,\mathrm{dex}$; $\Delta(\log \tau) = 0.025\,\mathrm{dex}$; $\Delta R_{\rm rem} = 0.01$; $\Delta(\log q) = 0.05\,\mathrm{dex}$; $\Delta A_i = 0.25$;

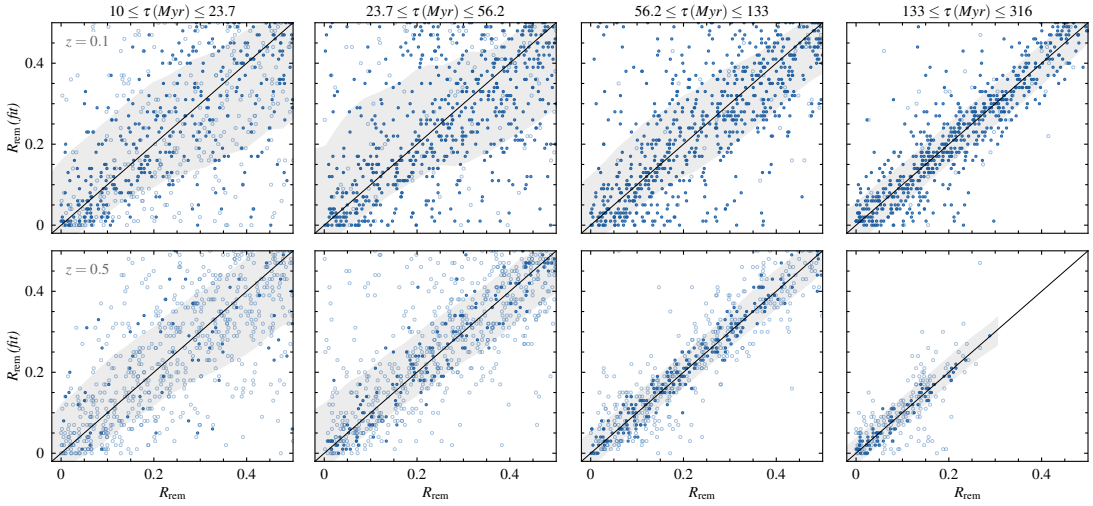

Figure 3.8: The fitted (vertical axes) versus input (horisontal axes) remnant ratio of the $z = 0.1$ (upper panel) and $z = 0.5$ (lower panel) mock catalogues. Each column represents a log-uniform source age bin. Gray regions represent a 1σ uncertainty in the scatter, corresponding to the unflagged sources (filled markers). A tightening in the scatter is seen as the source age increases, likely reflecting the greater magnitude of radiative losses discussed in Sect. 3.5.2. The dearth of sources with higher values of $R_{\rm rem}$ in the $z = 0.5$ sample arises due to the complete depletion of electrons capable of producing emission at these frequencies (e.g. see Fig. 4 of Turner 2018).

Table 3.6: The set of observing conditions used to sample mock radio source populations simulated in Sect. 3.5.1.

Survey type	Freq. (MHz)	Sensitivity (μJy beam^{-1})	Resolution ($''$)
LOFAR-like *(wide-band)*	150	70	6
LOFAR-like *(sub-band)*	130	100	6
	170		
MeerKAT-like	1400	6	10

and $\Delta s = 0.1$. Sources are simulated for the same halo mass, however here we take the mean of the environment profiles.

Bayesian parameter estimation is conducted as follows. Images are synthesised at 150 MHz and 1.4 GHz, and degraded by a set of survey limitations shown in Tab. 3.6. This is done both for mock radio sources and those stored in the grid as model outputs. Telescope-degraded images are then used to measure the radio source attributes shown in Tab. 3.7. Following the parameter inversion described in Sect. 3.4.4.2, the attributes measured for mock radio sources are compared with those used as model outputs, in order to constrain their intrinsic parameters. Here, we simultaneously fit for the pseudo-randomly sampled parameters, and treat the redshift and halo mass as known.

Sources are flagged if their angular size falls below $\theta = 60''$, or if their 150 MHz integrated flux densities fall below $S_{150} = 100$ mJy. This decision is motivated by the typical current observational constraints used to construct complete radio galaxy samples (e.g; Brienza et al., 2017; Godfrey et al., 2017; Mahatma et al., 2018; Jurlin et al., 2020; Quici et al., 2021). The results of this parameter inversion are explored in the following sections.

Finally, we note that the Karl G. Jansky Very Large Array Sky Survey (VLASS; Lacy et al., 2020) represents a high-frequency (2−4 GHz), high-resolution ($2.''5$), all-sky (decl.$> -40°$) radio survey, which is expected to achieve $\sigma = 70\mu$Jy beam^{-1} sensitivity. Despite marginally increasing the frequency leverage over 1.4 GHz, we do not consider a VLASS-like observation due to the compar-

Table 3.7: The set of radio source attributes used to constrain the energetics of the mock radio source populations described in Sect. 3.5.1.

Attribute	Scale
150 MHz radio luminosity	$\log_{10}$
largest linear size	$\log_{10}$
observed axis ratio (150, 1400) MHz	linear
extent 1 (150, 1400) MHz	linear
extent 2 (150, 1400) MHz	linear
$(150 - 1420)$ MHz spectral index	linear
$(150 - 1420)$ MHz spectral curvature	linear

atively poorer surface brightness sensitivity to extended radio emission; without a handle over the fainter (older) lobe electrons, we expect the observed backflow to be much less constraining on the remnant off-time.

3.5.2 Fitted energetics

We expect that the parameter inversion may be less effective for some sets of parameters due to the non-linear application of radiative losses across our parameter space. In particular, the two extent attributes, and to a lesser degree the lobe width attribute, rely on the surface brightness distribution of ageing synchrotron-emitting lobe plasma. The ageing is quantified through the time-derivative of the Lorentz factor of a given packet of synchrotron-emitting electrons, γ, as follows (Kaiser et al., 1997):

$$\frac{d\gamma}{dt} = -\frac{a_1\gamma}{3t} - \frac{4\sigma_{\mathrm{T}}\gamma^2\left(u_B + u_C\right)}{3m_e c}, \tag{3.12}$$

where the first and second terms encode adiabatic and radiative losses respectively. Here, the derivative is taken with respect to the age of the injected plasma, t, where a_1 gives the exponent with which the volume of the lobe grows adiabatically, σ_{T} is the cross section for Thompson scattering, and u_B & u_C are the energy densities of the magnetic field and CMB respectively.

Comparisons between their mock and fitted intrinsic parameters are presented

in Fig. 3.7 for the two mock catalogues described in Sect. 3.5.1. Firstly, although with varying degrees of confidence (as indicated by the scatter), we find that the fit of each parameter broadly closely matches the 1:1 relation with its mock equivalent. The jet power and source age are fit with greater confidence than the equipartition factor and remnant ratio, demonstrating the former two property's dependence on observable parameters; e.g. the jet power and source age are tightly constrained by the radio luminosity and linear size respectively, at least for active lobed sources (Turner & Shabala, 2015). However, it is encouraging to find that the equipartition factor and remnant ratio are generally recovered as well.

The jet power is less confidently predicted using the RAiSE-based parameter inversion for lower-powered sources, as shown in Fig. 3.7. This is unlikely a selection effect, in which the stochastic perturbations due to instrumental noise are more significant for fainter sources associated with lower-powered jets, since the same sizeable broadening is observed in the $z = 0.1$ (brighter) catalogue. Instead, this is likely due to the strong correlation between jet power and the lobe magnetic field strength, and thus energy density u_B (e.g. see Eqn. A5 of Turner et al. 2018a). The rate of energy loss from the synchrotron-emitting electrons is therefore expected to be much greater in higher jet power sources (Eqn. 3.12), thus leading to a greater rate of change in the extent attributes as the remnant ages. Qualitatively this is consistent with the results of Turner (2018), who find a rapid dimming in higher-powered remnants in stark contrast to lower-powered sources whose flux density is maintained over a greater duration (see their Fig. 4).

We also find that the energetics of the $z = 0.5$ sample are fit with greater confidence (see also discussion in next paragraph). Again referring to Eqn. 3.12, this result is unsurprising; the energy density of the CMB scales with redshift as $u_c \propto z^4$, meaning the magnitude of the energy losses sustained throughout the remnant phase will be greater.

We investigate if the sizeable scatter in the remnant ratio is partially due

to one of the other model parameters. In particular, we expect the radiative losses in the remnant phase will be related to the off-time, rather fractional time spent in the remnant phase (e.g. integrating Eqn. 3.12 for constant volume; i.e. $a_1 = 0$). As a result, we expect the synchrotron losses to reduce the extent attributes in approximate proportion to the time spent in the off-phase. The ability of the RAiSE-based parameter inversion to constrain the remnant ratio is therefore expected to correspondingly be much less effective in young sources (i.e. the off-time is smaller for a given remnant fraction). To consider this potential sensitivity in our method, we group the mock catalogues into four source age bins uniformly-spaced in $\log \tau$. The fitted remnant ratio, in each source age bin, compared to the mock remnant ratio is presented in Fig. 3.8. We find that the scatter in the predicted remnant ratio reduces considerably for the older source age bins, as expected from the above discussion.

Overall, the results presented here show promise for modelling the energetics of remnant AGNs, and notably, using spatial attributes of their lobes to constrain the remnant phase. The predictive power of this technique improves when the magnitude of the energy losses sustained during the remnant phase are greater; this is unsurprising, as the technique relies on the reduction in extent to constrain the ageing during this phase. The method makes reliable estimates of the remnant ratio associated with older sources, in contrast to young sources for which the fitted remnant ratio is less trustworthy.

3.5.3 Identifying remnant radio galaxies

As we have demonstrated the ability of our method to estimate the remnant ratio with reasonable accuracy, this raises the question of whether we can use the same method to select remnant radio galaxies. Part of the difficulty here is ascertaining a definition for active and remnant sources based on the fitted remnant ratio parameter; logically, active sources would only correspond to $R_{\rm rem} = 0$ (i.e. zero off-time), however in practice it would be impossible to distinguish a very recently

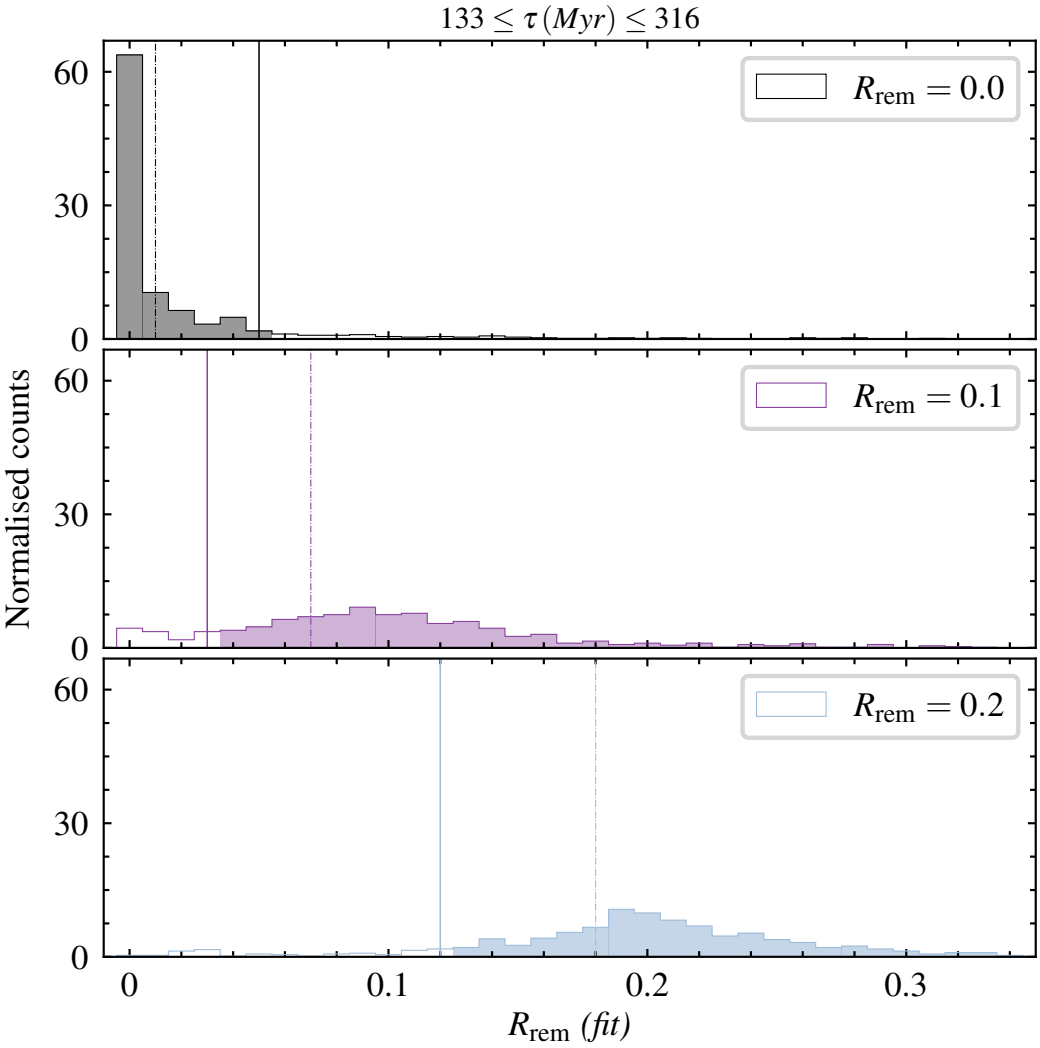

Figure 3.9: Normalised count representing the distribution of fitted remnant ratios of mock samples with $R_{\rm rem} = 0$ (black), $R_{\rm rem} = 0.1$ (purple), and $R_{\rm rem} = 0.2$ (blue). We set the bin size in each distribution to $\Delta R_{\rm rem} = 0.01$, to reflect spacings in the grid. Each sample is simulated at redshift $z = 0.1$, and only the oldest source-age bin $(133 \leq \tau \leq 316)$ Myr is shown. Solid and dotted vertical lines are shown to represent the $68^{\rm th}$ and $95^{\rm th}$ percentiles in each sample, respectively; these represent upper bounds for the active population, and lower bounds for the remnant samples.

Mock sample		Active		Remnant ($R_{\rm rem} = 0.1$)		Remnant ($R_{\rm rem} = 0.2$)	
Redshift	*Source age (Myr)*	($68^{\rm th}$ *perc.*)	($95^{\rm th}$ *perc.*)	($68^{\rm th}$ *perc.*)	($95^{\rm th}$ *perc.*)	($68^{\rm th}$ *perc.*)	($95^{\rm th}$ *perc.*)
$z = 0.1$	$10.0 \leq \tau < 23.7$	≤ 0.00	< 0.05	> 0.07	> 0.02	> 0.15	> 0.08
	$23.7 \leq \tau < 56.2$	≤ 0.00	< 0.12	> 0.07	> 0.01	> 0.15	> 0.06
	$56.2 \leq \tau < 133.0$	< 0.01	< 0.10	> 0.07	> 0.01	> 0.16	> 0.06
	$133.0 \leq \tau \leq 316.0$	< 0.01	< 0.05	> 0.07	> 0.03	> 0.18	> 0.12
$z = 0.5$	$10.0 \leq \tau < 23.7$	≤ 0.00	< 0.05	> 0.06	> 0.01	> 0.14	> 0.03
	$23.7 \leq \tau < 56.0$	≤ 0.00	< 0.03	> 0.08	> 0.05	> 0.17	> 0.13
	$56.2 \leq \tau < 133.0$	< 0.01	< 0.03	> 0.09	> 0.06	> 0.19	> 0.17
	$133.0 \leq \tau \leq 316.0$	≤ 0.00	< 0.02	> 0.09	> 0.08	> 0.19	> 0.18

Table 3.8: The recovery rate of active and remnant radio sources simulated in Sect. 3.5.3. Three mock radio source catalogues ($N = 5000$) are created at $z = 0.1$ and $z = 0.5$, with remnant ratios fixed to $R_{\rm rem} = 0, 0.1, 0.2$, respectively. For each redshift (column 1) and source age bin (column 2), the $68^{\rm th}$ and $95^{\rm th}$ percentiles of the fitted remnant ratio distribution are reported (columns $3 - 8$).

switched-off source from an active source.

By creating mock radio source catalogues with known remnant ratios, we can use the distribution in the fitted remnant ratio to quantify the probability that: 1) an active radio source is fit with a non-zero remnant ratio; and 2) an "unambiguous" (i.e. $R_{\rm rem} \geq 0.1$) remnant radio source is fit with $R_{\rm rem} = 0$. To do this, we follow the method outlined in Sect. 3.5.1 to create three mock catalogues per redshift. Each catalogue contains 5000 sources, and the remnant ratios are fixed at $R_{\rm rem} = 0, 0.1, 0.2$, respectively. For each redshift and source age bin, we characterise the $68^{\rm th}$ and $95^{\rm th}$ percentiles of the fitted remnant ratio distribution; these serve as upper bounds for the $R_{\rm rem} = 0$ catalogue, and lower bounds for the $R_{\rm rem} \geq 0.1$ catalogues. An example of this is demonstrated in Fig. 3.9 for the highest source age bin at $z = 0.1$, and we summarise our results in Tab. 3.8 for all the redshift and source age bins.

We find that the recovery rate of active radio galaxies is high; in 95% of the cases, the fitted remnant ratio is $R_{\rm rem} \leq 0.1$ (the actual value being 0%), which is true across all redshift and source age bins (column 4 of Tab. 3.8). We conclude similar results for the $R_{\rm rem} = 0.1$ remnant radio galaxies; in 95% of the cases, the fitted remnant ratio is $R_{\rm rem} > 0.01$ (column 6 of Tab. 3.8), meaning that active sources are not contaminated by $R_{\rm rem} = 0.1$ remnants, at this level. For example, if examining a sub-catalogue of $z = 0.1$ radio source with fitted ages of 133 to 316 Myrs, we can confidently (at 2σ level) say that those with remnant ratio $R_{\rm rem} < 0.03$ will not have significant contamination from "unambiguous"-remnants and can therefore be classified as active sources. Conversely, those objects with fitted remnant ratios $R_{\rm rem} > 0.05$ will not have significant contamination from active sources and can be classified as remnants. We examine the same statistics for the $R_{\rm rem} = 0.2$ sample, and reassuringly find no contamination of active sources from this population.

3.6 Conclusions

This paper investigates a new technique to constrain the energetics of remnant radio galaxies based on the backflow of their lobe plasma. We employ observations of the remnant radio galaxy J2253-34 together with mock radio source populations, in order to verify the method and examine its applications and limitations. The approach taken to explore this technique, and the insights gathered, are summarised below.

First, we use established spectral ageing techniques to derive a precise measurement of the off-time in J2253-34; this is needed to independently validate the results of our new method. To do this, we collect new radio observations using the MeerKAT, ATCA and uGMRT telescopes (Sect. 3.2). The injection index is tightly constrained by jointly fitting the JP spectra arising from narrow regions across the lobes (Sect. 3.3.4.1). We then make precise measurements of the break frequency and remnant ratio by fitting the TCI model to the integrated radio lobe spectrum (Sect. 3.3.4.2); here, the previously-fitted injection index is used as a model input. Our key results are summarised as follows:

- We develop a PYTHON implementation of synchrotron spectral ageing models, as well as algorithms to fit these models to observed radio data. We release this code, the SYNCHROFIT library, to the broader astrophysics community for its relevance to modelling the synchrotron spectra from active galaxies and supernovae remnants (Sect. 3.3.2).

- To place the tightest constraints on the break frequency and remnant ratio, the injection index should be independently fit and used as an input on the CI model; this can be done by considering individual JP spectra across the lobes (cf. Shulevski et al., 2017).

- The shape of the Tribble spectral ageing models is (at most) weakly dependent on the average magnetic field of the underlying Maxwell-Boltzmann distribution (Sect. 3.3.3). These models, which likely provide a more re-

alistic treatment of a turbulent magnetic field, can therefore be fit to observed radio data without needing prior knowledge of the lobe magnetic field strength.

- The remnant ratio in J2253-34 is tightly constrained as $R_{\rm rem} = 0.23 \pm 0.02$.

Our new method utilises the lobe surface brightness distribution to parameterise the backflow of plasma, and exploits the RAiSE dynamics and emissivity model. The high-resolution hydrodynamical simulation underpinning the RAiSE code enables the synthesis of mock surface-brightness maps, which are used to measure predicted radio source attributes. These are compared with observations so that the intrinsic source properties can be obtained via a parameter inversion. We apply this method to constrain the energetics of J2253-34, and obtain the following results:

- We propose two new attributes to quantify the spectral ageing of lobe plasma as it flows away from the hotspot towards the core. The "extent 1" attribute considers how far back the lobe visibly sweeps towards the core, and the "extent 2" attribute considers the surface brightness of the lobe at the core, relative to the peak surface brightness.

- We implement a RAiSE-based parameter inversion using these two new attributes, in addition to the lobe radio luminosity, size, and axis ratio, to constrain a remnant ratio of $R_{\rm rem} = 0.26 \pm 0.02$ for J2253-34. Importantly, this is consistent at the 1σ level with that constrained by our spectral fitting, verifying our approach to constrain the dynamics of the remnant phase based on the surface brightness distribution of the lobe backflow.

- By comparing different sets of attributes, we find that the break frequency is the dominates the "extent" attributes fitting of the energetics; particularly the equipartition factor and remnant ratio. By excluding the break frequency and extent attributes from the fitting, we find that the spec-

tral index and curvature, alone, do not offer enough constraining power to uniquely fit the source energetics.

- For J2253-34, we accurately measure a two-sided jet kinetic power of $Q = 3.98^{+0.36}_{-0.40} \times 10^{38}\,\mathrm{W}$, a lobe magnetic field strength of $B = 0.20 \pm 0.02\,\mathrm{nT}$, and importantly an active and remnant timescale of $t_{\mathrm{on}} = 37.2 \pm 4.3\,\mathrm{Myr}$ and $t_{\mathrm{rem}} = 13.1 \pm 1.5\,\mathrm{Myr}$.

We then used synthetic radio lobes, simulated for a typical 150 MHz LOFAR-like and 1.4 GHz MeerKAT-like observation, to further examine the limitations of our proposed method with respect to intrinsic radio source parameters. Our key results are summarised as follows:

- The jet power, source age, equipartition factor, and remnant ratio are consistently recovered, noting that the former two are constrained with high precision. This result builds on the work conducted by Turner et al. (2018b) for active sources only, who similarly find that the jet power, source age, and equipartition factor are constrained from the source size, radio luminosity, and break frequency.

- Our results show that that the parameters are more accurately fit for radio sources with: higher redshifts, due to increased strength of IC losses; higher-powered jets, due to increase in magnetic field strength; and for a greater duration of the remnant phase. We therefore find that the constraining power of our method increases when the magnitude of the energy losses, sustained during the remnant phase, are greater.

- Remnant ratios fitted by this method can be trusted if the measured source age is large, and conversely, is less accurate for younger sources. To interpret the on/off-times fit by this method, one should first consider the age of the source to determine if the fitted remnant ratio is estimated reliably.

- We find that our method is capable of selecting active and remnant radio galaxy candidates. At low redshift ($z \sim 0.1$), we find that sufficiently aged sources ($\tau > 50\,\mathrm{Myr}$) fitted with $R_{\mathrm{rem}} \leq 0.1$ are active radio galaxies within a confidence of 95%; this extends to sources as young as $\tau \sim 10\,\mathrm{Myr}$ at higher redshifts ($z \gtrsim 0.5$). Similarly, we find that sources fit with $R_{\mathrm{rem}} \geq 0.1$ are true remnant radio galaxies within a confidence of 95%; these classifications are more robust at higher redshift.

We emphasise that while our mock simulations have examined a LOFAR-MeerKAT scenario, we expect for the outcomes to remain applicable to the EMU all-sky survey, with a few minor subtleties. In the 887 MHz band, EMU is expected to provide comparable yet slightly shallower sensitivity ($\sigma \approx 30\,\mu\mathrm{Jy/beam}$) and coarser spatial resolution ($\theta \approx 10''$) than a MeerKAT observation (see e.g. Gürkan et al., 2022). As discussed in this work, high surface-brightness sensitivity is needed to minimise the observational bias towards young (bright) plasma regions. Similarly, high spatial resolution ensures that the parameterised spatial attributes are strongly mapped to the structure of lobes, allowing for smaller differences to be detected between morphologically-similar sources. While it is plausible for EMU to therefore offer less constraining power than a MeerKAT-observation, the ability to map survey noise and spatial resolution onto synthetic sources means that the survey limitations can be directly modelled and captured in the fitting uncertainties. It is also worth mentioning that if survey sensitivity and resolution are limiting factors, implementing larger radio luminosity and physical size cuts can conveniently reduce the effects of the survey limitations. However this would come at the cost of reducing the range of observed jet powers and lifetimes, and would limit the sample to lower redshifts.

The outcomes of this work show promising applications to studying the energetic impact of radio-loud AGNs on their environments, in particular, through studying remnant radio galaxies. However, although this method is clearly successful for remnants with $R_{\mathrm{rem}} \lesssim 0.23$, for much older remnants the model as-

sumptions in the version of RAiSE used in this work may no longer capture all the necessary physics, for example buoyancy and Rayleigh-Taylor instability; capturing these physical processes will be an important step necessary for modelling aged remnants, e.g. Blob 1 with $R_{\rm rem} \sim 0.8$. Other complexities, such as dynamic or non cluster-centered environments, can lead to asymmetries in the radio lobe morphologies; e.g. in jet lengths, as well as lobe luminosities. Hydrodynamical simulations of the jet and lobe evolution in such environments already exist (see; Yates-Jones et al., 2021), which can incorporate the calculation of the resolved adiabatic and radiative loss processes following Yates-Jones et al. (2022). While the direct outputs of such hydrodynamical simulations can be implemented in the grid-based approach of this work, their synthesis is computationally expensive and can realistically only coarsely sample any given parameter space. The RAiSE framework can naturally consider asymmetries by allowing its governing differential equations for the source expansion to be applied on arbitrarily small solid angle elements; in this manner, future work can utilise modified versions of this code that include relevant physical processes to efficiently simulate millions of mock sources densely throughout the intrinsic parameter space.

Acknowledgements

BQ acknowledges a Doctoral Scholarship and an Australian Government Research Training Programme scholarship administered through Curtin University of Western Australia. NHW is supported by an Australian Research Council Future Fellowship (project number FT190100231) funded by the Australian Government. We acknowledge the Pawsey Supercomputing Centre which is supported by the Western Australian and Australian Governments. The Australia Telescope Compact Array is part of the Australia Telescope National Facility which is funded by the Australian Government for operation as a National Facility managed by CSIRO. We thank the staff of the GMRT that made these observations possible. GMRT is run by the National Centre for Radio Astrophysics of the Tata Insti-

tute of Fundamental Research. We additionally would like to thank Aleksandar Shulevski for his helpful suggestions that have improved our manuscript.

Chapter 4

Constraining evolutionary jet models with remnant radio galaxies

In the following chapter, I present my third major contribution of work undertaken during this thesis. The contents of this chapter are in preparation for submission as "The jet power and lifetime function of local ($0.02 \leq z \leq 0.2$*) remnant radio galaxies" to the Monthly Notices of the Royal Astronomical Society. The draft manuscript is adapted for consistency with the rest of the Thesis.*

Abstract

The energy coupling efficiency of active galactic nucleus (AGN) outbursts is known to differ significantly with factors including the jet kinetic power, duration of the outburst, and properties of the host galaxy cluster. As such, constraints on their jet power and lifetime functions are crucial to quantify the role of kinetic-mode AGN feedback on the evolution of galaxies since $z \sim 1$. In this work, we address this issue by measuring the energetics of a sample of 79 low-redshift ($0.02 \leq z \leq 0.2$) remnant radio galaxies compiled from all-sky radio surveys. Remnant

lobes directly encode the complete duration of the jet phase, making them an excellent laboratory for investigating AGN lifetimes. The jet kinetic power and outburst duration of each remnant are determined using the RAiSE dynamical model based on the surface brightness distribution observed in multi-frequency radio images. We compare the energetics constrained for this sample to those predicted for mock radio source populations – with various intrinsic functions for jet power and lifetime distributions – to correct for survey selection biases imposed on our sample. The intrinsic jet power and lifetime functions that yield a selection-biased mock population most similar to our observed sample are found using Bayesian inference. Our analysis places robust constraints on assumed power-law indices for the intrinsic jet power and lifetime functions: $p(Q) \propto Q^{-1.5\pm0.1}$ and $p(t_{\rm on}) \propto t_{\rm on}^{-1.0\pm0.1}$ respectively. We discuss the implication of these findings for feedback regulated accretion and the self-regulating nature of jet activity. The methodology proposed in this work can be extended to active radio galaxies in future studies.

4.1 Introduction

In the concordance view of galaxy formation and evolution, relativistic jets associated with radio-loud active galactic nuclei (AGNs) play a critical role in regulating the gas residing in the interstellar and circumgalactic environments. On small (galactic) scales, the jets are capable of dispelling large amounts of molecular gas (e.g. Nesvadba et al., 2008; Dasyra & Combes, 2011; Morganti et al., 2013; Emonts et al., 2014; Morganti et al., 2015; Kakkad et al., 2018; Morganti et al., 2021), and can seemingly promote (Nesvadba et al., 2008; Dasyra & Combes, 2012; Morganti et al., 2013; Mukherjee et al., 2021) or suppress (Croft et al., 2006; Tortora et al., 2009; Crockett et al., 2012; Dugan et al., 2017) star formation. On larger scales, the buoyant rise of jet-inflated bubbles excavate cavities in their hot intracluster environments (e.g. Churazov et al., 2002), which act to suppress the cooling flows at the centre of cool-core clusters (Fabian et al., 2003; Forman et al.,

2005; McNamara & Nulsen, 2007; Mittal et al., 2009; Alexander & Hickox, 2012; Fabian, 2012). Recent findings also show that 'maintenance-mode feedback', the self-regulating mechanism by which the jets maintain a heating/cooling balance in their hot atmospheres, must be invoked in galaxy formation models to explain, in particular, the suppression of star formation in the most massive galaxies (e.g. Bower et al., 2006; Croton et al., 2006; Shabala & Alexander, 2009; Raouf et al., 2017).

Despite the various successes of modern galaxy formation models (e.g. Dubois et al., 2014; Vogelsberger et al., 2014; Schaye et al., 2015), constraints from observations are still required to quantify the global energetic impact of AGNs, and to elucidate the connection between the environment and fueling of the supermassive black hole (SMBH). One valuable insight lies in the observed mass-dependence of the radio loud fraction, $f_{\rm RL}$, which rises with the stellar mass of the host galaxy (Best et al., 2005) and most likely achieves ubiquity ($\approx 100\%$) amongst the most massive galaxies (Sabater et al., 2019); precisely the objects in which feedback is required the most. Treating $f_{\rm RL}$ as a proxy for the AGN jet duty cycle, the result implies a clear connection between the fueling of the SMBH and the surrounding environment. Yet, questions still remain regarding the nature of this relationship. Principally, if it is AGN feedback that links the quenching of star formation to the prevalence of the jets, then the energies involved must be quantified to understand how this process occurs. Additionally, the $f_{\rm RL}$ cannot separate between objects with rapid duty-cycles versus those with a large ratio of active to inactive jet phases. This distinction is important considering that such objects will have vastly different duty cycles, and will thus differ in their feedback efficiencies (Yates et al., 2018).

Valuable constraints towards AGN feedback mechanisms can be derived by examining the distribution of AGN jet kinetic powers and lifetimes. For a single AGN outburst, its total energy output can be found by integrating the instantaneous jet kinetic power (the jet power herein) over the the duration of the outburst

(the jet lifetime herein). Considering that the jets are ultimately produced by accretion onto the SMBH (Lynden-Bell, 1969), we can expect each of these jet properties to be set by the conditions of and around the black hole; namely mass accretion rate and spin for jet power (Daly, 2009, 2016, 2021), and the underlying accretion mechanism for the duty cycle (Novak et al., 2011; Gabor & Bournaud, 2013). It follows that the distribution in jet powers and lifetimes not only constrains the energies released by AGNs, but also begins to probe the underlying mechanisms responsible for the production and fueling of the jets. Considering also the mass-dependence of the AGN jet duty cycle, reconciling the global properties of the jets together with those of their environment are an important step towards linking AGN fueling and feedback.

Throughout the decades, a variety of techniques have been presented to measure the jet powers and lifetimes of radio-loud AGNs. The diffuse lobes inflated by the jets contain synchrotron-emitting plasma that forms an approximately power-law spectrum at radio frequencies. The energy-dependent synchrotron loss rate allows for a derivation of the plasma age based on the observed spectral steepening in the radio spectrum (e.g. Parma et al., 2007; Murgia et al., 2011; Brienza et al., 2016; Duchesne et al., 2020), and is referred to in the literature as the 'spectral ageing' method (e.g. Myers & Spangler, 1985). A shortcoming of this method is the requirement of the lobe magnetic field strength, which in turn requires knowledge of the equipartition factor and the pressure in the ambient environment. By making several assumptions regarding the lobes, e.g. their composition and minimum energy, inferences of the jet power can be made based on their observed radio luminosity (Willott et al., 1999). Comparisons of these estimates against more sophisticated methods shows a general agreement (e.g. see Turner & Shabala, 2015; Ineson et al., 2017), however with an appreciable level of scatter in part due to the departure from the underlying assumptions, but also due to the confounding impact of the source age and environment (Godfrey & Shabala, 2013; Hardcastle & Krause, 2013). Cavities in the hot X-ray emitting

intracluster gas allow for robust estimates to be made of the pdV work done by the expanding lobes; with an assumption about the source age (discussed above), inferences of the jet power can then be made. However, this technique is generally limited to low redshifts ($z \lesssim 0.5$) as the trade-off between resolution and surface brightness sensitivity in X-ray observations prevents measurements of the shape of the gas density profile beyond the cluster core (e.g. Turner & Shabala, 2020).

Dynamical model-based methods have increasingly proved an attractive alternative for measuring the intrinsic properties of AGN jets. The current generation of analytical models (e.g.Turner et al. 2018a; Hardcastle 2018; Turner et al. 2023; see Turner & Shabala 2023 for a review) match the evolutionary histories predicted by modern relativistic hydrodynamic simulations (e.g. Hardcastle & Krause, 2013, 2014; English et al., 2016; Yates et al., 2018; English et al., 2019; Yates-Jones et al., 2021) whilst including a full treatment of radiative and expansion losses in their synchrotron emissivity calculations. The energetics of radio-loud AGNs can be constrained by comparing simulated attributes of synthetic radio sources (e.g. size and luminosity) against those for the observed objects. This comparison is typically done through a Bayesian parameter inversion (e.g. see Turner & Shabala, 2015; Turner et al., 2018b; Turner, 2018; Mahatma et al., 2020; Turner et al., 2020; Quici et al., 2022), allowing the intrinsic radio source parameters to be fitted. Such methods have the ability to simultaneously constrain the jet power and active lifetime of a radio source, in addition to the lobe magnetic field strength (Turner et al., 2018b) or host redshift (Turner et al., 2020), based on its angular size and multi-frequency radio spectrum. Quici et al. (2022) showed that high-resolution radio images at two frequencies (e.g. 151 MHz and 1.4 GHz; typical of large-sky surveys) can provide sufficient constraining power in a Bayesian parameter inversion to fit at least four intrinsic jet parameters including the duration of the remnant phase, $t_{\rm off}$. However, such parameter inversions rely on the ability of the underlying model to capture the necessary physics needed to explain the observation. For example,

the analytical model of Turner et al. (2023) does not currently capture processes such as jet precession or a bending of the jet, and may therefore be inapplicable towards certain active radio sources; on the other hand, these issues are less critical for the remnant phase as regions of enhanced emission associated with the jets will rapidly fade due to adiabatic expansion and radiative loss mechanisms (e.g. see Mahatma 2023 for a review).

Recently, Jurlin et al. (2020) selected an observationally-complete sample of radio galaxies from the LOFAR Two-metre Sky Survey (LoTSS; Shimwell et al., 2019, 2022). Through the application of forward modelling facilitated by the *Radio AGN in Semi-analytic Environments* (RAiSE; see Turner et al., 2023) model, Shabala et al. (2020) used this sample to constrain the intrinsic (or true) jet power and lifetime functions (see also Hardcastle et al. 2019 for a similar approach). Their approach relied on the comparison between mock and observed distributions in flux density and angular size, as well as the constraints from the observed fraction of remnant and restarted radio sources. Their work demonstrated that power-law lifetime models were needed to reproduce the observed properties of their reference sample, unlike constant-age models which underpredict the fraction of remnant radio galaxies. This study sets a solid foundation for ongoing work in this field, however, we propose to instead constrain the energetics of individual objects following the method of Quici et al. (2022) and then directly compare the selection-biased jet power and active age distributions to mock catalogues.

In this work, we combine and extend the approaches taken by Shabala et al. (2020) and Quici et al. (2022) to quantify the intrinsic jet power and lifetime functions for a sample of remnant radio galaxies. Such objects are unique in that they allow for a direct measurement of the full duration of the jet outburst, thus offering tight constraints on the AGN jet lifetime function. First, we identify a sample of 79 remnant radio galaxies brighter than 0.5 Jy, with angular sizes $\theta \geqslant 4'$, and within a redshift range of $0.02 < z < 0.2$ (Sect. 4.2). Next, we adopt

the method of Quici et al. (2022) to fit their intrinsic parameters, allowing us to probe their observed jet power and active age distributions (Sect. 4.3). To deal with the inherent selection biases, we construct mock remnant catalogues based on an assumed jet power and lifetime function, and filter the resulting radio source population by our sample selection criteria (Sect. 4.4). We test a grid of jet power and lifetime models, and compare their predictions to our observed sample statistics to constrain the true jet power and lifetime functions (Sect. 4.5). Our results are described in Sect. 4.6.

Throughout this work, we assume the ΛCDM concordance cosmology with $\Omega_M = 0.3$, $\Omega_\Lambda = 0.7$ and $H_0 = 70\,\mathrm{km\,s^{-1}\,Mpc^{-1}}$ (Planck Collaboration et al., 2016).

4.2 Low-redshift sample of remnants

We compile a sample of remnant radio galaxies from a range of large-sky radio surveys to form the observational basis for the later analysis in this work (Sect. 4.2.1). The radio galaxies in this parent sample are cross-matched with infrared identified host galaxies, which are then matched to obtain optical pass-band photometries and redshifts (Sect. 4.2.2). From these value-added products, we estimate the host galaxy stellar masses, and thus infer the masses of their dark matter haloes (Sect. 4.2.3). We then use literature-established methods to select remnant lobes from our parent radio galaxy sample (Sect. 4.2.4). Finally, following the method of Quici et al. (2022), we measure the observable attributes of each remnant lobe needed to constrain its energetics (Sect. 4.2.5).

4.2.1 Parent radio galaxy sample

We outline the steps followed to select a parent sample of radio galaxies from existing large-sky surveys. We impose the selection criteria that the radio sources are brighter than 0.5 Jy at 150 MHz ($S_{150\,\mathrm{MHz}} \geqslant 0.5\,\mathrm{Jy}$) and larger than four

Survey	Frequency (MHz)	Sensitivity (mJy/beam)	Resolution ($''$)	Declination limit $\delta_{\rm J2000}$
GLEAM	88-216	~ 7	120	$\leqslant +30°$
TGSS	151	~ 5	25	$\geqslant -53°$
RACS	887	~ 0.25	~ 25	$\leqslant +30°$
NVSS	1400	~ 0.45	45	$\geqslant -40°$
VLASS	3000	~ 0.12	3	$\geqslant -40°$

Table 4.1: Important properties of the all-sky radio surveys used in this work. Each row represents a unique radio survey (column 1), for which the observing frequencies (column 2), root mean square sensitivities (column 3), angular resolutions (column 4), and Declination limits (column 5) are shown.

arcminutes in size ($\theta > 4'$); this ensures the measured radio source attributes are not heavily degraded either by (relatively) poor surface brightness sensitivity or a lack of spatial sampling across the lobe.

4.2.1.1 Radio survey availability

We consider sources selected by both the GaLactic and Extragalactic All-sky MWA (GLEAM; Hurley-Walker et al., 2017) survey and the Rapid ASKAP Continuum Survey (RACS; McConnell et al., 2020) to ensure radio images are present at two or more frequencies, whilst maximising the potential sample of remnant radio galaxies. These two surveys both cover the following declination range: $-85° \leqslant$ Decl. $\leqslant 30°$. We supplement these observations with images from other large-sky surveys with partial coverage of this region: the TIFR GMRT Sky Survey (TGSS; Intema et al., 2017), the NRAO VLA Sky Survey (NVSS; Condon et al., 1998) and the Very Large Array Sky survey (VLASS; Lacy et al., 2019). The properties of these surveys are summarised in Tab. 4.1. Importantly, the observational parameter space provided by the GLEAM survey, principally the low-frequency coverage and low spatial-resolution, minimises the deselection of aged remnant lobes.

4.2.1.2 Integrated flux density cut: $S_{150\,\mathrm{MHz}} \geqslant 0.5\,\mathbf{Jy}$

We begin the parent sample compilation by considering all radio components brighter than $S_{150\,\mathrm{MHz}} \geqslant 0.5\,\mathrm{Jy}$. We conduct this step using the GLEAM survey due primarily to its enhanced surface brightness sensitivity to large-scale structure. As a preliminary step, we incorporate the GLEAM 4 Jansky catalogue (G4Jy; White et al., 2020b,a), which offers a complete, GLEAM-selected sample of radio galaxies brighter than 4 Jy at 151 MHz, and also offers robust host galaxy associations. Importantly, all sources in the G4Jy catalogue meet the integrated flux criteria of our sample, and are thus filtered through to our candidate sample. To avoid any duplicates of these sources, we remove components comprising the radio galaxies present in the G4Jy sample from the GLEAM catalogue prior to further source selection. This is done using a cone search centered at the coordinates of the G4Jy centroid, setting the radius of the search equivalent to reported angular size.

We now need to identify all GLEAM-selected radio sources with an integrated flux density of $0.5 \leqslant S_{150\,\mathrm{MHz}}(\mathrm{Jy}) \leqslant 4$. For each component in the GLEAM catalogue, we use the fitted $72-216$ MHz spectral index (α_{72}^{216}) and reference 200 MHz integrated flux density ($S_{200\,\mathrm{fit}}$) to compute the 150 MHz integrated flux density; we use this value over that measured from the 154 MHz GLEAM wide-band, in order to reduce the measurement uncertainty due to white noise. Components with flux densities of $S_{150\,\mathrm{MHz}} \geqslant 0.5\,\mathrm{Jy}$ are added to our candidate sample. However, recognising that extended ($\theta > 4'$) radio galaxies can appear as multiple components even in the GLEAM catalogue (e.g. see Fig. 4.1), we must also consider radio sources for which the sum of their component flux densities exceeds our required threshold (even if each individual component is below that threshold). To do this, we perform a cone search within the remaining GLEAM catalogue to internally cross match all components within a $\theta = 18'$ radius; i.e. based on the largest angular size reported in the G4Jy catalogue. Component groups with a total flux density $S_{150\,\mathrm{MHz}} \geqslant 0.5\,\mathrm{Jy}$ are also considered added to our candidate

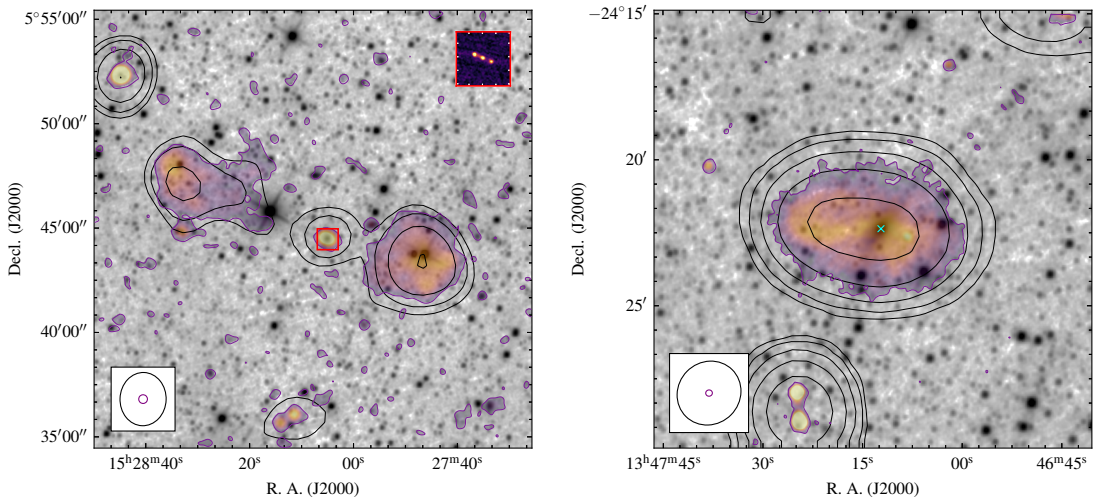

(a) J1528+0544 (b) J1317-2422

Figure 4.1: Example overlays used to manually inspect the GLEAM-selected radio sources. Gray-scale background images represent the AllWISE $W1$ bands. Each radio source is shown at 200 MHz as seen by GLEAM (solid black contours), and as seen by RACS at 887 MHz (semi-transparent images); the shape of their restoring beams are shown in the lower-right corner by the black and purple ellipses, respectively. For Fig. 4.1a, a close-up view around the host galaxy coordinates, as seen at 3 GHz by VLASS, is shown in the upper-right corner. For Fig. 4.1b, the coordinates of the host galaxy are marked by the cyan cross.

sample.

Following this approach, we identify a total of 3071 candidate radio sources brighter with $S_{150} \geqslant 0.5$ Jy.

4.2.1.3 Extended radio galaxy cut: $\theta \geqslant 4'$

We next need to identify which of our radio source candidates are: (1) extended radio galaxies larger than $\theta \geqslant 4'$, and (2) are not comprised of components associated with unrelated radio sources. Considering the size of this sample is just on the limit of what can be handled manually, we perform this step largely through a visual inspection to ensure our classifications are robust. However, we perform two initial cuts to remove compact radio galaxies from our sample, as we now briefly discuss.

We use the Tool for OPerations on Catalogues And Tables (TOPCAT) software, with a search radius of $\theta = 2'$ (i.e. the size of the GLEAM resolution at 200 MHz), to perform an internal cross match within the TGSS catalogue (for Decl. $\geqslant -40°$) to search for all isolated components within this radius. We then filter the TGSS components for sources with a integrated-to-peak flux density ratio less than 1.3; i.e. definitely compact. These TGSS objects are cross-matched with the GLEAM catalogue, and we remove the associated GLEAM components from the sample. We perform the same internal cross match within the NVSS catalogue to search for isolated components in this survey, and cross-match these outputs with the GLEAM catalogue. By calculating a two-point spectral index between 151 MHz and 1.4 GHz, GLEAM components are excluded if the measured spectral index is greater than zero (i.e. brighter at higher frequencies). This is a conservative cut, considering that radio galaxy lobes should have a spectral index at least steeper than $\alpha = -0.5$, and is designed to exclude compact objects such as gigahertz peaked spectrum objects and blazars.

The remaining radio galaxy candidates are visually inspected to check that the components are associated with an actual radio galaxy and meet the angular size cut ($\theta \geqslant 4'$). We use the coordinates of their radio centroid to create $0.5° \times 0.5°$ postage stamps from the GLEAM, TGSS, RACS and VLASS radio images. For multi-component source candidates, we take the radio centroid as the mean of the individual component coordinates. Importantly, the (relative) high resolution and surface brightness sensitivity of the RACS radio imaging made it possible to inspect the radio morphologies of each candidate radio source in sufficient detail. We use the SAOImageDS9 (Joye & Mandel, 2003) software to manually measure the largest angular size (LAS) across the lobes. Sources were discarded if the measured LAS failed to reach the required angular size criterion. Objects were also discarded if their GLEAM component(s) were associated with unrelated sources. This was true for both single-component sources, i.e. where the singular GLEAM component was in fact multiple radio sources, as well as

multi-component sources, i.e. where the GLEAM components themselves were revealed to be unrelated. These decisions were aided with infrared images indicating potential host galaxies locations (discussed in Section 4.2.2), and also aided with the discarding of diffuse radio emission associated with nearby star-forming galaxies (SFGs).

Finally, following this approach, we arrived at a parent sample of 795 radio galaxies with $S_{151} > 0.5\,\mathrm{Jy}$ and $\theta \geqslant 4'$. To prepare our sample for further analysis, we compile the integrated flux densities for each source from the five GLEAM wide-bands, RACS and NVSS (for Decl. $\geqslant -40°$).

4.2.2 Cross matching the host galaxies

Constraining the host galaxies of our radio sources is essential to model their intrinsic parameters. In this section, we cross match our radio galaxy sample to the WISE all-sky survey (Sect. 4.2.2.1), and use the WISE object IDs to automatically cross match our sample against various online data bases in order to obtain their optical passband photometries (Sect. 4.2.2.2), as well as their redshifts (Sect. 4.2.2.3). Unless otherwise stated, all database cross matching outlined in this section is performed using the VizieR catalogue service[1].

4.2.2.1 The AllWISE data Release

We perform our initial host galaxy cross match with respect to the AllWISE Data Release (Cutri et al., 2021) publicly available on VizieR[2]. We choose this survey considering it covers the full declination range occupied by our sample, and also probes a wavelength range well suited to the detection of dust-obscured host galaxies. Additionally, its most sensitive passband (W1, $\lambda = 3.4\,\mu\mathrm{m}$) has a high angular resolution of $\sim 4''$, comparable to that of VLASS. We create similar postage stamps to those discussed in Sect. 4.2.1.3 for the $\lambda = 3.4\,\mu\mathrm{m}$ band of

[1] https://vizier.cds.unistra.fr/
[2] https://vizier.cds.unistra.fr/viz-bin/VizieR?-source=II/328

the *Wide-field Infrared Survey Explorer* (*WISE*; Wright et al., 2010) survey, i.e. the WISE $W1$ band from the AllWISE data release (Cutri et al., 2021). These images were used to identify the coordinates of the likely host galaxy based on the orientation of the radio emission with respect to the galactic environment. For radio sources with a clear radio core and/or central jet, we took the host galaxy as that which coincided with the origin of the radio emission. We used the highest resolution radio data available, which at minimum was provided by RACS, however in many cases was improved on by VLASS imaging. For radio sources without a clear radio core, we recorded the likely coordinate of the host galaxy based on the orientation of the diffuse lobe plasma with respect to the surrounding galaxies. We note, although the host galaxy identification is often challenging for remnant radio galaxies (see e.g. Brienza et al., 2017; Quici et al., 2021), we did not encounter any cases where the host galaxy associated was ambiguous. We obtain the WISE object ID for the candidate host galaxies identified using the *WISE* $W1$ images (see Fig. 4.1).

4.2.2.2 Optical passband photometry

We require g and i passband optical photometry of each host galaxy to estimate the host galaxy stellar mass, however, no single survey provides coverage of our entire radio galaxy sample. As such, we compile measurements from various surveys, specifically the Panoramic Survey Telescope and Rapid Response System (Pan-STARRS1; Chambers et al., 2016), the Sloan Digital Sky Survey Data Release 12 (SDSS DR12; Alam et al., 2015), and the Skymapper Southern Sky Survey (SMSS; Wolf et al., 2018). Using the coordinates of the WISE object IDs obtained in the section above, we perform a cone search of each database using a $\theta = 5''$ search radius to retrieve the best positional match for each object. The results of our cross matching are shown in Fig. 4.2, which demonstrates the on-sky distribution of the data available for each host galaxy. For each survey, we obtain the AB magnitudes in the g and i passbands. For regions below a

declination of $-40°$, photometries are taken from SMSS. Photometries are otherwise taken from PanSTARRS, however for a small fraction of these objects ($\sim 1\%$), the PanSTARRS photometry is either missing in one of the passbands, or has a poorer signal to noise ratio than that in SDSS. In these two cases, optical magnitudes are sourced from SDSS instead.

In order to minimise any potential systematic biases that could lead to inconsistent stellar-mass estimates from multiple surveys for the same galaxy, we apply corrections to the SMSS and SDSS g and i magnitudes to align them with PanSTARRS, which serves as the reference due to its overlap with both surveys. The galaxies in our sample that appear in the overlapping region with PanSTARRS are used for independent corrections of the g and i bands in each survey. By comparing magnitudes between the two surveys for each band, we derive a linear correction that is applied as a function of the PanSTARRS magnitude to ensure that the bulk of the magnitudes are in agreement (see Fig. 4.3 for comparison of derived stellar masses).

4.2.2.3 Host galaxy redshifts

To obtain redshift information for our radio sources, we use the astroquery (Ginsburg et al., 2019) PYTHON module to cross match our host galaxy coordinates with the NASA/IPAC Extragalactic Database[3] (NED). For each radio source, we perform a $\theta = 2'$ cone search around the coordinates of the host galaxy, and filter the outputs for objects with catalogued redshifts in NED. Through this approach, redshifts are found for 540 out of the original 795 host galaxies. We also record the classification of each redshift type, whether the redshifts are spectroscopic or photometric, based on the original references for each catalogued redshift. Overall, our sample contained 329 spectroscopic, and 211 photometric redshifts. Our redshift distribution is shown in Fig. 4.4. Photometric redshifts are indeed far less reliable than those constrained by spectroscopy; the uncertainty in

[3] https://ned.ipac.caltech.edu/

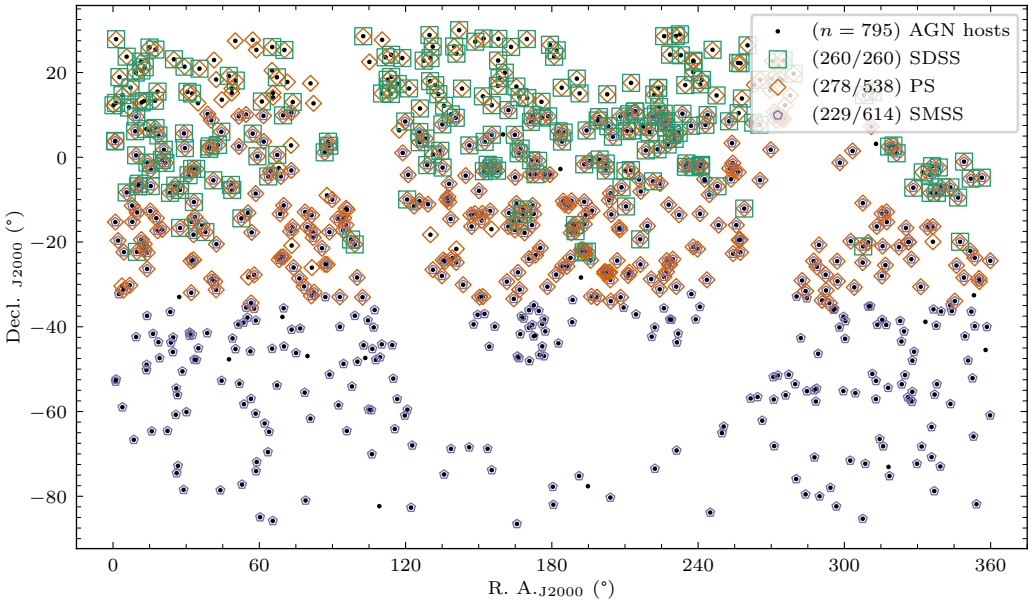

Figure 4.2: Sky coverage of the broadband optical surveys cross matched to our extended radio galaxy sample. Shown are the coordinates of the host galaxies (black circles), together with their cross-matched positions in the SDSS catalogue (green squares), the PanSTARRS catalogue (orange diamonds), and the SMSS catalogue (purple pentagons).

their estimates will vary based on the method used as well as as the quality and availability of the photometric data, however approximating a typical uncertainty as $\sigma_z \approx 0.1$ appears to be fairly representative of their confidence margin (e.g. Oyaizu et al., 2008; Banerji et al., 2008; Lima et al., 2008). As a sample cut, we limit the redshift distribution to $0.02 < z < 0.2$, to reduce the contamination from sources with photometric redshifts (but see also discussion in Sect. 4.3.1.2). At $z \geqslant 0.2$ our photometric redshifts become more numerous than spectroscopic which, considering the redshift is needed to perform the parameter inversion, may introduce an unwanted systematic into the fitted energetics.

Since these redshifts are heterogeneously-selected, we can not comment on the redshift completeness of our sample. However, we clarify that the method undertaken for this work is not reliant upon volume-complete radio galaxy samples. In Sect. 4.4, the predictions made by forward modelling a given jet power and lifetime model are made specific to the intrinsic property distributions of

the selected remnant sample. This includes the redshift distribution, which in principle means that the results should not be biased by redshift incompleteness.

4.2.3 The sample environments

The properties of the environment within which the source expands need to be quantified to successfully model the evolutionary history of a radio galaxy. In the RAiSE model, the environment can be parameterised by the mass of the cluster halo or galaxy sub-halo, which is related to a gas density profile based on an assumption of a typical shape of a cluster profile and a gas mass fraction (baryonic-to-dark ratio). Later in Sect. 4.3 we will allow for this parameter to vary as part of the fitting of the radio source evolution. However, to help guide this process, we will estimate the stellar masses of the host galaxies (Sect. 4.2.3.1) to then infer their total halo masses (Sect. 4.2.3.2). This step will eliminate improbable halo mass values (by using a Gaussian prior) when fitting the evolution of the radio sources.

4.2.3.1 Deriving the stellar masses

Taylor et al. (2011) demonstrated an empirical relation between the rest-frame $(g-i)$ colour and mass-to-light ratio (M_*/L_i) of a galaxy. To estimate the stellar masses, we use their linear best fit (e.g. see their Eqn. 8):

$$\log[M_*/M_\odot] = -0.68 + 0.70(g-i) - 0.4m_i - 2\log\left(\frac{d_\mathrm{L}}{10\,\mathrm{pc}}\right), \tag{4.1}$$

where m_i is the apparent magnitude in the photometric i-band (AB system), d_L is the luminosity distance, and the 1σ uncertainty corresponding to the derived M_*/L_i is ~ 0.1 dex. The stellar masses of each host galaxy are estimated using this equation based on the photometries presented in Sect. 4.2.2.2. For sources found in the overlap between different optical surveys, we compare their stellar mass estimates to validate their broad agreement. Considering that we

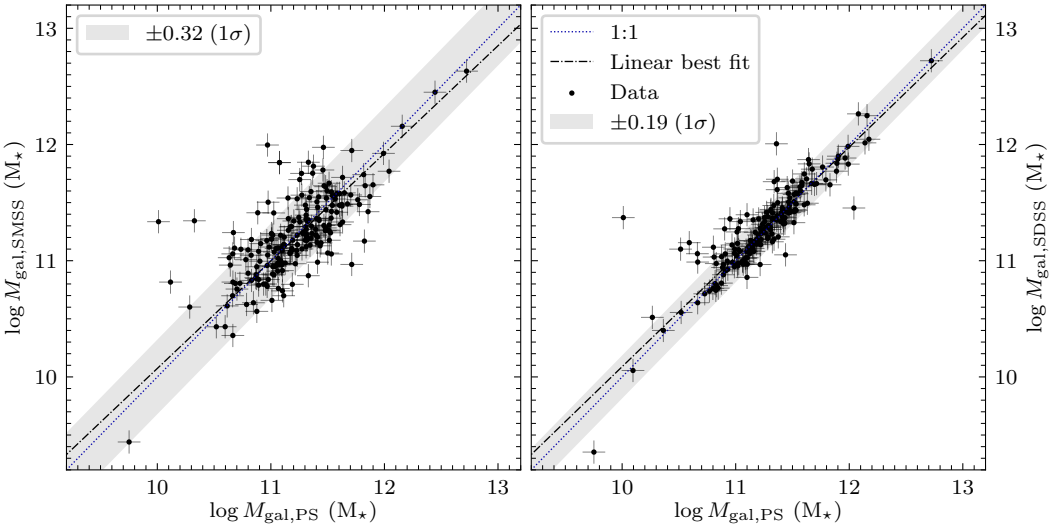

Figure 4.3: Consistency check for stellar masses derived using the $(g-i)$ colors from the PanSTARRS, SMSS and SDSS surveys. In each panel the PanSTARRS-based mass estimate (horisontal axis) is compared to the SMSS-based mass estimate (left panel) and the SDSS-based mass estimate (right panel). The standard deviation of the differences calculated between the two mass estimates is shown in the label for each panel, and represented by the blue-shaded region.

previously calibrated the SMSS and SDSS magnitudes against those measured by PanSTARRS, we thus compare the SMSS-derived and SDSS-derived stellar masses to those derived using PanSTARRS. For each comparison, we find the linear best fit to the data, and also compute a standard deviation of their residual (see Fig. 4.3).

Reassuringly, our results demonstrate good agreement between all three stellar mass estimates. While the scatter is clearly larger for the SMSS-PanSTARRS comparison, both comparisons show a near 1:1 relationship, and thus do not appear to be systematically offset. We assume the same holds true for the entire sample (e.g. outside the overlapping regions). To account for the noisier SMSS data, we assign a 0.32 dex uncertainty (e.g. the 1σ deviation of the scatter) on the SMSS-derived stellar masses.

4.2.3.2 Inferring the halo masses

Turner & Shabala (2015) converted between stellar and halo masses based on the

mock population outputs of the semi-analytic galaxy evolution (SAGE) model of Croton et al. (2006). The median and variance in this relationship is approximated by a broken power law fit as follows (Turner & Shabala, 2019):

$$\log M_{\rm H} = \frac{\left(10^{\log M_\star - {\rm SH_V}}\right)^{\alpha} \times 10^{\rm SH_W}}{\left(1 + \left(10^{\log M_\star - M_{\rm crit}}\right)^4\right)^{\frac{\alpha}{4}+\frac{\beta}{4}}} \pm \left(\delta z_0 + \delta z_1 z + \delta z_2 z^2\right), \tag{4.2}$$

where $\alpha = \alpha_{z0} + \alpha_{z1} z$, $\beta = \max\left\{\beta_{z0} + \beta_{z1} z, \beta_{\rm min}\right\}$ and $M_{\rm crit}$ is given by:

$$M_{\rm crit} = \max\left\{\left(c^0_{z0} + c^0_{z1} z + c^0_{z2} z^2 + c^0_{z3} z^3\right), \left(c^1_{z0} + c^1_{z1} z + c^1_{z2} z^2 + c^1_{z3} z^3\right)\right\}, \tag{4.3}$$

for the constants provided in Tab. 4.2. We use Eqn. 4.2 to infer the halo masses for our remnant sample. The uncertainty in $\log M_{\rm H}$ is added in quadrature with the uncertainty on $\log M_\star$, to give a final uncertainty on the halo mass estimates (see Fig. 4.4).

In Sect. 4.3, we will fit the intrinsic parameters of our remnant sample via the RAiSE-based parameter inversion. This will include fitting for the halo mass of each object, partially to deal with any systematics that may exist in our stellar and/or halo mass derivations; e.g. the small fraction of sources which appear to have unreasonably massive haloes ($M_{\rm H} > 10^{15}\,{\rm M}_\star$). The estimates we have derived here will thus act to constrain the fitting of the halo mass by providing a mean value and width of a Gaussian prior based on halo mass estimate and its 1σ uncertainty.

4.2.4 Classifying remnant radio galaxies

To classify remnant radio galaxies, we base our methods on the results of Brienza et al. (2017), Mahatma et al. (2018), Jurlin et al. (2020) and Quici et al. (2021), who show that remnants can display a wide range of observed properties. In Sect. 4.4, we will apply forward modelling to directly constrain the energetics of the sample of remnant radio galaxies compiled here. For this reason, provided

Parameter	Value
SH_V	8.88365129
SH_W	10.8533119
α_{z0}	0.618427576
α_{z1}	0.081724472
β_{z0}	3.016728391
β_{z1}	-0.868969294
$\beta_{\min}$	1.130765
c^0_{z0}	10.91946225
c^0_{z1}	-0.03789275
c^0_{z2}	0.02863088
c^0_{z3}	-0.05209548
c^1_{z0}	5.94896664
c^1_{z1}	3.49199821
c^1_{z2}	-1.05060664
c^1_{z3}	0.12026139
δz_0	0.29811592
δz_1	-0.07074894
δz_2	0.01121627

Table 4.2: Values for the parameters used in Eqn. 4.2 to infer the halo mass based on the stellar mass of the host galaxy.

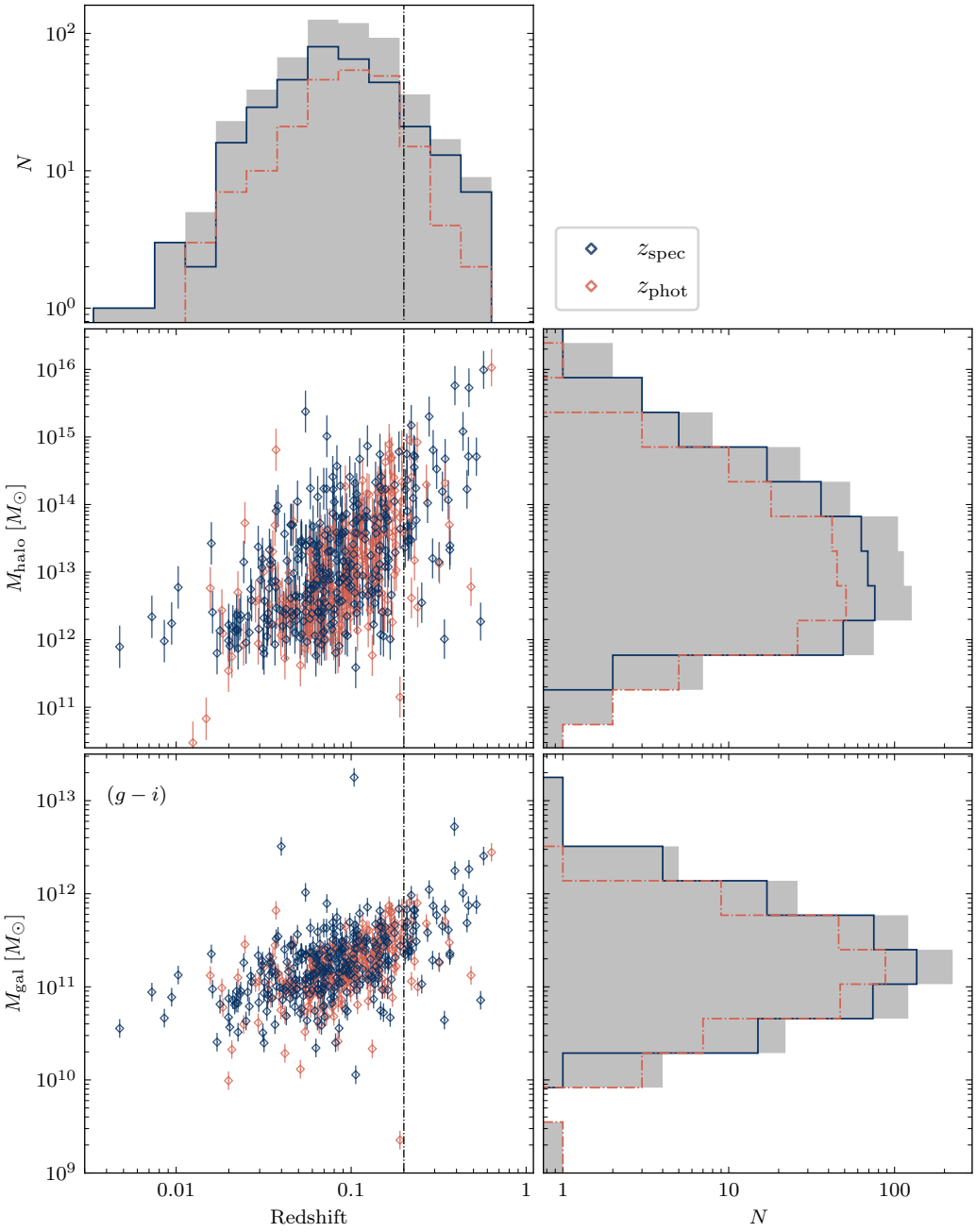

Figure 4.4: The redshift, stellar and halo mass distributions for our parent radio galaxy sample. The two scatter plots show the derived halo masses (upper panel) and stellar masses (lower panel) as a function of redshift. Spectroscopic and photometric redshift are denoted using blue and salmon colors, respectively. Each histogram shows the one-dimensional distribution in the parameter adjacent to the plot. Light grey bars are used to denote the full sample (spectroscopic and photometric).

our methods do not preferentially select, for example, the oldest/youngest remnants, we prioritise our remnant selection for reliability (e.g. how confident we are in our classification) rather than completeness (e.g. how certain we are we have identified all the remnants in our parent sample). Furthermore, despite the observational differences between remnant and restarted radio galaxies, the latter are equally as valuable towards our work. Restarted radio galaxies are defined as those in which multiple episodes of activity are observed concurrently. Importantly, the associated remnant lobes are no different to those associated with an inactive nucleus, and thus can be modelled through a RAiSE-based parameter inversion provided the two epochs of radio activity do not overlap spatially. With this in mind, we use the cutouts created in Sect. 4.2.1.3 and adopt several criteria to perform our remnant (and restarted) radio galaxy selection.

Prior to our remnant selection, for each source we calculate several flags of remnant classification based on its observed radio properties. First, radio sources are flagged if they do not exhibit radio emission from the core. We classify a core detection if radio emission at the coordinates of the host galaxy is significant above the 3σ level, where σ denotes the local RMS noise. This step is performed uniformly across our sample using the RACS data, but additionally includes VLASS data for Decl. $\geqslant -40^{\circ}$ sources. The core status is flagged as ambiguous if radio emission is present above this level, but is not unresolved by the resolving beam as one might anticipate in the case of a restarted jet. Additionally, using the VLASS and/or RACS data as above, sources are flagged if they do not show compact features such as jets or hotspots. Next, we calculate a 'low surface brightness' flag based on the mean 151 MHz lobe surface brightness (in mJy/arcmin^{-2}). Using the RACS data, we use the POLYGON_FLUX[4] code (Hurley-Walker et al., 2019) to trace the 3σ footprint of each radio source, and thus quantify the area projected by the lobes. Together with the 151 MHz GLEAM integrated flux density, we then evaluate an average surface brightness,

[4] https://github.com/nhurleywalker/polygon-flux

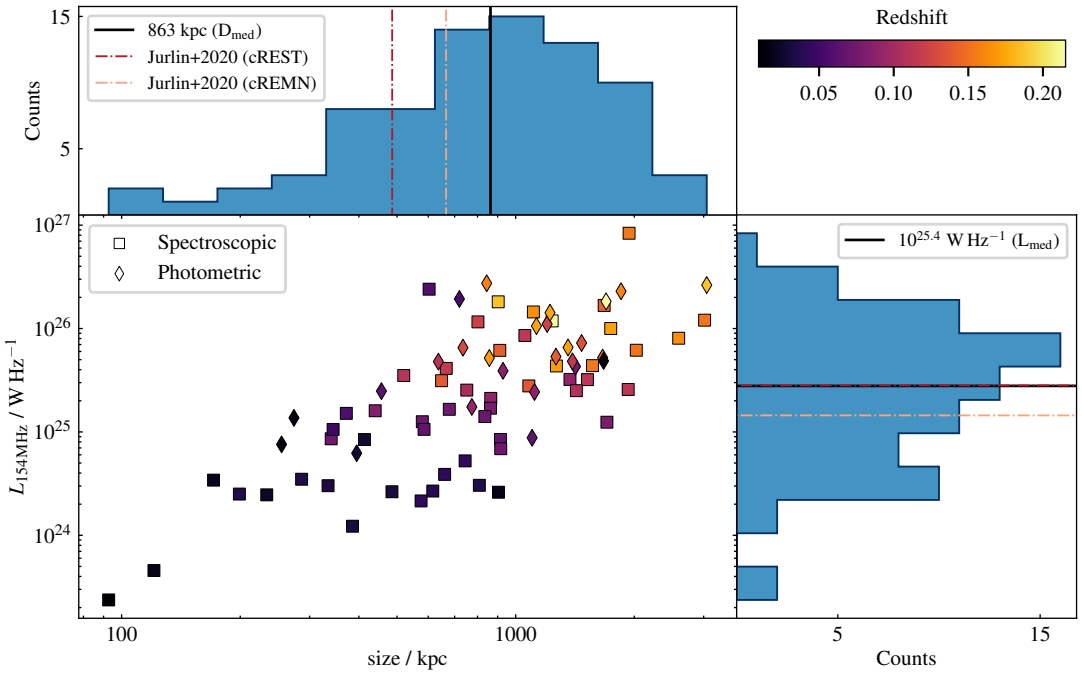

Figure 4.5: Radio luminosity–linear size distribution for our sample of 79 candidate remnant and restarted radio sources. Markers are used to represent spectroscopic (square) and photometric (diamond) redshifts. Marker colours are linearly mapped to the source redshift, as shown by the upper-right panel. The radio luminosity is calculated at 154 MHz and includes a k-correction based on the derived low-frequency spectral index. One dimensional distributions for each quantity are shown in the adjacent panels, with the median value represented by a solid black line. The median values reported by Jurlin et al. (2020) are also shown for their candidate remnants (salmon dot-dashed line) and candidate restarters (red dot-dashed line).

and flag sources that fall below 50 mJy/arcmin^{-2}. We calculate an 'ultra-steep spectrum' flag, based on a global spectral index fitted to the integrated lobe spectrum. For each source, we fit the global spectral energy distribution (between the lowest and highest frequency available) in log-log space using a simple linear model, and flag sources if the fitted spectral index steepened beyond $\alpha = -1.2$.

We are now able to select remnant radio galaxies from our parent sample using the flags above described above. The 'absent radio core criterion' (Quici et al., 2021, Chapter 2), in principle, can classify sources as remnant if they do not exhibit significant radio emission at the host galaxy. However, Jurlin et al. (2021) showed that faint radio emission from the core, perhaps due to the jets not

completely shutting off, can still coincide with remnant radio galaxy lobes. For sources where the core is classified as 'ambiguous', we adapt the 'morphological' criterion (Brienza et al., 2017) and classify sources as remnant if the following two conditions are met: 1) their lobes are flagged as having 'low surface brightness', and 2) the sources do not exhibit any jets/hotpots. In support of this step, we select the known remnant radio galaxy associated with NGC 1534 (Hurley-Walker et al., 2015; Duchesne & Johnston-Hollitt, 2019), which has unambiguously remnant lobes, yet also shows weak radio emission at the host galaxy. Finally, in line with the restarted radio galaxy classification techniques of Jurlin et al. (2020), we additionally select remnant lobes if a clear radio core is observed, however their lobes exhibit the following properties: their lobes are flagged as 'low surface brightness' and as 'ultra-steep spectrum', and do not exhibit any compact features (jets/hotspots).

Following these methods, we obtain a final sample of 79 candidate remnant radio galaxies within $0.02 \leqslant z \leqslant 0.2$. The selected candidates are shown in Fig. C.1. We emphasise that the methods outlined in this section have been designed in view of selecting a statistically meaningful sample of remnant radio galaxies from which we can use population statistics to constrain our mock simulations. Despite this, it is important to note that the remnant classification methods used in this work select only candidates for remnant lobes. Furthermore, as VLASS has a declination limit of $\delta_{\mathrm{J2000}} \geq -40°$, the classification of the nature of radio emission from the core is heterogeneous to the survey data, and thus the remnant classification is not uniform across the sample. On the issue of sample reliability (i.e. active radio galaxies incorrectly classified as remnant), we expect this would impact the results by artificially steepening the constrained jet-lifetime distribution. This is because an active radio galaxy is observed part way through its full jet phase, meaning the true jet lifetime is longer than what is constrained. On the other hand, we expect for sample completeness (i.e. not identifying all remnants within the parent sample) to pose less of an issue on the results, as

we do not expect the observability of the radio core to introduce a bias towards the age of the selected remnant. As the modelling in Sect. 4.3 depends upon the relative shape of the observed jet power and age distributions, the issue of sample completeness should mostly contribute simply to increased counting errors due to smaller-number statistics.

Further in Sect. 4.5.2.2, we compare our best-fit jet kinetic power and active age distributions to the results of Shabala et al. (2020), who perform a similar simulation-based study using the radio galaxy sample compiled by Jurlin et al. (2020). We must emphasize that the sample selection of Jurlin et al. (2020) differs significantly to that of our sample; their sample is selected around a minimum angular-size limit of $\theta = 60''$, and while there is no integrated flux density requirement, sources must have a peak flux density greater than $200\,\mu$Jy/beam at 150 MHz to be detected by their LOFAR observations. Furthermore, the median redshift distribution in their sample is $z \approx 0.5$, and is in stark contrast to our upper limit of $z = 0.2$. As such, we examine the impacts of the sample selection biases between the two samples by deriving the 154 MHz radio luminosity and physical size of our sources. Our results are shown in Fig. 4.5 and summarised in Tab. 4.3. Despite the sample selection differences, the resulting radio luminosities and physical sizes are broadly comparable. Jurlin et al. (2020) are able to achieve both higher and lower radio luminosities than that of our sample, which is unsurprising given the superior sensitivity of their LOFAR observations. Combining the redshift limits in Tab. 4.3 together with an approximation of the sky area covered by each sample, we find that the co-moving volume of our sample is approximately 12 times greater; this would explain the greater physical-size tail of our sample, given that the space density of such giant radio galaxies is low (e.g. see; Schoenmakers et al., 2001).

Despite the similarities in radio luminosity and physical size, we can not assert that the two samples are drawn from the same underlying distributions in, for example, AGN jet duty cycle, since it is unclear whether the mechanisms re-

Table 4.3: A comparison of the range of observed radio luminosities, physical sizes, and redshifts between the sample selected as part of this work, and the sample of Jurlin et al. (2020). We note that without access to their raw data, the limits shown for Jurlin et al. (2020) are approximations based on their Figures 4. and 7. This is sufficient for the purpose of broadly comparing the parameter space probed by both samples.

Author	$L_{154\,\mathrm{MHz}}$ (W/Hz)	Physical size (kpc)	Redshift
This work	$10^{23.4} \leq L_R \leq 10^{26.9}$	$92 \leq D \leq 3054$	$0.01 \leq z \leq 0.2$
Jurlin+2020	$10^{22.5} \lessapprox L_R \lessapprox 10^{27.5}$	$125 \lessapprox D \lessapprox 1375$	$0.03 \lessapprox z \lessapprox 1.125$

sponsible for triggering SMBHs evolve across cosmic times. As a result, the seed distributions in jet kinetic power and jet lifetime, from which these samples are selected from, may exhibit differences that can not be resolved within the present scope of this work. This is discussed at length in Sect. 4.5.2.

4.2.5 Measuring the radio source attributes

To fit the intrinsic parameters for our selected remnant radio galaxies, attributes are needed to constrain their evolutionary histories. In the framework for the RAiSE-based parameter inversion, observed radio source attributes are compared to those extracted from synthetic radio sources. Using a maximum likelihood algorithm to compare the two attribute sets, the most probable evolutionary history can thus be inferred through the intrinsic parameters which offer the closest match to observation (assuming that there is no degeneracy for a set of attributes with respect to the intrinsic parameters). It follows, then, that the quality and number of measured radio source attributes (unique constraints) must be adequate to the constrain the underlying parameters. For this work, we implement the result of Quici et al. (2022), who showed that attributes related to the observed surface brightness distribution of remnant lobes help to constrain the duration of the remnant phase.

With this in mind, and given the quality of the radio data available to us (see Sect. 4.2.1.1), the following radio source attributes are of particular interest to

us:

- a reference radio luminosity,
- a largest linear size,
- the two extent attributes, which describe the lobe surface brightness distribution (e.g. Quici et al., 2022)
- a low frequency spectral index,
- and a measure of spectral curvature.

To measure the reference radio luminosity, L_ν, we use the 154 MHz integrated flux density measured for each remnant. The decision to measure this attribute using GLEAM data is motivated by the sensitivity to low surface brightness emission and relatively low calibration uncertainty (e.g. approximately 8%; Hurley-Walker et al., 2017). However, for three of our selected remnants, blending with unrelated components resulted in an uncertain measurement of their S_{154}. For these sources, we measured their reference radio luminosity at 887 MHz using RACS data (which can be equally well predicted by RAiSE).

To measure the largest linear size and the two extent attributes, we use the method of Quici et al. (2022), who parameterise these attributes by fitting the lobe surface brightness profiles with skewed Gaussian functions (e.g. see their Sect. 4.2.2). As part of their analysis, they demonstrated that the extent attributes are mostly affected by the spectral ageing of the oldest plasma, meaning that higher-frequency measurements are more constraining. We therefore measure the extent attributes at 887 MHz, considering that the RACS observations provide the optimal trade-off between frequency, sensitivity, and spatial resolution; for example, while NVSS probes higher frequencies, the restoring beam is also larger, and thus does not offer much constraining power.

To measure the low-frequency spectral index, $\alpha_{\rm low}$, we use the five GLEAM 30GHz-wide bands (ranging between 88 MHz and 200 MHz) to fit the low-frequency

spectral energy distributions for our remnants. In the ideal case, the spectral index is measured across all five bands. However, for a handful of cases, blending from unrelated components (which becomes increasingly worse towards lower frequencies) makes this measurement problematic. For two such sources, the low-frequency spectral index was measured between 154 MHz and 200 MHz. To derive the spectral index, spectral data points were fit in log-log space (flux density and frequency) using a simple linear fit.

To measure the spectral curvature, SPC, we measured a higher-frequency two-point spectral index, α_{high}, and calculated the difference with α_{low}. To measure this attribute, we used one of two ways. If the radio source was detected by NVSS, α_{high} was calculated between 887 MHz and 1.4 GHz. Consequently, if the radio source fell below the NVSS declination limit (Dec. $= -40°$), or above the declination limit but was undetected by NVSS, we calculated α_{high} between 200 MHz and 887 MHz. We found that all sources detected by NVSS were also detected by RACS, which is unsurprising considering the deeper and comparatively lower-frequency observations provided by RACS.

With this approach, the radio source attributes are measured for each remnant in our sample. Using these attributes, we now seek to model the evolutionary histories of our remnants, and thus constrain their energetics. This is discussed in the following section.

4.3 Constraining the sample energetics

The energetics of an observed radio source can be constrained via a RAiSE-based parameter inversion – a method that exploits the ability of the RAiSE model to convert from intrinsic parameter space into observed attribute space. In the following section, we describe the adoption of this method to quantify the energetics for the sample of remnants compiled in the previous section. Briefly summarised, synthetic radio sources are generated across a multi-dimensional grid of input parameters that are expected to influence the observed properties (Sect. 4.3.1). The

parameter space is inverted by measuring synthetic attributes from the simulated surface brightness maps, whilst imposing the redshift and survey limitations of each radio source. (Sect. 4.3.2.1). By comparing the synthetic and observed radio source attributes via a maximum-likelihood algorithm, and applying Bayesian priors (halo mass and equipartition factor), the relative likelihood of each model is evaluated across the entire parameter space. We use a grid-search approach to fit the intrinsic model parameters and estimate their uncertainties (Sect. 4.3.2.2). We use these results to explore the observed distributions in the fitted parameters (Sect. 4.3.3).

4.3.1 Creating the RAiSE simulation grid

The RAiSE simulations that underlie this work play a key role in both estimating the energetics of each observed remnant (Sect. 4.3.2.2), and generating mock remnant populations required later in this chapter (Sect. 4.4). Towards both of these aims, we must ensure that the input parameter space covers the full breadth of plausible values, and that the resolution in each dimension is at least comparable to the associated fitting uncertainty. Below, a detailed setup of the RAiSE simulation is outlined.

4.3.1.1 Initial setup

To predict the evolutionary histories of a radio source, we use the Turner et al. (2023) 'jet+lobe' RAiSE model, for which the associated PYTHON code is publicly available on GitHub[5]. Radio sources are simulated using the `RAiSE_run` function, which generates spatially-resolved images of the lobe synchrotron radiation for an set of model inputs. Two such inputs, `frequency` and `resolution`, control the properties of the output images. For computational efficiency, we set `resolution=poor`, which sets the number of Lagrangian particles used in the surface brightness calculation equal to 1,792,000. Even in its lowest setting, the

[5] github.com/rossjturner/RAiSEHD

particle resolution remains sufficiently high to effectively trace the particle histories (Turner et al., 2023). To match the combined frequency coverage provided by the GLEAM, RACS, and NVSS radio surveys, the synchrotron radiation is synthesised at 88, 151, 200, 887 and 1400 MHz. Other input parameters, those that control the dynamics of the lobe formation and the internal structure of the jet, are held constant and set to default values that have been calibrated against hydrodynamical simulations (see Tab. 1 of Turner et al., 2023). The remaining inputs, those related to the dynamics and energetics of the lobes, represent dynamically relevant parameters that we will need to fit for each source and are discussed in the following section. Finally, in these simulations we seed the radio source environments based on a halo mass, which places the radio source at the centre of a spherically-symmetric, double-beta gas density profile. This uses observational constraints of galaxy clusters (Vikhlinin et al., 2006) to assume a mean shape for the gas density profile, and uses outputs of the Semi-Analytic Galaxy Evolution (Croton et al., 2006) model to make an assumption of the mean gas mass fraction (the fraction of the total halo mass locked in baryonic matter).

4.3.1.2 The input parameter space

The RAiSE-based parameter inversion uses attributes measured for an observed radio source to infer its intrinsic parameters. In this approach, a hyper-dimensional grid of order k is required to fit k number of parameters, where each dimension is a list of uniformly-gridded values (in either log- or linear-space). Our main goal is to fit the energetics of each radio source, meaning we need to fit the jet power and active age. However, we also want to account for other intrinsic properties that will have an influence on the observed radio source properties, thus ensuring that the fitted energetics are not systematically incorrect. These properties are: the remnant ratio (fractional time spent in a remnant phase), halo mass, equipartition factor in the lobes, and energy injection index. The intrinsic parameter space is thus created by uniformly gridding each aforementioned parameter be-

Table 4.4: The properties of the parameter space upon which the RAiSE simulation grid is created. Each row represents a dimension of the simulation grid, which is gridded between an upper/lower limit (column 3) using a fixed resolution (column 5), and comprises a total of N values (column 6). This parameter space results in a total of 8.63×10^7 synthetic radio sources.

Input parameter	Symbol	Value(s)	Unit	Resolution	N
Redshift	z	0.1	-	-	1
Jet power	Q	$10^{36.5}$ - $10^{40.0}$	W	0.1 dex	36
Active age	$t_{\rm on}$	$10^{6.5}$ - $10^{8.5}$	Myr	0.05 dex	41
Remnant ratio	$R_{\rm rem}$	0.000 - 0.700	-	0.025	29
Halo mass	$M_{\rm H}$	$10^{11.8}$ - 10^{15}	$M_\odot$	0.2 dex	16
Equipartition factor	q	$10^{-2.7}$ - $10^{-0.7}$	-	0.1 dex	21
Injection index	s	2.2 - 2.7	-	0.1	6
Initial axis ratio	A_0	2.5	-	-	1

tween an upper/lower limit, using a specified resolution (see Tab. 4.4 for details). Due to computation constraints, we assume a fixed value for the initial axis ratio, $A_0 = 2.5$, consistent with observations of 3CRR FR-II radio galaxies (Turner et al., 2018b).

Ideally, to fit the intrinsic parameters for our remnant sample, a unique RAiSE simulation grid would be created at the redshift of each remnant. However, for 79 observed remnants, the added cost to the total computation time makes this approach unfavourable. Considering that the redshift range for our observed remnant sample is low (0.02 - 0.2), and that the simulated rest frame properties (such as radio luminosity and physical size) can be scaled by any redshift, we consider a much-less computationally expensive option whereby the RAiSE simulation is executed at a single redshift, $z = 0.1$. It is important to note that RAiSE principally requires the redshift to correctly calculate the contribution of the inverse Compton (IC) energy losses, due to the CMB energy density, towards the total radiative losses. For a distribution of observed redshifts, this will introduce a relative uncertainty into the IC calculation as follows:

$$\delta(u_{\rm C}) = \frac{u_{\rm C,\,sim}}{u_{\rm C,\,obs}} \approx \left(\frac{z_{\rm sim}+1}{z_{\rm obs}+1}\right)^4, \tag{4.4}$$

Recalling that the radiative energy loss rate is proportional to $\gamma^2(u_B+u_C)$ (see Eqn. 3.12), we can therefore expect the overall uncertainty towards the calculation of the radiative energy losses to increase under the following conditions: when the true redshift deviates further from $z_{\rm sim} = 0.1$, i.e. as $|z_{\rm obs} - z_{\rm sim}|$ increases; for older and lower-powered remnants (where u_B decreases); and for higher-redshift remnants (where u_C increases). However, by fixing the redshift of the simulation to $z = 0.1$, we do not expect this uncertainty to dominate our results considering the narrow redshift range of our remnant sample (0.02 - 0.2).

Following this approach, the RAiSE simulation grid is constructed by simulating the radio source evolutionary histories for each point in the input parameter space. Each point contains spatially-resolved maps of the synchrotron radiation expected at the frequencies specified in Sect. 4.3.1.1. The integrated radio luminosities (for each input frequency) and the true physical size (measured from hotspot to hotspot) are also are calculated by default for each RAiSE model.

4.3.2 Modelling the intrinsic parameters

The energetics of each remnant can now be estimated using the RAiSE simulation as a theoretical expectation. To do this via a parameter inversion, the simulation must first be scaled to match the redshift of the observation. Synthetic images must be degraded to match the sensitivity and angular resolution of the radio observations, after which the synthetic attributes can be extracted. A comparison between the observed and synthetic radio source attributes is facilitated by a maximum likelihood algorithm, which gives the probability of a particular model offering the true description of the observation. Evaluating the likelihood for each unique model constrains the energetics within the entire parameter space, allowing for the intrinsic parameters to be estimated using a grid search algorithm. This process is detailed in the following section.

4.3.2.1 Inverting the RAiSE simulation

To model the energetics of each remnant, the parameter space is inverted according to the redshift and survey limitations of each remnant. To begin, the spatially-resolved synchrotron-emission maps are recast into the frame of the observed radio source using its redshift; doing so converts the pixel values from a luminosity (W/Hz) into a flux density (Jy), and similarly converts the scale of the pixel from a physical size (kpc) into an apparent size ($''$). By convolving these images to a desired resolution, simulated radio source attributes can be extracted. However, each of these steps take up the vast majority of the total computation time required to invert the parameter space. As such, to cut down on computation time, we applied some preliminary logic to only invert RAiSE models that were broadly compatible with the observed radio luminosity and physical size, e.g. as shown by:

$$\begin{cases} |\log(L_{\nu,\mathrm{sim}}) - \log(L_{\nu,\mathrm{obs}})| \leqslant a_{\mathrm{tol}} \\ |\log(D_{\nu,\mathrm{sim}}) - \log(D_{\nu,\mathrm{obs}})| \leqslant b_{\mathrm{tol}} \end{cases} ,$$

where the acceptable range for the radio luminosity and size is controlled by a tolerance factor, a_{tol} and b_{tol}, respectively. We perform this cut in logarithmic space due, to approximately-linear relation between: $\log Q$ and $\log L_\nu$ (e.g. see Fig. 9 of Turner & Shabala 2015); and $\log t_{\mathrm{on}}$ and $\log D$ (e.g. see Fig. 7 of Turner et al. 2018b). For this work, we set $a_{\mathrm{tol}} = b_{\mathrm{tol}} = 0.3$ (i.e. a range of $\pm$ 0.3 dex). Applying this preliminary cut avoided the unnecessary convolution and fitting of images for which the simulated radio luminosity and size were already incompatible with the given observation. Excluding these models is also consistent with the result of Turner & Shabala (2015), who showed that the observed radio luminosity and physical size offer the dominant constraints on the underlying jet power and active age; i.e. the parameters we principally need to fit.

After applying this cut, synthetic images are convolved using a 2D Gaussian kernel in order to match the angular resolution at the specified frequency (e.g. to mimic a RACS observation, images at 887 MHz are convolved to a resolution of $25'' \times 25''$). By dividing through by the volume of the restoring beam, the images are converted into surface brightness maps with pixel values in units of Jy/beam. Simulated radio source attributes, matching those measured for each remnant (Sect. 4.2.5), are extracted from the survey-degraded (i.e. angular resolution and sensitivity) surface brightness maps (see Quici et al., 2022, Sect. 3.4.3). Following this approach, the parameter space is inverted for each observed remnant, resulting in a corresponding grid of simulated radio source attributes (inverted attribute grid).

4.3.2.2 Bayesian parameter estimation

Following Quici et al. (2022), the energetics of each remnant are fitted using a maximum likelihood algorithm applied to the inverted attribute grid. Briefly summarised, the AIC[6] corresponding to each RAiSE model was calculated by comparing the observed and synthetic attributes via the likelihood function (Eqn. 3.9). The optimal model was selected as that which minimised the AIC, after which the probability of each model was calculated relative to the best-fit. It is important to note that the probabilities evaluated in this way encode only the agreement between simulation and observation, and do not reflect the Bayesian priors that exist for several parameters. For this work, the evaluated probabilities are multiplied through by two priors. First, the logarithmic equipartition factor is known to be approximately Gaussian-distributed ($\mu \approx -1.73$, $\sigma \approx 0.53$: Turner et al., 2018b). Additionally, estimates of the halo masses were previously made by considering the $(g-i)$ stellar mass. By making the assumption that the measurement uncertainties are Gaussian-distributed in $\log M_{\rm H}$, and, that the stellar-mass estimates did not encode any systematic offsets, a Gaussian prior was also applied

[6]Here, the AIC is calculated for $k = 6$, denoting number of free (fitted) parameters.

on the halo mass.

Following this approach, the energetics of each remnant were constrained within the gridded parameter space. The optimal set of parameters are evaluated as those that maximise the probability density function. Similarly, the shape of the probability density function characterises the uncertainty in each fitted parameter. In the following section, we use these fitting statistics to characterise the global jet power and active age distributions fitted for the sample.

4.3.3 The observed jet-power and lifetime distributions

We have now constrained he energetics of each observed remnant using the RAiSE-based parameter inversion. Considering the sample is specifically selected for remnant radio galaxies, the active age fitted for each source directly constrains the full duration of the jet outburst. In the following sections, we will generate mock predictions for the observed jet power and active age distributions, and compare these with observation in order to constrain the true distributions in jet kinetic power and lifetime. As such, we must first characterise the observed jet power and active age distributions probed by our sample of remnants.

We use Monte-Carlo statistics to characterise the shape and uncertainty in the fitted jet power and lifetime distirbution. Each MC realisation consists of a sample of 79 (the sample size) jet powers and lifetimes, based on randomly sampling the probability density function in the fitted parameters. The distributions are then binned and normalised (area equal to unity) in a two-dimensional parameter space (i.e. in jet power and active age), where the bins are set based on the gridded parameter space of the RAiSE simulation grid. Repeating this for 1000 realisations, the expectation and uncertainty at each bin is then derived by calculating the mean and standard deviation of the simulated counts. Our results are shown in Fig. 4.6.

Importantly, due to the selection bias, these distributions do not represent the true underlying statistics for these variables. We can see that the observed jet

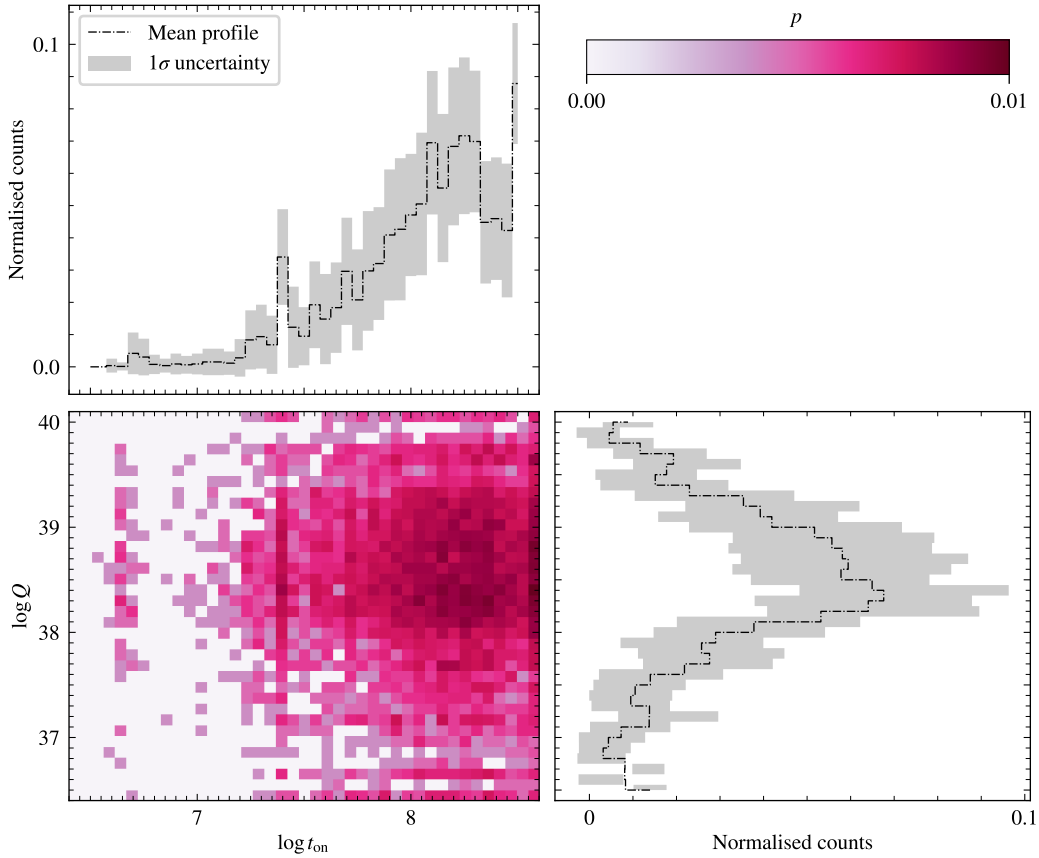

Figure 4.6: The observed distributions in jet power (lower right) and active age (upper left) fitted for our remnant sample. Monte-Carlo simulations are used to build up the observed sample statistics in each parameter. A two-dimensional grid (lower right) shows the observed sample statistics in $(Q, t_{\rm on})$-space. A colour-map is used to indicate the density of sources at each pixel.

power distribution peaks at $\log Q \approx 38.5$, and shows an observed dearth of low-powered sources; this turn-over is likely due to Malmquist bias (see also Sect. 4.4 below), which describes the preferential selection of bright objects in sensitivity-limited surveys. A similar effect, primarily due to the minimum angular size cut, can be seen for the active age distribution, which peaks at $\log t_{\rm on} \approx 8.25$. In Sect. 4.4, we will create mock remnant catalogues based on an assumed evolutionary jet model, and model their selection biases to generate predictions for their observed jet power and active age distributions; these predictions will be compared to our observed distributions, in order to constrain the true jet power and lifetime models. To this end, it is worth noting that although no obvious correlation exists between our observed jet powers and active ages, binning these distributions in $(Q, t_{\rm on})$-space means that we are not forcing their selection to be independent of one another.

4.4 Simulating the observed energetics

Due to selection biases in the survey, the fitted distributions of jet power and active age for our remnant sample (see Sect. 4.3.3) will not represent the underlying population statistics. For the observed sample statistics to offer valid constraints on their true distributions, we must first account for the selection effects that inherently constrain the range of evolutionary histories that may plausibly be observed. To approach this problem, we use the synthetic radio-frequency surface brightness images to determine the range of plausibly-selected evolutionary histories. First, we generate mock remnant catalogues for an assumed jet power and lifetime distribution, and model how the selection bias modifies the observed energetics (Sect. 4.4.1). After the confounding variables (e.g. the distributions in redshift, halo mass, equipartition, injection index) are controlled for (Sect. 4.4.1), the predictions made for the observed jet power and active age distribution can be meaningfully compared to our actual sample (Sect. 4.4.2).

4.4.1 Modelling the selection bias

Mock catalogues of remnant radio galaxies are created by weighting the probability of the parameter space investigated in the RAiSE simulation. To model the effect selection bias has on the observed energetics, two separate weighting schemes are required. First, the simulation needs to be weighted by an underlying jet power and active age distribution (Sect. 4.4.1.1); we refer to this weighting as $W_{\text{jet-age}}$, which controls the assumed shape of the underlying distributions we will later try to constrain. To compute the selection bias, $W_{\text{selection}}$, a binary weighting is assigned to each synthetic source depending on whether or not the source would have passed the sample selection criteria. The RAiSE simulation can then be sampled using the product of the two weighting schemes, resulting in mock observed energetics that correctly encode the sample selection biases.

4.4.1.1 The input jet power and lifetime distributions

We begin with the assumption that a simple power-law model is sufficient to describe the distributions of the radio-loud AGN jet powers and lifetimes. Observational constraints on the AGN radio luminosity function (RLF) show that the shape of the RLF is a broken power law (e.g. see; Sabater et al., 2019; Franzen et al., 2021). Considering that, to first order, the radio luminosity is correlated with jet power (noting that the age and environment also have a confounding impact, e.g. Godfrey & Shabala 2013; Hardcastle & Krause 2013), and that our sample preferentially selects high-powered remnants (see Fig. 4.6), we assume our assumption holds for the jet power distribution. On the other hand, simulations of feedback-regulated black hole accretion show that the Eddington-scaled mass accretion rate, $\dot{m} = \dot{M}_{\text{BH}}/M_{\text{Edd}}$, follows a power spectrum consistent with pink noise (e.g. see; Novak et al., 2011; Gaspari et al., 2017). These simulations predict that the jets triggered at the black hole are described by a lifetime distribution apparently consistent with a $p(t_{\text{on}}) \propto t_{\text{on}}^{-1}$ power-law slope. We also make the assumptions that the two distributions (jet power and active age) are

seeded independently; that is, that no intrinsic correlation exists between these two quantities. Future work (see also Sect. 4.5) may involve more complex model assumptions, however given our relatively small sample size, and that the observed energetics do not appear correlated (see Fig. 4.6), we will treat these as two independent mechanisms.

With these assumptions, we can model the jet power and lifetime functions as probability density functions described as follows:

$$p(Q)\,dQ \propto Q^a\,dQ; \quad p(t_{\rm on})\,dt_{\rm on} \propto t_{\rm on}^b\,dt_{\rm on}; \tag{4.5}$$

where a and b give the power-law indices for the jet power and active age distributions of each jet outburst (i.e. not considering likelihood of observing), respectively. However, as the parameter space of the RAiSE simulation is uniformly gridded in $\log Q$ and $\log t_{\rm on}$, weighting the simulation using the above expressions would fail to account for the non-uniform grid spacing when transformed to linear space. This is important considering that, for example, the bin of sources represented by $\log t_{\rm on} = 7.5$ is an order of magnitude wider than that represented at $\log t_{\rm on} = 6.5$. As such, the above expressions are adapted by the bin correction as follows:

$$p(\log Q)\,d\log Q \propto Q^{a+1} \ln 10\,d\log Q, \tag{4.6}$$

$$p(\log t_{\rm on})\,d\log t_{\rm on} \propto t_{\rm on}^{b+1} \ln 10\,d\log t_{\rm on}. \tag{4.7}$$

Considering that radio galaxies are a temporally-evolving phenomena, the corresponding active age distribution encoded in observed radio samples (without any selection biases present) is set by the jet lifetime distribution multiplied by an extra factor of $t_{\rm on}$. This extra factor comes from the direct proportionality between the probability of observing a source and the duration of time over which the source is active for; observing a source with $t_{\rm on} = 1\,{\rm Gyr}$ will be a factor of 10^3 more likely than a source with $t_{\rm on} = 1\,{\rm Myr}$, since the older source is active over

a much larger window in time. This means that for a jet lifetime distribution described by Eqn. 4.7, the corresponding active age distribution will have the form:

$$p(\log t_{\rm on})\, d\log t_{\rm on} \propto t_{\rm on}^{b+2} \ln 10\, d\log t_{\rm on}. \tag{4.8}$$

The observed distribution shown in Fig. 4.6, and indeed any active age distribution constrained from observed radio galaxy samples, will encode this observing effect. By weighting the RAiSE simulation grid using Eqn. 4.6 and 4.8, we are now able to create mock populations for a range of distributions in jet power and active age. However, to correctly simulate the observing of *remnant* radio galaxy populations, one final modification is needed to uniformly weight the passage of time during the remnant phase.

To construct mock remnant radio galaxy populations, we must ensure that the temporal evolution in the post-jet phase is weighted uniformly; that is, $p(t_{\rm off})\, dt_{\rm off}$ = constant prior to applying selection effects. In the RAiSE simulation grid, the temporal evolution of radio sources is uniformly gridded in $\log t_{\rm on}$ and $R_{\rm rem}$ (see Sect. 4.3.1). These two quantities map together to give the duration of the remnant phase as follows:

$$t_{\rm off} = (t_{\rm on} R_{\rm rem})/(1 - R_{\rm rem}), \tag{4.9}$$

which reveals the non-uniform gridding of $t_{\rm off}$. However, we have already corrected the non-uniform gridding of $t_{\rm on}$ in Eqn. 4.9, so we only need ensure the ratio $t_{\rm off}/t_{\rm on}$ is uniformly spaced. For a fixed $t_{\rm on}$, we therefore need $t_{\rm off}/t_{\rm on}$ to be constant, such that $p\big(t_{\rm on}, (t_{\rm off}/t_{\rm on})\big)\, d(t_{\rm off}/t_{\rm on})$ = constant. We derive the following relationship:

$$d(t_{\rm off}/t_{\rm on}) = \left(\frac{\tau}{t_{\rm on}}\right)^2 dR_{\rm rem}, \tag{4.10}$$

with which we weight the parameter space of the RAiSE simulation grid. To determine $W_{\text{jet-age}}$, the weights at each point in the parameter space are calculated by taking the product of the individual weights calculated by equations 4.6, 4.8,

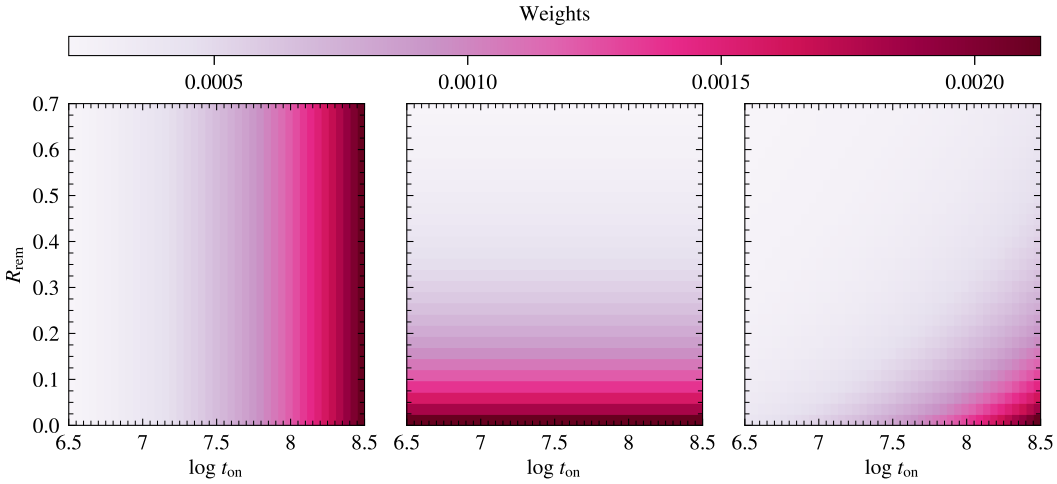

Figure 4.7: The 2D dimensional cross section of the RAiSE simulation grid, showing the weightings applied to the remnant ratio (vertical axis) and the active age (horizontal axis). Three panels are shown: the left shows the weighting applied by Eqn. 4.7 (assuming $b = 0.5$); the middle shows the weighting applied by Eqn. 4.10; and the right panel shows the final weighting applied to the RAiSE simulation outputs.

and 4.10. An example of this is demonstrated in Fig. 4.7.

4.4.1.2 Applying the selection criteria

To replicate the selection biases inherent to the observed sample (Sect. 4.2.1), each synthetic source in the RAiSE simulation grid needs to be tested against the sample selection criteria to determine whether the source would have been selected as part of the sample. To determine whether a synthetic source meets the sample selection criteria of our sample, three key criteria merit consideration: 1) the minimum integrated flux density; 2) the minimum surface brightness; and 3) the minimum angular size measured along the radio lobes. The modelling of each selection criteria is discussed below, and is intended to replicate the steps outlined in Sect. 4.2.

To construct the parent catalogue of radio sources, the GLEAM catalogue was used to select radio sources brighter than 0.5 Jy at 154 MHz (e.g. $S_{154} \geqslant 0.5$ Jy). For each synthetic radio source, the 154 MHz integrated flux density is calculated based on the forward-modelled radio luminosity and the given mock

redshift. As such, we assume that the synthetic sources fainter than this threshold would not have made it into our sample. Considering that the GLEAM catalogue contains only the components with a signal to noise larger than 5σ, where σ is the GLEAM local RMS in Jy/beam, this sets the condition for the minimum surface brightness criteria. To do this, the synthetic 154 MHz synchrotron emission maps are convolved to match the GLEAM resolution at 154 MHz. Using these surface brightness maps, we assume that synthetic sources with a peak flux density fainter than the 5σ GLEAM sensitivity would not have been detected, and thus will be missed by our selection. Finally, our sample contains radio sources with a projected angular size greater than $\theta = 4'$ in RACS. To model this selection criteria, the synthetic 887 MHz synchrotron emission maps are reprojected for a given mock redshift, and convolved to match the RACS resolution at 887 MHz. For this step, we assume all the observed radio sources lie in the plane of the sky. Considering only the regions of the lobes brighter than 750 μJy/beam ($\approx 3\sigma$), we use the surface brightness maps to discard sources whose largest angular size falls below our sample threshold. To model the bias due to these sample selection criteria, we construct a binary selection grid as follows:

$$W_{\text{selection}} = \begin{cases} 1, & \text{selected} \\ 0, & \text{not selected} \end{cases}, \tag{4.11}$$

where the synthetic source is weighted either as unity (the source passes the selection criteria), or zero (the source fails any of the selection criteria). Modelling the selection in this way can thus be thought of as a binary 'yes/no' filter, where the probability of selecting a source is unchanged if the source passes selection criteria, but is set to zero if the selection criteria is not satisfied.

We note, the framework above only models the selection due to the parent sample selection criteria (i.e. Sect. 4.2.1), and does not consider the potential selection biases due to the remnant selection methods we have used. For this work, we assume that as soon as a source switches off it will show observable

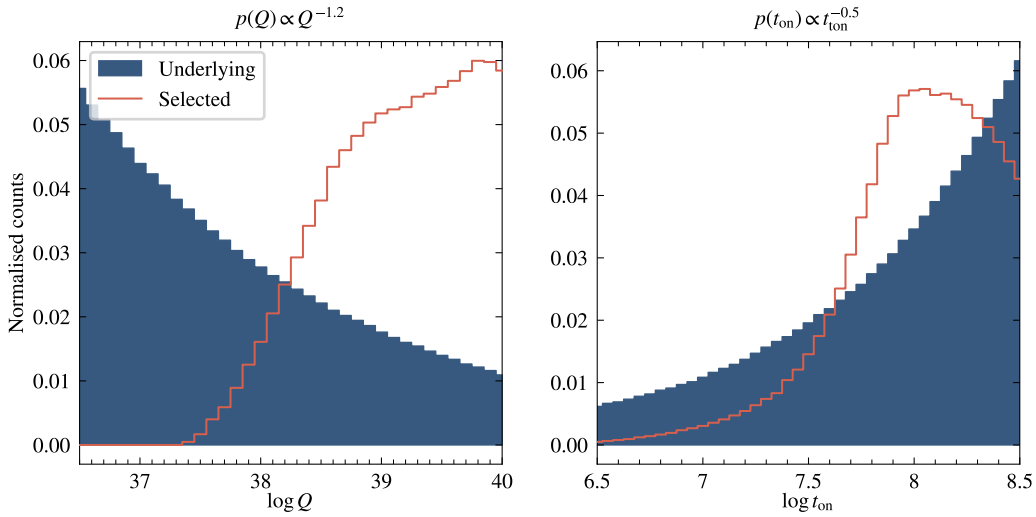

Figure 4.8: Underlying distributions (blue bars) of the jet power (left panel) and active age (right panel) are filtered through our sample selection criteria (Sect. 4.2.1) to explore the bias propagated onto their observable counterparts (black steps). The mock catalogue is simulated at $z = 0.1$, $\log H = 14.0$, $\log\ q = -1.7$, $s = 2.2$, and encodes the energetics described by $p(Q) \propto Q^{-1.2}$ and $p(t_{\rm on}) \propto t_{\rm on}^{-0.5}$.

signatures consistent with a remnant radio galaxy; in other words, the remnant radio galaxies forward modelled by our mock catalogues are ones that we should be able to classify. This assumption may not hold for extremely young remnants, for example those in which $\rm t_{off}$ is smaller than the light travel time along the jet, $\rm t_{light\text{-}travel}$[7], however we do not expect this to be a problem for the off-times probed by our sample selection.

Following this approach, the selection of each source is evaluated for the entire RAiSE simulation. Importantly, by evaluating $W_{\rm jet\text{-}age}$ and $W_{\rm selection}$, predictions for the observed jet power and active age distributions can be made for any underlying assumptions and sample selection criteria. To make predictions for the observed energetics, the RAiSE simulation grid is sampled using the element-wise multiplication of the two weighting schemes: i.e. $W_{\rm jet\text{-}age} \circ W_{\rm selection}$.

As an example, a mock population of $z = 0.1$ remnant galaxies is generated

[7]For a distance of $D = 100\,$kpc, information travelling at a speed $v = 0.3\,c$ would take $\sim 1\,$Myr to reach the hotspot from the SMBH

for a jet power $\left(p(Q) \propto Q^{-1.2}\right)$ and active age $\left(p(t_{\rm on}) \propto t_{\rm on}^{-0.5}\right)$ distribution, and filtered through the selection criteria of our remnant sample. The effect the selection bias has on the resulting observed energetics is shown in Fig. 4.8. Although the exact nature of the observed distributions will depend on both the underlying energetics and the selection criteria, we can comment on the broad features that are consistent with what we expect. The bias against lower-powered and shorter-lived sources is clearly seen: these sources are fainter and have a smaller physical sizes, and are thus precisely the objects that would be preferentially deselected from our sample. Higher-powered jets produce stronger lobe magnetic fields, in turn resulting in shorter fading timescales during the remnant phase (e.g. Turner et al., 2018b; Turner, 2018; Quici et al., 2022); this effect is likely responsible for the observed flattening towards $Q = 10^{40}\,\mathrm{W}$. Similarly, the downturn observed towards the longest-lived sources is likely a combination of two factors: and the expansion of the source driving down the lobe surface brightness (e.g. Turner, 2018; Shabala et al., 2020), and the decrease in the integrated radio luminosity due to Rayleigh-Taylor mixing of the lobe plasma with the environment (e.g. see Fig. 3 of Turner & Shabala 2015).

Importantly, these results show us survey selection biases can greatly transform the observed nature of the true jet power and active age distributions. Our approach so far, however, has neglected the impact the remaining sample properties will have on these results. To demonstrate this impact, we take the evolutionary jet model ($a = -1.2$, $b = -0.5$) shown in Fig. 4.8 and compute $W_{\text{jet-age}} \circ W_{\text{selection}}$ at two different redshifts ($z = 0.01$ and $z = 0.05$). We examine how the selection biases impact the sampling in $(Q, t_{\rm on})$-space, as demonstrated in Fig. 4.9. Unsurprisingly, this reveals that there is a redshift dependence for the regions of the parameter space that can plausibly be observed, such that lowered-powered and shorter-lived sources become inaccessible at higher redshifts. Considering that our sample has a distribution in redshift, and indeed in other variables such as environment, the confounding impact these variables have on

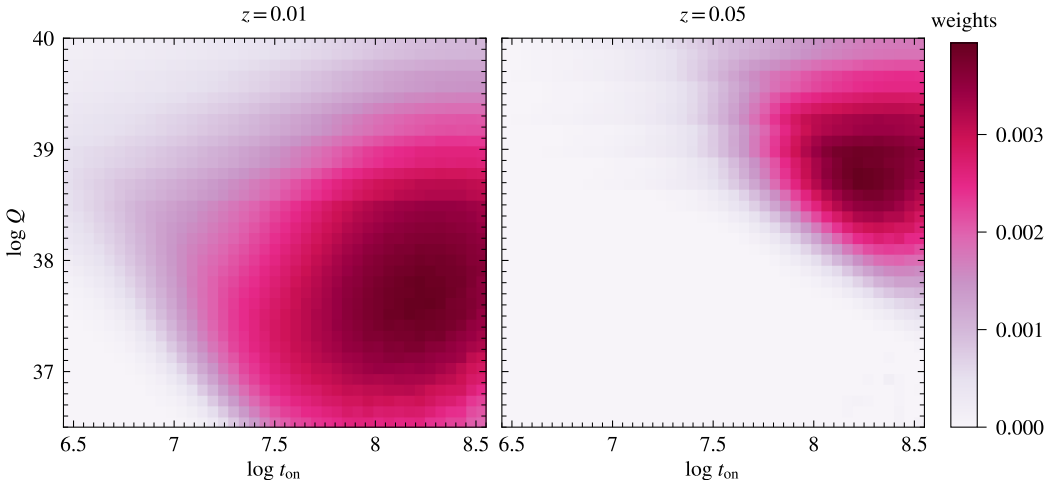

Figure 4.9: A two-dimensional slice of the RAiSE simulation grid, weighted based on the underlying energetics and selection criteria used in Fig. 4.8. The selection bias is evaluated at two redshifts: $z = 0.01$ (left panel), and $z = 0.05$ (right panel). The weighting applied at each jet power, Q, and active age t_{on}, is demonstrated using the sequential colour map.

the selected jet powers and active ages needs to be modelled, in order to make comparable predictions to the energetics fitted in Fig. 4.6. This is discussed in the following section.

4.4.2 Controlling for the global properties of the sample

The range of plausibly-selected evolutionary histories are dependent upon redshift (e.g. Fig. 4.9), in addition to the ambient gas density, equipartition factor, and injection index, albeit less significantly than the jet power and age. The selection biases computed for our mock catalogues must therefore take into account how these parameters are distributed for our sample. To do this, we initially assume that their underlying distributions are the same as what we observe (Sect. 4.4.2.1). After applying the sample selection biases, these distributions will likely differ somewhat; we therefore iteratively apply small corrections to their underlying distributions, thus controlling for the confounding variables in our analysis (Sect. 4.4.2.2).

4.4.2.1 Weighting the initial priors

The dimensionality of the RAiSE simulation grid is increased to include a redshift axis. Redshifts are uniformly gridded between $(0, 0.2)$ using a resolution of $dz = 0.001$, and simply scale the observed properties of the synthetic radio sources. As previously discussed in Sect. 4.3.1, this assumes that the evolutionary histories are independent of the redshift, which we know not to be true, however the differences are expected to be insignificant across the designated redshift range.

Next, we use the observed statistics in each parameter to weight their corresponding mock distributions; e.g. the observed redshift distribution acts as a prior to weight the pseudo-redshift axis. We treat the observed redshift distribution under the assumption of zero measurement uncertainty, to reduce the computationally-intensive nature of these mock simulations. Although we acknowledge that this assumption may not hold for the photometric redshifts, we anticipate that any deviation will not significantly affect the overall properties of the distribution. It is however worth mentioning that the Monte-Carlo underpinning of these mock simulations inherently enables the propagation of the redshift measurement uncertainty into the final model predictions, which may be an avenue to explore in future work. The observed redshifts are binned with respect to the pseudo-redshift axis, after which the area under the distribution is normalised to unity. In this way, each value gridded along the pseudo-redshift axis is weighted based on the height at each bin, thus encoding the observed redshift distribution into the mock sampling weights. We note, empty bins are assigned a weighting of zero, meaning there is a null probability of finding a source with that particular parameter value.

Similarly to the redshift, the observed distribution of each confounding variable is built up via sample statistics. However, unlike the redshift, we employ Monte-Carlo (MC) simulations to sample the observed distribution in each confounding variable; doing so respects the uncertainties on each parameter fitted by modelling the evolutionary histories of each remnant (Sect. 4.3.2.2). For each

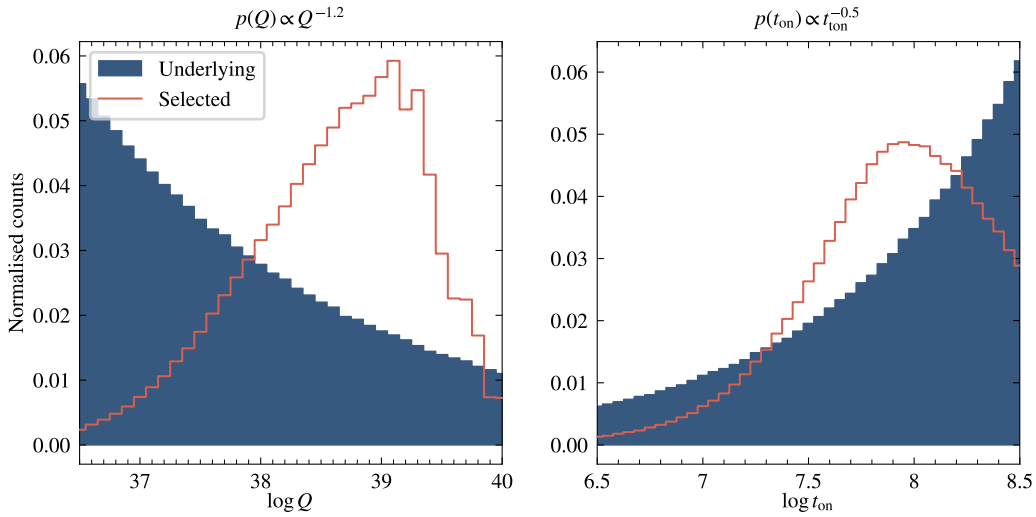

Figure 4.10: Same as Fig. 4.8, but now including the prior weightings derived from the sample distributions in redshift and confounding variables (Sect. 4.4.2.1).

confounding variable, an $M \times N$ sample of values is simulated; here, M rows denotes the number of remnants in the sample, and N denotes the size of the sample created for each source. As described previously for the pseudo-redshift axis, the observed distributions in each confounding variable are then used to weight their corresponding axis in the RAiSE simulation grid.

Following this approach, each axis of the RAiSE simulation grid is weighted according to the observed statistics of the remnant sample. In Fig. 4.10, we replicate the example shown in Fig. 4.8, demonstrating the effect of considering the remaining properties of our sample. The most notable difference is the turn-off towards the highest-powered jets; a feature that is also observed for our remnant sample (Fig. 4.6). The reason for this is most likely due to higher-powered jets being less likely to form lobes in low-density environments (i.e. balistic expansion; Falle, 1991; Turner & Shabala, 2023).

4.4.2.2 Controlling for the confounding variables

In the previous section, we weighted the redshift and confounding-variable distributions by making the assumption that their underlying distributions are de-

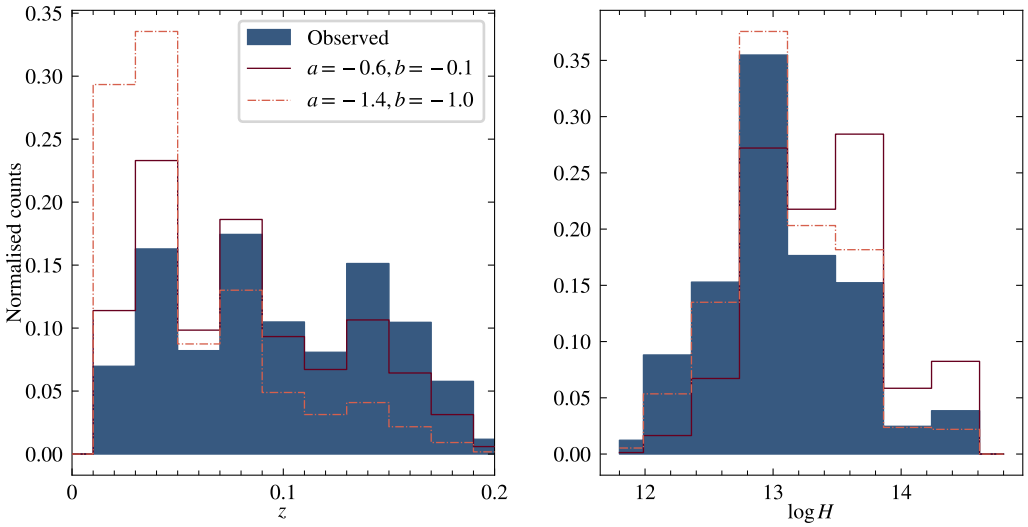

Figure 4.11: The observed redshift (left panel) and halo mass (right panel) distributions predicted for two separate mock catalogues (solid red and dot-dashed salmon steps) created for different jet power and active age distributions (see exponents in figure label). Mock catalogues are filtered by the selection criteria of our sample, and are weighted by the distributions observed for the redshift and the confounding variables (filled-blue bars).

scribed by those observed for our sample. Considering that the observed attributes of radio sources, and therefore their selection, is moderated by these properties, we know that this assumption is unlikely to be true. To illuminate the issue here, we generate two mock catalogues with different underlying energetics, weight their redshift and confounding-variable distributions following the method outlined in the previous section, and finally apply the selection criteria of our sample. The mock redshift and halo mass distributions, resulting after applying the selection biases, are shown in Fig. 4.11.

First of all, Fig. 4.11 demonstrates that the selection bias does indeed moderate the shape of the observed redshift and halo mass distribution; we focus on these two, as they appear to differ the most after applying the selection criteria. The output distributions do not match the input, meaning that the observed statistics of our remnant sample must have been selected from a currently-unknown underlying distribution. This result also tells us that the selection bias of these variables is dependent upon the underlying energetics, considering that

the predicted distributions differ between the two different models. The manner by which the outputs differ to the input is consistent with our expectation. For each model, the output redshift distribution is skewed towards lower-redshifts; for a fixed jet power and active age distribution, the highest redshift bin will have the narrowest range of plausibly-selected evolutionary histories. The model with the flatter exponents (more high-powered and long-lived sources) expectedly incurs less attenuation with respect to redshift. As for the halo mass distribution, the bias is evident for environments with a low ambient density. Output halo mass distributions are under-predicted at low values of H, where high-powered jets are less likely to form lobes. For sufficiently-steep models (more low-powered and short-lived sources), the highest-mass bins also appear to be under-populated; this is likely due to jets failing to grow to the required angular size.

Overall, these results tell us that the assumptions made for the underlying distributions of these confounding variables need to be corrected, such that the distributions predicted after the selection biases are applied match those observed for our sample. Without this correction, predictions made by our mock catalogues will have systematic errors when comparing to our observed sample. We note, although the discussion above has focused on the redshift and halo mass distribution, the same principle applies to the distribution in equipartition factor and injection index.

To develop the required corrections, we modify the original weightings (Sect. 4.4.2.1) in such a way that gives us the observed distributions after the underlying energetics are weighted and the selection biases are applied, in effect, solving for their underlying distributions. To do this, for each variable (e.g. redshift, halo mass, equipartition factor, injection index) we bin the distributions of the observed and mock samples based on the discrete values of the RAiSE simulation grid, and normalise the area under the distribution to equal unity. For each bin, we compute the ratio of heights between the observed and mock samples (e.g. $N_{\mathrm{observed}}/N_{\mathrm{mock}}$). The ratio quantifies how significant the selection bias is at each

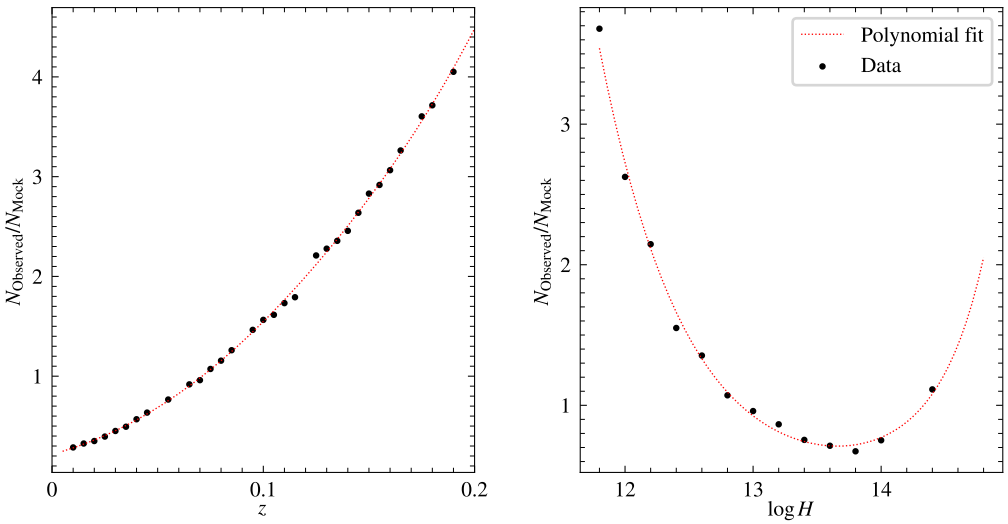

Figure 4.12: Example of the scaling factors required to bring the height of each mock bin equivalent to the observed sample statistics. Each point represents the ratio of bin heights between the observed and mock distributions. To model the corrections as a smooth continuous function, the data are fit by a third-order polynomial, as shown by the red dot-dashed line.

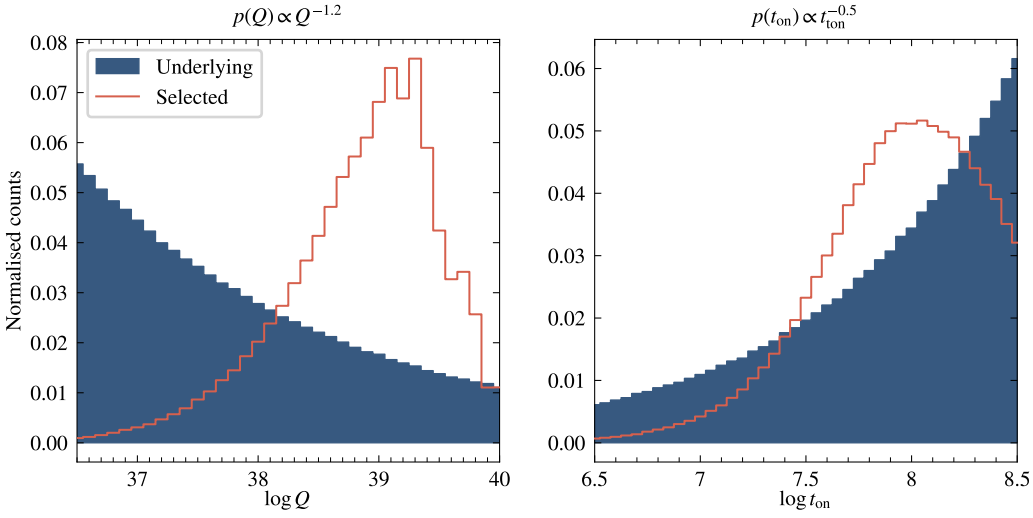

Figure 4.13: Same as Fig. 4.10, but now including the selection bias-corrected weightings applied to the distributions in redshift and confounding variables (Sect. 4.4.2.2)

bin, which we expect to vary smoothly across the parameter space. Mock catalogues are re-sampled, scaling the sampling weights of each variable by the inverse of the ratio (see Fig. 4.12). This can be done iteratively over several iterations, however we find that a single round of corrections is sufficient to bring the mock distributions in agreement with our remnant sample.

Finally, with these corrections, we are able to produce mock catalogues that are correctly weighted for their redshift and other confounding-variable distributions. The predictions made by these catalogues, e.g. see Fig. 4.13, can now compared to the observed jet power and active age distribution of our sample, in order to constrain their underlying distributions. This is explored in the following section.

4.5 Results and discussion

Using the method outlined in Sect. 4.4, we can now separate the impact of selection bias from our observed jet power and active lifetime distributions, allowing us to infer their underlying seed distributions.

4.5.1 Constraining the seed distributions

Following the methodology described in Section 4.4, we generate mock catalogs in a two-dimensional grid defined by the power-law indices (a, b) where each cell provides the inputs to a potential evolutionary model. The power law index for the jet power distribution is binned into discrete intervals within $a = -2.6$ to -0.6, using a precision of $\delta a = 0.1$. Similarly, the power-law index for the lifetime distribution is partitioned into intervals within $b = -2$ to -0.5, using a precision of $\delta b = 0.05$.

We first investigate whether our mock catalogues exhibit discernible differences when influenced by the selection biases. We compare the predicted jet power distribution between two scenarios: a steep jet power distribution with

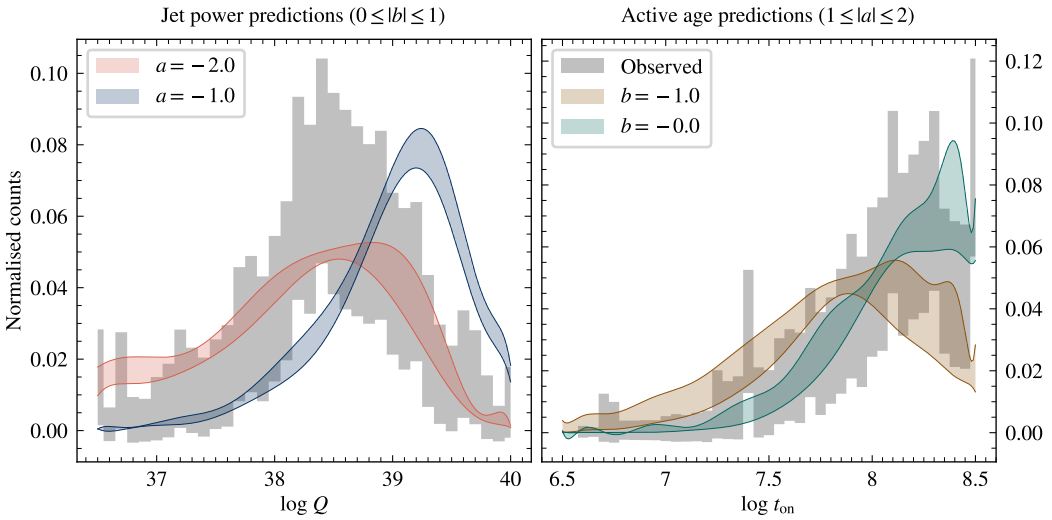

Figure 4.14: Smoothed predictions for the observed distributions in jet power (left panel) and active age (right panel) made by various mock populations. The left panel shows predictions made by a steep ($a = -2.0$, salmon colored) and shallower ($a = -1.0$, blue colored) jet power model, evaluated for all age distributions. The right panel shows predictions made by a steep ($b = -1.0$, brown colored) and shallower ($b = 0$, green colored) ageing model. evaluated for all jet power models with $1 \leqslant |a| \leqslant 2$.

$a = -2.0$ (many low-powered jets) and a shallow distribution with $a = -1.0$ (fewer low-powered jets), and consider all age models within $-1 < b < 0$. Similarly, we compare the predicted lifetime distribution between the following two scenarios: a steep distribution with $b = -1.0$ (many short-lived jets) and a shallower distribution with $b = 0$ (fewer short-lived jets), and consider all jet power models within $-2 < a < -1$. Figure 4.14 presents our findings, which are compared with the observed sample statistics from Figure 4.6. Encouragingly, despite the stringent selection criteria, the shape of the predicted distributions (after selection biases are applied) are measurably different; those corresponding to shallower seed distributions exhibit a turn-over at approximately one order of magnitude greater than the steeper seed distribution.

Fig. 4.14 further illustrates the intertwined relationship between the seed jet power and active age distributions, and their selection-biased counterparts. For a given jet power model, the shape of the observed jet power distribution is

somewhat influenced by the underlying jet lifetime model, and vice versa. This indicates that while the observed distribution primarily constrains its corresponding seed distribution (i.e., observed jet powers constrain the jet power model, observed active ages constrain the lifetime model), there should in principle be weaker constraints stemming from the complementary distribution (i.e., observed active ages aiding in constraining the jet power model, and vice versa).

To constrain the evolutionary jet model, the mock jet power and active age distributions are binned in $(Q, t_{\rm on})$-space to match the binning of the observed distributions (see Fig. 4.6). The likelihood function (Eqn. 3.9) is evaluated by considering the mock and observed constraints at each point in this parameter space, from which we calculate the AIC for two free parameters ($k = 2$). This calculation assumes that each data point (pixel) offers an independent measurement on the number of sources in that particular $(Q, t_{\rm on})$ bin, which is not true considering that there is a correlation between the number of sources in neighbouring bins. We note however that the uncertainty on the observed $(Q, t_{\rm on})$ distribution is estimated via Monte-Carlo simulation (see Sect. 4.3.3), and encodes the effect of this correlation. We select the optimal jet model as that which minimises the AIC, and we compute the relative probability of each model as $p_i = e^{({\rm AIC}_i - {\rm AIC}_{\rm best})/2}$. To constrain the power-law indices, the probability density function is mapped across (a, b)-space, and is marginalised for each distribution. This is shown in Fig. 4.15.

The ellipsoidal shape of the probability density function shows that the modelled power-law distributions for the jet power and lifetime functions are tightly constrained in (a, b)-space, lending confidence towards the robustness of our estimates. Some covariance in the 2D probability density function can be seen, implying that the quantities are not fitted completely independent of each other. Considering that the models are seeded independently, this effect is likely driven by the selection bias. To quantify our parameter estimates, we approximate the 1D marginal probability density functions using a Gaussian function to char-

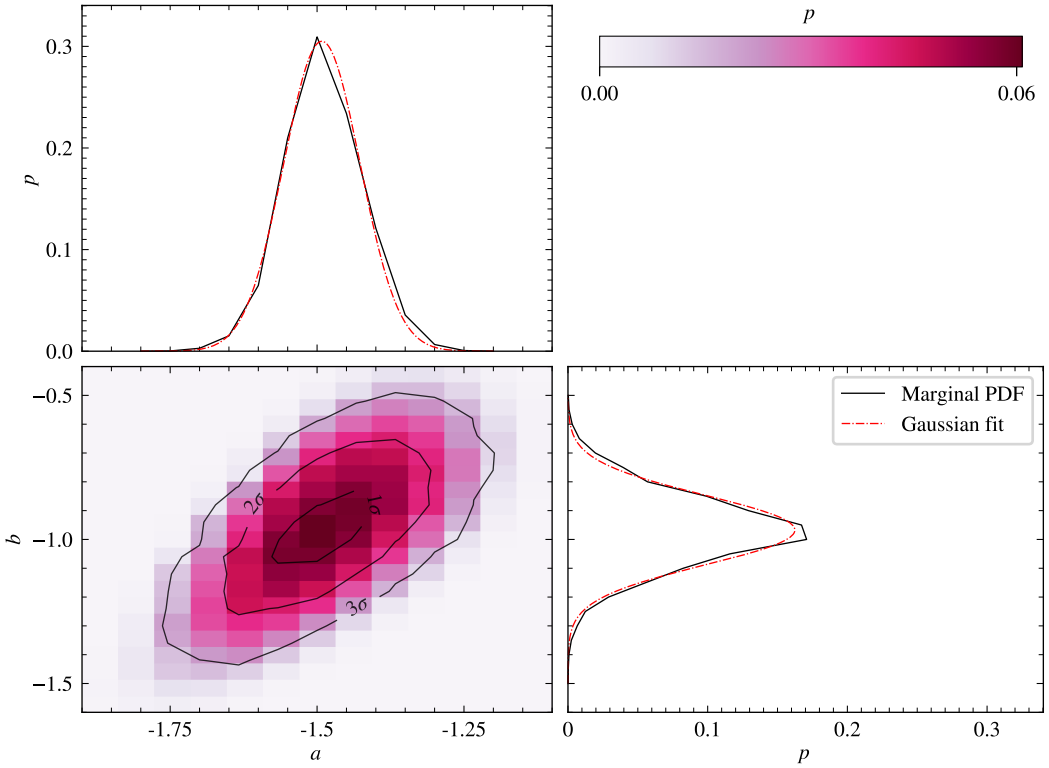

Figure 4.15: The relative fitting probabilities evaluated for each jet power and lifetime model. The corresponding probability density function (PDF) mapped in (a, b)-space is shown in the bottom left panel. A sequential colour-map is used to indicate the probability for each model, and is shown using a logarithmic stretch. Contours denote the 1σ, 2σ and 3σ confidence intervals. The adjacent panels demonstrate the PDF marginalised for a (upper left panel), and b (lower right panel), as shown by the solid black curves. The red dot-dashed curves show the Gaussian approximations of the marginal PDFs.

acterise the peak-probable value and the 1σ standard deviation. As such, we constrain the power-law slopes of the jet power and lifetime distributions as:

$$\begin{aligned} p(Q) &\propto Q^{-1.5\pm0.1} \\ p(t_{\rm on}) &\propto t_{\rm on}^{-1.0\pm0.1} \end{aligned} \quad . \tag{4.12}$$

The jet power and active lifetime distributions predicted by this model are compared to the observed distributions in Fig. 4.16. We can see that the shape of the mock active age distribution agrees with observation; the mock distribution follows the same initial rise in number counts as the observed distribution towards

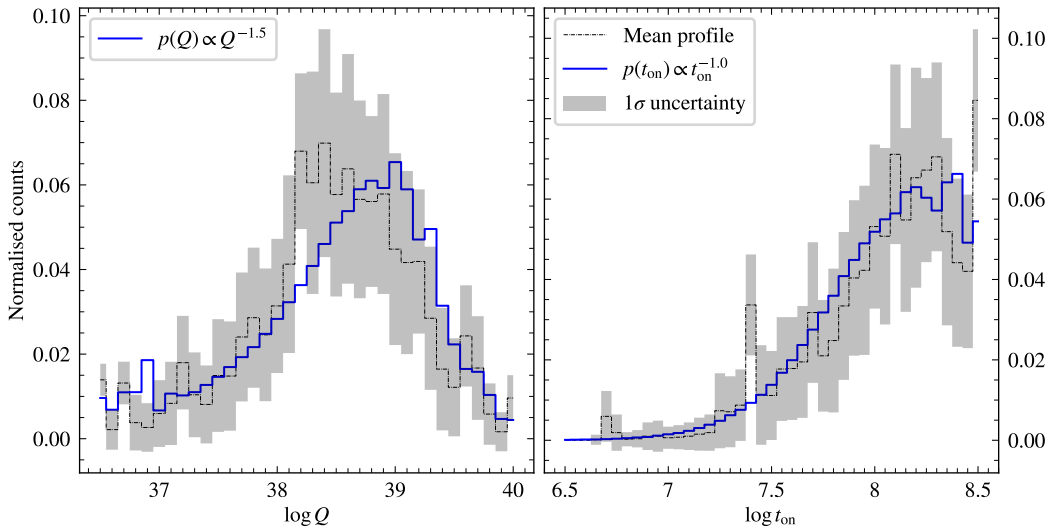

Figure 4.16: Same as Fig. 4.6, but overlaying the predictions made by our best-fit jet power and lifetime model (i.e. $p(Q) \propto Q^{-1.5}$ and $p(t_{\rm on}) \propto t_{\rm on}^{-1.0}$).

longer-lived sources, and exhibits a similar turnover at $t_{\rm on} = 10^{8.25}$ Myr. Within uncertainties, the general shape of the mock jet power distribution also appears consistent with observation; the number density of sources at the higher and lower-powered ends are in agreement with each other, and the turn overs in each distributions are comparable. However, several potential inconsistencies should be pointed out. Firstly, the turnover in the mock jet power distribution ($Q = 10^{39}$ W) occurs at roughly an order of magnitude higher than that in the peak-probable observed distribution ($Q \approx 10^{38.2}$ W). Secondly, the rate at which the mock distribution falls off towards low-powered sources is not as steep as what appears to be the case for our observed sample. In fact, by manually inspecting the predictions made our mock catalogues (but see Fig. 4.14), we find that no model is able to simultaneously replicate each of these features. Flatter values of a give the correct fall-off towards low Q, but turn over at much higher jet powers. Steeper values of a predict a closer turn over to what is observed, but over predict the number density of low-powered objects.

We speculate that one potential explanation could be that the true jet power function flattens below a certain jet power, Q_*, which would be expected if the broken power-law nature of the AGN radio luminosity function is driven directly

by shape of the jet power function. Such a model should in principle provide a solution to the two inconsistencies outlined above; by flatting below some Q_*, the expected fall-off towards low-powered sources should be sharper than what is currently shown by our mock catalogue in Fig. 4.6. Considering our relatively low sample size ($N = 79$), we have chosen not to fit a broken power-law jet power model for this work. Nevertheless, under the assumption that the jet power function is indeed more appropriately described by a broken power law, our results here show a promising future application for radio galaxy populations revealed by next-generation radio surveys.

4.5.2 Comparison with literature

4.5.2.1 AGN radio luminosity functions

Historically, our strongest constraints towards the shape of the true jet power function have come from the radio-loud AGN radio luminosity function. Extensive work exists within the literature that constrains the AGN RLF, and we focus on several recent results to examine the consistency with our model expectations.

Using the GLEAM radio survey, Franzen et al. (2021) measured the 200 MHz radio luminosity function for local (median $z \approx 0.064$) radio galaxies. By fitting their observed AGN RLF using a broken power-law model, they constrain a power-law slope of $\alpha_{\mathrm{RLF}} = -1.76$ above a critical radio luminosity ($L_\star = 10^{25.76}\,\mathrm{W\,Hz^{-1}}$). Using a theory-driven first-order approximation of the conversion between radio luminosity and jet power, $Q \propto L_\nu^{6/7}$ (Willott et al., 1999; Kaiser & Best, 2007), this suggests that the power-law slope in their corresponding jet power function is $a \approx -2$. Though considerably steeper than the power-law index constrained by our method ($a = -1.50 \pm 0.09$), comparing these values must be exercised with caution. Since the observed radio luminosity of a radio source is strongly confounded by its jet power, age, and ambient environment (Hardcastle & Krause, 2013; Shabala & Godfrey, 2013; Yates et al., 2018), the resulting scatter in the AGN RLF prevents the direct inference of the jet power function. The

effects of a selection bias may also contribute towards the apparent mismatch between the fitted jet power slopes. Although powerful radio sources will have bright radio luminosities, such sources will also have large physical sizes, which may contribute to a deselection from brightness-limited radio surveys.

It is interesting to note that the 150 MHz AGN RLF measured by Shimwell et al. (2019), who used radio sources selected as part of the first data release of the LOFAR Two-Metre Sky Survey (LoTSS DR1; Shimwell et al., 2019), appears flatter at the high-luminosity end as compared to Franzen et al. (2021). It is entirely possible that this is driven by their low-number statistics at brighter luminosity bins, since their sample probes a smaller cosmological volume at low redshifts. However, taking their result at face value would imply a flatter jet power distribution at high jet powers, and thus qualitatively in better agreement with our fitted value.

4.5.2.2 Constraints from previous forward modelling

In recent years, several authors have employed forward modelling to constrain the bulk properties of radio-loud AGNs based on the distributions in their observed attributes. Hardcastle et al. (2019) used the dynamical model of Hardcastle (2018) to apply forward modelling to radio-loud AGNs unveiled by LoTSS DR1. As part of their analysis, they tested the validity of two different lifetime models in which the observed active ages were distributed uniformly in either linear age ($b = 0$ in this work), or in logarithmic age ($b = -1$ in this work). They assumed a jet power distribution of $p(Q)dQ \propto Q^{-1}$. To examine the validity of their lifetime models, the linear size distributions were forward modelled for each model assumption, and compared to the observed size distributions for three radio luminosity bins. Their main finding (see their Sect. 4.2) is that neither lifetime distribution was able to simultaneously explain the observed size distributions. Their linear age model gave excellent agreement with the size distributions in the brightest two bins, however vastly under-predicted the fraction

of small ($< 100\,\mathrm{kpc}$) radio sources in the faintest bin. On the other hand, at the highest two luminosity bins, their log-uniform lifetime distribution vastly over-predicted the compact fraction, and simultaneously under-predicted the observed size distributions. We return to these results further below.

Shabala et al. (2020) employed RAiSE forward-modelling to constrain the jet power and lifetime distributions for a LOFAR-selected sample of radio galaxies. For a given evolutionary jet model, they forward-modelled radio galaxy populations, applied survey selection biases, and compared their predicted angular size and flux density distributions to those observed for their sample. In particular, they tested power-law and constant-age models, and found that both could plausibly explain the observed properties of their active radio sources. To break down the degeneracy between the two ageing models, they compared the mock remnant and restarted fractions with observation, and found that power-law ageing models offered much better agreement. In particular, they found that a model with $p(Q) \propto Q^{-1}$ and $p(t_{\rm on}) \propto t_{\rm on}^{-1}$ offered excellent agreement with their observed sample, with $p(t_{\rm on}) \propto t_{\rm on}^{-0.5}$ also offering good agreement.

Commenting on the consistency between our results and those of the two aforementioned studies is difficult, considering that the both the methodologies we have adopted and the radio galaxy samples we have used are different. Both Shabala et al. (2020) and our work constrain the same optimal lifetime model ($b \sim -1$), and is tentatively in agreement with Hardcastle et al. (2019). Both these authors find considerably flatter jet power models, which may be a result of the sample selection. In Sect. 4.5, we speculated that the true jet power function may be more appropriately described by a broken power law, such that a flattening would occur below some critical value. The jet powers fitted by Shabala et al. (2020) for their sample show a peak in their distribution at $Q \approx 10^{37.7}\,\mathrm{W}$ (see their Fig. 3), almost an entire order of magnitude lower than our sample. We therefore speculate that the flatter jet power distribution constrained in their work could simply be a consequence of their sample probing a lower-powered

portion of the jet power function.

It should also be noted that the method taken for this work is considerably different to the approaches taken by the two aforementioned authors. In our approach, we have directly fitted the observed jet powers and active ages of individual sources and then applied corrections for selection biases that transform the true shape of their distributions. On the other hand, both Hardcastle et al. (2019) and Shabala et al. (2020) inferred their intrinsic model properties based only on the distributions of the observed radio source attributes (flux density and/or angular size). One potential issue with this approach is that both the radio luminosity and physical size are confounded by jet power and age, meaning their distributions could plausibly be explained by various evolutionary jet models. For example, while Shabala et al. (2020) find good agreement for both $b = -1$ and $b = -0.5$, our results instead show that $b = -0.5$ can not be compatible with the observed active age distribution (see Fig. 4.15 and discussion below).

As a consistency check, we filter the two models of Hardcastle et al. (2019), and the two plausible models of Shabala et al. (2020) through our selection criteria, and compare their expectations to our fitted jet power and active age distributions. This is shown in Fig. 4.17. We focus on the comparison between the mock and observed ages, since the mismatch in the jet power distribution has been discussed in Sect. 4.5 (see also Fig. 4.14). We can see that for their $b = -1$ models, the observed active ages appear over- and under-predicted for younger ($t_{\rm on} \leqslant 10^8\,{\rm Myr}$) and older ($t_{\rm on} \geqslant 10^8\,{\rm Myr}$) sources, respectively. This is not surprising; the higher-powered jets allow for more younger sources to pass the angular size/flux density cuts, whereas the increased radiative losses are pushing more aged remnants below the surface brightness/flux density limit. The $b = -0.5$ model appears to compensate somewhat for this, however the model is clearly incompatible considering the associated jet power distribution. Finally, we find that the $b = 0$ model vastly over-predicts the distribution of long-lived sources, and exhibits a sharper rise with age in comparison to observation. We

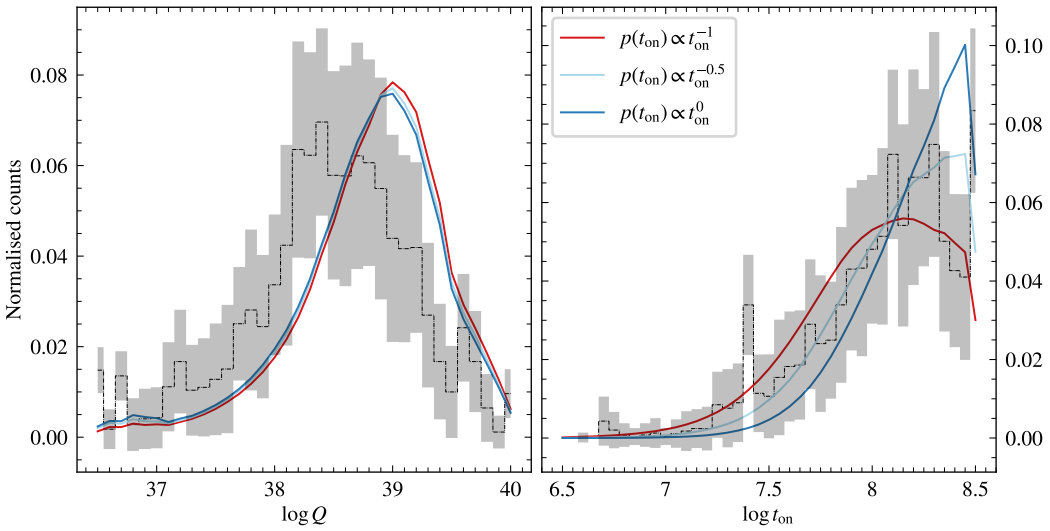

Figure 4.17: Models constrained by Hardcastle et al. (2019, H19) and Shabala et al. (2020, S20) are filtered by the selection biases of our sample, and their expected jet powers and active ages are compared to our observed sample distributions. Three models are shown, each with the same assumption of the jet kinetic power function ($a = -1$), but with varying lifetime functions. The model with $b = -1$ is shown in red (H19, S20), that with $b = -0.5$ is shown in light-blue (S20), and that with $b = 0$ is shown in dark-blue (H19). Model predictions are smoothed using a 0.3 dex kernel.

note our results here are not intended to invalidate those of the previous authors, considering that their sample properties and selection biases are unaccounted for in this comparison. Rather, we only propose that such models can not be true for the intrinsic parameter space occupied by our sample, and should be resolved in future work by using larger and more representative radio galaxy samples.

Importantly, the results shown in Fig. 4.17 highlight the advantage of the approach taken for this work; by directly fitting to the observed jet power and active age distributions, our results are not hampered by their confounding impact on the observed attributes of radio sources. Finally, it is worth pointing out that the active age distribution fitted for our remnant sample offers direct evidence against constant age models, and is in support of the conclusions of Shabala et al. (2020). Considering that we have directly measured the full lifetime of the jets in these sources, we would expect the fitted active ages to occupy a single value, within fitting uncertainties, if their underlying lifetimes were that of a constant age.

4.5.3 Application to active radio galaxy populations

While the approach taken for this work focused solely on remnant radio galaxies, our methods for simulating mock radio source populations can be generalised to the wider radio-loud AGN population; e.g., to active radio galaxies, which make up $\sim 80\%$ of the observed radio source population (e.g. see; Jurlin et al., 2020). As mentioned in Sect. 4.1, the active age measured for an active radio galaxy represents the age at which the source is observed, τ, not the true duration of its jet active phase. This pushed Turner & Shabala (2015) to make an assumption about the true lifetimes of the jets based on age fitted for each source; i.e. $\tau = t_{\rm on}/2$, which says that on average a source will be observed halfway through its true jet lifetime. It is however worth noting that an alternative approach to the problem could involve directly simulating an observed τ distribution. For a mock radio source, τ can be simulated by uniformly sampling, in linear space,

the range bounded by $t = 0$ and $t = t_{\rm on}$. For any underlying $t_{\rm on}$ model, a corresponding τ distribution can thus be simulated and filtered by the selection criteria, as outlined in Sect. 4.4. For a large mock catalogue, averaging over the noise fluctuations due to random sampling, a mean expectation for the selection-biased age distribution, e.g. (τ), can be created. Importantly, by applying the selection biases, (τ) essentially characterises the distribution of $\tau = t_{\rm observed}/2$, where $t_{\rm observed}$ gives the duration over which the source will remain detected and selected as part of the sample. Of course, a caveat with this method is it relies on probing the average observed age distribution, meaning that samples much larger than that of this work will be needed to confidently measure the height at each age bin.

4.6 Conclusion

Within the framework of radio-loud AGN feedback, the existence of remnant radio galaxies is naturally explained by the self-regulating impact the jets have on their supply of fuel. The active and inactive phases in the jet activity are encoded in observations of active, remnant and restarted radio sources, and represent key components of the underlying jet evolutionary lifecycle. Due to its profound connection to AGN feedback, the energies injected by the jets is a topic of much interest. In this work, we have approached this problem by constraining the underlying jet kinetic power and lifetime functions for a sample of low redshift ($0.02 \leqslant z \leqslant 0.2$) remnant radio galaxies. Our approach exploits the physics of remnant lobes by directly measuring the full duration of their active phase, thus placing firm constraints on the jet lifetime function.

We used all-sky multi-frequency radio data to compile sources around a fixed selection criteria, i.e. $S_{154} \geqslant 0.5\,{\rm Jy}$ and $\theta \geqslant 4'$, and identified remnant lobes using variety of literature-established methods (Sect. 4.2). The evolutionary histories of each source were then constrained using the RAiSE dynamical model. Simulated radio source attributes were compared with observation through a parameter

inversion, which allowed fitting of, amongst other parameters, the jet kinetic power and active age for each remnant (Sect. 4.3). However, due to selection bias, the fitted jet power and active age distributions do not represent their true underlying population statistics. To combat this, we demonstrated that mock remnant populations can be simulated for assumed (power law) models of their jet powers and lifetimes, and filtered by the sample selection criteria. By accounting for the observed distribution in, principally, redshift and environment, predictions for the selection-biased jet power and active age distributions can be made for our sample (Sect. 4.4). Using this framework, we generated mock catalogues of remnant populations over a range of plausible power-law indices for the jet power and lifetime functions, and produced selection-biased distributions for the observed jet powers and active ages. The mock predictions were compared with observation, which allowed us to constrain the optimal jet evolutionary model (Sect. 4.5).

We summarise our results as follows:

- We constrain a jet kinetic power function described as $p(Q) \propto Q^{-1.5\pm0.1}$, and a lifetime function described as $p(t_{\rm on}) \propto t_{\rm on}^{-1.0\pm0.1}$.

- Our results are consistent with the expectations of feedback-regulated accretion simulations, which consistently predict a power-law spectrum in the black hole accretion rates, consistent with a $p(t_{\rm on}) \propto t_{\rm on}^{-1}$ lifetime distribution triggered at the black hole.

- Our constrained jet power function appears broadly consistent with the shape of the high-luminosity end of the AGN radio luminosity function constrained by Shimwell et al. (2019) and Franzen et al. (2021). We speculate that the true jet power function is better described by a broken power-law model, in which the jet kinetic power function flattens towards lower values.

- Our jet lifetime distribution aligns remarkably well with the fitted distributions of Shabala et al. (2020) and Hardcastle et al. (2019). However,

our approach allows us to impose more precise constraints on the range of plausible models, thanks to directly fitting the observed jet power and lifetimes, rather than relying on the overall distribution of observed radio galaxy properties.

Despite the focus of this work on remnant radio galaxy, our methodology is certainly applicable to active radio galaxy populations. Considering these objects dominate flux and volume limited samples, their statistical significance is an attractive property that should be exploited in similar analyses. In particular, following the method of this work, such objects represent an ideal laboratory for constraining the underlying jet kinetic power function. The jet lifetime function may also be constrained, however would require additional modelling to simulate the selection of a radio source throughout its jet active phase.

Finally, we articulate that the ability to generate mock predictions, based on any sample distributions and selection criteria, is an exciting prospect for future work. By modelling the sample selection biases, jet evolutionary models can be constrained from the full range of observed jet powers and ages, importantly, including shorter-lived and low jet power sources that are preferentially deselected from radio surveys. Considering these are precisely the objects that make up the dominant fraction of radio-loud AGNs, constraints on their energetics are vital towards feedback studies. With the advent of new generation radio surveys such as LoTSS, the Evolutionary Map of the Universe (EMU; Norris, 2011), and eventually those produced by the Square Kilometer Array, constraints on the global energetics of radio-loud AGNs will dramatically improve. Not only will these surveys provide large, statistically-significant samples of radio galaxies, their sensitivity and angular resolution will allow for much lessened selection biases. This will allow, for example, the testing of higher-order models (e.g. double power-law jet kinetic power models), and investigating whether the correlations exist between the jet kinetic powers and lifetimes. Furthermore, with the inclusion of higher-quality optical/infrared (e.g. the LOFAR-WEAVE survey; Smith et al.,

2016) and X-ray (e.g. eROSITA; Predehl et al., 2021) data, our methodology can be extended to explore the environmental impact on AGN fueling.

Chapter 5

Conclusion

In this chapter, I summarise the research undertaken as part of this thesis, and discuss the main results and implications for future work.

5.1 Research summary

In this thesis, I have investigated how remnant radio galaxies can form critical tools to improve our understanding of AGN populations and their life-cycles. This work is based on my initial work to create a consolidated catalogue of remnants from multi-frequency radio observations and implementation of state-of-the-art dynamical models to infer the physical characteristics of individual objects. My work began by exploring the established remnant selection methods in order to examine their viability in future radio surveys (Quici et al., 2021, Chapter 2). Building on these results, I then developed a new dynamical model-based method to identify remnant radio galaxies and measure their intrinsic radio source parameters (Quici et al., 2022, Chapter 3). To take advantage of this technique, I measured the jet kinetic power and active age distributions for a sample of remnant radio galaxies, and used these to constrain models for the jet kinetic power and lifetime functions (Chapter 4). In the following sections, I summarise the research motivations, methodologies, and results of the work presented in each

chapter.

5.1.1 Remnant radio galaxies discovered in a multi-frequency survey

Motivation

The subject of the remnant fraction – the fraction of radio-loud AGN observed in a remnant phase – has gained much attention in recent years with the advent of new-generation, low-frequency radio surveys. The remnant phase is a key component in the evolution of radio galaxy lobes, and thus offers valuable constraints on the physics of AGN jet evolution. In particular, Hardcastle (2018) and Shabala et al. (2020) demonstrated that the observed remnant fraction allows for constraints to be placed on the radio-loud AGN lifetime functions. Prior to the commencement of this work, several constraints on the remnant fraction existed, yet some inconsistency in the results appeared to exist at a level significant to the method of Shabala et al. (2020). In this chapter of work, I exploited the sensitive, high-frequency and high-resolution images provided by GLASS to construct a uniformly-selected sample of remnant radio galaxies.

Methodology

First, I compiled an observationally-complete parent sample of radio galaxies within a $7.62\,\mathrm{deg}^2$ area of sky. Using deep MIDAS data, I selected all radio sources brighter than 10 mJy at 216 MHz. Using GLASS (5.5 GHz) and EMU ES (887 MHz) data, I then selected sources with a largest angular size greater than $25''$. Using the near-infrared VIKING images to examine the radio source environments, radio sources were removed if the extended radio emission traced the optical component of a star forming galaxy. Following this approach, I selected a parent sample of 104 radio galaxies.

I adopted the 'absent radio core' criterion to select candidate remnant radio

galaxies on the basis that these sources did not show evidence of an active nucleus. The criterion was evaluated using the 5.5 GHz GLASS data, where the detection of a radio core was decided at the 3σ level. A total of 10 remnant radio galaxies were selected via this approach.

For each remnant candidate, I obtained low-resolution photometry (to obtain total flux densities) at 5.5 and 9 GHz, and measured a low-frequency (119-375 MHz) and high-frequency (887 MHz-5.5 GHz) spectral index. In addition to this, I estimated the 216 MHz core prominence (CP) for each source in the parent radio galaxy sample. To do this, I re-scaled the 5.5 GHz peak flux density of the core to 216 MHz, assuming a flat-spectrum radio core. For remnant candidates, upper limits were instead calculated based on the 3σ limit on the radio core flux density.

Results

Within the parent sample of 104 radio galaxies, my method identified 10 remnant radio galaxies candidates, which constrained a 10/104 ($\lesssim 10\%$) upper limit to the observed fraction of remnant radio galaxies. Although this result was consistent with several LOFAR-based studies (Brienza et al., 2017; Mahatma et al., 2018), I was unable to unambiguously confirm the remnant classification in a majority of the selected candidates.

Of the ten selected remnant candidates, only four displayed the unambiguous lobe characteristics of a remnant radio galaxy such as: an ultra-steep or highly-curved radio spectrum, or; relaxed, amorphous lobe morphologies absent compact features such as hotspots. In the remaining remnant candidates, compact high-frequency emitting regions were observed in the GLASS images, consistent with jetted-hotspots. The radio spectral energy distributions in these sources showed no significant evidence of spectral steepening, and exhibited spectral indices within $-0.9 \leq \alpha \leq -0.6$, consistent with those typically found for active radio sources. These results implied one of two scenarios. Either these remnant

candidates are genuine, in which case the jets must have switched off recently due to the continuing presence of compact high-frequency lobe emission, or the sources are in-fact misclassified active radio galaxies, in which case the absent radio core technique suffered heavy pollution from spurious contaminants.

In an attempt to ascertain the correct scenario, I investigated the 216 MHz CP distribution as a function of the total 216 MHz flux density, and examined whether the upper limits placed on the remnant candidates could help to solidify their classification. I found that the remnant candidates with the highest (and therefore weakest) upper limits on their CP were in-fact those unambiguously classified as a remnant. I speculated that this result was due to the rapid evolution in radio luminosity during the remnant phase, which would act to increase the upper limit on the CP as the remnant continued to age. On the other hand, remnant candidates with hotspots were found to exhibit much lower CP upper limits; however, they were not found to exceed the lowest values measured for the core-detected radio galaxies. As such, I was unable to confirm the remnant classification in these objects.

5.1.2 Selecting and modelling remnant radio galaxies with limited spectral coverage

Motivation

Remnant radio galaxies offer valuable insights into the physics of radio-loud AGN. Not only do they probe the final stages in radio galaxy evolution, they also provide valuable constraints towards the lifetime function of radio-loud AGNs. Such fields of study will be greatly aided by the new generation of low-frequency radio surveys, however may be limited by the existing methods for the selection and modelling of remnant radio galaxies. Surveys such LoTSS, MIGHTEE, APERTIF, EMU, and eventually those produced by the SKA will provide high-resolution observations with excellent sensitivity to low surface-brightness emission, but will

unlikely have comparably-deep high-frequency ($\nu > 5\,\mathrm{GHz}$) analogues that are required by the conventional remnant classification (Jurlin et al., 2020) and modelling (Turner, 2018) methods. In this chapter of work I therefore approached this problem from a new perspective, which used the observed surface brightness distribution of remnant radio lobes to help constrain their evolutionary histories. The key methods and results of this work are summarised below in two parts, addressing first the development and verification of the method, followed by further insights gained from mock radio source catalogues.

Development and verification of method

To provide an independent verification of our method, I performed detailed spectral modelling of the $z = 0.2133$ remnant radio galaxy J2253-34, which was identified as a remnant by Quici et al. 2021 (Chapter 2). First, I obtained sensitive, high-resolution radio observations at 417, 682 MHz (uGMRT), 1.4 GHz (MeerKAT), and 5.5, 9 GHz (ATCA). Using apertures of $\theta = 8''$, I extracted the radio spectra arising from narrow regions across the lobes, and applied the TJP (Tribble Jaffe-Perola) model to fit for the global injection index ($s = 2.25 \pm 0.05$). Together with archival GLEAM data, I used the fitted injection index and modelled the integrated radio spectrum of the lobes using the TCI (Tribble continuous injection) model. This allowed us to fit the break in the frequency spectrum ($\nu_\mathrm{b} = 1.26^{+0.06}_{-0.05}\,\mathrm{GHz}$), and importantly the remnant ratio ($R_\mathrm{rem} = 0.23 \pm 0.02$), which describes the ratio of remnant phase to the total lifetime of the source.

To develop our dynamical model-based method, I exploited the Turner et al. (2022) 'jet+lobe' RAiSE model which produces hydrodynamic-informed synchrotron emission maps of synthetic radio lobes. As a way to constrain the duration of the remnant phase, our method relies on the expected fading of the synchrotron emission from older, less energetic electrons in the part of the lobe closest to the core. I therefore required a metric that could be used to compare this property between simulation and observation, and as such implemented

skewed Gaussian functions to fit the surface brightness distribution of the lobes. Importantly, via this approach I was able to quantify two 'extent' observational attributes, which parameterised how far back the lobe observably swept towards the host galaxy.

To verify our method, the intrinsic parameters of J2253-34 were fitted via a RAiSE-based parameter inversion using two different sets of constraints. First, I generated a grid of RAiSE models in jet power, source age and equipartition factor, and fit these parameters using a 151 MHz radio luminosity, size and break frequency. Importantly, all synthetic sources in this grid of RAiSE models were simulated with $R_{\rm rem} = 0.23$, so as to match the value fitted for J2253-34 via spectral modelling. Next, I generated a second grid of RAiSE models in jet power, source age, equipartition factor, and remnant ratio, and fit these parameters using a 151 MHz radio luminosity, size, the 'extent' attributes, a low-frequency spectral index, and a three-point spectral curvature measure between 151 MHz (LOFAR) and 1.4 GHz (MeerKAT) frequencies. Importantly, as this represented our realistic "absent spectral modelling" case, our objective here was to test whether the extent attributes were capable of constraining the duration of the remnant phase.

Although with slightly larger fitting uncertainties, our results showed that the fitted jet power ($3.98^{+0.36}_{-0.40} \times 10^{38}$ W and $6.32^{+2.11}_{-1.63} \times 10^{38}$ W) and active ages ($t_{\rm on} = 43.3 \pm 4.3$ Myr and $t_{\rm on} = 37.2 \pm 4.3$ Myr) were in broad agreement between the two methods. The remnant ratio fitted via the RAiSE-based parameter inversion was $R_{\rm rem} = 0.26^{+0.04}_{-0.03}$, consistent with that constrained via spectral modelling. With these results, I argued in favour of the proof of concept that the energetics of remnant radio loud AGNs can be constrained via our proposed method.

Insights from mock catalogues

To further test the validity of our method, I used mock catalogues of remnant radio galaxies to understand the parameter space over which the technique may

be expected to work/break down. Mock remnant catalogues were simulated uniformly across a range of plausible jet powers, lifetimes, magnetic fields, and remnant ratios. To obtain insights applicable to modern radio surveys, synchrotron surface brightness maps were generated at the typical observing frequencies of LOFAR (150,MHz) and MeerKAT (1.4,GHz). To replicate realistic observing conditions, the synthesized images were degraded by the RMS sensitivity and spatial resolution of their respective survey analogs. Observable attributes associated with the "absent spectral modeling" case (as above) were extracted from the degraded images for each synthetic source. These observed attributes were then used as inputs to fit the intrinsic properties of the radio sources using the parameter inversion method. By comparing the fitted and input parameters of each synthetic source, the capabilities and limitations of the technique were studied across the model parameter space.

I found that the jet power, source age, equipartition factor, and remnant ratio were consistently fit by our method, though the jet power and source age were constrained with the highest precision. Our results implied that the technique is expected to deliver more confident results when the magnitude of the energy losses sustained in the remnant phase are greater, which is true in the following cases: higher redshifts, due to increased strength of IC losses; higher-powered jets, due to the increase in magnetic field strength; and for a greater duration of the remnant phase.

To examine how well the technique was able to classify remnant radio galaxies, I considered the accuracy in the fitted remnant ratios. I found that remnant ratios fitted by this method can be trusted if the measured source age is large, and conversely, is less accurate for younger sources. To interpret the on/off-times fit by this method, and thus the classification of remnant radio galaxies, one should first consider the age of the source to determine if the fitted remnant ratio is estimated reliably. To quantify the selection efficiency, I simulated an active ($R_{\rm rem} = 0$) and several remnant ($R_{\rm rem} = 0.1, 0.2$) mock catalogues, and examined

their distributions in the fitted remnant ratios. At low redshift ($z \sim 0.1$), I found that sufficiently aged sources ($\tau > 50\,\mathrm{Myr}$) fitted with $R_{\mathrm{rem}} \leq 0.1$ are active radio galaxies within a confidence of 95%; this extends to sources as young as $\tau \sim 10\,\mathrm{Myr}$ at higher redshifts ($z \gtrsim 0.5$). Similarly, I found that sources fit with $R_{\mathrm{rem}} \geq 0.1$ are true remnant radio galaxies within a confidence of 95%. These classifications are expected to become more robust towards higher redshifts. Overall, our results here showed that our method is capable of selecting active and remnant radio galaxy candidates.

5.1.3 Constraining evolutionary jet models using remnant radio galaxies

Motivation

The energies imparted by AGNs onto their environments play a key role in the evolution of their host galaxies and large-scale environments. The jets launched from a supermassive black hole are triggered with some jet kinetic power and lifetime, which together enable the derivation of their total time-averaged energy budget. The jet power and lifetime functions of the radio-loud AGN population are thus an important prescription towards AGN feedback models, and also provide valuable insight into the accretion mechanisms responsible for triggering AGN jets. In this final chapter of work, I therefore set out to constrain the jet power and lifetime functions for a local sample of remnant radio galaxies.

Methodology

To constrain the jet power and lifetime function, I carried out several key methodological steps summarised below.

First, I compiled a sample of remnant radio galaxies to provide an observational reference frame for this work. Using a variety of all-sky radio surveys, I compiled a parent sample of radio galaxies brighter than $S_{154} = 0.5\,\mathrm{Jy}$ at 151 MHz,

larger than $\theta = 4'$ in projected angular size, and between the Declination range $-90° \leq \delta_{\rm J200} \leq 30°$. After visually cross matching the radio sources with their hosts, optical photometries and archival redshifts were obtained for each host. After limiting the sample to $0.02 \leq z \leq 0.2$, I estimated the stellar masses based on the $(g - i)$ colour and i-band magnitude, and used this estimate to infer the total mass in the galaxy halo. I used a combination of literature-established methods, e.g. the absent radio core criterion, the morphological criterion, and the ultra-steep spectrum criterion, to select remnant radio galaxies from the parent sample. Following these methods, I arrived at a sample of 79 local remnant radio galaxies. Finally, for each selected remnant, I measured a range of radio source attributes, which were needed to constrain their evolutionary histories.

Next, following the method of Quici et al. 2022 (Chapter 3), I constrained the jet power and active age of each source to characterise their sample distributions. I used the Turner et al. (2022) 'jet+lobe' RAiSE model to create a multi-dimensional grid of synthetic radio sources in jet power, active age, remnant ratio, halo mass, equipartition factor and injection index. The parameter space of the RAiSE simulation grid was inverted as per the redshift and survey limitations (sensitivity and angular resolution) of each source, and the simulated radio source attributes were extracted from the synchrotron surface brightness maps. I used a maximum likelihood algorithm to compare simulated to observed attributes, and used a grid-search to fit each model parameter. The sample distributions in jet power and active age were compiled, and revealed the unphysical lack of lower-powered and shorter-lived radio sources caused by selection effects.

To deal with these inherent sample selection biases, I employed forward modelling of mock remnant populations to directly model the effect of my sample selection criteria. First, I assumed simple power-law models to describe the underlying form of the AGN jet power ($p(Q) \propto Q^a$) and lifetime ($p(t_{\rm on}) \propto t_{\rm on}^b$) distribution, which were used to weight the parameter space of the RAiSE simulation. Next, for a given mock redshift, I used the synchrotron surface brightness

maps to test whether the synthetic radio sources would have passed the sample selection criteria, and described the outcome using a binary 'yes/no' filter. To eliminate systematic errors, the confounding variables in the mock catalogues (redshift, halo mass, equipartition factor, injection index) were controlled for by ensuring their mock distributions matched observation after the selection biases were applied. Following this approach, mock distributions in the observed jet powers and active ages could be generated for any assumed jet power and lifetime model.

Results

To constrain an evolutionary jet model, mock remnant catalogues were generated with different exponents for the power-law distributions of both jet power and lifetime. Exponents were searched between $-2.6 \leq a \leq -0.6$ and $-2 \leq b \leq -0.5$ for the jet power and active age models, respectively. For each mock catalogue, the mock observed jet powers and active ages were binned in $(Q, t_{\rm on})$-space, and compared to observation using a maximum likelihood algorithm. The key outcomes of this work are summarised below.

The main result of this work was that I tightly constrained a jet power function of the form $p(Q) \propto Q^{-1.50\pm0.09}$, and a lifetime function of the form $p(t_{\rm on}) \propto t_{\rm on}^{-1.0\pm0.12}$. The mock jet power and active age distribution predicted by this model were demonstrated to have good agreement with the shape of the observed sample distributions, however I speculated that a broken power-law model for the jet power function may have provided a better fit to the data; such an assumption would be expected if the broken power-law shape of the AGN radio luminosity function is directly due to the underlying jet powers. Our fitted lifetime function was in excellent agreement with the results of Hardcastle et al. (2019) and Shabala et al. (2020), and I argued that the apparent inconsistency between the constrained jet power models (i.e. they fit $a = -1$) is likely due to inconsistencies in sample selection and methodologies. As an interesting side

outcome of this work, the distribution of active ages fitted for our remnant sample provided direct evidence against models in which AGNs live up to the same age, and supported the conclusion of Shabala et al. (2020).

5.2 Discussion and future work

In this thesis, I have conducted three independent pieces of work presented in Chapters 2, 3, and 4. A discussion of the results of these works is presented in each chapter, and I now move to address some of the wider implications and prospects for future work. First, I discuss the insights gathered regarding the advantages in studying remnant radio galaxies in context of radio-loud AGN physics (Sect. 5.2.1). Next, I discuss the lessons learnt regarding the selection of remnant radio galaxies from the next generation of radio surveys, and suggest some considerations for the future selection of these objects (Sect. 5.2.2). Finally, I discuss the insights from the AGN jet power and lifetime functions fitted in this thesis, and propose some exciting future directions to study the triggering of black hole jets (Sect. 5.2.3).

5.2.1 Remnant radio galaxies as laboratories to study the physics of radio-loud active galactic nuclei

While in previous decades even the detection of remnant radio galaxies was challenging due to survey limitations, the growing number of new generation radio surveys with high spatial resolution and excellent sensitivity to low surface-brightness emission (e.g. LoTSS) have proven to be excellent both for the detection and subsequent classification of remnant radio galaxies. Population studies of radio galaxy samples, in which the observed fraction and bulk properties of remnant radio galaxies were constrained, were used to place observational constraints onto the predictions made by various mock radio source populations with unique AGN life-cycle assumptions (see Hardcastle 2018 and Shabala et al. 2020). These stud-

ies have shown that the observed properties of their remnant samples (such as the physical sizes and radio luminosities) help to constrain the AGN jet-power and lifetime functions, and that the observed remnant fraction can be a powerful constraint to distinguish between constant and power-law age models. These results underline the value that remnant radio galaxies offer towards studying the evolution of radio-loud AGN, and it is with this idea in mind that I summarise the new insights gathered across this thesis.

The methodology employed in Chapter 4 differs significantly from the approaches used by Hardcastle 2018 and Shabala et al. 2020 in terms of how the jet and lifetime functions were constrained. While the aforementioned studies constrained their evolutionary models from the bulk distribution of several observed radio-source properties, the method presented in Chapter 4 utilised selection-biased distributions in the jet kinetic powers and lifetimes in order to constrain their seed distributions. Both approaches required modelling of the survey selection biases, however due to the confounding impact that jet power and age have on observed properties such as radio luminosity and size, the method I have developed is more effective at disentangling the true seed distributions by directly examining the sample jet power and lifetimes. While this distinction would equally hold for active radio galaxies, it is important to recognise that unlike an active radio galaxy, a radio galaxy remnant offers a direct measurement of the lifetime of its jet phase. As such, future studies investigating the duration of the jet phase in relation to other black hole properties would significantly benefit by leveraging the valuable constraints provided by remnant radio galaxy lobes regarding their embedded evolutionary histories.

Another key outcome of the work conducted in Chapter 4 was the ability to model and apply sample selection biases to synthetic radio sources. With this method, I am able to construct model distributions of the jet properties, which form close to the black hole, and generate testable predictions for their expected radio source populations. By adopting this method, future studies will be able

to place even greater constraints on the physics of AGN jet triggering (discussed in more detail in Sect. 5.2.3), using the intrinsic properties measured from radio galaxy populations. In this work, I have exploited dynamical models to constrain radio source energetics via parameter inversions. These methods have powerful applications to future radio surveys, in that they can simultaneously constrain various intrinsic properties using radio observations alone. One shortcoming of this method, however, is that the complexity of the model limits the objects which can plausibly be modelled. For example, a precession or a bending of the jets can lead to atypical lobe morphologies, rendering the constraints from their observed surface brightness distributions less meaningful. Furthermore, the typical 'continuous injection' spectra of radio lobes can also be modified by processes such as self absorption in the hotspots, or even renewed activity in the AGN jets. With this in mind, it is worth highlighting that remnant radio galaxies can provide a convenient solution to many of these issues. Upon cessation of the nuclear activity, the jets will disappear approximately over the light travel time, and will cease to contribute to the global characteristics of the lobes. Without the strong region of pressure provided by the jets, hot spots or any other compact emission regions left over from the previous jet activity, will quickly disappear due to the turbulent mixing of the lobe plasma. One caveat here is that the buoyant rising and Rayleigh-Taylor instability of remnant lobe plasma, which has an increasing impact with age on the observed properties of the lobes, is not currently captured by the RAiSE model; based on the numerical modelling of English et al. (2019), these processes should give rise to a faster decay in the lobe radio luminosity. The necessary framework from hydrodynamic simulations is already in place to integrate these physical processes into dynamical models (e.g. Yates et al., 2018; English et al., 2019), and will be an important step towards modelling the evolutionary histories of sufficiently aged remnants.

To summarise, remnant radio galaxies are excellent objects to study the physics of radio-loud AGNs. As part of my work, I show that the energetics

of remnant lobes can be constrained from radio survey data alone, and demonstrate their application towards constraining fundamental processes at the black hole. By encoding the full duration of their previous active jet phase, remnants provide a direct sampling of the jet lifetimes of radio-loud AGNs, and as such offer powerful constraints towards the AGN lifetime function.

5.2.2 Approaching the selection of remnant radio galaxies

In light of the discussion in the previous section, techniques to select remnant radio galaxies from radio survey data need to be robust. In this thesis, I confronted the selection of remnant radio galaxies via established methods, and have also proposed a novel dynamical model-based method in which the constrained remnant ratio determines the classification. In this section, I discuss the insights gathered regarding the selection of remnant radio galaxies, and suggest some future directions that may improve how these objects are selected from the next generation of radio surveys.

Observation-based methods:

In Quici et al. 2021 (Chapter 2), I demonstrated a trade-off between core-based and lobe-based remnant selection methods. The clear advantage to selecting remnant radio galaxies based on the absence of nuclear activity within the host, is the ability to identify those immediately after the jets have switched off. As expected, the absent radio core criterion selected sufficiently young remnants, which would otherwise have been missed (at least for given frequency coverage) by spectral classifications of the lobes. However, considering a significant fraction of selected remnant candidates displayed high-frequency hotspots and no evidence of spectral ageing up to 9 GHz, I concluded that the selected remnant sample was potentially contaminated by incorrectly-classified active radio sources. This underlines the shortcoming of the core-based method, which is that due to survey sensitivity limitations, the apparent absence of radio emission from the core does

not robustly confirm the remnant classification of the lobes.

The next generation of radio surveys (e.g. LoTSS, EMU, MIGHTEE, APERTIF, VLASS) will provide sensitive images of the sky with high spatial-resolution – in principle, the two key components necessary for detecting radio cores. These surveys will cover a low to intermediate frequency range ($\sim$ 0.1-2 GHz), and it is impractical to expect a high-frequency ($\nu \gtrsim 5$ GHz) analog with an appropriately-matched surface brightness sensitivity. In light of the discussion above, the immediate question this raises is as follows: if the absent radio core criterion is needed to select recently switched-off remnants, how do we break down the degeneracy between the properties of a recently switched-off remnant, versus an active radio galaxy with an undetected radio core? Ultimately, the question that needs answering is at what point (if at all) are the upper limits on the radio emission from the core significant enough to rule out an active radio core? In addition to this, to constrain the upper limit on the radio core emission, which metric is better – radio core luminosity, or, the radio core prominence? Radio galaxy samples compiled from the aforementioned surveys will have the required statistical significance to confront these questions, and will shed important light onto the robustness of these methods.

As another avenue for future exploration, it would be interesting to examine the insights provided by dynamical radio source models concerning the classification of (young) remnant lobes. As discussed in this thesis, spectral-based classifications of remnant lobes, e.g. ultra-steep or highly-curved radio spectra, rely on the preferential steepening of higher-frequency radio spectra resulting from the energy-dependent synchrotron loss rate. The spectral evolution of the remnant plasma is more rapid at higher energies, and is precisely why the selection of younger remnants requires higher observing frequencies. This raises the question, is it possible to rule out a remnant classification if the lobes *do not* show evidence of spectral steepening (within uncertainties) out to a given high frequency? A robust Bayesian approach to this problem could involve sim-

ulating mock remnant catalogues for our best assumption of the AGN jet power and lifetime functions, and using the forward-modelled radio source observables to examine, for example, the following questions: for what value of the remnant ratio should a source exhibit a detectable spectral steepening, or alternatively, for a given low remnant ratio (say $R_{\rm rem} = 0.1$), what fraction of sources should exhibit a detectable spectral steepening?

Another desired insight from simulations and dynamical models pertains to the prevalence and evolution of the hotspots after the jets switch off. For FR-II radio galaxies, the jet energy injection sites are over-pressured and contain strong magnetic field strengths. Considering also that the emission arising from the hotspot is driven by the youngest injected plasma, we can expect the hotspot to fade rapidly during the remnant phase. One caveat here however is the adiabatic expansion of the hotspot, which could plausibly give rise to an appreciably long-lived region of bright, compact radio emission. While currently the RAiSE model does not capture the necessary physics of the post-jet phase to model the adiabatic expansion of the hotspot, hydrodynamic simulations could be used to characterise the necessary particle histories. Such work should in turn shed important light on whether the selection of remnant radio galaxies should be robust to the presence/absence of hotspots, and similarly at what frequency should we expect genuine remnants to lack these compact features.

Dynamical model-based methods: a new approach to remnant selection?

In Quici et al. 2022 (Chapter 3), I demonstrated that the remnant ratio fitted by our dynamical model-based method can be used to classify active and remnant lobes. This technique utilises constraints derived from the observed surface brightness distribution of the lobes, which encode the plasma age distribution and thus the duration of the remnant phase. In many ways, the technique offers a combination of the established spectral and morphological-based classifications of

remnant lobes; by probing the bulk flow of the lobe plasma, the spectral evolution is constrained for the distribution of plasma ages (as opposed to a single integrated measurement), and therefore greater sensitivity to recently switched-off remnants.

The main advantage of this technique is that it does not require high-frequency ($\nu \gtrsim 5\,\mathrm{GHz}$) radio data to constrain the evolution in the remnant phase. The technique relies on detectable changes in the lobes to constrain the physics of the remnant phase, and so it comes as no surprise that the magnitude of the sustained energy losses limits the selection efficiency; this occurs for sources that have shorter timescales (in the active and/or the remnant phase), are lower-powered, and are at lower redshift. Nevertheless, with the aid of mock remnant catalogues, I showed that the technique is robust to the selection of remnants as young as $R_{\mathrm{rem}} = 0.1$, using frequencies as high as $\sim 1\,\mathrm{GHz}$. Therefore, while the technique is extremely suitable to the next generation of radio surveys, it is worth mentioning that the inclusion of higher radio frequencies will only further improve its constraining power. The requirement for sufficient model complexity is another limitation to this method, however as previously discussed in Sect. 5.2.1, this challenge is much less significant for radio sources without an active jet.

Setting aside the merits and shortcomings discussed above, a question that may arise pertains to the practical usefulness of this method in selecting remnants, considering the significant obstacle posed by relying on the redshift of the host galaxy. To address this question, we need to consider why the selection of remnants is important towards the study of radio galaxy life-cycles and AGN physics. Certainly if we treat the discovery/selection of remnants as its own independent research aim, e.g. to quantify their observed sample statistics, then the argument against selecting remnants using this technique is clear. However, if the objective is to employ remnants as a laboratory for further investigating the physical mechanisms associated with the duty-cycle and evolution of AGN jets, the emphasis extends beyond their selection to additionally encompass the

extraction of meaningful insights from their observations. The results of Shabala et al. (2020) showed that the observed fraction of remnants, alone, does not constrain AGN jet-triggering models without insights from forward modelling based partly on an observed redshift distribution. My work in Chapter 4 demonstrated that the intrinsic properties of remnant radio galaxies offer powerful constraints towards the jet power and lifetime functions, however, this could not have been achieved without prior knowledge of the host galaxy redshifts. Even considering the results of various single-object remnant studies (e.g. Cordey, 1987; Parma et al., 2007; Brienza et al., 2016; Duchesne & Johnston-Hollitt, 2019; Randriamanakoto et al., 2020; Singh et al., 2021; Quici et al., 2022), knowledge of the redshift was required to measure properties such as the spectral ages or lobe magnetic field strengths. It would appear then that in many current studies of remnant radio galaxies, particularly towards the research questions outlined above, the acquisition of redshift data is already a requirement. As such, assuming that redshift information is already available for a catalogue of extended radio galaxies, our dynamical model-based approach serves as a complementary tool to identify remnants and extract valuable insights into their underlying jet properties – both of which are important ingredients towards studying AGN duty-cycle studies. Finally, it is worth mentioning that sensitive, wide-area spectroscopic galaxy surveys, such as the William Herschel Telescope Enhanced Area Velocity Explorer instrument LOFAR survey (WEAVE-LOFAR; Smith et al., 2016) and the Wide-Area VISTA Extragalactic Survey (WAVES; Driver et al., 2016) will enable the compilation of radio galaxy samples with much greater spectroscopic completeness.

5.2.3 The jet power and lifetime functions of radio-loud AGNs

In Chapter 4, I presented a novel approach towards constraining models for the AGN jet power and lifetime functions. In this section, I discuss the key advantages

this framework brings, and highlight several exciting research questions that can be confronted with the next generation of radio surveys.

Constrained directly or via bulk inference?

Historically, our strongest constraints towards the shape of the true jet power function have come from the radio-loud AGN radio luminosity function. Extensive work exists within the literature that constrains the AGN RLF, and I focus on several recent results to examine the consistency with our model expectations.

Using the GLEAM radio survey, Franzen et al. (2021) measured the 200 MHz radio luminosity function for local (median $z \approx 0.064$) radio galaxies. By fitting their observed AGN RLF using a broken power-law model, those authors constrained a power-law slope of $\alpha_{\rm RLF} = -1.76$ above a critical radio luminosity ($L_\star = 10^{25.76}\,{\rm W\,Hz^{-1}}$). Using a theory-driven first-order approximation of the conversion between radio luminosity and jet power, $Q \propto L_\nu^{6/7}$ (Willott et al., 1999; Kaiser & Best, 2007), this suggests that the power-law slope in their corresponding jet power function is $a \approx -2$. Though considerably steeper than the power-law index constrained by our method ($a = -1.50 \pm 0.09$), comparing these values must be exercised with caution. Since the observed radio luminosity of a radio source is strongly confounded by its jet power, age, and ambient environment (Hardcastle & Krause, 2013; Shabala & Godfrey, 2013; Yates et al., 2018), the resulting scatter in the AGN RLF prevents the direct inference of the jet power function. The effects of a selection bias may also contribute towards the apparent mismatch between the fitted jet power slopes; while powerful radio sources will have bright radio luminosities, such sources will also have large physical sizes, which may contribute to their deselection from brightness-limited radio surveys. Of course, it is important to mention here the unaccounted-for uncertainty in the bright-end slope of the AGN RLF due to small number statistics.

In principle, predictions for the AGN RLF can be made by our best-fit jet model, and compared with observation in order to examine the consistency. This

approach would conveniently solve the issue of the confounding nature between jet power, age, and environment, since these effects are directly modelled by the input distributions of these variables. However, a robust comparison would require knowledge of the AGN halo mass functions underlying their samples. Additionally, modelling their selection biases would require knowledge of their redshift distributions, as well as filtering the RAiSE simulation grid through the survey selection criteria specific to their samples. Such an analysis is beyond the scope of this work, however is an interesting opportunity for future analysis. Based on the results of Shimwell et al. (2019) and Franzen et al. (2021), it would appear that our best-fit jet power function is not in tension with the observed AGN RLF.

Black hole fueling, accretion, and jet production

The ability to measure the jet power and lifetime functions of radio-loud AGNs is an exciting outcome of Chapter 4, and one that should be applied to future studies using the next generation of radio surveys. In that chapter of work, the selection criteria used to compile the parent radio galaxy sample were designed with practical limitations in mind. To ensure that the spatial attributes were not heavily degraded by the moderate angular resolution of RACS $\theta_{\mathrm{FWHM}} \approx 25''$, the sample was intentionally selected against a large ($\theta \geq 4'$) minimum angular size criterion. Due to the strong correlation between the physical sizes of radio galaxies and their active ages, a consequence of such a large angular size cut was that the observed active ages were heavily biased towards longer-lived jets.

Furthermore, considering that at present the measuring of the radio source attributes is a manual step, this process can become rather time consuming for a large sample of radio sources. With this in mind, both our minimum flux density and angular size thresholds additionally helped to keep the sample size sufficiently low. The caveat here is that with smaller sample sizes, the combined counting and fitting errors have a larger overall impact on the uncertainty in the

observed jet power and active age distributions, which decrease the precision with which the evolutionary jet models can be constrained. In addition to this, I also speculated that higher-order jet power functions, as well as models in which the jet power and lifetimes are correlated, may provide a more realistic treatment of the AGN jet physics. Such models can be constrained via the method outlined in Chapter 4, however such analysis will require sample sizes much larger than that used in our work.

The next generation of radio surveys will offer the parameter space needed to confront the considerations outlined above. The high spatial-resolution provided by surveys such as LoTSS and EMU ($\theta = 5''$ - $10''$) will enable the compilation of radio galaxy samples against much more lenient minimum angular size selection criteria. Similarly, the unparalleled surface brightness sensitivities in these surveys will allow for much lower minimum flux density selection criteria, which in turn will greatly aid the selection of lower-powered jets.

As part of the outcomes presented in Chapter 4, I identified several interesting opportunities for future research. First, by comparing the predictions of our best-fitted jet power function to our observed jet power distribution, I provided tentative evidence in favour of a broken power-law jet kinetic power function. With less stringent sample selection criteria, access to a larger fraction of lower-powered radio sources will help to directly fill out this portion of the parameter space. This will help to ascertain whether the jet power function does indeed flatten towards lower jet powers, and if so, will offer the constraints needed to parameterise this flattening. Such an analysis should also clear up the apparent inconsistency between the jet power exponent fitted by our work ($b = -1.60 \pm 0.09$) versus that fitted by Shabala et al. 2020 ($b = -1$); I speculated that the mismatch could be driven by real or methodological effects, however no further comments can be made unless a similar study is extended to a more representative sample of radio galaxies.

Another research question that would benefit greatly by the methodology

carried out in Chapter 4 relates to whether different jet-triggering mechanisms exist for different radio galaxy populations – as has been suggested by a variety of authors (e.g. Pimbblet et al., 2013; Kaviraj et al., 2015; Marshall et al., 2018; Hardcastle et al., 2019). Provided a sufficiently large sample as well as value-added information of the host-galaxy such as the black hole mass, stellar mass, halo mass, or redshift, it will be possible for the sample to be split into various bins across these parameters, and thus for the jet power and lifetime distributions to be investigated separately across these populations. Changes in the slope of the lifetime distribution would be strong evidence in favour of different fueling mechanisms.

5.2.4 Measuring the environments of radio-loud AGNs

Though not the focus of this thesis, in Chapter 4 I placed dynamical model-based constraints on the halo mass for each sample remnant. By inspecting the probability density functions in the fitted RAiSE parameters, it was shown that the fitted halo masses were constrained with Gaussian-like uncertainty, implying that this parameter should be able to be constrained from radio observations alone. This presents an interesting opportunity to explore whether the properties of the intra-cluster environments of radio-loud AGN can be constrained purely from the observed radio source properties of radio galaxy lobes. Considering that the heating and cooling of hot intra-cluster gas plays such a crucial role in the feedback of radio-loud AGN, the ability to quantify the environment within which the radio jets expand, using radio survey-data alone, would be a powerful tool to study the environment-jet coupling.

One plausible way by which this question could be tested could be to utilise a 3CRR sub-sample of bright, FR-II radio galaxies, studied by Ineson et al. (2017), who used X-ray inverse-Compton data to constrain the integrated X-ray luminosity and profile of the hot gas. These sources are covered by a wide range of radio surveys spanning low ($\sim 150\,\mathrm{MHz}$) to high ($\geq 5\,\mathrm{GHz}$) frequencies, and so we can

expect tight observational constraints on their integrated radio luminosities, sizes, break frequencies, and spatial attributes such as the extent at various frequencies. Following the methods of Chapters 3 & 4, the dynamical model-based method would then be used to fit the intrinsic radio source parameters, only with one key difference in that the environment environment would be parameterised by a critical gas density and a scale radius (both of which are model inputs to the RAiSE dynamical model). By validating the derived outputs against the independently-measured values of Ineson et al. (2017), the results would shed light into the possibility of quantifying the environments of radio-loud AGNs using only the observed properties of radio galaxy lobes.

5.3 Concluding remarks

The end-of-life "remnant" phase of a radio galaxy continues to be a fascinating topic of research within the study of radio-loud AGN physics. With the advent of new-generation radio surveys and cutting-edge theoretical models, the once elusive class of radio galaxy has quickly become an object of close examination, and will continue to be an integral component in the study of radio-loud AGN evolution. This thesis has adopted a synergy of observation-based and model-driven analysis to shed light on the properties and selection of remnant radio galaxies, the evolutionary processes that occur within remnant lobes, as well as the implications remnants have towards evolutionary models of active galactic nuclei jets. The key highlight of this research was the development of a novel technique to constrain the intrinsic radio source parameters from low-frequency ($\leq 1.4\,\mathrm{GHz}$) observations of remnant lobes, which was subsequently applied to a sample of remnants in order to constrain their seed distributions in jet kinetic power and lifetime. With the continual improvement in the quality of astronomical survey data, the insights gathered across this thesis hint towards a bright future, in which remnants help to confront the key questions related to AGN duty cycles and evolution.

Appendices

Appendix A

The following appendix table belongs to Chapter 2.

No.	Column name	Unit	Description
1	MIDAS_name	J hh:mm:ss-dd:mm:ss	Name of radio source in J2000 format.
2	MIDAS_RA	deg	Right Ascension of MIDAS source.
3	MIDAS_Dec	deg	Declination of MIDAS source.
4	AGN_status	–	Activity state of AGN.
5	FR_classification	–	Fanaroff & Riley Classification: FR-I, FR-II.
6	LAS	arc-seconds	Largest angular size measured from EMU-ES.
7	Hotspots (L1)	–	Number of GLASS hotspots present in L1.
8	Hotspots (L2)	–	Number of GLASS hotspots present in L2.
9	peak_flux_core	μJy/beam	5.5 GHz radio core peak flux density.
10	err_peak_flux_core	μJy/beam	Error on 5.5 GHz radio core peak flux density.
11	S_{118}	mJy	Integrated flux density at MHz.
12	err_S_{118}	mJy	Error on integrated flux density at MHz.
13	S_{154}	mJy	Integrated flux density at MHz.
14	err_S_{154}	mJy	Error on integrated flux density at MHz.
15	S_{186}	mJy	Integrated flux density at MHz.
16	err_S_{186}	mJy	Error on integrated flux density at MHz.
17	S_{216}	mJy	Integrated flux density at MHz.
18	err_S_{216}	mJy	Error on integrated flux density at MHz.
19	S_{399}	mJy	Integrated flux density at MHz.
20	err_S_{399}	mJy	Error on integrated flux density at MHz.

21	S_{887}	mJy	Integrated flux density at MHz.
22	err_S_{887}	mJy	Error on integrated flux density at MHz.
23	S_{1400}	mJy	Integrated flux density at MHz.
24	err_S_{1400}	mJy	Error on integrated flux density at MHz.
25	S_{2100}	mJy	Integrated flux density at MHz.
26	err_S_{2100}	mJy	Error on integrated flux density at MHz.
27	S_{5500}	mJy	Integrated flux density at MHz.
28	err_S_{5500}	mJy	Error on integrated flux density at MHz.
29	S_{9000}	mJy	Integrated flux density at MHz.
30	err_S_{9000}	mJy	Error on integrated flux density at MHz.
31	CP	–	216 MHz core prominence.
32	GAMA_IAUID	–	ID of host galaxy in GAMA photometry catalogue.
33	Host_RA	deg	Right ascension of host galaxy.
34	Host_Dec	deg	Declination of host galaxy.
35	z	–	Redshift.
36	z_type	–	Redshift type: Spectroscopic, Photometric, lower-limit.
37	mag_K_s	–	Host galaxy VIKING K_s-band magnitude.
38	NED_Object_Name	–	Name of NED object corresponding to the GAMA_IAUID.
39	log10_L_{216}	log10(W Hz^{-1})	216 MHz radio power.
40	LLS	kpc	Largest linear size.

Table A.1: Column descriptions corresponding to the supplementary electronic table. The MIDAS_Name is derived using the MIDAS_RA and MIDAS_Dec columns. Entries without a GAMA_IAUID, mag_Ks, or NED_Object_Name are assigned a value of '−99'. Hotspots (L1) and Hotspots (L2) refer to the number of GLASS hotspots found in each lobe, where L1 and L2 refer to the lobe and counter-lobe. We define L1 as having the smaller position angle measured in a counter-clockwise direction from the North.

Appendix B

This appendix table belongs to Chapter 3

Table B.1: Summary of the integrated radio spectrum compiled for J2253-34.

Telescope	Type	Frequency (MHz)	Bandwidth (MHz)	Integrated flux density (mJy)
MWA Phase I	Survey (GLEAM)	119.04	30.72	238 ± 35
		154.88		194 ± 35
uGMRT	Pointed observations	417	250	114.00 ± 8.88
		682		79.8 ± 5.2
ASKAP	Survey (EMU early-science)	887	288	64.1 ± 3.2
MeerKAT	Pointed observations	911	42	63.17 ± 1.89
		1022	120	57.44 ± 1.85
		1422	153	41.28 ± 1.34
		1653	30	35.28 ± 1.08
VLA	Survey (NVSS)	1400	50	42.4 ± 3.05
ATCA	Pointed observations	2000	500	29.58 ± 1.77
		2868		19.60 ± 1.17
		4782		10.50 ± 0.42
		5243		9.38 ± 0.37
		5746		7.93 ± 0.32
		6216		6.84 ± 0.27
		8284		4.13 ± 0.19
		8726		3.84 ± 0.16
		9253		3.41 ± 0.15
		9716		3.08 ± 0.14

Appendix C

Image cutouts and spectral energy distributions of the 79 remnant candidates selected as part of Chapter 4.

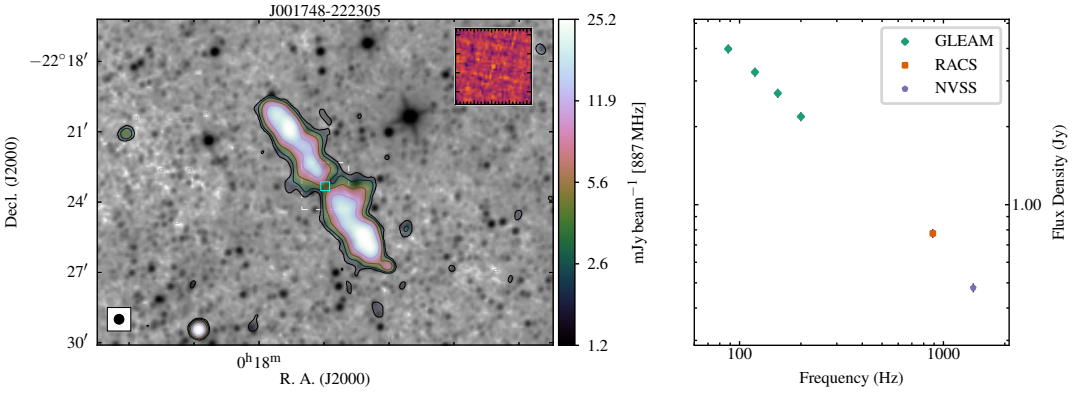

J001748-222305

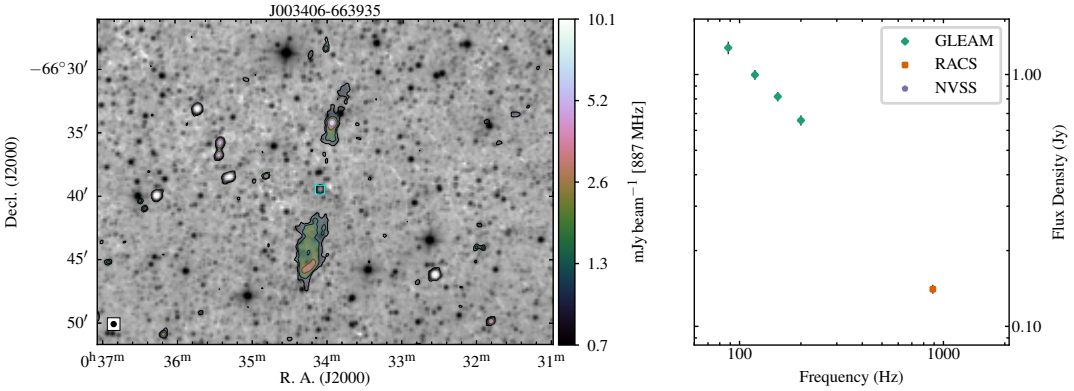

J003406-663935

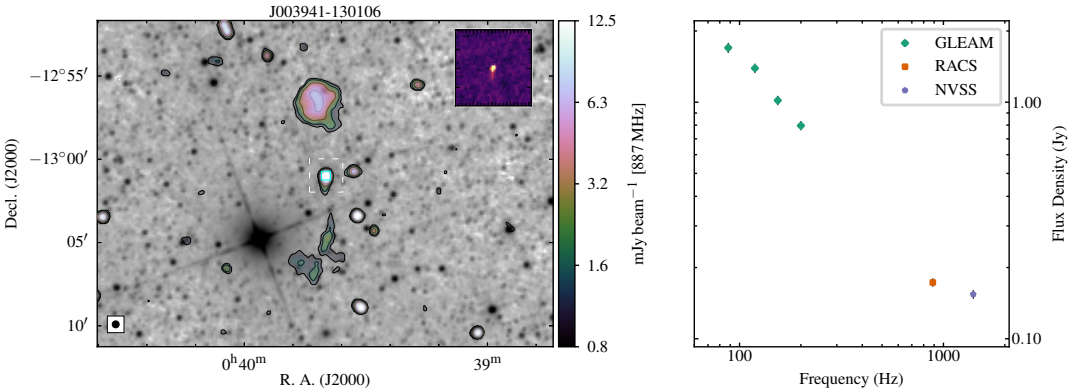

J003941-130106

Figure C.1: Remnant candidates from Chapter 4. *Left:* The radio source is overlaid onto a WISE W1-band background with a logarithmic stretch. Radio contour levels are specified by the on the right-hand colour bar. The inset in the upper-right corner provides a VLASS view of the region bounded by the dashed box. *Right:* The integrated flux density of the source.

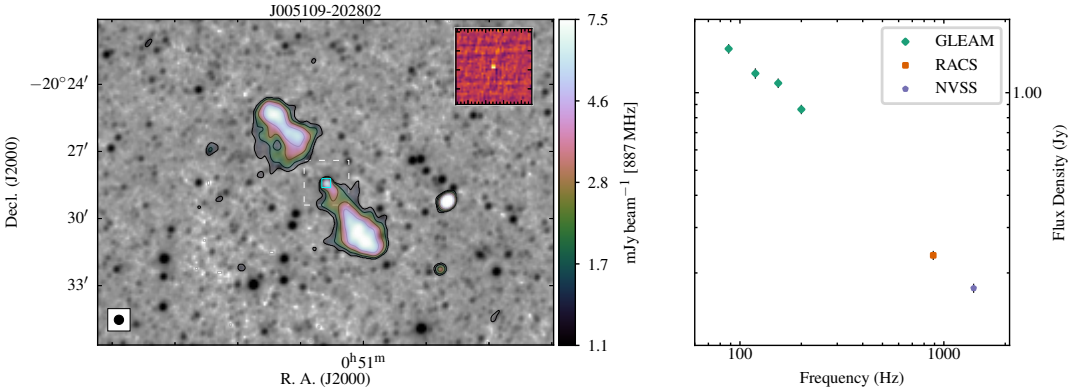

J005109-202802

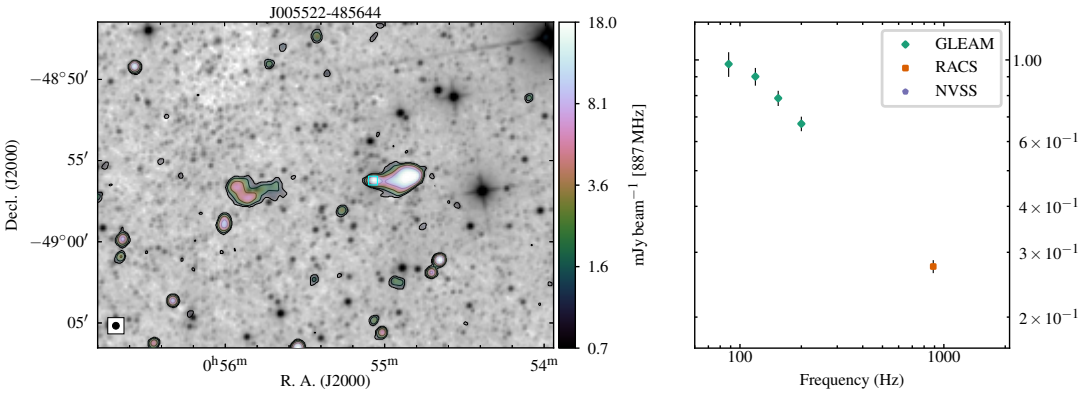

J005522-485644

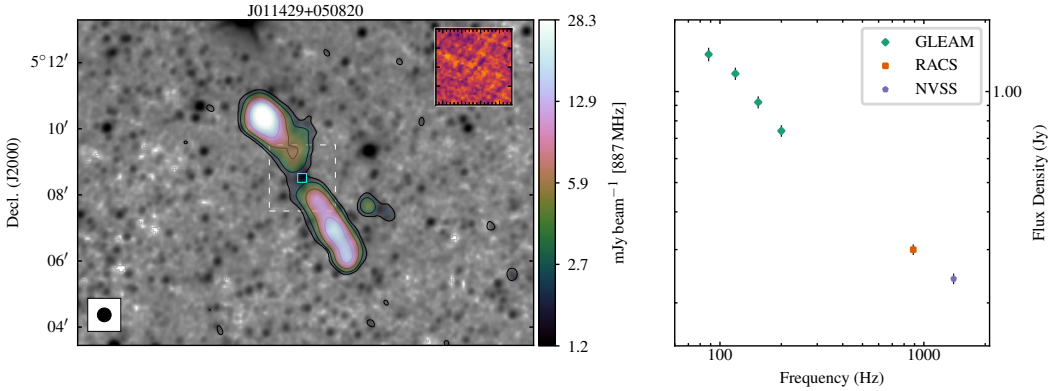

J011429+050820

Figure C.1: Continued

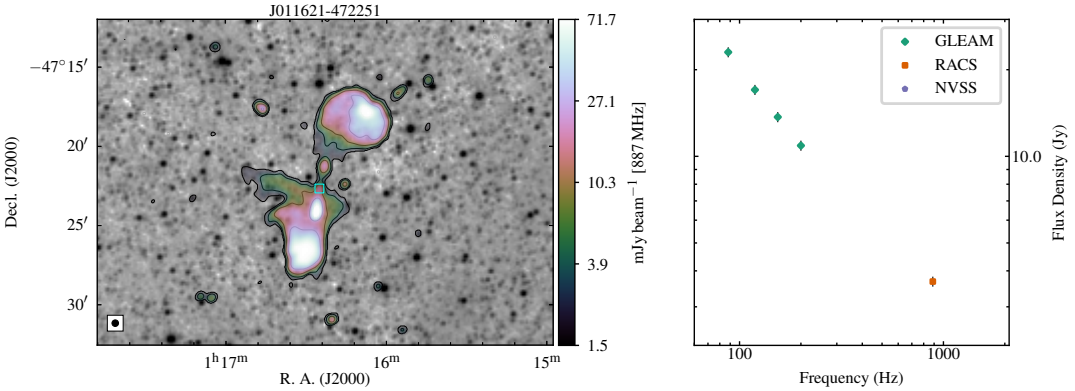

J011621-472251

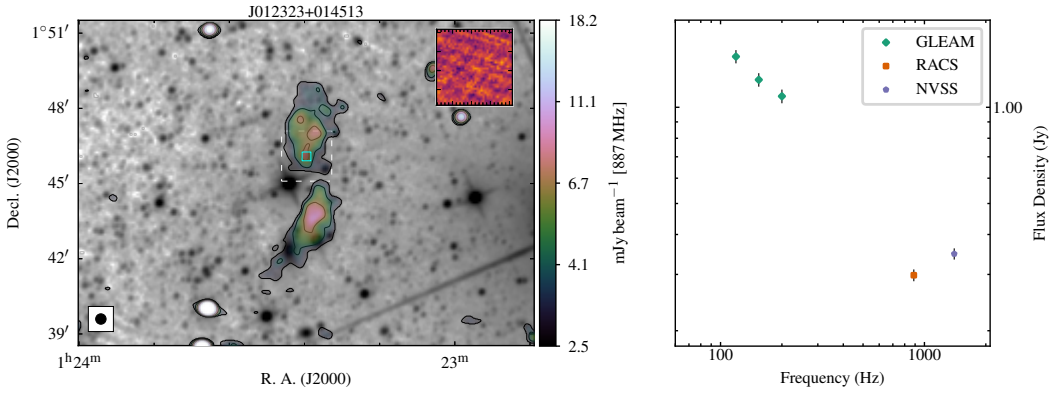

J012323+014513

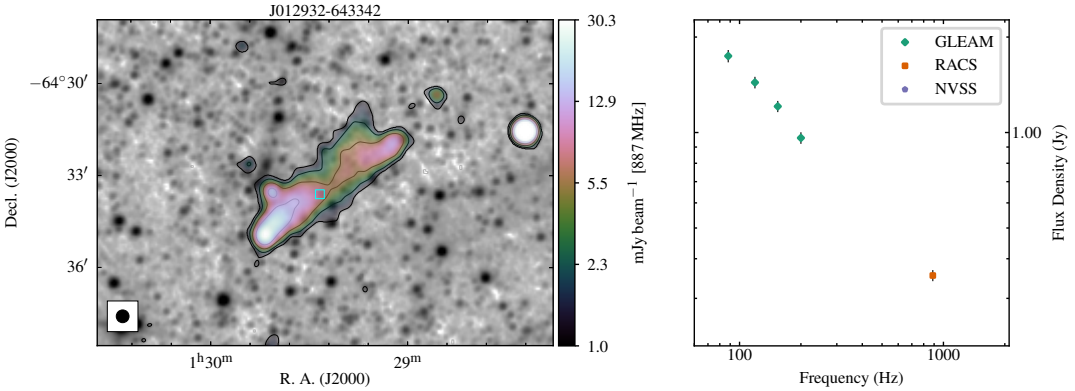

J012932-643342

Figure C.1: Continued

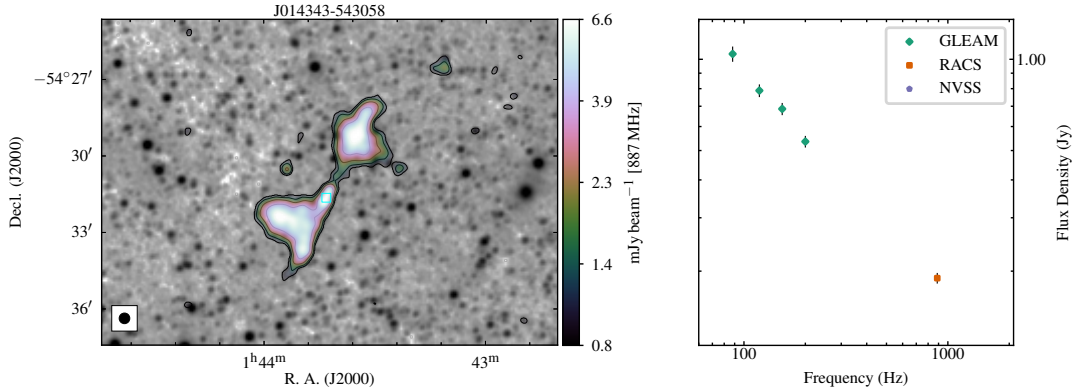

J014343-543058

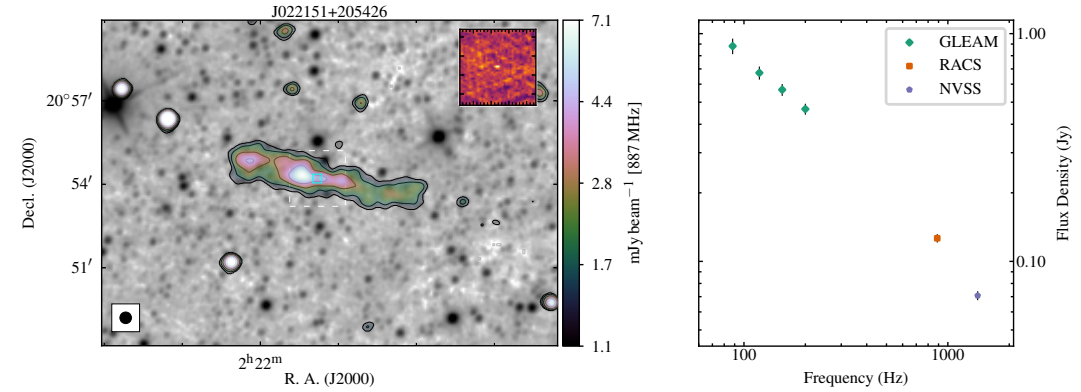

J022151+205426

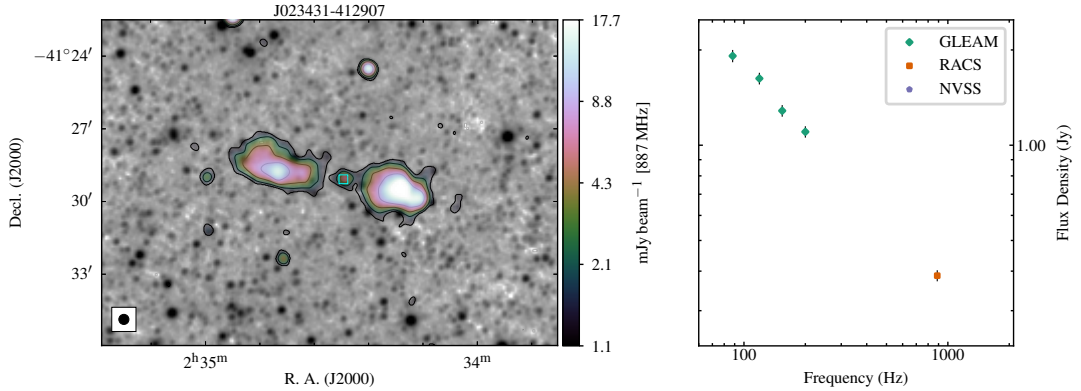

J023431-412907

Figure C.1: Continued

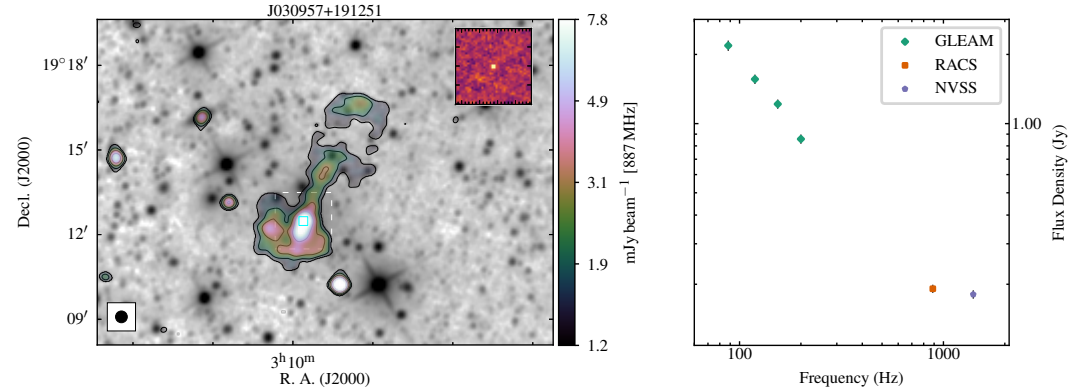

J030957+191251

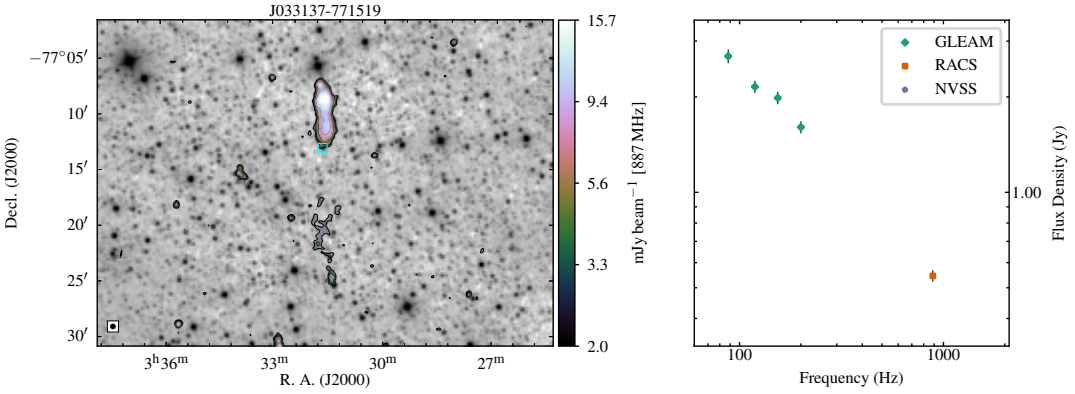

J033137-771519

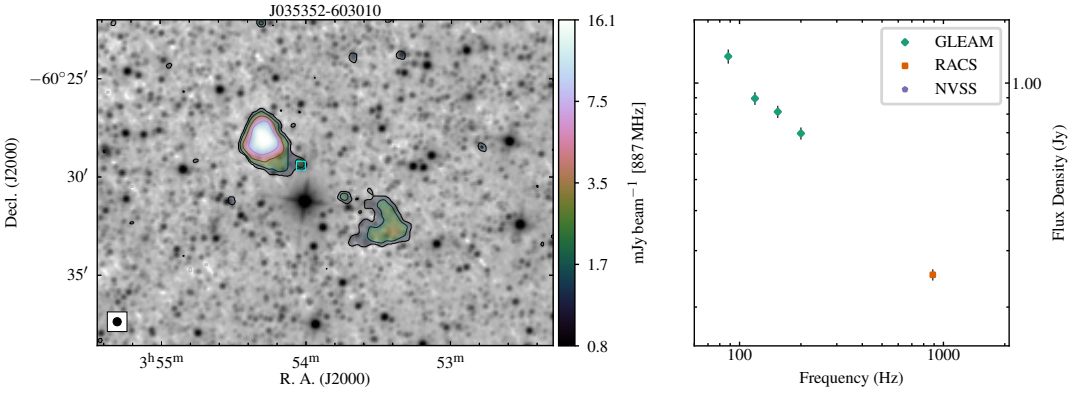

J035352-603010

Figure C.1: Continued

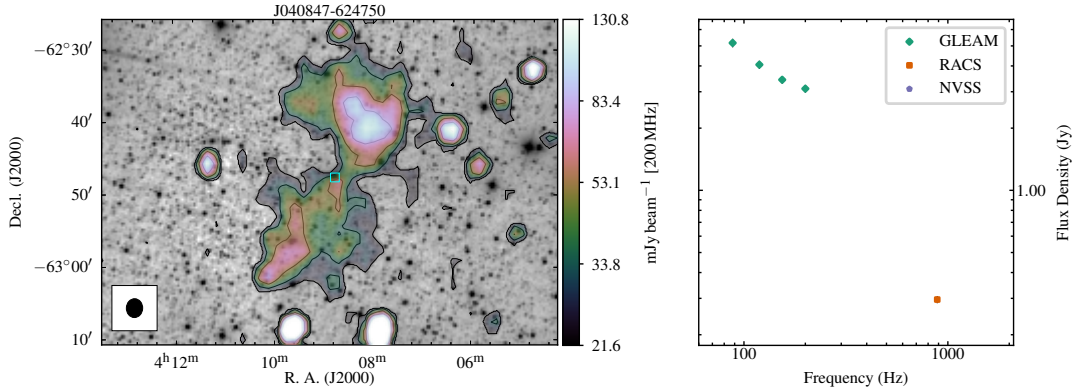

J040847-624750

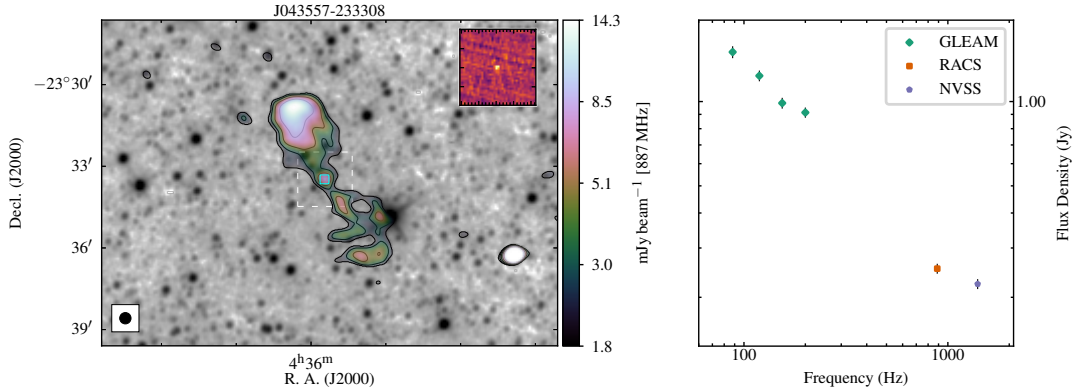

J043557-233308

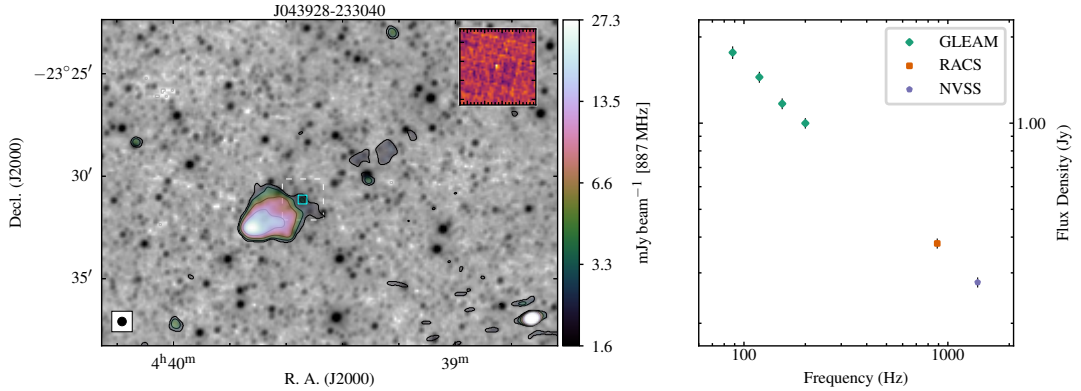

J043928-233040

Figure C.1: Continued

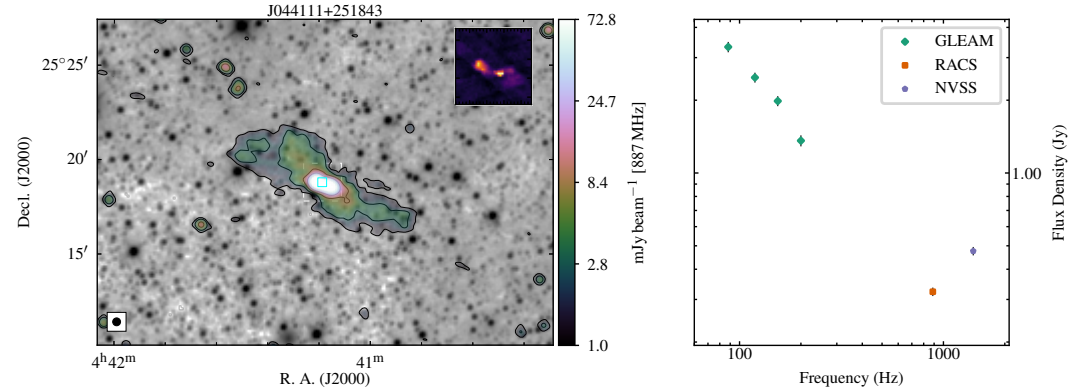

J044111+251843

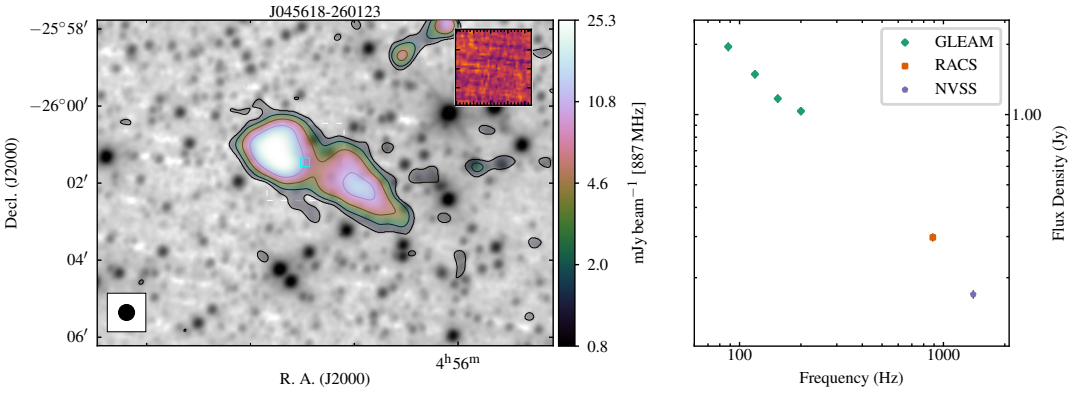

J045618-260123

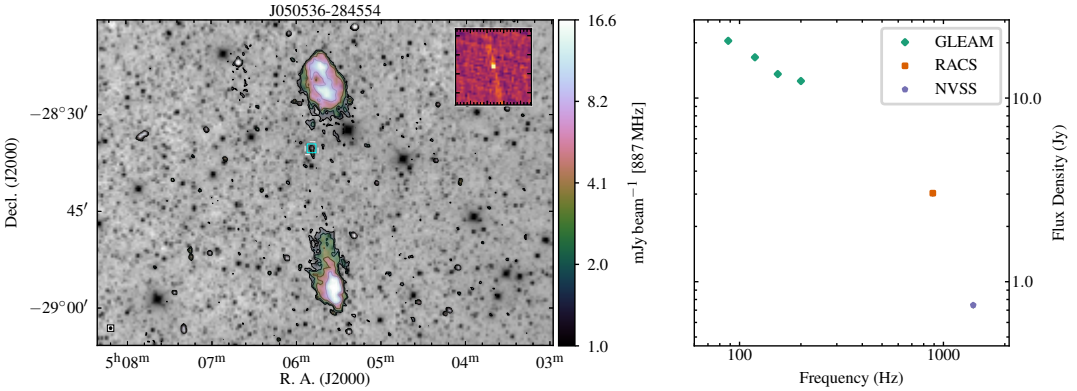

J050536-284554

Figure C.1: Continued

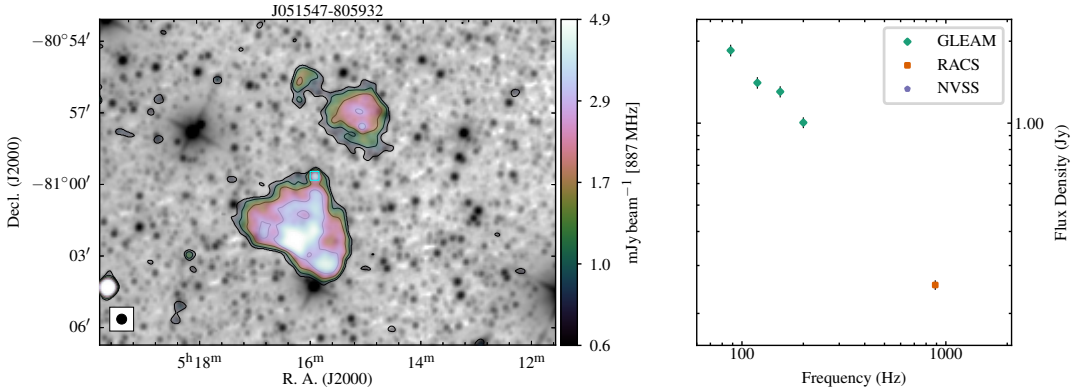

J051547-805932

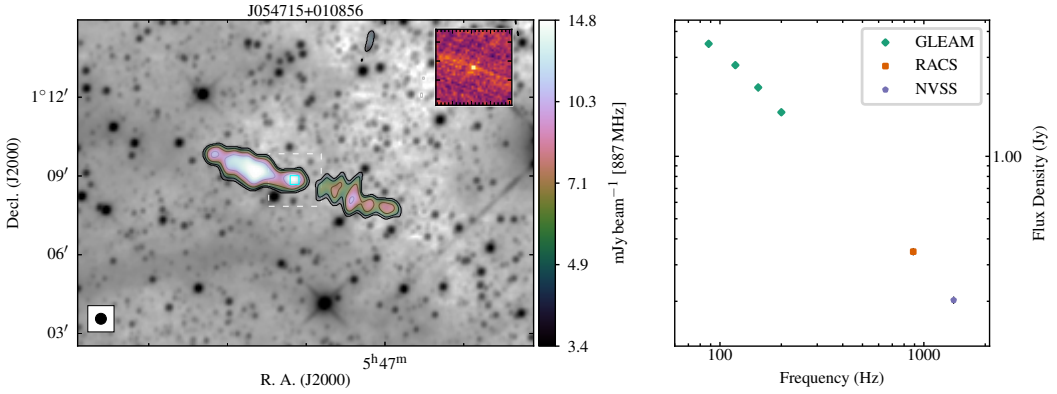

J054715+010856

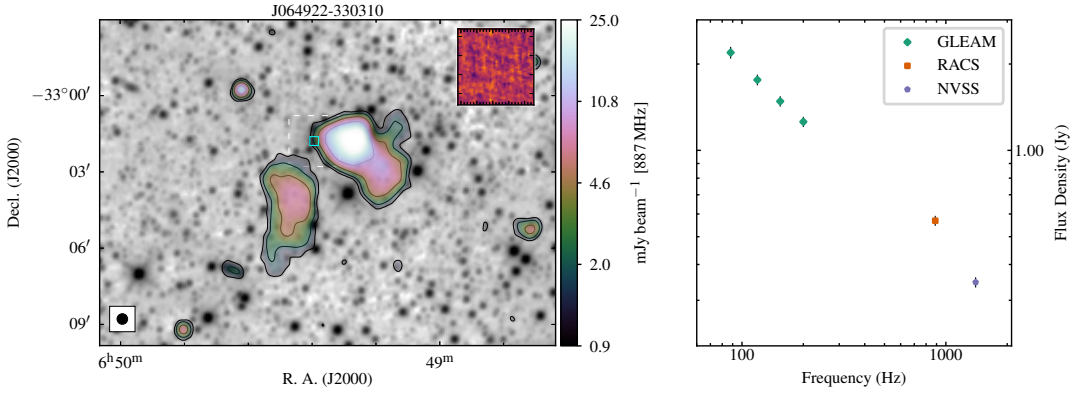

J064922-330310

Figure C.1: Continued

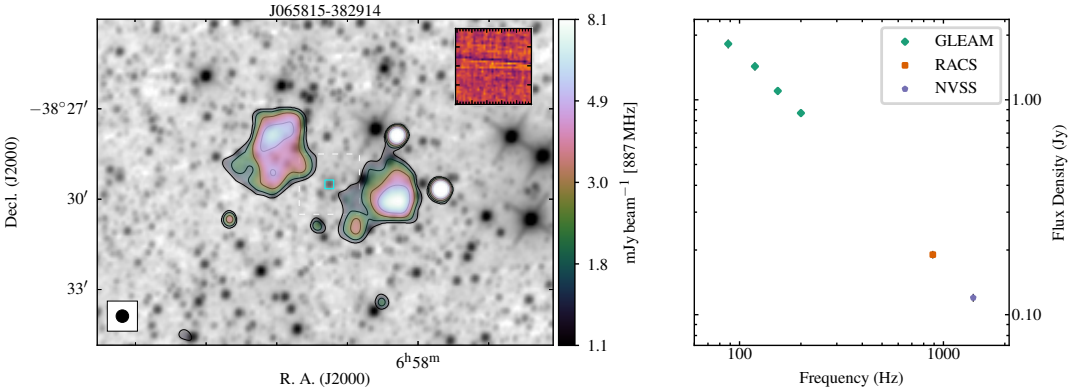

J065815-382914

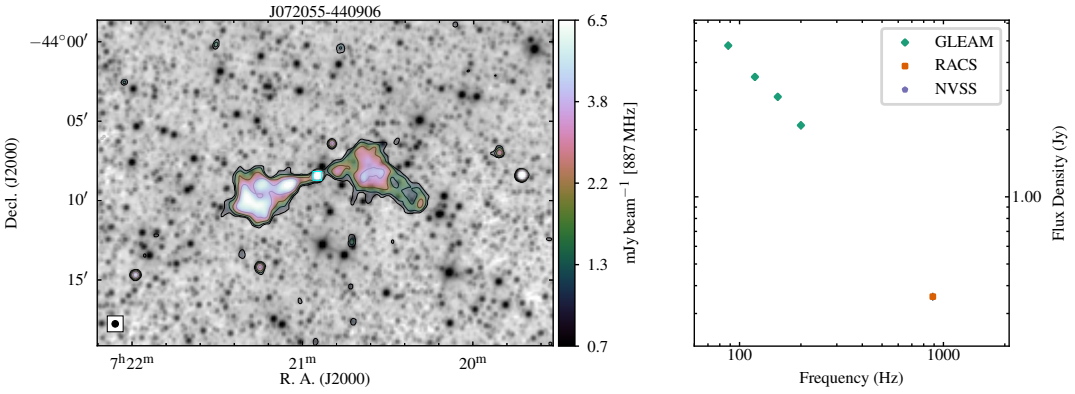

J072055-440906

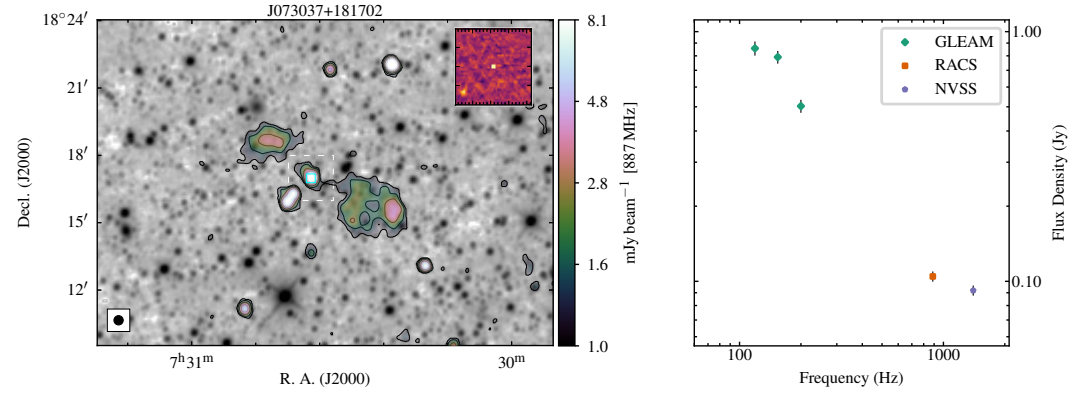

J073037+181702

Figure C.1: Continued

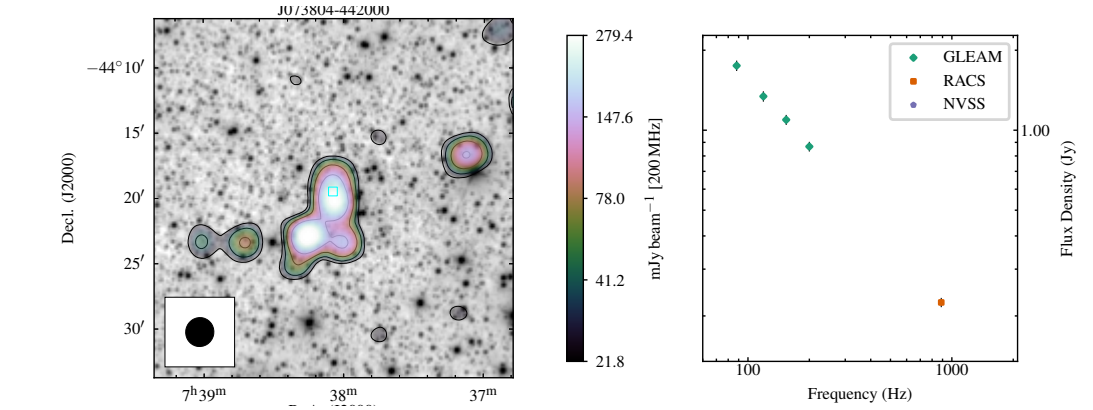

J073804-442000

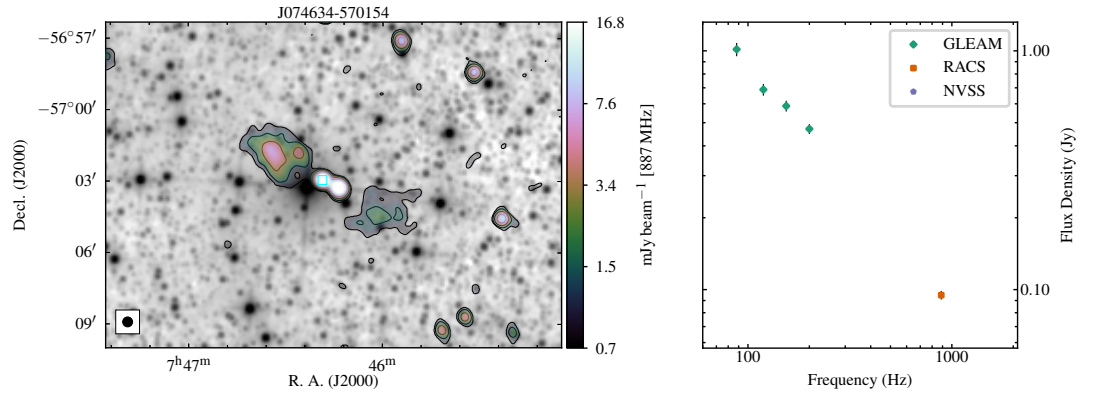

J074634-570154

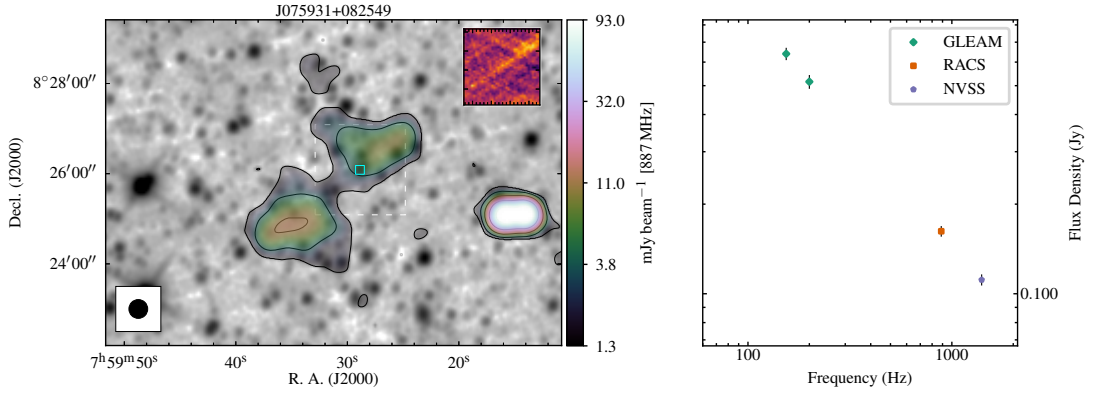

J075931+082549

Figure C.1: Continued

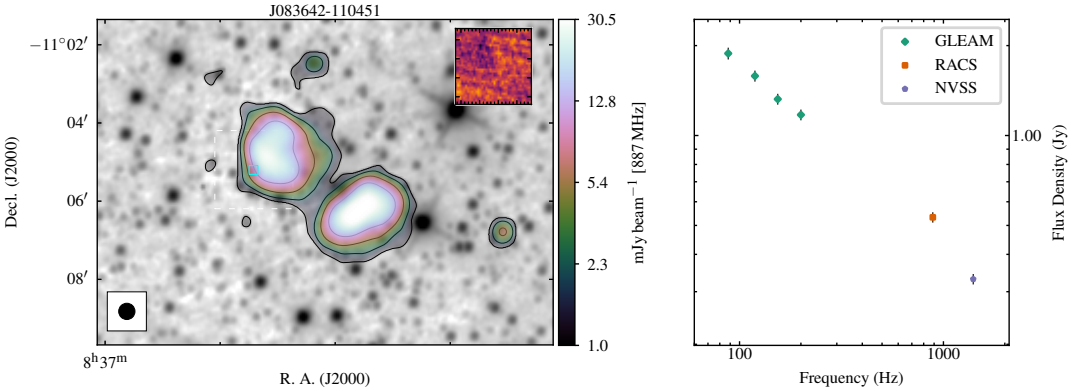

J083642-110451

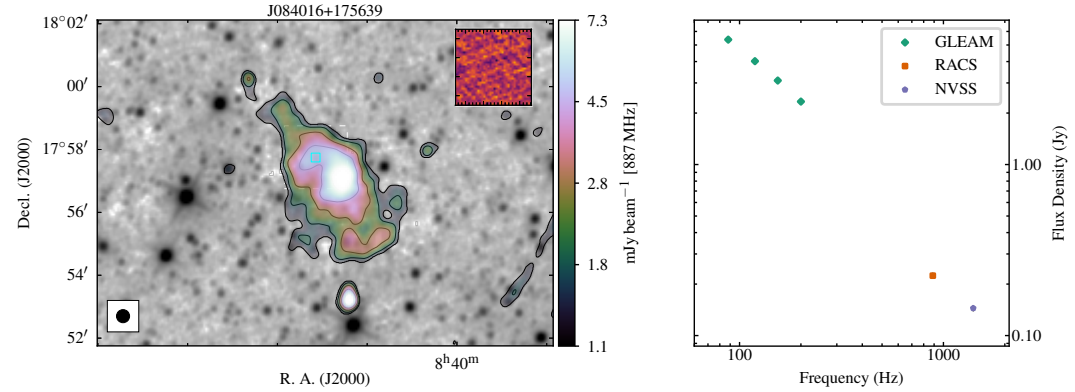

J084016+175639

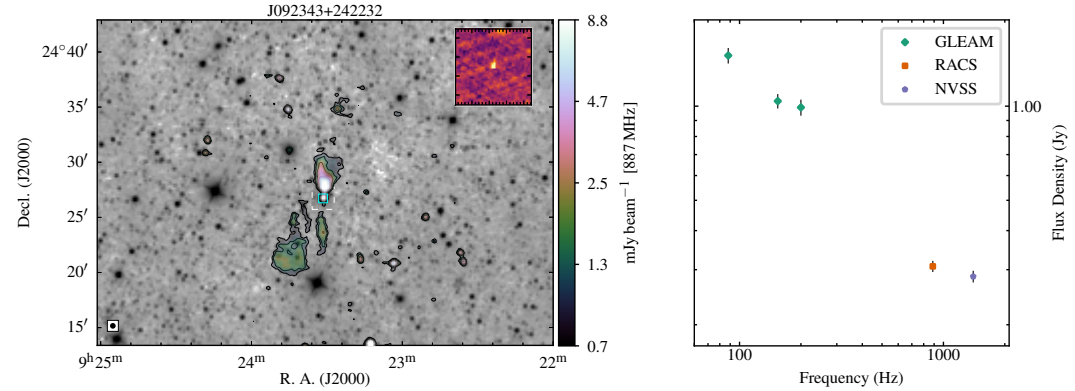

J092343+242232

Figure C.1: Continued

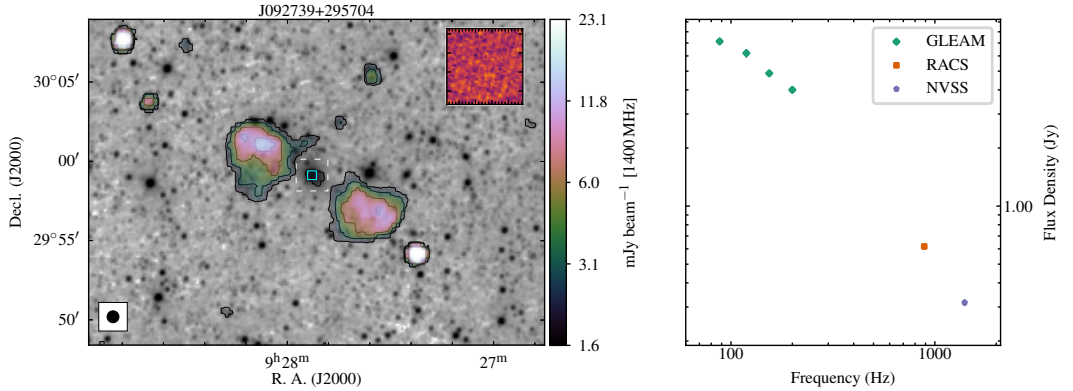

J092739+295704

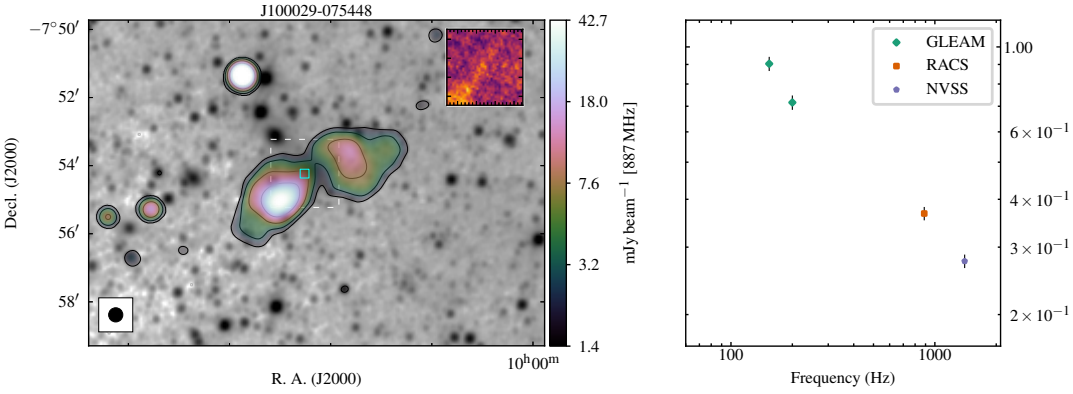

J100029-075448

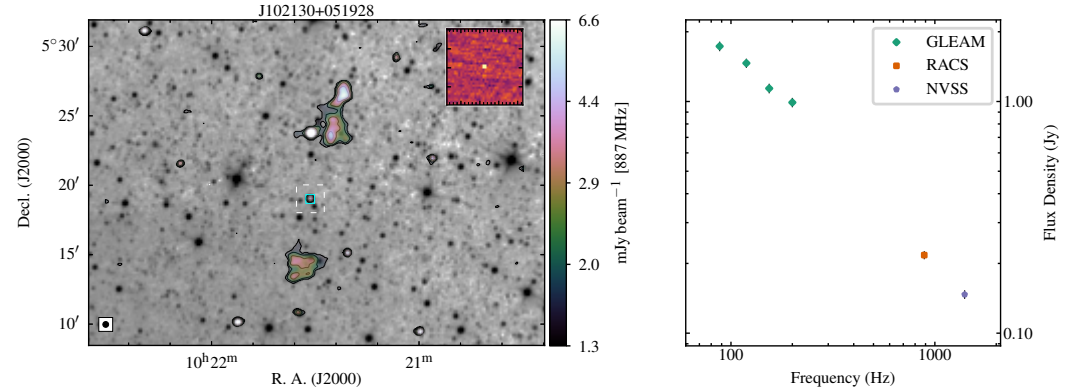

J102130+051928

Figure C.1: Continued

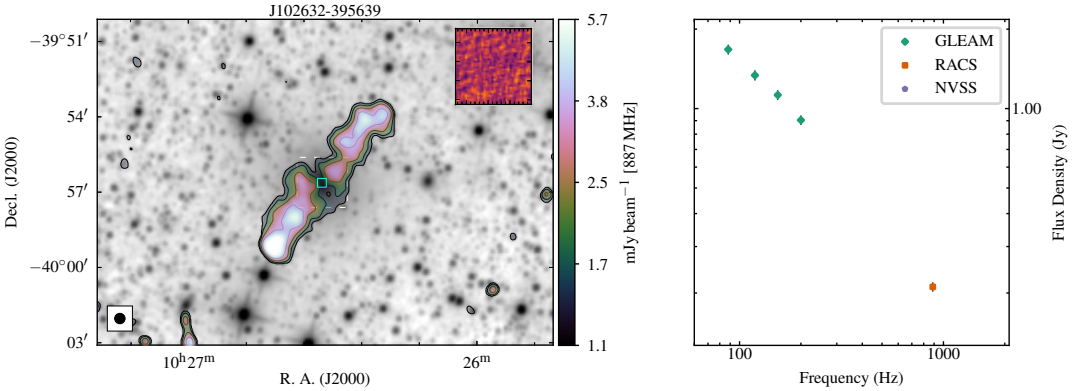

J102632-395639

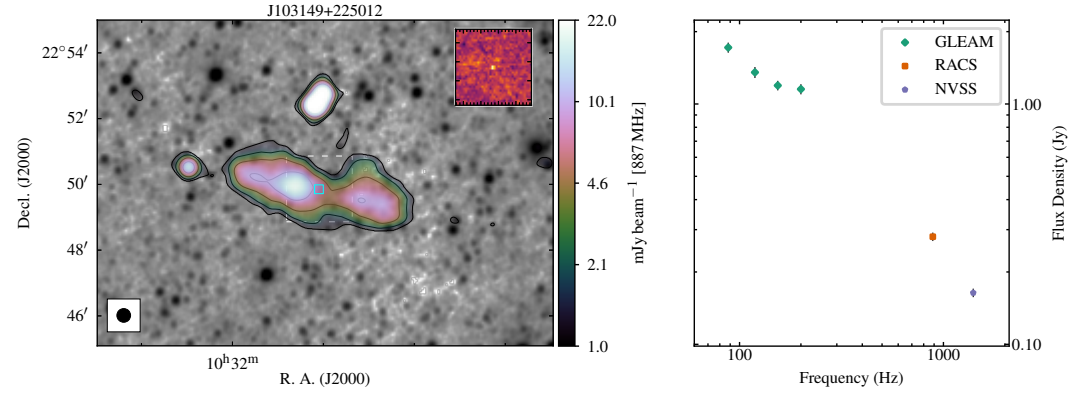

J103149+225012

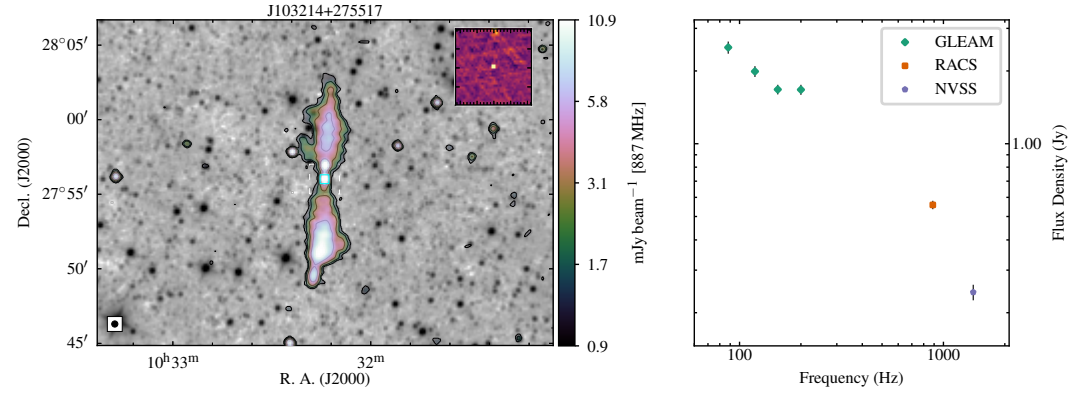

J103214+275517

Figure C.1: Continued

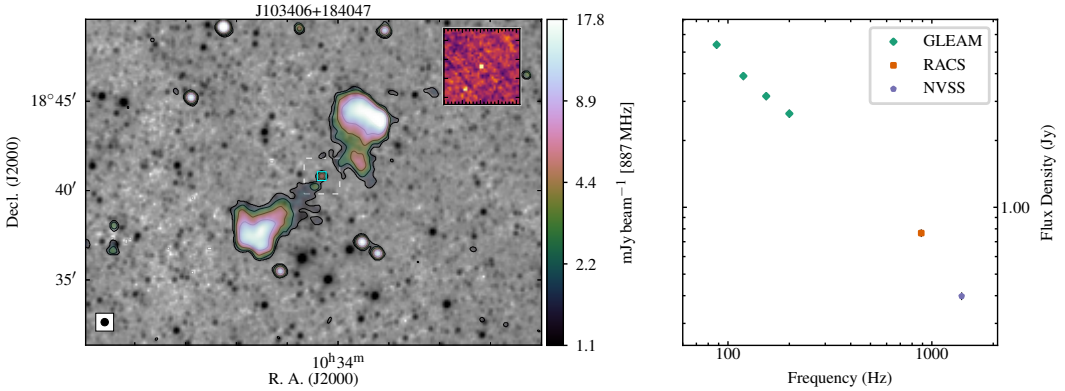

J103406+184047

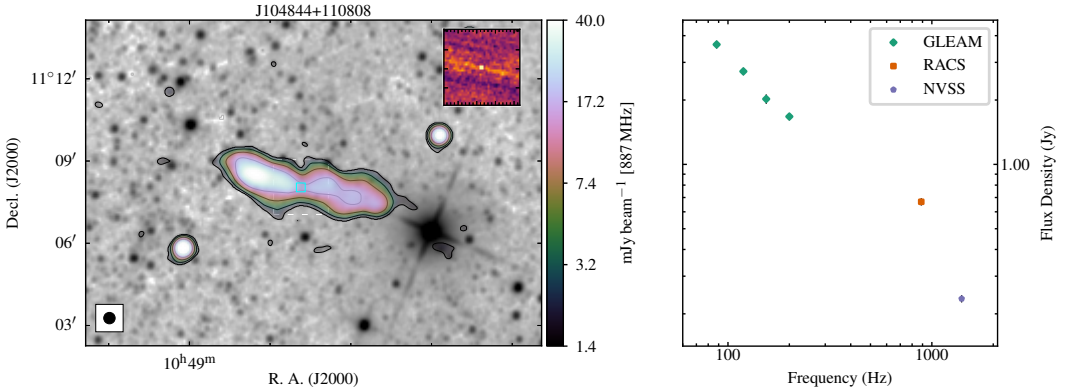

J104844+110808

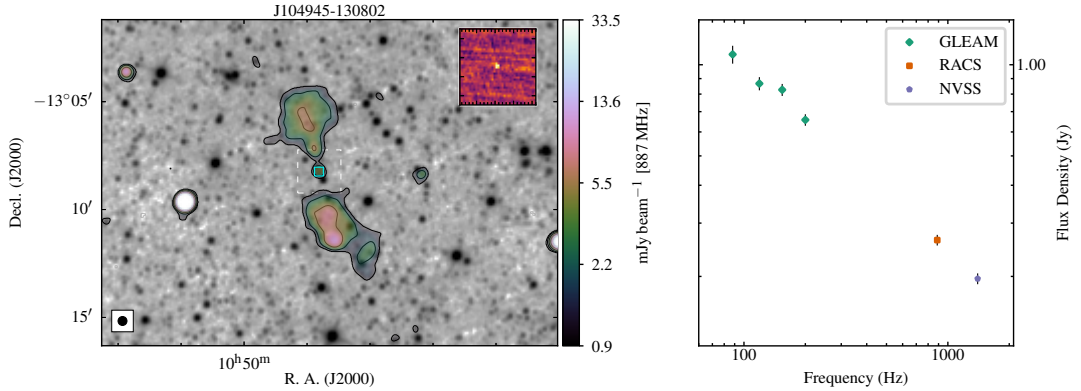

J104945-130802

Figure C.1: Continued

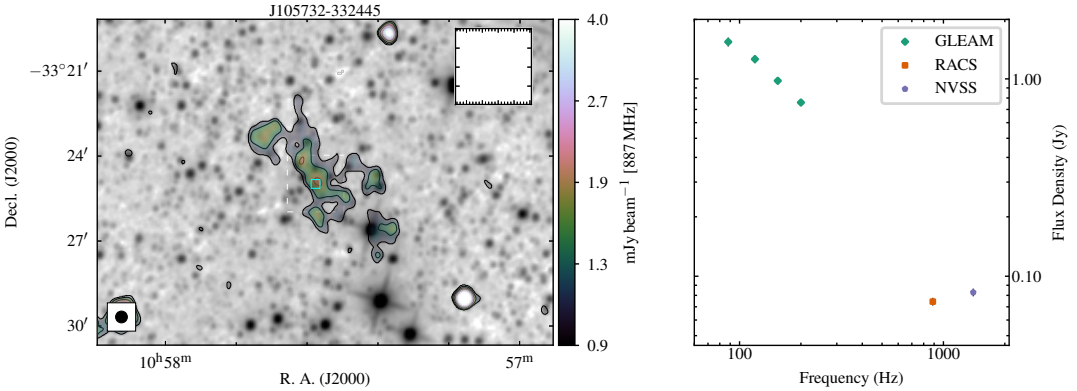

J105732-332445

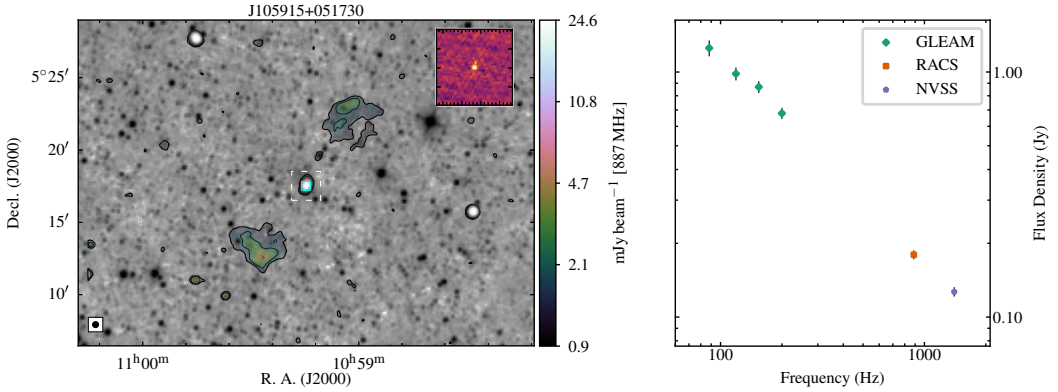

J105915+051730

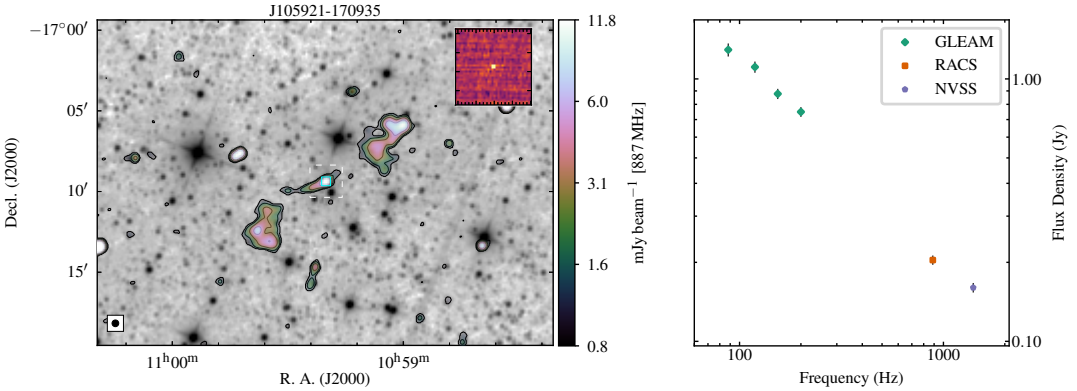

J105921-170935

Figure C.1: Continued

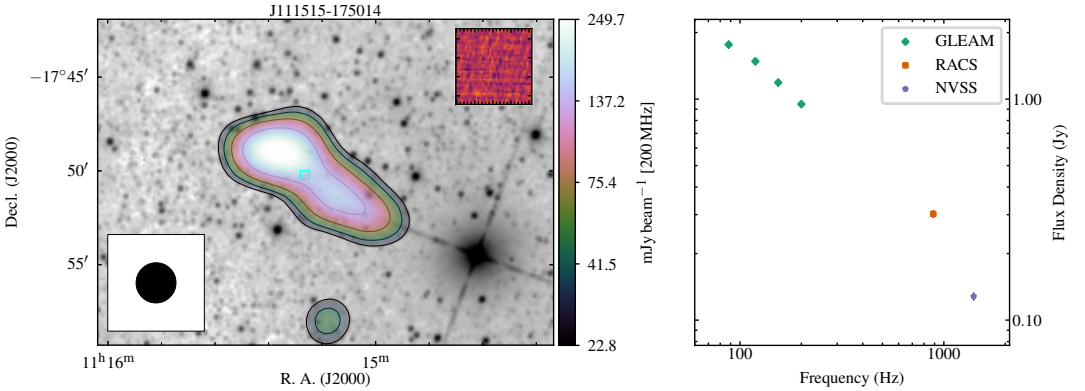

J111515-175014

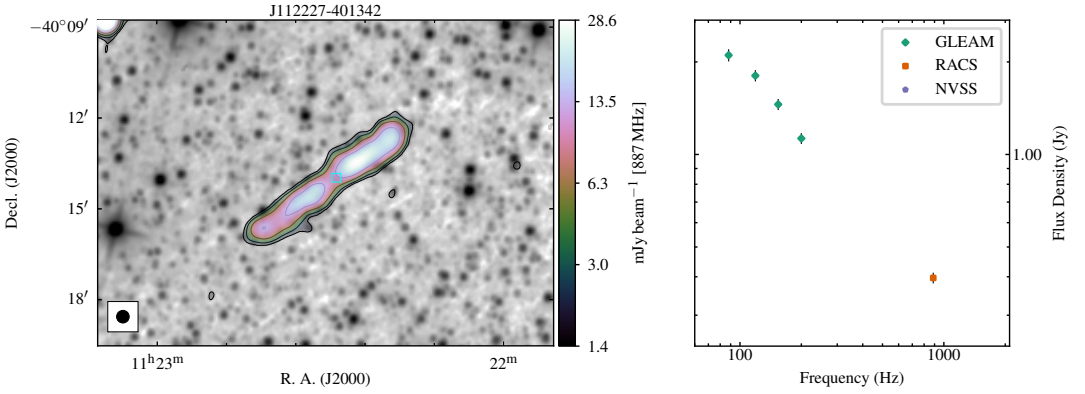

J112227-401342

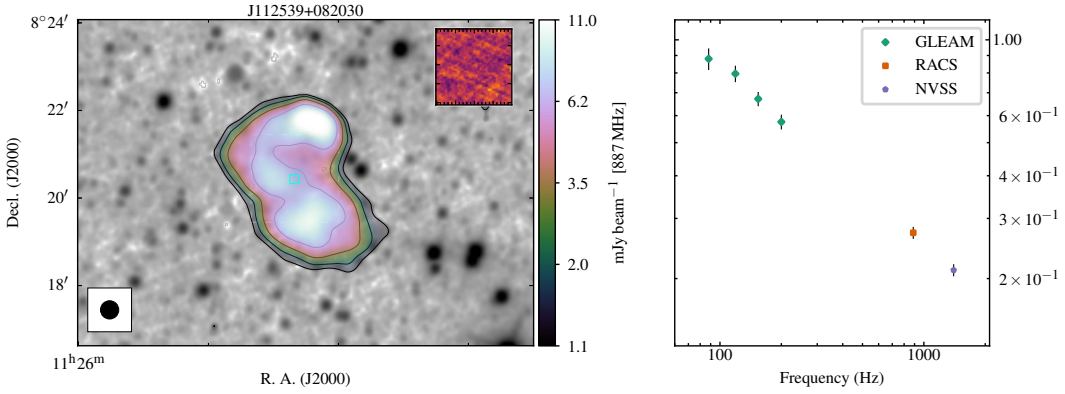

J112539+082030

Figure C.1: Continued

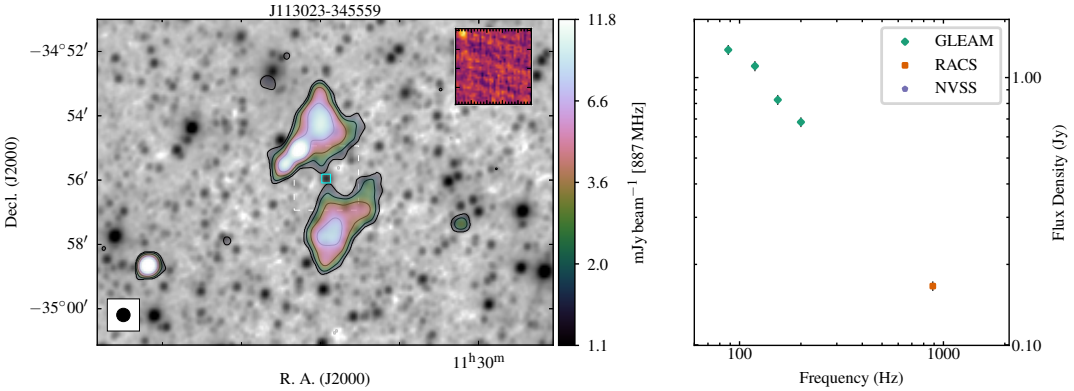

J113023-345559

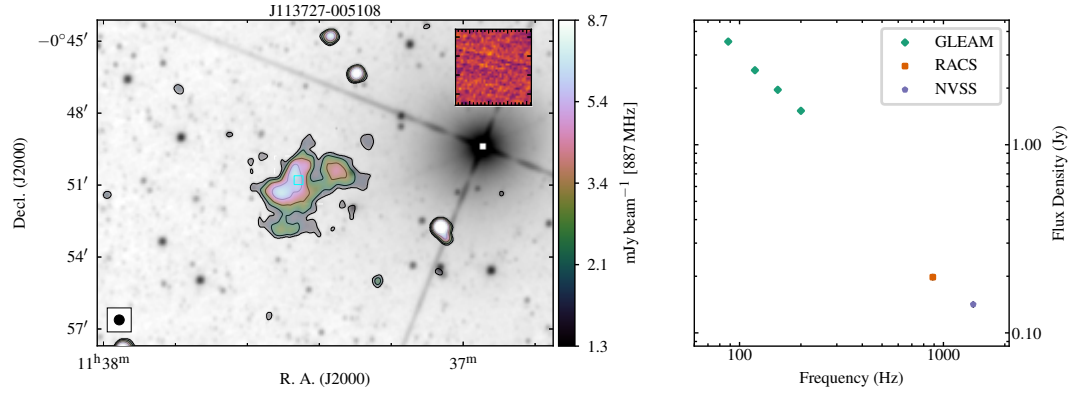

J113727-005108

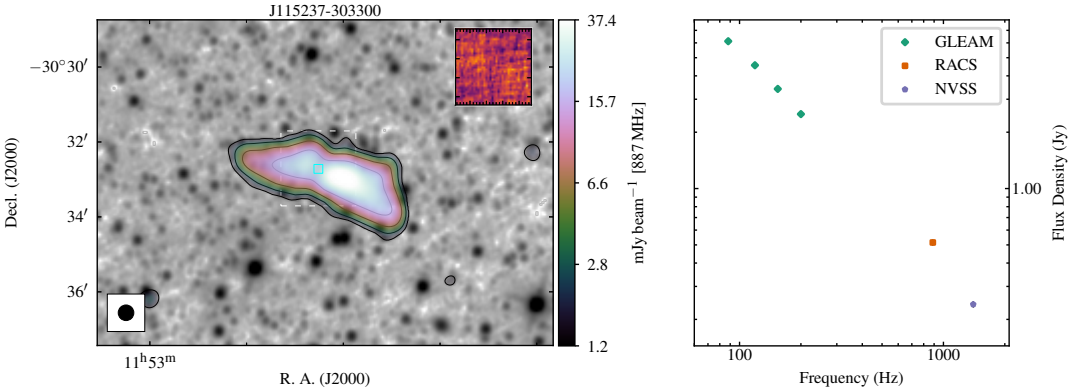

J115237-303300

Figure C.1: Continued

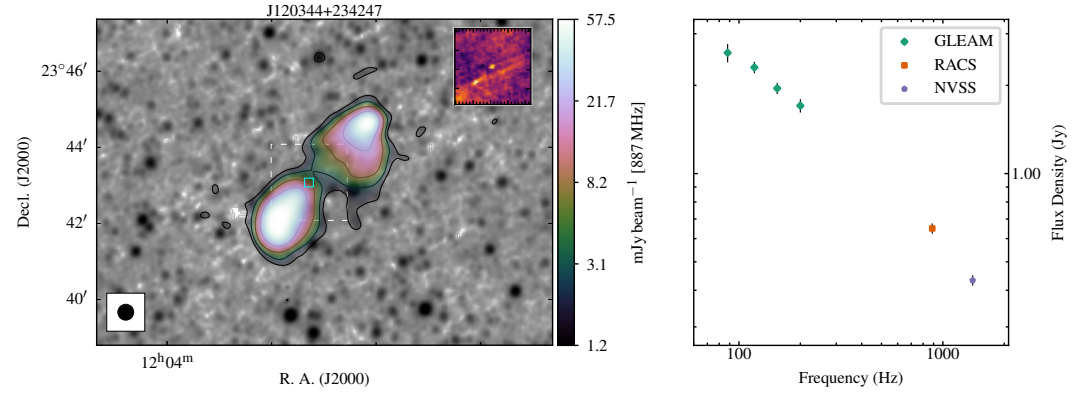

J120344+234247

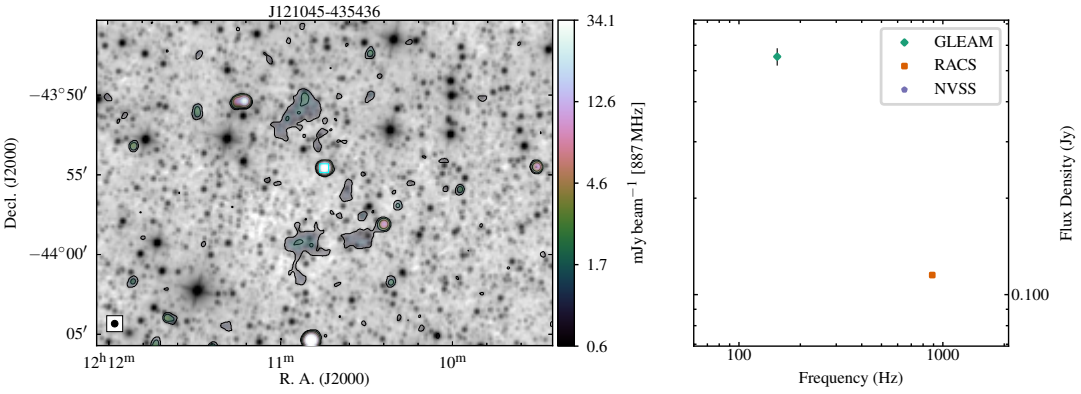

J121045-435436

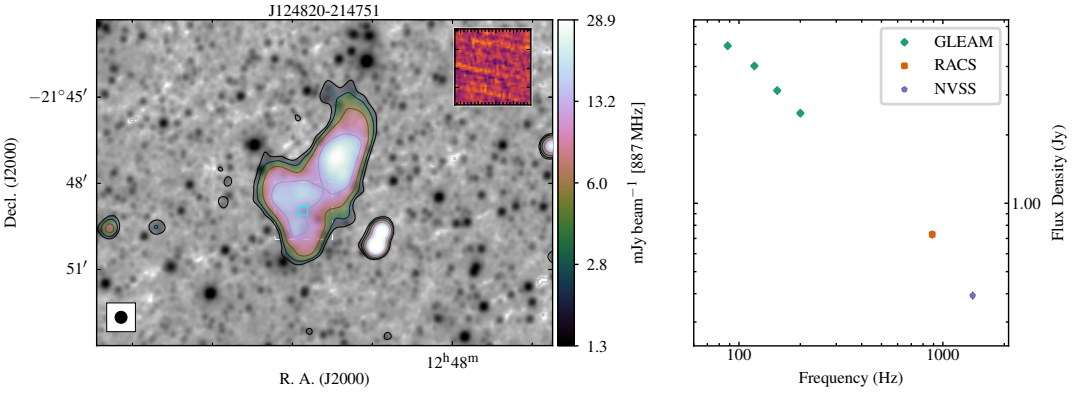

J124820-214751

Figure C.1: Continued

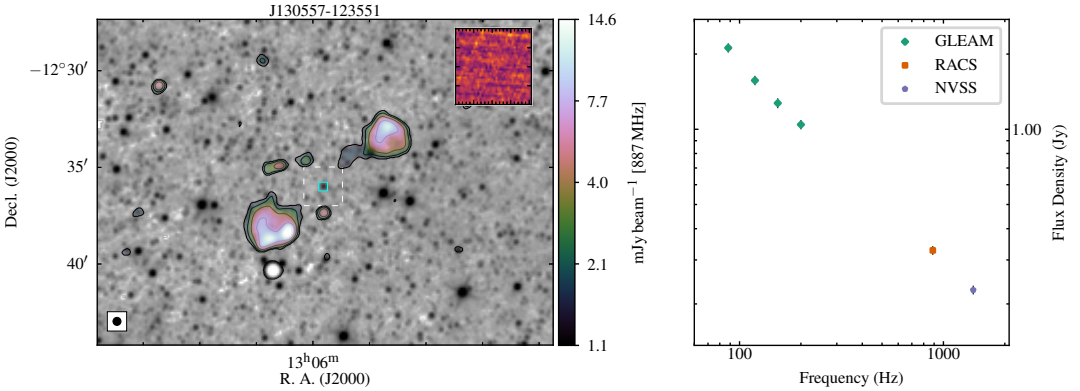

J130557-123551

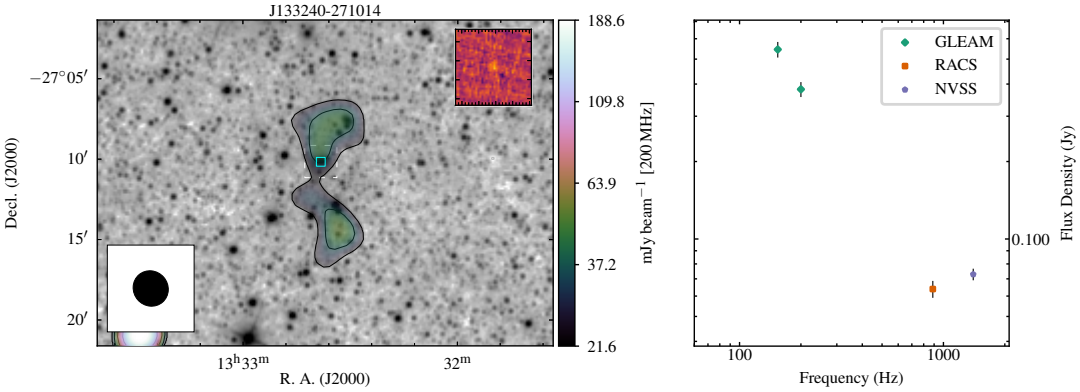

J133240-271014

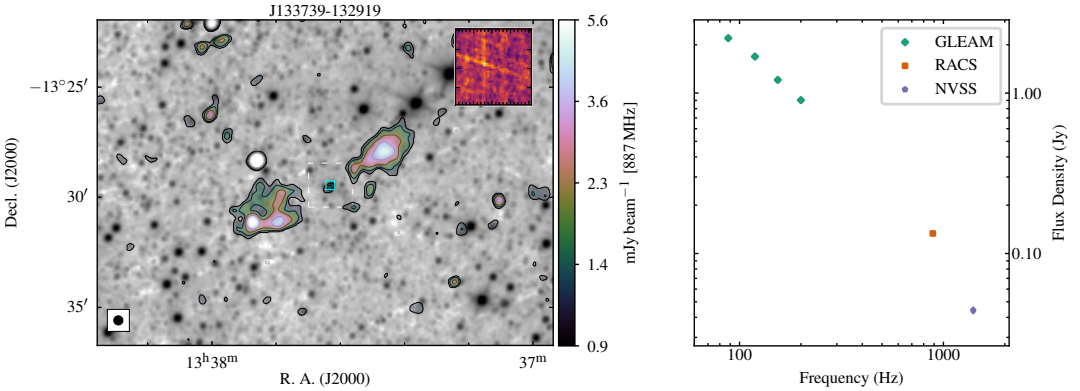

J133739-132919

Figure C.1: Continued

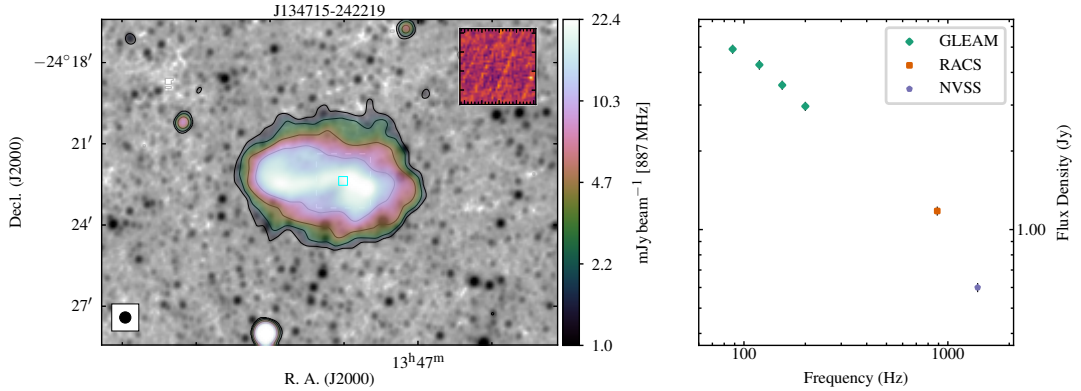

J134715-242219

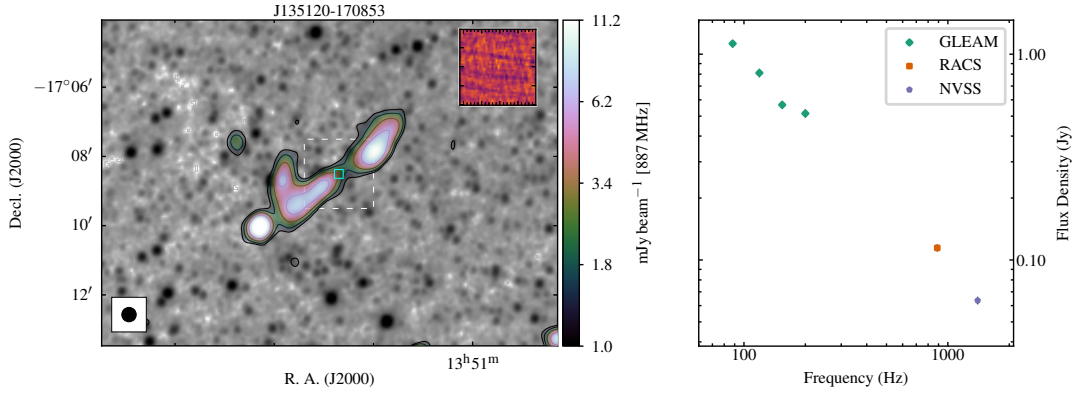

J135120-170853

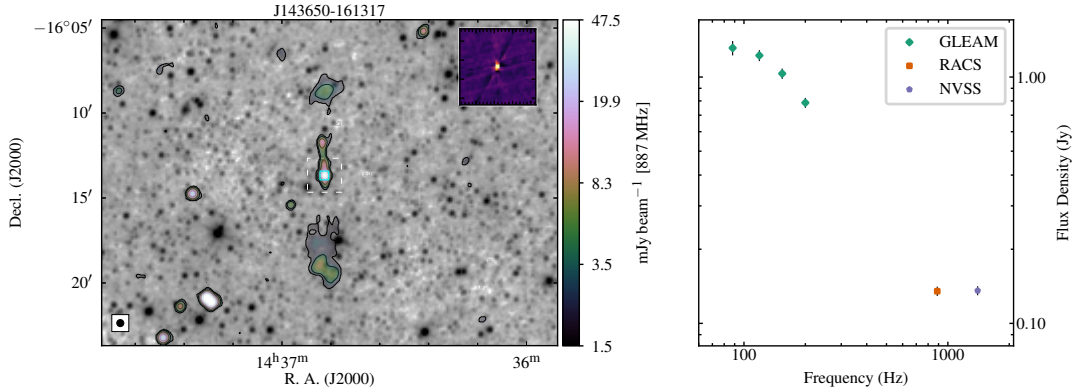

J143650-161317

Figure C.1: Continued

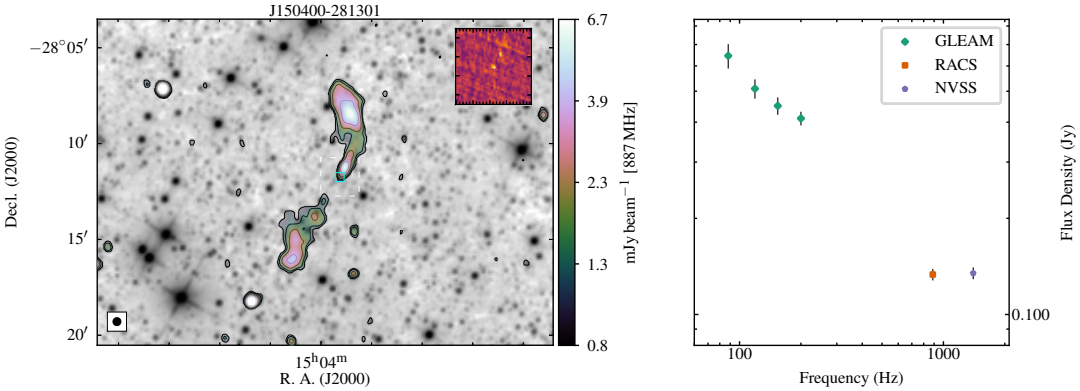

J150400-281301

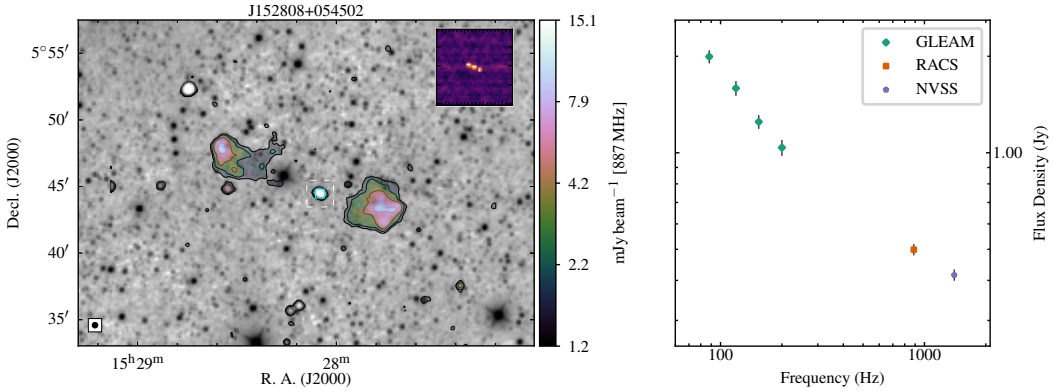

J152808+054502

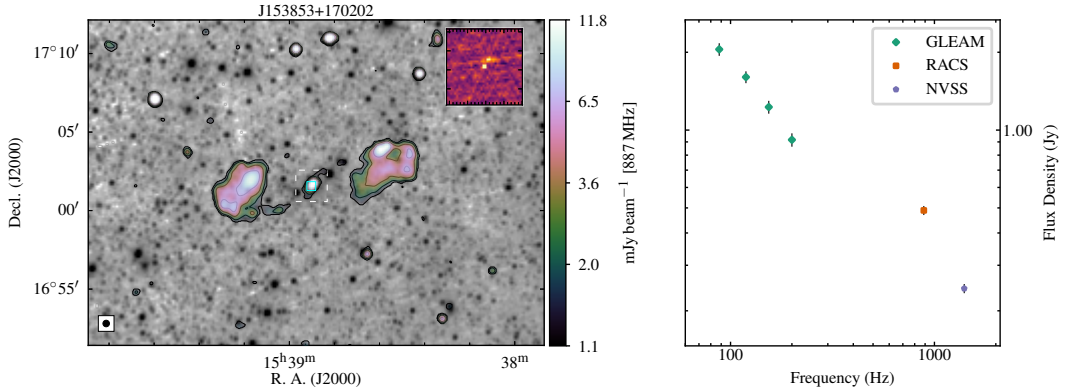

J153853+170202

Figure C.1: Continued

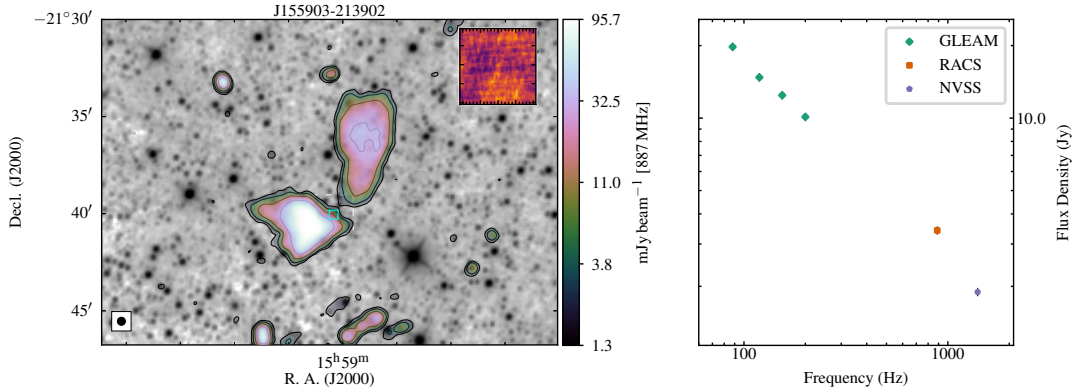

J155903-213902

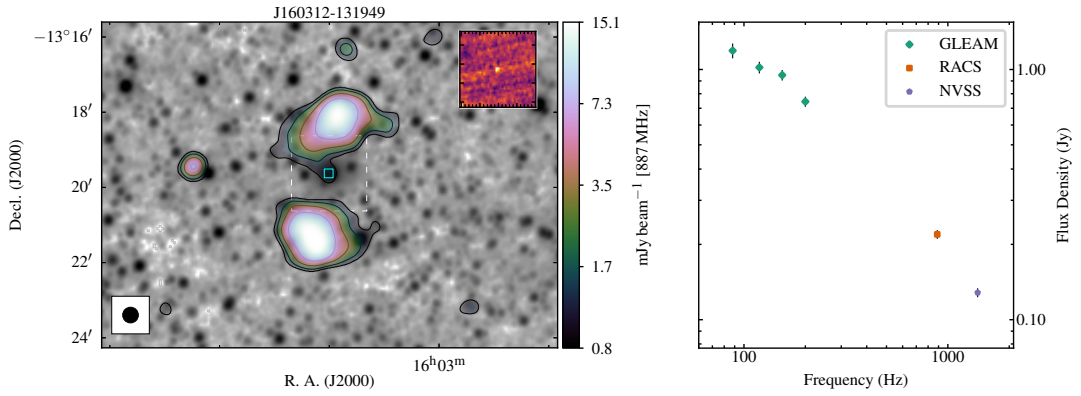

J160312-131949

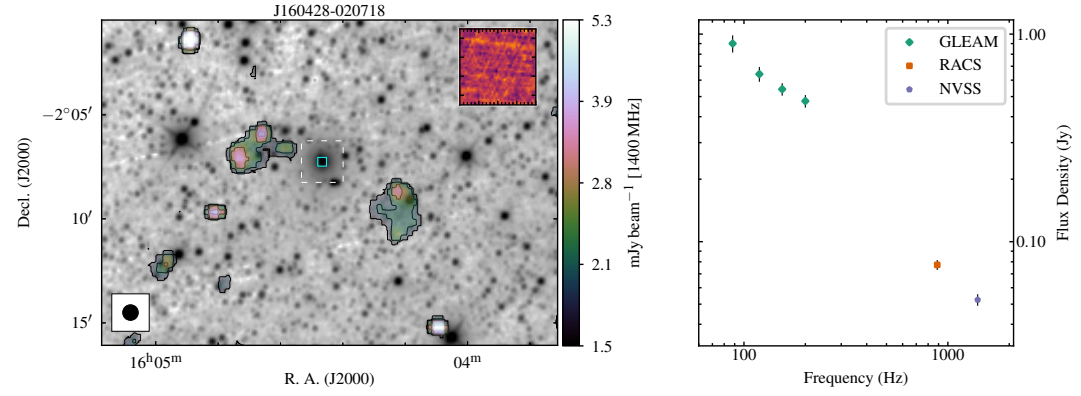

J160428-020718

Figure C.1: Continued

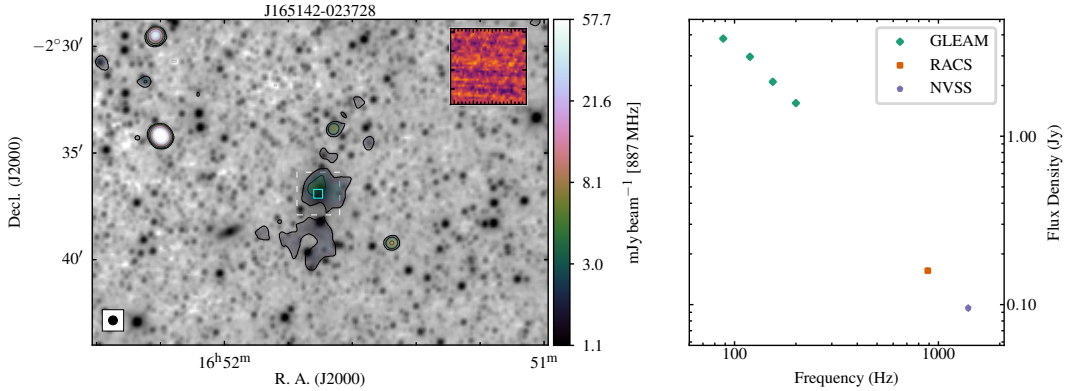

J165142-023728

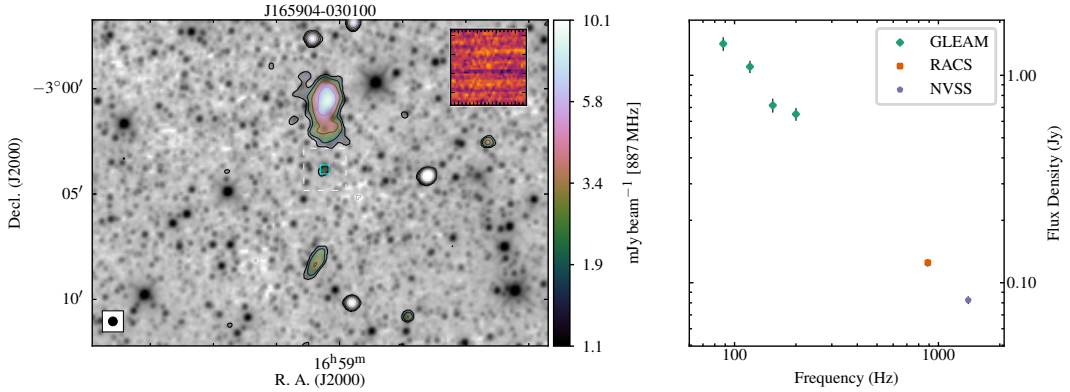

J165904-030100

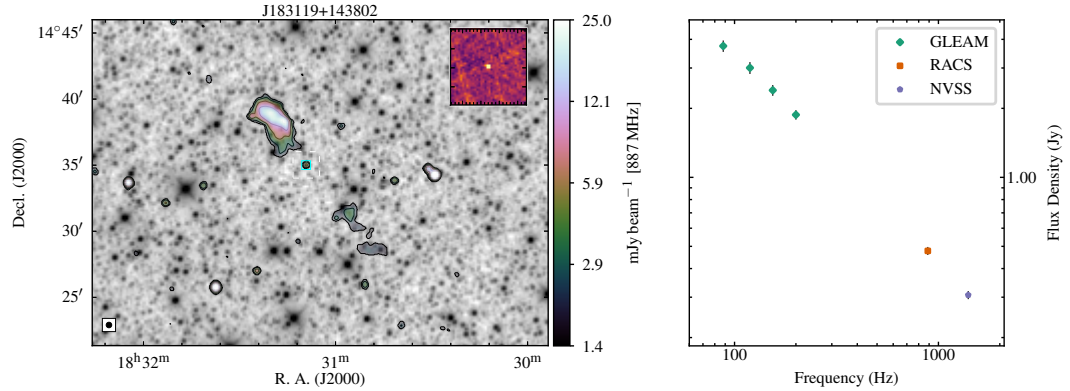

J183119+143802

Figure C.1: Continued

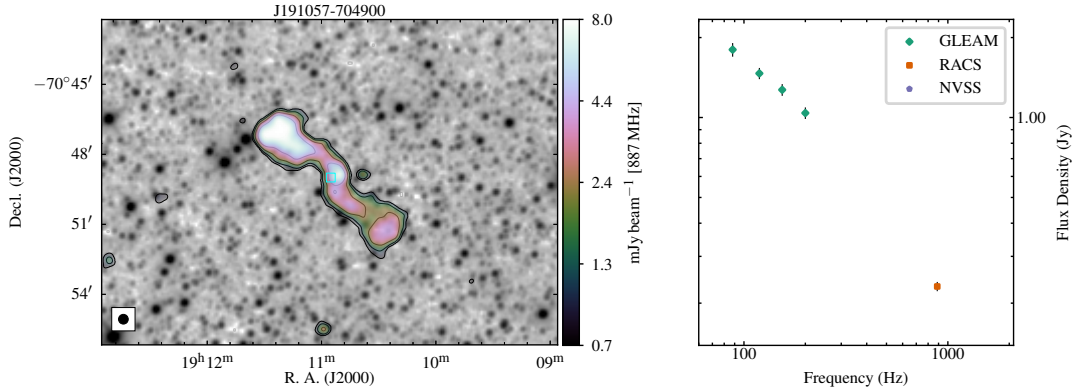

J191057-704900

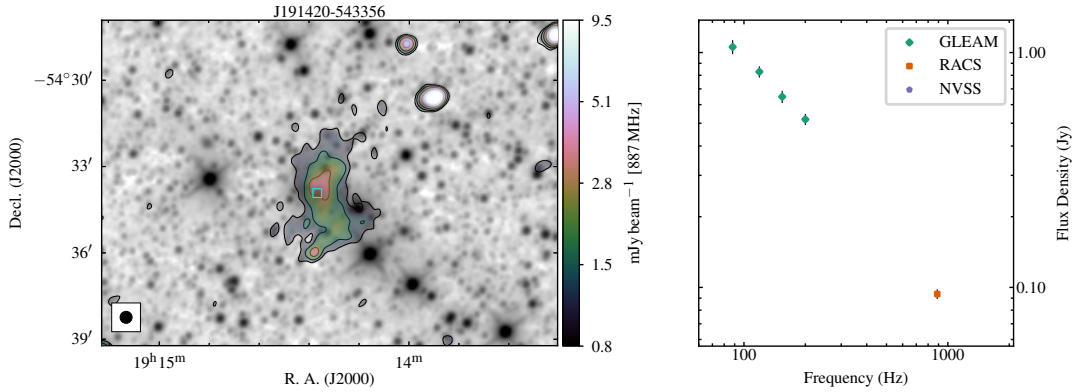

J191420-543356

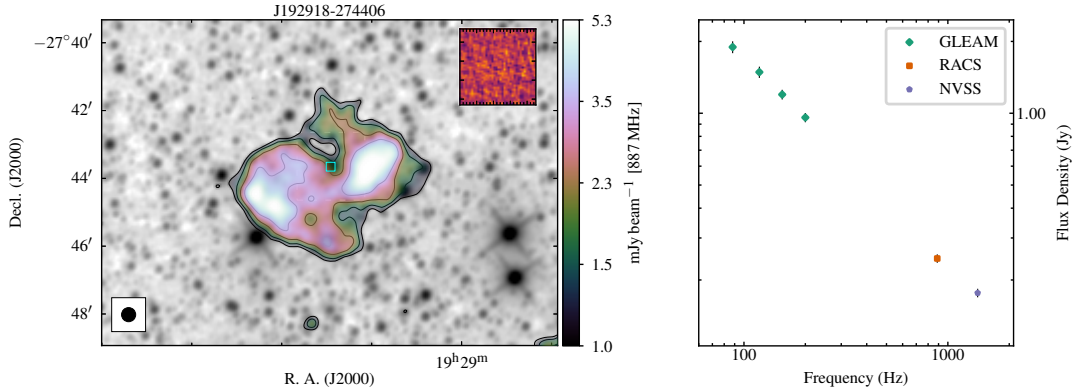

J192918-274406

Figure C.1: Continued

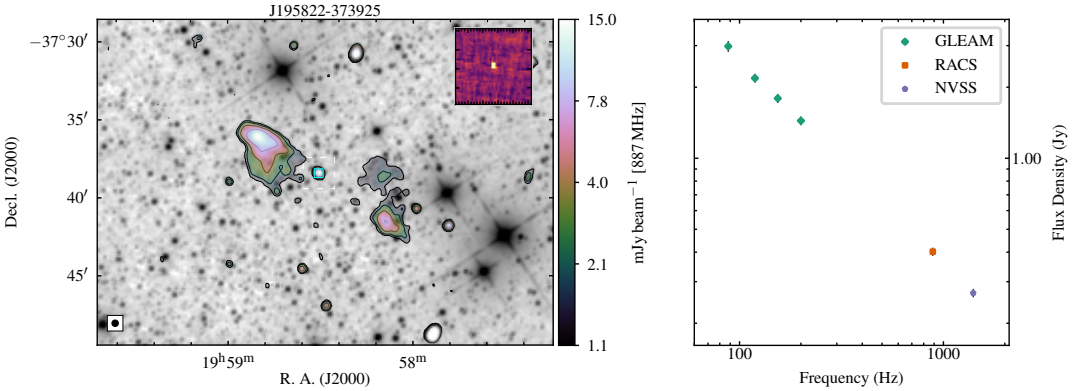

J195822-373925

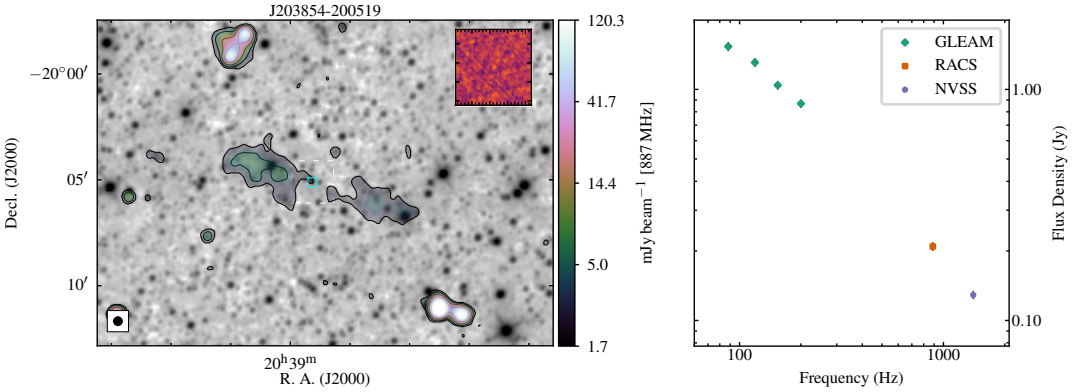

J203854-200519

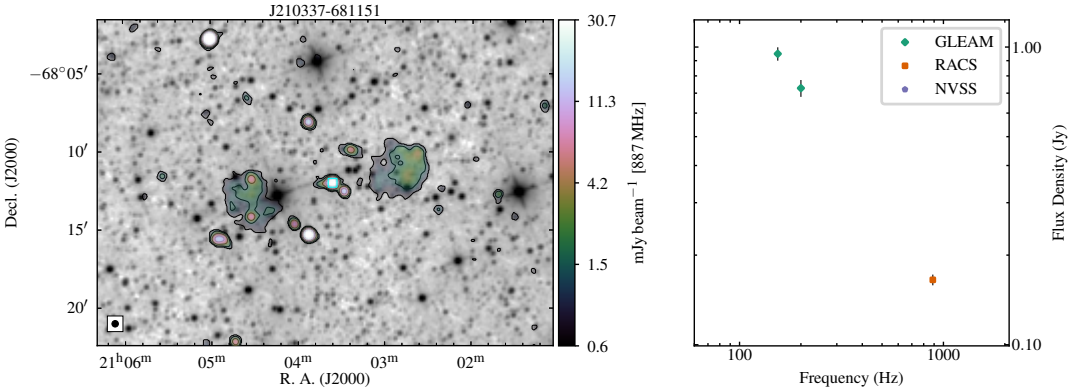

J210337-681151

Figure C.1: Continued

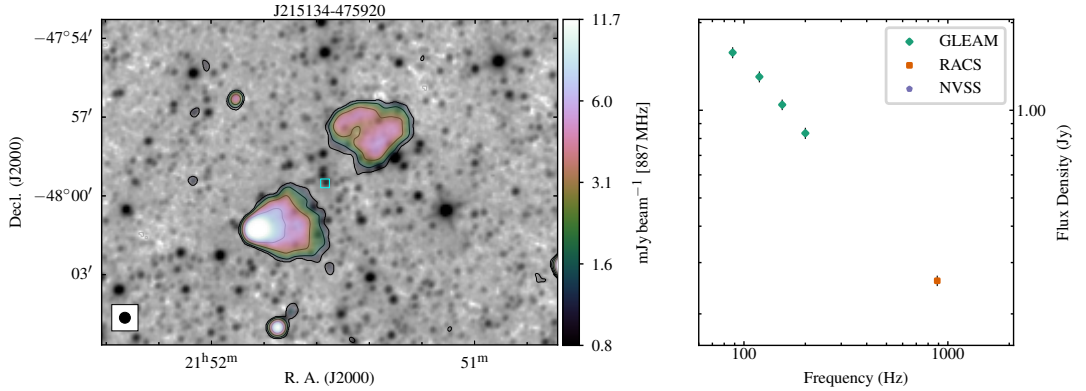

J215134-475920

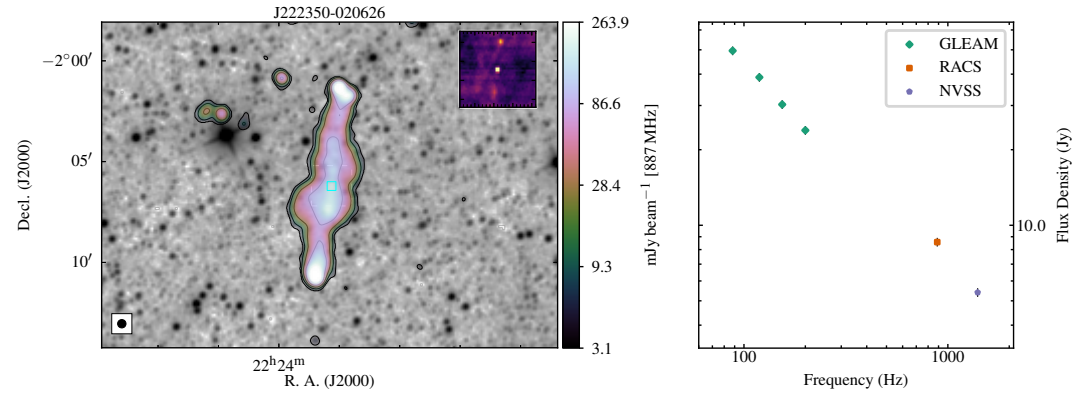

J222350-020626

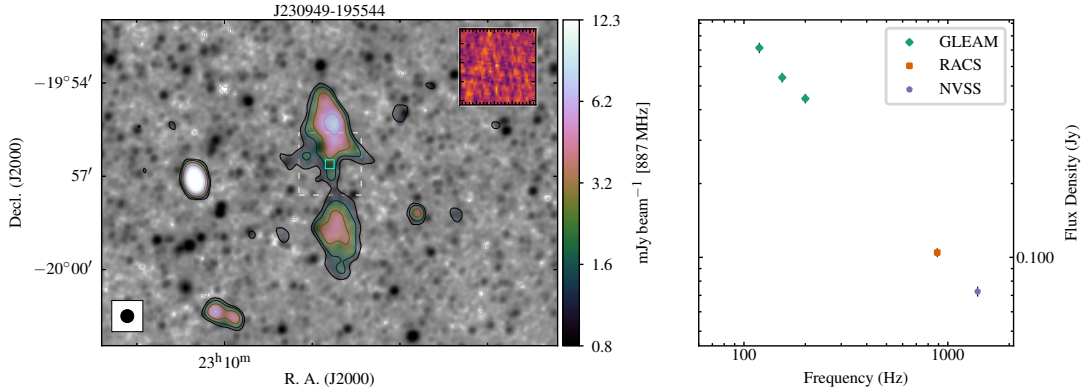

J230949-195544

Figure C.1: Continued

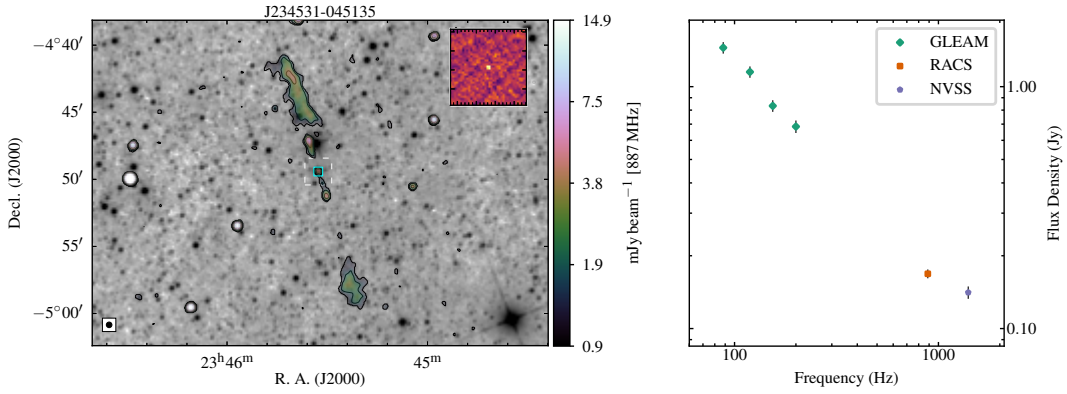

J234531-045135

Figure C.1: Continued

Bibliography

H. Akaike (1974). 'A New Look at the Statistical Model Identification'. *IEEE Transactions on Automatic Control* **19**:716–723.

S. Alam, et al. (2015). 'The Eleventh and Twelfth Data Releases of the Sloan Digital Sky Survey: Final Data from SDSS-III'. *The Astrophysical Journal Supplement Series* **219**(1):12.

D. M. Alexander & R. C. Hickox (2012). 'What drives the growth of black holes?'. *New Astronomy Review* **56**(4):93–121.

P. Alexander (2000). 'Evolutionary models for radio sources from compact sources to classical doubles'. *Monthly Notices of the Royal Astronomical Society* **319**(1):8–16.

S. W. Allen, et al. (2001). 'ASCA and ROSAT observations of nearby cluster cooling flows'. *Monthly Notices of the Royal Astronomical Society* **322**(3):589–613.

H. Andernach, et al. (2021). 'Discovery of 178 Giant Radio Galaxies in 1059 deg2 of the Rapid ASKAP Continuum Survey at 888 MHz'. *Galaxies* **9**(4):99.

Astropy Collaboration, et al. (2013). 'Astropy: A community Python package for astronomy'. *Astronomy and Astrophysics* **558**:A33.

M. Banerji, et al. (2008). 'Photometric redshifts for the Dark Energy Survey and VISTA and implications for large-scale structure'. *Monthly Notices of the Royal Astronomical Society* **386**(3):1219–1233.

P. D. Barthel, et al. (1985a). 'Two-epoch observations of the core radio structure in extended quasars.'. *Astronomy and Astrophysics* **151**:131–136.

P. D. Barthel, et al. (1985b). 'The large and small scale radio structure of 3C 236.'. *Astronomy and Astrophysics* **148**:243–253.

A. P. Beardsley, et al. (2020). 'Science with the Murchison Widefield Array: Phase I results and Phase II opportunities - Corrigendum'. *Publications of the Astronomical Society of Australia* **37**:e014.

S. Bellstedt, et al. (2020). 'Galaxy And Mass Assembly (GAMA): assimilation of KiDS into the GAMA database'. *Monthly Notices of the Royal Astronomical Society* **496**(3):3235–3256.

P. N. Best (2009). 'Radio source populations: Results from SDSS'. *Astronomische Nachrichten* **330**(2):184–189.

P. N. Best, et al. (2005). 'The host galaxies of radio-loud active galactic nuclei: mass dependences, gas cooling and active galactic nuclei feedback'. *Monthly Notices of the Royal Astronomical Society* **362**(1):25–40.

G. Bicknell, et al. (2014). 'Relativistic Jets in Active Galactic Nuclei'. *JPS Conference Proceedings* **2**:015098.

G. V. Bicknell (1995). 'Relativistic Jets and the Fanaroff-Riley Classification of Radio Galaxies'. *The Astrophysical Journal Supplement Series* **101**:29.

J. Binney, et al. (2007). 'Bubbles as tracers of heat input to cooling flows'. *Monthly Notices of the Royal Astronomical Society* **377**(1):142–146.

R. G. Bower, et al. (2006). 'Breaking the hierarchy of galaxy formation'. *Monthly Notices of the Royal Astronomical Society* **370**(2):645–655.

G. B. Brammer, et al. (2008). 'EAZY: A Fast, Public Photometric Redshift Code'. *The Astrophysical Journal* **686**(2):1503–1513.

M. Brienza, et al. (2017). 'Search and modelling of remnant radio galaxies in the LOFAR Lockman Hole field'. *Astronomy and Astrophysics* **606**:A98.

M. Brienza, et al. (2016). 'LOFAR discovery of a 700-kpc remnant radio galaxy at low redshift'. *Astronomy and Astrophysics* **585**:A29.

M. Brienza, et al. (2020a). 'Radio spectral properties and jet duty cycle in the restarted radio galaxy 3C388'. *Astronomy and Astrophysics* **638**:A29.

M. Brienza, et al. (2020b). 'Radio spectral properties and jet duty cycle in the restarted radio galaxy 3C388'. *arXiv e-prints* p. arXiv:2003.13476.

M. Brienza, et al. (2018). 'Duty cycle of the radio galaxy B2 0258+35'. *Astronomy and Astrophysics* **618**:A45.

D. S. Briggs (1995). 'High Fidelity Interferometric Imaging: Robust Weighting and NNLS Deconvolution'. In *American Astronomical Society Meeting Abstracts*, vol. 187 of *American Astronomical Society Meeting Abstracts*, p. 112.02.

G. Bruni, et al. (2019). 'A Discovery of Young Radio Sources in the Cores of Giant Radio Galaxies Selected at Hard X-Rays'. *The Astrophysical Journal* **875**(2):88.

A. Caccianiga, et al. (2017). 'SDSSJ143244.91+301435.3 at VLBI: a compact radio galaxy in a narrow-line Seyfert 1'. *Monthly Notices of the Royal Astronomical Society* **464**(2):1474–1480.

J. R. Callingham, et al. (2017). 'Extragalactic Peaked-spectrum Radio Sources at Low Frequencies'. *The Astrophysical Journal* **836**(2):174.

J. R. Callingham, et al. (2015). 'Broadband Spectral Modeling of the Extreme Gigahertz-peaked Spectrum Radio Source PKS B0008-421'. *The Astrophysical Journal* **809**(2):168.

C. L. Carilli & P. D. Barthel (1996). 'Cygnus A'. *Astronomy and Astrophysics Reviews* **7**(1):1–54.

A. Cattaneo, et al. (2009). 'The role of black holes in galaxy formation and evolution'. *Nature* **460**(7252):213–219.

A. Celotti & A. C. Fabian (1993). 'The kinetic power and luminosity of parsec-scale radio jets - an argument for heavy jets.'. *Monthly Notices of the Royal Astronomical Society* **264**:228–236.

K. C. Chambers, et al. (2016). 'The Pan-STARRS1 Surveys'. *arXiv e-prints* p. arXiv:1612.05560.

Y. Chen, et al. (2007). 'Statistics of X-ray observables for the cooling-core and non-cooling core galaxy clusters'. *Astronomy and Astrophysics* **466**(3):805–812.

E. Churazov, et al. (2001). 'Evolution of Buoyant Bubbles in M87'. *The Astrophysical Journal* **554**(1):261–273.

E. Churazov, et al. (2002). 'Cooling flows as a calorimeter of active galactic nucleus mechanical power'. *Monthly Notices of the Royal Astronomical Society* **332**(3):729–734.

J. J. Condon, et al. (1998). 'The NRAO VLA Sky Survey'. *The Astronomical Journal* **115**(5):1693–1716.

R. A. Cordey (1987). 'IC 2476 - A possible relic radio galaxy'. *Monthly Notices of the Royal Astronomical Society* **227**:695–700.

C. S. Crawford, et al. (1999). 'The ROSAT Brightest Cluster Sample - III. Optical spectra of the central cluster galaxies'. *Monthly Notices of the Royal Astronomical Society* **306**(4):857–896.

R. M. Crockett, et al. (2012). 'Triggered star formation in the inner filament of Centaurus A'. *Monthly Notices of the Royal Astronomical Society* **421**(2):1603–1623.

S. Croft, et al. (2006). 'Minkowski's Object: A Starburst Triggered by a Radio Jet, Revisited'. *The Astrophysical Journal* **647**(2):1040–1055.

J. H. Croston, et al. (2004). 'X-ray emission from the nuclei, lobes and hot-gas environments of two FR II radio galaxies'. *Monthly Notices of the Royal Astronomical Society* **353**(3):879–889.

J. H. Croston, et al. (2018). 'Particle content, radio-galaxy morphology, and jet power: all radio-loud AGN are not equal'. *Monthly Notices of the Royal Astronomical Society* **476**(2):1614–1623.

D. J. Croton, et al. (2006). 'The many lives of active galactic nuclei: cooling flows, black holes and the luminosities and colours of galaxies'. *Monthly Notices of the Royal Astronomical Society* **365**(1):11–28.

R. M. Cutri, et al. (2021). 'VizieR Online Data Catalog: AllWISE Data Release (Cutri+ 2013)'. *VizieR Online Data Catalog* p. II/328.

P. Dabhade, et al. (2017). 'Discovery of giant radio galaxies from NVSS: radio and infrared properties'. *Monthly Notices of the Royal Astronomical Society* **469**(3):2886–2906.

P. Dabhade, et al. (2020). 'Giant radio galaxies in the LOFAR Two-metre Sky Survey. I. Radio and environmental properties'. *Astronomy and Astrophysics* **635**:A5.

D. Dallacasa, et al. (1995). 'A sample of small size compact steep-spectrum radio sources. I. VLBI images at 18 cm.'. *Astronomy and Astrophysics* **295**:27–42.

D. Dallacasa, et al. (2013). 'A sample of small-sized compact steep-spectrum radio sources: VLBI images and VLA polarization at 5 GHz'. *Monthly Notices of the Royal Astronomical Society* **433**(1):147–161.

R. A. Daly (2009). 'Bounds on Black Hole Spins'. *The Astrophysical Journal Letters* **696**(1):L32–L36.

R. A. Daly (2016). 'Spin properties of supermassive black holes with powerful outflows'. *Monthly Notices of the Royal Astronomical Society* **458**(1):L24–L28.

R. A. Daly (2021). 'Black hole mass accretion rates and efficiency factors for over 750 AGN and multiple GBH'. *Monthly Notices of the Royal Astronomical Society* **500**(1):215–231.

K. M. Dasyra & F. Combes (2011). 'Turbulent and fast motions of H_2 gas in active galactic nuclei'. *Astronomy and Astrophysics* **533**:L10.

K. M. Dasyra & F. Combes (2012). 'Cold and warm molecular gas in the outflow of 4C 12.50'. *Astronomy and Astrophysics* **541**:L7.

C. De Breuck, et al. (2000). 'A sample of 669 ultra steep spectrum radio sources to find high redshift radio galaxies'. *Astronomy and Astrophysics Supplement Series* **143**:303–333.

H. R. de Ruiter, et al. (1990). 'VLA observations of low luminosity radio galaxies. VII - General properties'. *Astronomy and Astrophysics* **227**(2):351–361.

J. Delhaize, et al. (2021). 'MIGHTEE: are giant radio galaxies more common than we thought?'. *Monthly Notices of the Royal Astronomical Society* **501**(3):3833–3845.

M. Donahue, et al. (2000). 'Hubble Space Telescope Observations of Vibrationally Excited Molecular Hydrogen in Cluster Cooling Flow Nebulae'. *The Astrophysical Journal* **545**(2):670–694.

S. P. Driver, et al. (2016). 'The Wide Area VISTA Extra-Galactic Survey (WAVES)'. In N. R. Napolitano, G. Longo, M. Marconi, M. Paolillo, & E. Iodice (eds.), *The Universe of Digital Sky Surveys*, vol. 42 of *Astrophysics and Space Science Proceedings*, p. 205.

S. P. Driver, et al. (2011). 'Galaxy and Mass Assembly (GAMA): survey diagnostics and core data release'. *Monthly Notices of the Royal Astronomical Society* **413**(2):971–995.

G. Drouart, et al. (2020). 'The GLEAMing of the first supermassive black holes'. *Publications of the Astronomical Society of Australia* **37**:e026.

Y. Dubois, et al. (2014). 'Black hole evolution - III. Statistical properties of mass growth and spin evolution using large-scale hydrodynamical cosmological simulations'. *Monthly Notices of the Royal Astronomical Society* **440**(2):1590–1606.

S. W. Duchesne & M. Johnston-Hollitt (2019). 'The remnant radio galaxy associated with NGC 1534'. *Publications of the Astronomical Society of Australia* **36**:e016.

S. W. Duchesne, et al. (2020). 'Murchison Widefield Array detection of steep-spectrum, diffuse, non-thermal radio emission within Abell 1127'. *Publications of the Astronomical Society of Australia* **37**:e037.

P. Duffy & K. M. Blundell (2012). 'The non-thermal emission of extended radio galaxy lobes with curved electron spectra'. *Monthly Notices of the Royal Astronomical Society* **421**(1):108–115.

Z. Dugan, et al. (2017). 'Feedback by AGN Jets and Wide-angle Winds on a Galactic Scale'. *The Astrophysical Journal* **844**(1):37.

A. C. Edge (2001). 'The detection of molecular gas in the central galaxies of cooling flow clusters'. *Monthly Notices of the Royal Astronomical Society* **328**(3):762–782.

A. C. Edge, et al. (2002). 'A survey of molecular hydrogen in the central galaxies of cooling flows'. *Monthly Notices of the Royal Astronomical Society* **337**(1):49–62.

B. H. C. Emonts, et al. (2014). 'Outflow of hot and cold molecular gas from the obscured secondary nucleus of NGC 3256: closing in on feedback physics'. *Astronomy and Astrophysics* **572**:A40.

W. English, et al. (2016). 'Numerical modelling of the lobes of radio galaxies in cluster environments - III. Powerful relativistic and non-relativistic jets'. *Monthly Notices of the Royal Astronomical Society* **461**(2):2025–2043.

W. English, et al. (2019). 'Numerical modelling of the lobes of radio galaxies in cluster environments - IV. Remnant radio galaxies'. *Monthly Notices of the Royal Astronomical Society* **490**(4):5807–5819.

G. Fabbiano, et al. (1989). 'Radio Emission and the Hot Interstellar Medium of Early-Type Galaxies'. *The Astrophysical Journal* **347**:127.

A. C. Fabian (2012). 'Observational Evidence of Active Galactic Nuclei Feedback'. *Annual Review of Astronomy and Astrophysics* **50**:455–489.

A. C. Fabian, et al. (2003). 'A deep Chandra observation of the Perseus cluster: shocks and ripples'. *Monthly Notices of the Royal Astronomical Society* **344**(3):L43–L47.

A. C. Fabian, et al. (2000). 'Chandra imaging of the complex X-ray core of the Perseus cluster'. *Monthly Notices of the Royal Astronomical Society* **318**(4):L65–L68.

A. C. Fabian, et al. (2006). 'A very deep Chandra observation of the Perseus cluster: shocks, ripples and conduction'. *Monthly Notices of the Royal Astronomical Society* **366**(2):417–428.

S. A. E. G. Falle (1991). 'Self-similar jets.'. *Monthly Notices of the Royal Astronomical Society* **250**:581–596.

B. L. Fanaroff & J. M. Riley (1974). 'The morphology of extragalactic radio sources of high and low luminosity'. *Monthly Notices of the Royal Astronomical Society* **167**:31P–36P.

C. Fanti (2009). 'Radio properties of CSSs and GPSs'. *Astronomische Nachrichten* **330**(2):120–127.

L. Feretti, et al. (1984). 'High resolution radio and X-ray observations of A115.'. *Astronomy and Astrophysics* **139**:50–54.

C. Feruglio, et al. (2015). 'The multi-phase winds of Markarian 231: from the hot, nuclear, ultra-fast wind to the galaxy-scale, molecular outflow'. *Astronomy and Astrophysics* **583**:A99.

W. Forman, et al. (2005). 'Reflections of Active Galactic Nucleus Outbursts in the Gaseous Atmosphere of M87'. *The Astrophysical Journal* **635**(2):894–906.

T. M. O. Franzen, et al. (2021). 'The GLEAM 200-MHz local radio luminosity function for AGN and star-forming galaxies'. *Publications of the Astronomical Society of Australia* **38**:e041.

R. H. Frater, et al. (1992). 'The Australia Telescope - Overview'. *Journal of Electrical and Electronics Engineering Australia* **12**(2):103–112.

J. M. Gabor & F. Bournaud (2013). 'Simulations of supermassive black hole growth in high-redshift disc galaxies'. *Monthly Notices of the Royal Astronomical Society* **434**(1):606–620.

M. Gaspari, et al. (2017). 'Raining on black holes and massive galaxies: the top-down multiphase condensation model'. *Monthly Notices of the Royal Astronomical Society* **466**(1):677–704.

A. Ginsburg, et al. (2019). 'astroquery: An Astronomical Web-querying Package in Python'. *The Astronomical Journal* **157**:98.

G. Giovannini, et al. (1988). 'Radio nuclei in elliptical galaxies.'. *Astronomy and Astrophysics* **199**:73–84.

L. E. H. Godfrey, et al. (2017). 'On the population of remnant Fanaroff-Riley type II radio galaxies and implications for radio source dynamics'. *Monthly Notices of the Royal Astronomical Society* **471**(1):891–907.

L. E. H. Godfrey & S. S. Shabala (2013). 'AGN Jet Kinetic Power and the Energy Budget of Radio Galaxy Lobes'. *The Astrophysical Journal* **767**(1):12.

J. Graham, et al. (2008). 'The weak shock in the core of the Perseus cluster'. *Monthly Notices of the Royal Astronomical Society* **386**(1):278–288.

M. Gu, et al. (2009). 'The bulk kinetic power of radio jets in active galactic nuclei'. *Monthly Notices of the Royal Astronomical Society* **396**(2):984–996.

K. Gültekin, et al. (2009). 'The M-σ and M-L Relations in Galactic Bulges, and Determinations of Their Intrinsic Scatter'. *The Astrophysical Journal* **698**(1):198–221.

G. Gürkan, et al. (2022). 'Deep ASKAP EMU Survey of the GAMA23 field: properties of radio sources'. *Monthly Notices of the Royal Astronomical Society* **512**(4):6104–6121.

P. J. Hancock, et al. (2012). 'Compact continuum source finding for next generation radio surveys'. *Monthly Notices of the Royal Astronomical Society* **422**(2):1812–1824.

P. J. Hancock, et al. (2018). 'Source Finding in the Era of the SKA (Precursors): Aegean 2.0'. *Publications of the Astronomical Society of Australia* **35**:e011.

M. J. Hardcastle (2013). 'Synchrotron and inverse-Compton emission from radio galaxies with non-uniform magnetic field and electron distributions'. *Monthly Notices of the Royal Astronomical Society* **433**(4):3364–3372.

M. J. Hardcastle (2018). 'A simulation-based analytic model of radio galaxies'. *Monthly Notices of the Royal Astronomical Society* **475**(2):2768–2786.

M. J. Hardcastle & M. G. H. Krause (2013). 'Numerical modelling of the lobes of radio galaxies in cluster environments'. *Monthly Notices of the Royal Astronomical Society* **430**(1):174–196.

M. J. Hardcastle & M. G. H. Krause (2014). 'Numerical modelling of the lobes of radio galaxies in cluster environments - II. Magnetic field configuration and observability'. *Monthly Notices of the Royal Astronomical Society* **443**(2):1482–1499.

M. J. Hardcastle & L. W. Looney (2008). 'The properties of powerful radio sources at 90 GHz'. *Monthly Notices of the Royal Astronomical Society* **388**(1):176–186.

M. J. Hardcastle, et al. (2019). 'Radio-loud AGN in the first LoTSS data release. The lifetimes and environmental impact of jet-driven sources'. *Astronomy and Astrophysics* **622**:A12.

N. Häring & H.-W. Rix (2004). 'On the Black Hole Mass-Bulge Mass Relation'. *The Astrophysical Journal Letters* **604**(2):L89–L92.

C. M. Harrison (2017). 'Impact of supermassive black hole growth on star formation'. *Nature Astronomy* **1**:0165.

J. J. Harwood (2017). 'Spectral ageing in the era of big data: integrated versus resolved models'. *Monthly Notices of the Royal Astronomical Society* **466**(3):2888–2894.

J. J. Harwood, et al. (2016). 'FR II radio galaxies at low frequencies - I. Morphology, magnetic field strength and energetics'. *Monthly Notices of the Royal Astronomical Society* **458**(4):4443–4455.

J. J. Harwood, et al. (2015). 'Spectral ageing in the lobes of cluster-centre FR II radio galaxies'. *Monthly Notices of the Royal Astronomical Society* **454**(4):3403–3422.

J. J. Harwood, et al. (2013). 'Spectral ageing in the lobes of FR-II radio galaxies: new methods of analysis for broad-band radio data'. *Monthly Notices of the Royal Astronomical Society* **435**(4):3353–3375.

N. A. Hatch, et al. (2005). 'Detections of molecular hydrogen in the outer filaments of NGC1275'. *Monthly Notices of the Royal Astronomical Society* **358**(3):765–773.

T. M. Heckman, et al. (1989). 'Dynamical, Physical, and Chemical Properties of Emission-Line Nebulae in Cooling Flows'. *The Astrophysical Journal* **338**:48.

T. M. Heckman & P. N. Best (2014). 'The Coevolution of Galaxies and Supermassive Black Holes: Insights from Surveys of the Contemporary Universe'. *Annual Review of Astronomy and Astrophysics* **52**:589–660.

A. S. Hoffer, et al. (2012). 'Infrared and Ultraviolet Star Formation in Brightest Cluster Galaxies in the ACCEPT Sample'. *The Astrophysical Journal Supplement Series* **199**(1):23.

D. S. Hudson, et al. (2010). 'What is a cool-core cluster? a detailed analysis of the cores of the X-ray flux-limited HIFLUGCS cluster sample'. *Astronomy and Astrophysics* **513**:A37.

N. Hurley-Walker, et al. (2017). 'GaLactic and Extragalactic All-sky Murchison Widefield Array (GLEAM) survey - I. A low-frequency extragalactic catalogue'. *Monthly Notices of the Royal Astronomical Society* **464**(1):1146–1167.

N. Hurley-Walker, et al. (2019). 'Candidate radio supernova remnants observed by the GLEAM survey over 345° < l < 60° and 180° < l < 240°'. *Publications of the Astronomical Society of Australia* **36**:e048.

N. Hurley-Walker, et al. (2015). 'Serendipitous discovery of a dying Giant Radio Galaxy associated with NGC 1534, using the Murchison Widefield Array'. *Monthly Notices of the Royal Astronomical Society* **447**(3):2468–2478.

M. T. Huynh, et al. (2015). 'The ATLAS 5.5 GHz survey of the extended Chandra Deep Field South: the second data release'. *Monthly Notices of the Royal Astronomical Society* **454**(1):952–972.

M. T. Huynh, et al. (2020). 'The ATLAS 9.0 GHz survey of the extended Chandra Deep Field South: the faint 9.0 GHz radio population'. *Monthly Notices of the Royal Astronomical Society* **491**(3):3395–3410.

J. Ineson, et al. (2017). 'A representative survey of the dynamics and energetics of FR II radio galaxies'. *Monthly Notices of the Royal Astronomical Society* **467**(2):1586–1607.

H. T. Intema, et al. (2017). 'The GMRT 150 MHz all-sky radio survey. First alternative data release TGSS ADR1'. *Astronomy and Astrophysics* **598**:A78.

C. H. Ishwara-Chandra, et al. (2020). 'A wide-area GMRT 610-MHz survey of ELAIS N1 field'. *Monthly Notices of the Royal Astronomical Society* **497**(4):5383–5394.

W. J. Jaffe & G. C. Perola (1973). 'Dynamical Models of Tailed Radio Sources in Clusters of Galaxies'. *Astronomy and Astrophysics* **26**:423.

M. Jamrozy, et al. (2004). 'Spectral ageing in the relic radio galaxy B2 0924+30'. *Astronomy and Astrophysics* **427**:79–86.

M. Jarvis, et al. (2016). 'The MeerKAT International GHz Tiered Extragalactic Exploration (MIGHTEE) Survey'. In *MeerKAT Science: On the Pathway to the SKA*, p. 6.

S. Johnston, et al. (2007). 'Science with the Australian Square Kilometre Array Pathfinder'. *Publications of the Astronomical Society of Australia* **24**(4):174–188.

R. M. Johnstone, et al. (1987). 'The optical spectra of central galaxies in southern clusters : evidence for star formation.'. *Monthly Notices of the Royal Astronomical Society* **224**:75–91.

J. Jonas & MeerKAT Team (2016). 'The MeerKAT Radio Telescope'. In *MeerKAT Science: On the Pathway to the SKA*, p. 1.

S. G. Jorstad, et al. (2001). 'Multiepoch Very Long Baseline Array Observations of EGRET-detected Quasars and BL Lacertae Objects: Superluminal Motion of Gamma-Ray Bright Blazars'. *The Astrophysical Journal Supplement Series* **134**(2):181–240.

W. A. Joye & E. Mandel (2003). 'New Features of SAOImage DS9'. In H. E. Payne, R. I. Jedrzejewski, & R. N. Hook (eds.), *Astronomical Data Analysis Software and Systems XII*, vol. 295 of *Astronomical Society of the Pacific Conference Series*, p. 489.

N. Jurlin, et al. (2021). 'Multi-frequency characterisation of remnant radio galaxies in the Lockman Hole field'. *Astronomy and Astrophysics* **653**:A110.

N. Jurlin, et al. (2020). 'The life cycle of radio galaxies in the LOFAR Lockman Hole field'. *Astronomy and Astrophysics* **638**:A34.

C. R. Kaiser & P. Alexander (1997). 'A self-similar model for extragalactic radio sources'. *Monthly Notices of the Royal Astronomical Society* **286**(1):215–222.

C. R. Kaiser & P. N. Best (2007). 'Luminosity function, sizes and FR dichotomy of radio-loud AGN'. *Monthly Notices of the Royal Astronomical Society* **381**(4):1548–1560.

C. R. Kaiser, et al. (1997). 'Evolutionary tracks of FRII sources through the P-D diagram'. *Monthly Notices of the Royal Astronomical Society* **292**(3):723–732.

D. Kakkad, et al. (2018). 'Spatially resolved electron density in the narrow line region of z ¡ 0.02 radio AGNs'. *Astronomy and Astrophysics* **618**:A6.

R. Kale & C. H. Ishwara-Chandra (2021). 'CAPTURE: a continuum imaging pipeline for the uGMRT'. *Experimental Astronomy* **51**(1):95–108.

A. D. Kapinska, et al. (2015). 'Unravelling lifecycles and physics of radio-loud AGN in the SKA Era'. In *Advancing Astrophysics with the Square Kilometre Array (AASKA14)*, p. 173.

N. S. Kardashev (1962). 'Nonstationarity of Spectra of Young Sources of Non-thermal Radio Emission'. *Soviet Astronomy* **6**:317.

S. Kaviraj, et al. (2015). 'The triggering of local AGN and their role in regulating star formation'. *Monthly Notices of the Royal Astronomical Society* **452**(1):774–783.

N. Kawakatu, et al. (2016). 'Evidence for a significant mixture of electron/-positron pairs in FRII jets constrained by cocoon dynamics'. *Monthly Notices of the Royal Astronomical Society* **457**(1):1124–1136.

K. I. Kellermann, et al. (2004). 'Sub-Milliarcsecond Imaging of Quasars and Active Galactic Nuclei. III. Kinematics of Parsec-scale Radio Jets'. *The Astrophysical Journal* **609**(2):539–563.

K. I. Kellermann, et al. (1989). 'VLA Observations of Objects in the Palomar Bright Quasar Survey'. *The Astronomical Journal* **98**:1195.

E. Komatsu, et al. (2011). 'Seven-year Wilkinson Microwave Anisotropy Probe (WMAP) Observations: Cosmological Interpretation'. *The Astrophysical Journal Supplement Series* **192**(2):18.

S. S. Komissarov & A. G. Gubanov (1994). 'Relic radio galaxies: evolution of synchrotron spectrum'. *Astronomy and Astrophysics* **285**:27–43.

C. Konar, et al. (2012). 'Rejuvenated radio galaxies J0041+3224 and J1835+6204: how long can the quiescent phase of nuclear activity last?'. *Monthly Notices of the Royal Astronomical Society* **424**(2):1061–1076.

A. V. Kravtsov & S. Borgani (2012). 'Formation of Galaxy Clusters'. *Annual Review of Astronomy and Astrophysics* **50**:353–409.

J. H. Krolik (1999). *Active galactic nuclei : from the central black hole to the galactic environment*.

M. Lacy, et al. (2020). 'The Karl G. Jansky Very Large Array Sky Survey (VLASS). Science Case and Survey Design'. *Publications of the ASP* **132**(1009):035001.

M. Lacy, et al. (2019). 'The Karl G. Jansky Very Large Array Sky Survey (VLASS). Science case, survey design and initial results'. *arXiv e-prints* p. arXiv:1907.01981.

R. A. Laing (1994). 'Decelerating Relativistic Jets in FRI Radio Sources'. In G. V. Bicknell, M. A. Dopita, & P. J. Quinn (eds.), *The Physics of Active Galaxies*, vol. 54 of *Astronomical Society of the Pacific Conference Series*, p. 227.

R. A. Laing & J. A. Peacock (1980). 'The relation between radio luminosity and spectrum for extended extragalactic radio sources.'. *Monthly Notices of the Royal Astronomical Society* **190**:903–924.

L. Lara, et al. (1999). 'Restarting activity in the giant radio galaxy J1835+620'. *Astronomy and Astrophysics* **348**:699–704.

S. M. Lea, et al. (1973). 'Thermal-Bremsstrahlung Interpretation of Cluster X-Ray Sources'. *The Astrophysical Journal Letters* **184**:L105.

J. P. Leahy, et al. (2013). 'An Atlas of DRAGNs'. An Atlas of DRAGNs, edited by J.P. Leahy et al. Online at ¡A href="http://www.jb.man.ac.uk/atlas/"¿http://www.jb.man.ac.uk/atlas/¡/A¿.

M. J. Ledlow (1994). 'Radio Galaxies in Abell Rich Clusters'. In *American Astronomical Society Meeting Abstracts #184*, vol. 184 of *American Astronomical Society Meeting Abstracts*, p. 17.02.

M. Lima, et al. (2008). 'Estimating the redshift distribution of photometric galaxy samples'. *Monthly Notices of the Royal Astronomical Society* **390**(1):118–130.

J. Liske, et al. (2015). 'Galaxy And Mass Assembly (GAMA): end of survey report and data release 2'. *Monthly Notices of the Royal Astronomical Society* **452**(2):2087–2126.

M. S. Longair (2011). *High Energy Astrophysics*.

M. S. Longair & S. J. Lilly (1984). 'Identifications and spectra of extragalactic radio sources.'. *Journal of Astrophysics and Astronomy* **5**:349–368.

D. Lynden-Bell (1969). 'Galactic Nuclei as Collapsed Old Quasars'. *Nature* **223**(5207):690–694.

J. Magorrian, et al. (1998). 'The Demography of Massive Dark Objects in Galaxy Centers'. *The Astronomical Journal* **115**(6):2285–2305.

V. H. Mahatma (2023). 'The Dynamics and Energetics of Remnant and Restarting RLAGN'. *Galaxies* **11**(3):74.

V. H. Mahatma, et al. (2020). 'Investigating the spectral age problem with powerful radio galaxies'. *Monthly Notices of the Royal Astronomical Society* **491**(4):5015–5034.

V. H. Mahatma, et al. (2019). 'LoTSS DR1: Double-double radio galaxies in the HETDEX field'. *Astronomy and Astrophysics* **622**:A13.

V. H. Mahatma, et al. (2018). 'Remnant radio-loud AGN in the Herschel-ATLAS field'. *Monthly Notices of the Royal Astronomical Society* **475**(4):4557–4578.

M. A. Marshall, et al. (2018). 'Triggering active galactic nuclei in galaxy clusters'. *Monthly Notices of the Royal Astronomical Society* **474**(3):3615–3628.

D. McConnell, et al. (2016). 'The Australian Square Kilometre Array Pathfinder: Performance of the Boolardy Engineering Test Array'. *Publications of the Astronomical Society of Australia* **33**:e042.

D. McConnell, et al. (2020). 'The Rapid ASKAP Continuum Survey I: Design and first results'. *Publications of the Astronomical Society of Australia* **37**:e048.

M. McDonald, et al. (2012). 'A massive, cooling-flow-induced starburst in the core of a luminous cluster of galaxies'. *Nature* **488**(7411):349–352.

M. McDonald, et al. (2010). 'On the Origin of the Extended Hα Filaments in Cooling Flow Clusters'. *The Astrophysical Journal* **721**(2):1262–1283.

M. McDonald, et al. (2011). 'Star Formation Efficiency in the Cool Cores of Galaxy Clusters'. *The Astrophysical Journal* **734**(2):95.

J. P. McMullin, et al. (2007). 'CASA Architecture and Applications'. In R. A. Shaw, F. Hill, & D. J. Bell (eds.), *Astronomical Data Analysis Software and Systems XVI*, vol. 376 of *Astronomical Society of the Pacific Conference Series*, p. 127.

B. R. McNamara & P. E. J. Nulsen (2007). 'Heating Hot Atmospheres with Active Galactic Nuclei'. *Annual Review of Astronomy and Astrophysics* **45**(1):117–175.

B. R. McNamara & P. E. J. Nulsen (2012). 'Mechanical feedback from active galactic nuclei in galaxies, groups and clusters'. *New Journal of Physics* **14**(5):055023.

B. R. McNamara & R. W. O'Connell (1989). 'Star formation in cooling flows in clusters of galaxies.'. *The Astronomical Journal* **98**:2018–2043.

B. R. McNamara, et al. (2000). 'Chandra X-Ray Observations of the Hydra A Cluster: An Interaction between the Radio Source and the X-Ray-emitting Gas'. *The Astrophysical Journal Letters* **534**(2):L135–L138.

D. L. Meier (1999). 'A Magnetically Switched, Rotating Black Hole Model for the Production of Extragalactic Radio Jets and the Fanaroff and Riley Class Division'. *The Astrophysical Journal* **522**(2):753–766.

G. Miley (1980). 'The structure of extended extragalactic radio sources'. *Annual Review of Astronomy and Astrophysics* **18**:165–218.

R. Mittal, et al. (2009). 'AGN heating and ICM cooling in the HIFLUGCS sample of galaxy clusters'. *Astronomy and Astrophysics* **501**(3):835–850.

S. Molendi, et al. (2016). 'Where does the gas fueling star formation in brightest cluster galaxies originate?'. *Astronomy and Astrophysics* **595**:A123.

R. Morganti (2017a). 'Archaeology of active galaxies across the electromagnetic spectrum'. *Nature Astronomy* **1**:596–605.

R. Morganti (2017b). 'The many routes to AGN feedback'. *Frontiers in Astronomy and Space Sciences* **4**:42.

R. Morganti, et al. (2013). 'Radio Jets Clearing the Way Through a Galaxy: Watching Feedback in Action'. *Science* **341**(6150):1082–1085.

R. Morganti & T. Oosterloo (2018). 'The interstellar and circumnuclear medium of active nuclei traced by H i 21 cm absorption'. **26**(1):4.

R. Morganti, et al. (2015). 'The fast molecular outflow in the Seyfert galaxy IC 5063 as seen by ALMA'. *Astronomy and Astrophysics* **580**:A1.

R. Morganti, et al. (2021). 'Taking snapshots of the jet-ISM interplay: The case of PKS 0023-26'. *Astronomy and Astrophysics* **656**:A55.

D. Mukherjee, et al. (2021). 'Resolved simulations of jet–ISM interaction: Implications for gas dynamics and star formation'. *Astronomische Nachrichten* **342**(1140):1140–1145.

L. M. Mullin, et al. (2008). 'Observed properties of FRII quasars and radio galaxies at z < 1.0'. *Monthly Notices of the Royal Astronomical Society* **390**(2):595–621.

M. Murgia, et al. (2011). 'Dying radio galaxies in clusters'. *Astronomy and Astrophysics* **526**:A148.

S. T. Myers & S. R. Spangler (1985). 'Synchrotron aging in the lobes of luminous radio galaxies.'. *The Astrophysical Journal* **291**:52–62.

H. Nagai, et al. (2006). 'The Kinematic and Spectral Ages of the Compact Radio Source CTD 93'. *The Astrophysical Journal* **648**(1):148–157.

N. P. H. Nesvadba, et al. (2008). 'Evidence for powerful AGN winds at high redshift: dynamics of galactic outflows in radio galaxies during the "Quasar Era"'. *Astronomy and Astrophysics* **491**(2):407–424.

R. P. Norris (2011). 'Evolutionary Map of the Universe: Tracing Clusters to High Red-shift'. *Journal of Astrophysics and Astronomy* **32**(4):599–607.

G. S. Novak, et al. (2011). 'Feedback from Central Black Holes in Elliptical Galaxies: Two-dimensional Models Compared to One-dimensional Models'. *The Astrophysical Journal* **737**(1):26.

C. P. O'Dea (1998). 'The Compact Steep-Spectrum and Gigahertz Peaked-Spectrum Radio Sources'. **110**(747):493–532.

C. P. O'Dea & S. A. Baum (1997). 'Constraints on Radio Source Evolution from the Compact Steep Spectrum and GHz Peaked Spectrum Radio Sources'. *The Astronomical Journal* **113**:148–161.

C. P. O'Dea, et al. (2008). 'An Infrared Survey of Brightest Cluster Galaxies. II. Why are Some Brightest Cluster Galaxies Forming Stars?'. *The Astrophysical Journal* **681**(2):1035–1045.

C. P. O'Dea, et al. (1991). 'What Are the Gigahertz Peaked-Spectrum Radio Sources?'. *The Astrophysical Journal* **380**:66.

C. P. O'Dea, et al. (2009). 'Physical properties of very powerful FRII radio galaxies'. *Astronomy and Astrophysics* **494**(2):471–488.

A. R. Offringa, et al. (2014). 'WSClean: Widefield interferometric imager'.

A. R. Offringa & O. Smirnov (2017). 'An optimized algorithm for multiscale wideband deconvolution of radio astronomical images'. *Monthly Notices of the Royal Astronomical Society* **471**(1):301–316.

A. R. Offringa, et al. (2012). 'A morphological algorithm for improving radio-frequency interference detection'. *Astronomy and Astrophysics* **539**:A95.

T. Oosterloo, et al. (2010). 'The latest on Apertif'. In J. van Leeuwen (ed.), *ISKAF2010 Science Meeting*, p. 43.

M. Orienti (2016). 'Radio properties of Compact Steep Spectrum and GHz-Peaked Spectrum radio sources'. *Astronomische Nachrichten* **337**(1-2):9.

M. Orienti, et al. (2010). 'The last breath of the young gigahertz-peaked spectrum radio source PKS1518+047'. *Monthly Notices of the Royal Astronomical Society* **402**(3):1892–1898.

I. Owsianik & J. E. Conway (1998). 'First detection of hotspot advance in a Compact Symmetric Object. Evidence for a class of very young extragalactic radio sources'. *Astronomy and Astrophysics* **337**:69–79.

H. Oyaizu, et al. (2008). 'A Galaxy Photometric Redshift Catalog for the Sloan Digital Sky Survey Data Release 6'. *The Astrophysical Journal* **674**(2):768–783.

A. G. Pacholczyk (1970). 'Radio astrophysics. Nonthermal processes in galactic and extragalactic sources'. In *Series of Books in Astronomy and Astrophysics*.

P. Padovani, et al. (2017). 'Active galactic nuclei: what's in a name?'. **25**(1):2.

L. Page, et al. (2003). 'First-Year Wilkinson Microwave Anisotropy Probe (WMAP) Observations: Interpretation of the TT and TE Angular Power Spectrum Peaks'. *The Astrophysical Journal Supplement Series* **148**(1):233–241.

P. Parma, et al. (2007). 'In search of dying radio sources in the local universe'. *Astronomy and Astrophysics* **470**(3):875–888.

R. Penrose & R. M. Floyd (1971). 'Extraction of Rotational Energy from a Black Hole'. *Nature Physical Science* **229**(6):177–179.

C. B. Peres, et al. (1998). 'A ROSAT study of the cores of clusters of galaxies - I. Cooling flows in an X-ray flux-limited sample'. *Monthly Notices of the Royal Astronomical Society* **298**(2):416–432.

K. A. Pimbblet, et al. (2013). 'The drivers of AGN activity in galaxy clusters: AGN fraction as a function of mass and environment'. *Monthly Notices of the Royal Astronomical Society* **429**(2):1827–1839.

B. G. Piner, et al. (2006). 'The Fastest Relativistic Jets: VLBA Observations of Blazars with Apparent Speeds Exceeding 25c'. *The Astrophysical Journal* **640**(1):196–203.

Planck Collaboration, et al. (2014). 'Planck 2013 results. XVI. Cosmological parameters'. *Astronomy and Astrophysics* **571**:A16.

Planck Collaboration, et al. (2016). 'Planck 2015 results. XIII. Cosmological parameters'. *Astronomy and Astrophysics* **594**:A13.

E. C. D. Pope, et al. (2012). 'Investigating the properties of active galactic nucleus feedback in hot atmospheres triggered by cooling-induced gravitational collapse'. *Monthly Notices of the Royal Astronomical Society* **419**(1):50–56.

P. Predehl, et al. (2021). 'The eROSITA X-ray telescope on SRG'. *Astronomy and Astrophysics* **647**:A1.

A. M. Price-Whelan, et al. (2018). 'The Astropy Project: Building an Open-science Project and Status of the v2.0 Core Package'. *The Astronomical Journal* **156**:123.

B. Quici, et al. (2021). 'Remnant radio galaxies discovered in a multi-frequency survey'. *Publications of the Astronomical Society of Australia* **38**:e008.

B. Quici, et al. (2022). 'Selecting and modelling remnant AGNs with limited spectral coverage'. *Monthly Notices of the Royal Astronomical Society* **514**(3):3466–3484.

Z. Randriamanakoto, et al. (2020). 'J1615+5452: a remnant radio galaxy in the ELAIS-N1 field'. *Monthly Notices of the Royal Astronomical Society* **496**(3):3381–3389.

M. Raouf, et al. (2017). 'The many lives of active galactic nuclei-II: The formation and evolution of radio jets and their impact on galaxy evolution'. *Monthly Notices of the Royal Astronomical Society* **471**(1):658–670.

M. Raouf, et al. (2019). 'Feedback by supermassive black holes in galaxy evolution: impacts of accretion and outflows on the star formation rate'. *Monthly Notices of the Royal Astronomical Society* **486**(2):1509–1522.

S. Rawlings & M. J. Jarvis (2004). 'Evidence that powerful radio jets have a profound influence on the evolution of galaxies'. *Monthly Notices of the Royal Astronomical Society* **355**(3):L9–L12.

J. E. Reynolds (1994). 'A Revised Flux Scale for the AT Compact Array'. ATNF Internal Memo AT/39.3/040, Australia Telescope National Facility.

A. S. G. Robotham, et al. (2018). 'ProFound: Source Extraction and Application to Modern Survey Data'. *Monthly Notices of the Royal Astronomical Society* **476**(3):3137–3159.

B. Rocca-Volmerange, et al. (2004). 'The radio galaxy K-z relation: The 10^{12} $M_{\odot}$ mass limit. Masses of galaxies from the L_K luminosity, up to z > 4'. *Astronomy and Astrophysics* **415**:931–940.

K. Roettiger, et al. (1994). 'Relic Radio Emission in 3C 388'. *The Astrophysical Journal Letters* **421**:L23.

K. Ross, et al. (2023). 'Milliarcsecond structures of variable-peaked spectrum sources'. *Publications of the Astronomical Society of Australia* **40**:e005.

G. B. Rybicki & A. P. Lightman (1979). *Radiative processes in astrophysics*.

J. Sabater, et al. (2019). 'The LoTSS view of radio AGN in the local Universe. The most massive galaxies are always switched on'. *Astronomy and Astrophysics* **622**:A17.

E. M. Sadler (1990). 'Elliptical galaxies - getting to the heart.'. *Publications of the Astronomical Society of Australia* **8**(3):238–242.

E. M. Sadler, et al. (1989). 'Low-luminosity radio sources in early-type galaxies.'. *Monthly Notices of the Royal Astronomical Society* **240**:591–635.

D. J. Saikia & M. Jamrozy (2009). 'Recurrent activity in Active Galactic Nuclei'. *Bulletin of the Astronomical Society of India* **37**:63–89.

D. J. Saikia, et al. (2006). 'J0041+3224: a new double-double radio galaxy'. *Monthly Notices of the Royal Astronomical Society* **366**(4):1391–1398.

J. S. Sanders & A. C. Fabian (2008). 'Sound waves in the intracluster medium of the Centaurus cluster'. *Monthly Notices of the Royal Astronomical Society* **390**(1):L93–L97.

J. S. Sanders, et al. (2008). 'Cool X-ray emitting gas in the core of the Centaurus cluster of galaxies'. *Monthly Notices of the Royal Astronomical Society* **385**(3):1186–1200.

L. Saripalli, et al. (2012). 'ATLBS Extended Source Sample: The Evolution in Radio Source Morphology with Flux Density'. *The Astrophysical Journal Supplement Series* **199**(2):27.

R. J. Sault, et al. (1995). 'A Retrospective View of MIRIAD'. In R. A. Shaw, H. E. Payne, & J. J. E. Hayes (eds.), *Astronomical Data Analysis Software and Systems IV*, vol. 77 of *Astronomical Society of the Pacific Conference Series*, p. 433.

J. Schaye, et al. (2015). 'The EAGLE project: simulating the evolution and assembly of galaxies and their environments'. *Monthly Notices of the Royal Astronomical Society* **446**(1):521–554.

P. A. G. Scheuer (1974). 'Models of extragalactic radio sources with a continuous energy supply from a central object'. *Monthly Notices of the Royal Astronomical Society* **166**:513–528.

A. P. Schoenmakers, et al. (2001). 'A new sample of giant radio galaxies from the WENSS survey. I. Sample definition, selection effects and first results'. *Astronomy and Astrophysics* **374**:861–870.

A. P. Schoenmakers, et al. (2000). 'Radio galaxies with a 'double-double morphology' - I. Analysis of the radio properties and evidence for interrupted activity in active galactic nuclei'. *Monthly Notices of the Royal Astronomical Society* **315**(2):371–380.

S. Shabala & P. Alexander (2009). 'Radio Source Feedback in Galaxy Evolution'. *The Astrophysical Journal* **699**(1):525–538.

S. S. Shabala, et al. (2008). 'The duty cycle of local radio galaxies'. *Monthly Notices of the Royal Astronomical Society* **388**(2):625–637.

S. S. Shabala & L. E. H. Godfrey (2013). 'Size Dependence of the Radio-luminosity-Mechanical-power Correlation in Radio Galaxies'. *The Astrophysical Journal* **769**(2):129.

S. S. Shabala, et al. (2020). 'The duty cycle of radio galaxies revealed by LOFAR: remnant and restarted radio source populations in the Lockman Hole'. *Monthly Notices of the Royal Astronomical Society* **496**(2):1706–1717.

T. W. Shimwell, et al. (2022). 'The LOFAR Two-metre Sky Survey. V. Second data release'. *Astronomy and Astrophysics* **659**:A1.

T. W. Shimwell, et al. (2019). 'The LOFAR Two-metre Sky Survey. II. First data release'. *Astronomy and Astrophysics* **622**:A1.

A. Shulevski, et al. (2015). 'AGN duty cycle estimates for the ultra-steep spectrum radio relic VLSS J1431.8+1331'. *Astronomy and Astrophysics* **583**:A89.

A. Shulevski, et al. (2017). 'Radiative age mapping of the remnant radio galaxy B2 0924+30: the LOFAR perspective'. *Astronomy and Astrophysics* **600**:A65.

A. Shulevski, et al. (2012). 'Recurrent radio emission and gas supply: the radio galaxy B2 0258+35'. *Astronomy and Astrophysics* **545**:A91.

A. K. Singal (1988). 'Cosmic evolution of the physical sizes of extragalactic radio sourcesand their luminosity-size correlation.'. *Monthly Notices of the Royal Astronomical Society* **233**:87–113.

V. Singh, et al. (2021). 'Remnant Radio Galaxy Candidates of Small Angular Sizes'. *Galaxies* **9**(4):121.

D. J. B. Smith, et al. (2016). 'The WEAVE-LOFAR Survey'. In C. Reylé, J. Richard, L. Cambrésy, M. Deleuil, E. Pécontal, L. Tresse, & I. Vauglin (eds.), *SF2A-2016: Proceedings of the Annual meeting of the French Society of Astronomy and Astrophysics*, pp. 271–280.

V. Smolčić, et al. (2017). 'The VLA-COSMOS 3 GHz Large Project: Cosmic evolution of radio AGN and implications for radio-mode feedback since z 5'. *Astronomy and Astrophysics* **602**:A6.

I. A. G. Snellen, et al. (2000). 'On the evolution of young radio-loud AGN'. *Monthly Notices of the Royal Astronomical Society* **319**(2):445–456.

C. Stanghellini, et al. (2005). 'Extended emission around GPS radio sources'. *Astronomy and Astrophysics* **443**(3):891–902.

R. Subrahmanyan, et al. (1996). 'Morphologies in megaparsec-size powerful radio galaxies'. *Monthly Notices of the Royal Astronomical Society* **279**(1):257–274.

G. Tabor & J. Binney (1993). 'Elliptical galaxy cooling flows without mass drop-out.'. *Monthly Notices of the Royal Astronomical Society* **263**:323–334.

C. Tadhunter (2008). 'The importance of sub-relativistic outflows in AGN host galaxies .'. *Mem. Societa Astronomica Italiana* **79**:1205.

E. N. Taylor, et al. (2011). 'Galaxy And Mass Assembly (GAMA): stellar mass estimates'. *Monthly Notices of the Royal Astronomical Society* **418**(3):1587–1620.

M. B. Taylor (2005). 'TOPCAT & STIL: Starlink Table/VOTable Processing Software'. In P. Shopbell, M. Britton, & R. Ebert (eds.), *Astronomical Data Analysis Software and Systems XIV*, vol. 347 of *Astronomical Society of the Pacific Conference Series*, p. 29.

A. R. Thompson, et al. (1980). 'The Very Large Array.'. *The Astrophysical Journal Supplement Series* **44**:151–167.

S. J. Tingay, et al. (2013). 'The Murchison Widefield Array: The Square Kilometre Array Precursor at Low Radio Frequencies'. *Publications of the Astronomical Society of Australia* **30**:e007.

S. J. Tingay, et al. (2015). 'The Spectral Variability of the GHz-Peaked Spectrum Radio Source PKS 1718-649 and a Comparison of Absorption Models'. *The Astronomical Journal* **149**(2):74.

S. Tinti & G. de Zotti (2006). 'Constraints on evolutionary properties of GHz Peaked Spectrum galaxies'. *Astronomy and Astrophysics* **445**(3):889–899.

F. Tombesi, et al. (2015). 'Wind from the black-hole accretion disk driving a molecular outflow in an active galaxy'. *Nature* **519**(7544):436–438.

C. Tortora, et al. (2009). 'AGN jet-induced feedback in galaxies - II. Galaxy colours from a multicloud simulation'. *Monthly Notices of the Royal Astronomical Society* **396**(1):61–77.

G. R. Tremblay, et al. (2010). 'Episodic Star Formation Coupled to Reignition of Radio Activity in 3C 236'. *The Astrophysical Journal* **715**(1):172–185.

P. C. Tribble (1991). 'Radio emission in random magnetic field : radio haloes and the structure of the magnetic field in the Coma cluster.'. *Monthly Notices of the Royal Astronomical Society* **253**:147.

P. C. Tribble (1993). 'Radio spectral ageing in a random magnetic field.'. *Monthly Notices of the Royal Astronomical Society* **261**:57–62.

P. C. Tribble (1994). 'Synchrotron Emission in a Random Magnetic Field - the Effect of Spectral Ageing on Radio Images'. *Monthly Notices of the Royal Astronomical Society* **269**:110.

R. J. Turner (2018). 'Duty-cycle and energetics of remnant radio-loud AGN'. *Monthly Notices of the Royal Astronomical Society* **476**(2):2522–2529.

R. J. Turner, et al. (2020). 'RAiSERed: radio continuum redshifts for lobed active galactic nuclei'. *Monthly Notices of the Royal Astronomical Society* **499**(3):3660–3672.

R. J. Turner, et al. (2018a). 'RAiSE II: resolved spectral evolution in radio AGN'. *Monthly Notices of the Royal Astronomical Society* **473**(3):4179–4196.

R. J. Turner & S. S. Shabala (2015). 'Energetics and Lifetimes of Local Radio Active Galactic Nuclei'. *The Astrophysical Journal* **806**(1):59.

R. J. Turner & S. S. Shabala (2019). 'Cosmology with powerful radio-loud AGNs'. *Monthly Notices of the Royal Astronomical Society* **486**(1):1225–1235.

R. J. Turner & S. S. Shabala (2020). 'RAiSE X: searching for radio galaxies in X-ray surveys'. *Monthly Notices of the Royal Astronomical Society* **493**(4):5181–5194.

R. J. Turner & S. S. Shabala (2023). 'Dynamics of Powerful Radio Galaxies'. *Galaxies* **11**(4):87.

R. J. Turner, et al. (2018b). 'RAiSE III: 3C radio AGN energetics and composition'. *Monthly Notices of the Royal Astronomical Society* **474**(3):3361–3379.

R. J. Turner, et al. (2022). 'RAiSE: simulation-based analytical model of AGNjets and lobes'. *Monthly Notices of the Royal Astronomical Society* .

R. J. Turner, et al. (2023). 'RAiSE: simulation-based analytical model of AGN jets and lobes'. *Monthly Notices of the Royal Astronomical Society* **518**(1):945–964.

A. Tzioumis, et al. (2002). 'A sample of southern Compact Steep Spectrum radio sources: The VLBI observations'. *Astronomy and Astrophysics* **392**:841–850.

W. van Breugel, et al. (1984). 'Studies of kiloparsec-scale, steep-spectrum radio cores. I. VLA maps.'. *The Astronomical Journal* **89**:5–22.

S. van der Walt, et al. (2011). 'The NumPy Array: A Structure for Efficient Numerical Computation'. *Computing in Science Engineering* **13**(2):22–30.

M. P. van Haarlem, et al. (2013). 'LOFAR: The LOw-Frequency ARray'. *Astronomy and Astrophysics* **556**:A2.

A. Vikhlinin, et al. (2006). 'Chandra Sample of Nearby Relaxed Galaxy Clusters: Mass, Gas Fraction, and Mass-Temperature Relation'. *The Astrophysical Journal* **640**(2):691–709.

M. Vogelsberger, et al. (2014). 'Introducing the Illustris Project: simulating the coevolution of dark and visible matter in the Universe'. *Monthly Notices of the Royal Astronomical Society* **444**(2):1518–1547.

R. B. Wayth, et al. (2015). 'GLEAM: The GaLactic and Extragalactic All-Sky MWA Survey'. *Publications of the Astronomical Society of Australia* **32**:e025.

R. B. Wayth, et al. (2018). 'The Phase II Murchison Widefield Array: Design overview'. *Publications of the Astronomical Society of Australia* **35**:33.

R. Weinberger, et al. (2018). 'Supermassive black holes and their feedback effects in the IllustrisTNG simulation'. *Monthly Notices of the Royal Astronomical Society* **479**(3):4056–4072.

D. A. White, et al. (1997). 'An investigation of cooling flows and general cluster properties from an X-ray image deprojection analysis of 207 clusters of galaxies'. *Monthly Notices of the Royal Astronomical Society* **292**(2):419–467.

S. D. M. White & M. J. Rees (1978). 'Core condensation in heavy halos: a two-stage theory for galaxy formation and clustering.'. *Monthly Notices of the Royal Astronomical Society* **183**:341–358.

S. V. White, et al. (2020a). 'The GLEAM 4-Jy (G4Jy) Sample: I. Definition and the catalogue'. *Publications of the Astronomical Society of Australia* **37**:e018.

S. V. White, et al. (2020b). 'The GLEAM 4-Jy (G4Jy) Sample: II. Host galaxy identification for individual sources'. *Publications of the Astronomical Society of Australia* **37**:e017.

P. N. Wilkinson, et al. (1984). 'Peculiar radio structure in the quasar 3C380'. *Nature* **308**(5960):619–621.

A. G. Willis, et al. (1974). '3C236, DA240; the largest radio sources known'. *Nature* **250**(5468):625–630.

C. J. Willott, et al. (1999). 'The emission line-radio correlation for radio sources using the 7C Redshift Survey'. *Monthly Notices of the Royal Astronomical Society* **309**(4):1017–1033.

W. E. Wilson, et al. (2011). 'The Australia Telescope Compact Array Broadband Backend: description and first results'. *Monthly Notices of the Royal Astronomical Society* **416**(2):832–856.

C. Wolf, et al. (2018). 'SkyMapper Southern Survey: First Data Release (DR1)'. *Publications of the Astronomical Society of Australia* **35**:e010.

J.-H. Woo & C. M. Urry (2002). 'Active Galactic Nucleus Black Hole Masses and Bolometric Luminosities'. *The Astrophysical Journal* **579**(2):530–544.

D. M. Worrall & M. Birkinshaw (2014). 'Sliding not Sloshing in A3744: The Influence of Radio Galaxies NGC 7018 and 7016 on Cluster Gas'. *The Astrophysical Journal* **784**(1):36.

D. M. Worrall, et al. (2012). 'The jet-cloud interacting radio galaxy PKS B2152-699 - I. Structures revealed in new deep radio and X-ray observations'. *Monthly Notices of the Royal Astronomical Society* **424**(2):1346–1362.

E. L. Wright, et al. (2010). 'The Wide-field Infrared Survey Explorer (WISE): Mission Description and Initial On-orbit Performance'. *The Astronomical Journal* **140**(6):1868–1881.

P. M. Yates, et al. (2018). 'Observability of intermittent radio sources in galaxy groups and clusters'. *Monthly Notices of the Royal Astronomical Society* **480**(4):5286–5306.

P. M. Yates-Jones, et al. (2021). 'Dynamics of relativistic radio jets in asymmetric environments'. *Monthly Notices of the Royal Astronomical Society* **508**(4):5239–5250.

P. M. Yates-Jones, et al. (2022). 'PRAiSE: resolved spectral evolution in simulated radio sources'. *Monthly Notices of the Royal Astronomical Society* **511**(4):5225–5240.

N. L. Zakamska & J. E. Greene (2014). 'Quasar feedback and the origin of radio emission in radio-quiet quasars'. *Monthly Notices of the Royal Astronomical Society* **442**(1):784–804.